

ABSTRACT

Title of dissertation: **DISTURBANCE REJECTION
FOR U.A.S. AIRCRAFT USING
BIO-INSPIRED STRAIN SENSING**

Lina Castano, Doctor of Philosophy, 2015

Dissertation directed by: **Professor Sean J. Humbert
Department of Aerospace Engineering**

A bio inspired gust rejection mechanism based on structural inputs is proposed. Insect wings possess a wealth of sensor systems which typically consist of fast reflexive neuronal paths. Stretch and strain sensors on insect wings are used for flight control and can be found across many species. These are used for monitoring of bending and torsion during flight. The fast reflexive and proprioceptive mechanisms based on strain sensing found in nature are the inspiration for this work. A strain feedback controller allows for anticipation of the onset of rigid body dynamics due to gust perturbations. This anticipation stems from sensing of higher order states and the possibility of reacting before lower order states are reached. High bandwidth inner loop compensation is therefore enabled. Forces and moments are proportional to wing strain patterns and can be used in fast reaction inner loops. Strain sensors are used for providing an indirect estimation of the differential forces applied to the aircraft wing and therefore to the aircraft rigid body. These sensors can be distributed over the surface of the aircraft wing to encode multiple degree

of freedom disturbances. Sensor locations for disturbance rejection are determined based on metrics associated to the observability Grammian. The locations are pre-selected based on modal energy analyses and are chosen according to wide field integration patterns. A model for wide field integrated strain based on mass participation factors is proposed as well as one which is based on the physics of the forces and moments acting on the wing producing strain patterns which can be used for disturbance rejection. Models of the differential forces via strains on the wings are proposed. Strain feedback was implemented in four platforms under different types of disturbances. The platforms consisted of a glider, a quadrotor, a wing section for wind tunnel testing and an RC airplane with a full span wing. The disturbances included discrete gusts as well as turbulence. The results of using strain feedback showed not only to be faster than IMU estimations but also to be better when compared to a classical attitude controller implementation.

DISTURBANCE REJECTION FOR U.A.S. AIRCRAFT
USING BIO-INSPIRED STRAIN SENSING

by

Lina Castano

Dissertation submitted to the Faculty of the Graduate School of the
University of Maryland, College Park in partial fulfillment
of the requirements for the degree of
Doctor of Philosophy
2015

Advisory Committee:
Professor Sean J. Humbert, Chair/Advisor
Professor Inderjit Chopra
Professor Alison Flatau
Professor James Baeder
Professor Amr Baz, Dean's Representative

© Copyright by
Lina Maria Castano Salcedo
2015

Acknowledgments

I would like to acknowledge a number of people without whom this degree would not have been possible, or at least extremely unfeasible. Thank you God for allowing me to be part of this wonderful research institution and to learn every day from its wonderful professors, peers and friends. Physics for undergrad gave me the tools for understanding engineering problems, however engineering is a challenging field on its own and I am grateful to all the people who contributed to this work one way or the other in many different areas.

My gratitude goes out to my parents Flor and Fernando, and uncle Alvaro for their love and support during these years of being away and for encouraging me every single day, no matter what. Being an only child, their constant encouragement allowed me to have resilience among many life and academic circumstances. Thanks as well to friends Ps. Mario and Leonor, for their support and encouragement as well as aunt Cielo, who was also there during these years. I would like to thank a couple of special friends, Rosalia and Zohaib. Rosalia, thank you for the opportunity of joining Maryland, I love this place! and you are an amazing person. Thanks for your friendship and mentor-ship along the way. Zohaib thank you for your help along these years and for being a solid friend, thank you for your friendship. You are an amazing academic and person.

To my sponsors, Aurora Flight Sciences for supporting my degree, and Tony Thompson, from the USAF, whose vision gave birth to the inspiration of this wonderful project. Thanks also to Riley, program manager for the PWings project for

being great to work with. Thanks also to Simone and Terrence for the work with the glider while visiting UMD.

To Dr. Humbert, my advisor, thank you for giving me the opportunity to grow and become productive in the Autonomous Vehicle Lab (AVL). I appreciate the exciting project I worked on for this degree and which I will continue to develop. Thank you for sharing your controls expertise throughout your courses, I think the world of controls now!

Thanks also to Dr. Chopra, Dr. Flatau, Dr. Baeder and Dr. Baz, the dean's representative, for being part of my committee. I appreciate your time and feedback.

I would like to thank the AVL folks as well. Greg, thanks for being a colleague in the lab with whom it was always great to work with, thanks for your help and work collaboration. Thanks Hector, Badri and Alex for your help at different instances in time. Julia, thanks for being a great office mate and for helping out as well.

I would also like to thank Dr. Winkelmann and his lab, for supporting my projects throughout the years on many fronts: hardware, supplies, lab space, etc. The time as Dr. Winkelmann's TA in my second semester was definitely very formative for me in my career at UMD. I would like to thank Dr. Pines as well, for having taken me as his TA when I started out with Masters. I learned a lot that first semester! To Dr. Flatau, for her Comsol and hardware support. The work with Dr. Flatau for Masters laid out the sensors foundation for the present work.

Would like to thank Anand, and Marc Stora, from the Alfred Gessow Rotorcraft center on campus, as well as its director, Dr. Chopra. Thank you Anand and Marc for the work with wing properties testing in your lab. Thanks also to Mike

Sytsma, who helped us out at REEF in Florida with our wind tunnel tests as well as Andrew Kehlenbeck for helping out during the first round of tests. Thanks Max for wing fabrication and specs.

Would like to send a special thanks to Derrick Yeo, who not only piloted the aircraft for the flight tests but also did such an amazing job with the plane daq code and daq hardware. Thanks a lot Derrick!

Thanks also to James and Camli for starting out to collaborate on the CFD structures simulations. I hope that we can resume that work at some point.

Thanks to Ahmad Kasaei at the wind tunnel for the brief test of our setup and Evandro for the override box and hardware checkups.

I would like to thank also folks at the aerospace office; Lavita, Laura, Mike, Otto and Tom. Without y'all we couldn't possibly do our work!

Contents

| | |
|--|------|
| List of Figures | viii |
| List of Abbreviations | xiv |
| 1 Introduction | 1 |
| 1.1 Motivation | 1 |
| 1.1.1 Bio-Inspiration | 3 |
| 1.1.2 Strain feedback for gust alleviation | 5 |
| 1.1.3 Proprioceptive platforms | 7 |
| 1.1.4 Contributions in the perspective of the state of the art | 9 |
| 1.1.5 Organization of the dissertation | 11 |
| 2 Theoretical Framework | 13 |
| 2.1 Bio-inspired approach and distributed sensing | 14 |
| 2.1.1 Proprioception in nature | 15 |
| 2.1.1.1 Proprioception in humans | 15 |
| 2.1.1.2 Proprioception in birds | 19 |
| 2.1.1.3 Proprioception and strain sensing in insects | 21 |
| 2.1.2 Location and distribution of proprioceptors | 26 |
| 2.1.3 Proprioception in insect wings and flight control | 28 |
| 2.1.3.1 Location and distribution of sensilla on wings | 31 |
| 2.1.4 Distributed sensing in natural fliers | 33 |
| 2.1.5 Wave propagation | 34 |
| 2.2 State of the art | 36 |
| 2.2.1 Atmospheric disturbances | 37 |
| 2.2.2 Gust alleviation | 40 |
| 2.2.3 Static and dynamic loading of wing | 43 |
| 2.2.4 Aeroelastic models | 47 |
| 2.2.5 Strain sensing | 49 |
| 2.3 Strain feedback and controller framework | 51 |
| 2.3.1 Strain feedback | 53 |
| 2.3.2 Robust controller framework | 55 |
| 3 Theoretical considerations, Sensor placement and simulations | 62 |
| 3.1 Theoretical approach to strains vs disturbance force differentials | 63 |
| 3.1.1 Roll Moment | 63 |

| | | |
|---------|--|-----|
| 3.1.2 | Pitch Moment | 68 |
| 3.1.3 | Vertical Force | 73 |
| 3.1.4 | 6-DOF model | 74 |
| 3.2 | Strain based wide field integration (WFI) | 78 |
| 3.2.1 | 1D strain WFI | 78 |
| 3.2.2 | 2D strain WFI | 81 |
| 3.3 | Sensor placement | 83 |
| 3.3.1 | Sensor placement techniques | 83 |
| 3.3.2 | Theoretical Framework EFI and Grammian | 87 |
| 3.4 | 1D Sensor Placement Analysis | 90 |
| 3.4.1 | Wing FEM model | 90 |
| 3.4.2 | Sensor placement using MPF/gradient and EFI/Grammian | 91 |
| 3.5 | Gust simulations | 99 |
| 3.5.1 | ASWING aeroelastic model simulation | 99 |
| 3.5.1.1 | ASWING nonlinear simulation -3D gust | 100 |
| 3.5.1.2 | ASWING linear simulation -1D gust | 101 |
| 3.5.2 | Fluid structure interaction simulations- Static Aeroelastic (Comsol) | 106 |
| 3.6 | 2D sensor placement analyses (Comsol) | 111 |
| 3.6.1 | PWing test section | 111 |
| 3.6.1.1 | Wing FE model and sensor placement analysis | 111 |
| 3.6.2 | Flight test PWing | 123 |
| 3.6.2.1 | Wing FE model and sensor placement analysis | 125 |
| 4 | Experimental section and analysis | 130 |
| 4.1 | Glider experiments | 130 |
| 4.1.1 | Experimental Setup | 130 |
| 4.1.2 | Controls Setup | 135 |
| 4.1.3 | Experimental Results | 136 |
| 4.1.4 | Force/Strain Feedback using Proportional Gains | 136 |
| 4.1.5 | Aileron System Identification | 144 |
| 4.1.6 | Static Proportional Model | 144 |
| 4.1.7 | Dynamic Model | 148 |
| 4.2 | Quadrotor experiments | 152 |
| 4.2.1 | Strain Sensing | 154 |
| 4.2.2 | Sensor design for quadrotor arm | 158 |
| 4.2.3 | Heave disturbance rejection | 163 |
| 4.3 | Wing structural properties testing | 166 |
| 4.3.1 | Experimental setup | 166 |
| 4.3.2 | Bending and torsion properties | 169 |
| 4.4 | Wind tunnel tests | 174 |
| 4.4.1 | Experimental setup | 174 |
| 4.4.2 | Experimental results | 181 |
| 4.4.3 | System identification of output matrix | 191 |
| 4.4.4 | Discrete gust tests | 195 |

| | | |
|-----|--|-----|
| 4.5 | Flight testing | 199 |
| 5 | Summary and Conclusions | 208 |
| 5.1 | Summary | 208 |
| 5.2 | Conclusions | 214 |
| 5.3 | Future work | 217 |
| | Appendix A Strain sensors for aircraft wing applications | 219 |
| | Appendix B ATG characteristics | 224 |
| | Bibliography | 228 |

List of Figures

| | | |
|------|--|----|
| 1.1 | Commercial and military applications of UAS: a. Amazon prime air, a proposed multiple-rotor delivery system, b. Google project wing, a first generation R&D fixed wing delivery prototype, c. Aurora Orion, a long endurance unmanned aircraft system for military applications. | 2 |
| 1.2 | High bandwidth inner loop strain feedback | 7 |
| 1.3 | Pwings test articles for wind tunnel testing: UMD PWing (OTS foil gauges), Stanford PWing (Interconnected sensor network), Aurora PWing (fiber optic sensors) | 8 |
| 2.1 | Spinal reflex order and components [23] | 16 |
| 2.2 | Spinal reflex in the human body, in particular with stretch proprioceptive receptors and corresponding afferent/sensory neurons [23] | 17 |
| 2.3 | Stretch proprioceptive sensors in humans: a. muscle spindles and b. Golgi tendons [24] | 18 |
| 2.4 | Avian muscles for flight control [26]. | 20 |
| 2.5 | Different types of cuticular sensilla. a. sensillum trichoideum (hairs), b. sensillum basiconium, c. sensillum campaniformium, d. sensillum placodeum, e. sensillum coeloconium, f. sensillum ampullaceum, [35]. | 25 |
| 2.6 | Proprioceptors of the foreleg of periplaneta. The numbers in brackets show the number of sensilla in each group. Ellipses show orientations of campaniform sensilla [36]. | 26 |
| 2.7 | Distribution of camaniform sensilla in the stick insect's body [37]. | 27 |
| 2.8 | Campaniform sensilla on grasshopper wings | 30 |
| 2.9 | Distribution of camaniform sensilla on the wingblases of flies of different families of Diptera [39]. | 32 |
| 2.10 | Wave propagation measured with strain gauges: bimaterial beam (left) and experimentally recorded strain histories (right) [46] | 35 |
| 2.11 | Order of timescales in disturbance sensing | 36 |
| 2.12 | Turbulence production in the atmosphere [49] | 37 |
| 2.13 | Typical 1-cos gust shapes [50] | 38 |
| 2.14 | Ratio of Von Karman and Dryden PSD functions [52] | 39 |
| 2.15 | State space equations for rigid body motion and structural dynamics | 48 |
| 2.16 | 6-DOF coupled aeroelastic equations | 49 |
| 2.17 | Augmented attitude controller: load feedback to optimize the responsiveness of the attitude controller and to reject disturbances and errors in actuated body torque (excerpt from Thompson et al. [16]). | 52 |

| | | |
|------|--|-----|
| 2.18 | Strain Feedback implementation. | 55 |
| 2.19 | Fast inner loop for disturbance rejection | 56 |
| 2.20 | MIMO general case with input and output disturbances and noise | 59 |
| 2.21 | High bandwidth inner loop strain feedback | 61 |
| | | |
| 3.1 | Calculation of wide field integrated constants | 66 |
| 3.2 | Balance of bending moments for calculation of disturbance roll moment | 67 |
| 3.3 | Pitching moment at root of aircraft as a function of shear stresses along the wings | 70 |
| 3.4 | Different pitching moments at root as a consequence of maneuver or external inputs | 71 |
| 3.5 | Vertical force on aircraft and shear forces on the wings | 73 |
| 3.6 | 6-DOF coupled model for force/strain feedback | 75 |
| 3.7 | Formulation for the strain feedback MIMO controller based on SISO strain balance | 76 |
| 3.8 | 6-DOF formulation for the strain feedback MIMO controller based on system identified output matrices | 76 |
| 3.9 | 6-DOF formulation for the strain feedback MIMO controller with uncertainty in the Cmatrix | 77 |
| 3.10 | Strain wide field integration | 82 |
| 3.11 | 1D dimensional aluminum beam eigenstrain superposition (left) and 2D aluminum beam eigenstrain superposition (right). | 86 |
| 3.12 | First and second finite element eigenmodes of UAS wing | 91 |
| 3.13 | UAS normalized eigenstrains from finite element simulation | 92 |
| 3.14 | UAS normalized weighted eigenstrains using equal weights and MPF | 93 |
| 3.15 | Linearly weighted and MPF eigenstrain gradients | 94 |
| 3.16 | UAS wing MPF based sensor placement using weighted eigenstrains and gradient | 95 |
| 3.17 | UAS wing MPF based sensor placement using weighted eigenstrains and gradient | 95 |
| 3.18 | UAS wing EFI/Grammian sensor placement | 96 |
| 3.19 | Comparison of EFI/Grammian and MPF/Gradient sensor placement methods | 98 |
| 3.20 | ASWING definitions (excerpt from reference [72]) | 100 |
| 3.21 | Top view of aircraft model for ASWING simulation | 101 |
| 3.22 | Airplane vertical velocity and bank angle with and without gust, non-linear ASWING simulation | 102 |
| 3.23 | Strain feedback used in ASWING reduced order simulation | 104 |
| 3.24 | Roll disturbance on aircraft states | 104 |
| 3.25 | Impact of roll disturbance on sensors | 105 |
| 3.26 | Roll angle at different strain feedback proportional grains K, with derivative D=1 and integral I=2 gains. | 105 |
| 3.27 | Wind tunnel simulation of fixed wing with impinging vertical gust | 108 |
| 3.28 | Wind tunnel simulation of fixed wing with impinging vertical gust, strains are produced as a result of the impinging vertical gust | 109 |

| | | |
|------|--|-----|
| 3.29 | Wind tunnel simulation of fixed wing with impinging rotational gust: Fluid pressure profiles (left) and wing strains (right) | 110 |
| 3.30 | Principal strains for different impinging gusts: vertical gust (left) and torsional gust (right) | 111 |
| 3.31 | Airfoil geometric characteristics | 112 |
| 3.32 | Normal element size mesh of carbon layup wing | 113 |
| 3.33 | First six eigenstresses of carbon fiber wing | 115 |
| 3.34 | 2D view of first six eigenstresses of carbon fiber wing | 116 |
| 3.35 | Superposition of first six eigenstress modes (top view) | 118 |
| 3.36 | Strain gauge stretchable network in spanwise orientation (Structures and Composites Lab SACL, Stanford University) [8] | 119 |
| 3.37 | Sensor distributions based on SACL lab stretchable sensor network | 120 |
| 3.38 | First six principal strain directions of carbon fiber wing | 122 |
| 3.39 | Pwing Airfoil and full wingspan geometry | 123 |
| 3.40 | Flight Pwings for assembly with Apprentice Aircraft | 124 |
| 3.41 | FE model of flight test wing and meshed geometry | 125 |
| 3.42 | First few eigenstrain modes of flight wing | 126 |
| 3.43 | Eigenstrain modes of flight wing: linear weighting (left) and MPF-v weighted (right) | 127 |
| 3.44 | MPF-v weighted eigenstrain map for 8 sensors | 127 |
| 4.1 | Experimental setup of glider and launching mechanism | 131 |
| 4.2 | Glider plate and strain gauges | 132 |
| 4.3 | Experimental setup of glider and launching mechanism | 132 |
| 4.4 | VICON Setup: Vehicle marker setup(left) and VICON camera setup and vehicle (right) | 133 |
| 4.5 | Gust encountered by glider. | 135 |
| 4.6 | Controls used in strain feedback tests. | 135 |
| 4.7 | Classical controller used for controller types comparison. | 136 |
| 4.8 | Glider baseline roll angle curves: with no gust perturbation (top), and under a vertical asymmetric gust (bottom). | 137 |
| 4.9 | Glider mean roll for free flight and with vertical gust perturbation. | 138 |
| 4.10 | Glider mean roll for proportional gains $K=3$, $K=4$, $K=5$, and $K=6$ | 139 |
| 4.11 | Glider roll angle and strain feedback at gains $K=3$, 4, 5, 6 and baseline flight. | 140 |
| 4.12 | D2 metric between the perturbed data with no applied control and the one with applied strain feedback. | 140 |
| 4.13 | Controller comparison for roll gust rejection. TF= torque feedback, P=proportional. | 141 |
| 4.14 | Glider trajectories: in free flight, under the influence of a gust and using strain feedback. | 142 |
| 4.15 | Impact of weight on glider roll angle: Roll angle for glider weight and a payload of 4.4 grams (top) and Roll angle for glider weight and a payload of 10.9 grams (bottom) | 143 |
| 4.16 | Vicon camera setup for system identification | 144 |

| | |
|--|-----|
| 4.17 Step input of wing deflections and corresponding output of aileron deflections. | 145 |
| 4.18 Aileron deflection vs wing deflection for $K=1$. Each point is the result of averaging local points that correspond to the duration of the step input. | 146 |
| 4.19 Filtered data, where aileron output has been drawn around its mean value | 148 |
| 4.20 DJI Flamewheel quadrotor with strain sensing arm | 153 |
| 4.21 (a) Quad arm with amplifier circuit, (b) Static testing of RPM quadrotor arm | 160 |
| 4.22 (a)Hysteresis at a loading and unloading cycle, (b) Creep behavior of RPM quad arm | 161 |
| 4.23 (a) Photopolymer prototyped arm sections for MTS testing and (b) CAD model of the quadrotor arm without optimized cross-section | 161 |
| 4.24 Finite element simulations of stress under maximum expected quadrotor load: (a) Solid cross section, (b) Square hollow cross section and (c) Smoothed square hollow section, (d) striated cross section, (e) load cell cross section, (f)bi-rectangular cross section | 162 |
| 4.25 Strain sensing implementation: (a) Quad arms with different cross sections and (b)Quad arm vehicle implementation | 163 |
| 4.26 Fast inner loop for disturbance rejection | 164 |
| 4.27 Strain feedback performance metric | 164 |
| 4.28 Heave Velocity and Altitude Time History for Impulse Heave Disturbance for Varying Feedback Gain from Strain Gauge Sensing | 165 |
| 4.29 Height gauge setup for calculation of bending stiffness | 167 |
| 4.30 VICON setup for calculation of bending stiffness | 168 |
| 4.31 Clamps used for static testing and Vicon wing setup | 169 |
| 4.32 Load vs. tip displacement curves for estimation of EI with height gauge | 170 |
| 4.33 VICON processed data | 171 |
| 4.34 Strain gauge top half of full bridge | 175 |
| 4.35 Wing with sensor network | 175 |
| 4.36 Strain gauge amplification electronics | 176 |
| 4.37 REEF wind tunnel | 177 |
| 4.38 Wind tunnel wing setup | 178 |
| 4.39 Load cell axes | 179 |
| 4.40 Test setup with ATG | 180 |
| 4.41 6-axis sample data from load cell during steady test, mechanical pulses were used to synchronize data | 181 |
| 4.42 Calculated forces and moments vs wind tunnel speed for angle of attack) degrees and angle of attack 5 degrees | 183 |
| 4.43 Calculated lift and drag coefficients from wind tunnel data | 184 |
| 4.44 AG35-r Drela aifoil, from [109], rotated airfoil and lift/drag coefficients vs angle of attack. | 185 |
| 4.45 Ramp test to simulate sustained gusts (20 kts, 25 kts, 15 kts, 20 kts), AoA =5 deg; load cell forces and moments and strain sensor data. | 186 |

| | | |
|------|---|-----|
| 4.46 | Representative of interpolated strain rms measurements for steady wind velocity | 187 |
| 4.47 | Interpolated strain rms measurements for steady wind velocity at AoA 0 deg and AoA 5 deg | 188 |
| 4.48 | Comparison of max. rms strains during steady runs | 189 |
| 4.49 | Comparison of strains produced with wing tip loadings of 100gr and 200gr | 189 |
| 4.50 | ATG produced Lift force with and without strain feedback | 190 |
| 4.51 | Setup for Static system identification in the lift direction | 194 |
| 4.52 | Stanford wing wind tunnel gust setup | 195 |
| 4.53 | Static manual forcing with coupled components | 196 |
| 4.54 | Static manual decoupled forces and moments F_x , forces and moments (left), sensor data (right) | 196 |
| 4.55 | Static manual decoupled forces and moments F_y , forces and moments (left), sensor data (right) | 197 |
| 4.56 | Static manual decoupled forces and moments F_z , forces and moments (left), sensor data (right) | 197 |
| 4.57 | Cmatrices for manual F_x , F_y , F_z calculated with least squares estimator and colored noise | 198 |
| 4.58 | Cmatrices for design points: AoA 9 deg, $V=15$ kts (left) and AoA 3 deg, $V=20$ kts (right). | 198 |
| 4.59 | AoA=3 deg, $V=20$ kts, gusts, open loop | 199 |
| 4.60 | AoA=3 deg, $V=20$ kts, gusts, closed loop feedback S2 | 200 |
| 4.61 | AoA=3 deg, $V=20$ kts, gusts, closed loop feedback C average | 201 |
| 4.62 | AoA=3 deg, $V=20$ kts, gusts, closed loop feedback C matrix (sysID) | 202 |
| 4.63 | Filtered AoA 3 deg, $V=20$ F_y data to measure performance of feedback loop, d represents a decrease in the shift for the first gust which is proportional to the shift observed in the other gusts | 203 |
| 4.64 | Apprentice aircraft with modified instrumented wing | 203 |
| 4.65 | Strain signals and IMU recording and feedback for flight tests. | 204 |
| 4.66 | Apprentice aircraft and ground station during flight test preparation | 204 |
| 4.67 | Apprentice flight tests | 205 |
| 4.68 | Open loop flight data, eight bridges, 32 sensors | 205 |
| 4.69 | Flight data open loop, differential strain for sensors 4 and 5 and aircraft roll rate | 206 |
| 4.70 | Flight data closed loop, differential strain for sensors 4 and 5 and aircraft roll rate | 206 |
| 4.71 | Flight data closed loop, differential strain for sensors 4 and 5 and aircraft roll rate for flight section. | 207 |
| A.1 | Strain sensors for aircraft wings | 221 |
| A.2 | Strain sensors characteristics comparison chart | 222 |
| A.3 | Strain sensors advantages and disadvantages chart | 223 |
| B.1 | ATG turbulence grid | 224 |

| | | |
|-----|--|-----|
| B.2 | ATG turbulence statistics with wind tunnel throttle at 43.5 % and at $x/M=12.5$, from [1] | 225 |
| B.3 | ATG turbulence statistics mean core velocities: a. Mean core velocity at 7.21 m/s, b. Mean core velocity at TIX=3.9%, c. Mean core velocity at TIX=17.9%, d. Mean core velocity at TIX=20.7% | 227 |

List of Abbreviations

| | |
|---------------------|---------------------------------------|
| P | Force acting on one wing |
| Fv | Total vertical force |
| EI | Bending stiffness |
| ε_R | Strain on the right wing |
| ε_L | Strain on the left wing |
| $\Delta\varepsilon$ | Strain differential |
| c_w | Wide field integration constant |
| x | Span wise coordinate |
| y | Normal coordinate |
| z | Thickness |
| $H(s)$ | Aileron transfer function |
| Kp | Proportional constant |
| $ Tp$ | First order constant |
| Td | Time delay |
| y_s | Sensor outputs |
| Φ_{fs} | Matrix of target modes |
| q | Response vector of target modes |
| w | Measurement noise |
| Q | Fisher information matrix |
| Y_o | Observability Grammian |
| R | Intensity matrix |
| Ψ | Matrix of eigenvectors of Q |
| Γ | Matrix of eigenvalues of Q |
| E_{D_i} | Effective Independence |
| ε_i | Strain at location i |
| M | Bending Moment |
| q_w | Distributed force acting on one wing |
| q_i | Discrete force acting at location i |
| C_w | Wide field integration matrix |
| a | Local distance to fuselage |
| x_i | Spanwise location of sensor i |
| L | Roll moment |
| M_L | Left wing moment |
| M_R | Right wing moment |
| L_w | Wing length |
| RPM | Rapid prototype material |
| IMU | Inertial measurement unit |
| $U.A.S.$ | Unmanned aerial system |

Chapter 1: Introduction

1.1 Motivation

Unmanned aerial vehicles, systems and platforms are a growing field with increasing number of applications in areas where human life needs to be protected, areas which are of difficult access, unexplored goals or simply to perform tasks at a reduced cost compared to a human operator. Therefore some of the most promising and useful applications include: reconnaissance, aerial photography, search and rescue, transportation of supplies within nearby locations, civilian infrastructure maintenance and disaster prevention and mitigation. These tasks need to be carried in a way that is safe for the general population and the environment.

All these advantages however come at the price of increased instability, power constraints, payload limitations, reduced flight endurance, among other challenges. Autonomous flight is even more challenging, as ideally the aircraft will know how to avoid obstacles and stabilize itself amid a number of disturbances of the environment. In urban environments, avoidance of obstacles may be problematic, not only because of gusts, but because of ground-effect and related flow field phenomena when flying in the vicinity of walls and buildings. Light weight and slow flight speed of small air systems creates profound complications in aerodynamic efficiency and agility [1].



(a) Amazon Prime Air



(b) Google Project Wing



(c) Aurora Orion

Figure 1.1: Commercial and military applications of UAS: a. Amazon prime air, a proposed multiple-rotor delivery system, b. Google project wing, a first generation R&D fixed wing delivery prototype, c. Aurora Orion, a long endurance unmanned aircraft system for military applications.

Low wing loading, which is necessary for aerodynamic efficiency and reasonable flight endurance, exacerbates the problem of gust response. These platforms are also prone to aeroelastic or inertial coupling with the rigid body dynamics and the flexible structures, since many of these platforms are much more flexible than their large scale counterparts. Coupling may also occur with vortex shedding and other flow-separation phenomena [2].

Due to the promising advantages, both academia and industry have explored ways to address the challenges that these vehicles pose. The reduced scale for flight dynamics makes these smaller platforms more unstable and more susceptible to atmospheric disturbances.

1.1.1 Bio-Inspiration

This work is inspired in the fast reflexive mechanisms found in nature as applied to stabilization of small UAS platforms. In particular, strain sensing has not been fully explored in the sensing features presented herein. Furthermore, proprioceptive strain sensing mechanisms have been found in numerous examples in nature. Starting from the mammalian muscle spindles, golgi tendons and ruffini corpuscles, then going to herbst corpuscles in birds, and sensilla of insects, nature is rich in fast and reflexive mechanisms which allow for bioinspired controls. Insects not only have strain sensors but also possess a number of visual sensors, tactile sensors, and airspeed sensors for physiological and survival tasks. In particular, we are focusing on the strain sensing features of flying insects, as their distributed sensing is

constructed to aid in flight and navigation.

Campaniform sensilla is the closest mechanism to that of strain sensing in engineering. Its structure is such that in-plane deformations get translated into out of plane campaniform displacements, which activate the corresponding neuron. The distribution of these organs coincide for the most part with the location of insect wing veins, or the beams and trusses of insects. Therefore indicating that these organs benefit from bending and stresses produced during flight. It has also been observed that insects have these organs distributed along their wings and not just at the base of joints, which is also another popular location for sensilla along the insect body. These sensors allow the animal to monitor rate of flapping by firing neurons on each wing flap. These signals are combined with other sensing organs for flight stabilization. It has been observed as well that they use the campaniform close to the tip of their wings to monitor the passage of torsional waves during the flapping cycle. It is this precisely what inspires this work. The goal is to anticipate the onset of disturbances by measuring the passage of the disturbance by means of proprioceptive mechanisms such as those found in nature. The early detection of the disturbance is what would allow for faster reaction to it. The reaction mechanisms are proprioceptive in the sense that they are based on relative measurements to other parts of the insect body and/or wings.

Structural inputs are much faster than rigid body inputs to any controls system located at the fuselage of any aircraft. The reason being is that the frequencies are much higher than rigid body ones. However, for certain aircraft these aeroelastic modes become coincidental and therefore lead either to static or dynamic aeroelastic

divergence. If aeroelastic divergence is assumed not to be problematic for the system at hand, then there is an opportunity to use these waves for controls purposes.

1.1.2 Strain feedback for gust alleviation

Strain signals had been used in the past for load characterization studies, mode suppression, vibration suppression and others. The approach of this work however, intends to utilize strain signals not to provide precise rigid body state estimates but rather use them to access higher order states and correct for flight disturbances before they reach the aircraft plant dynamics. That is to say that the controller is not typical in the sense that full states are estimated but rather state differentials by means of strain measurements. Forces and moments at the center of gravity are unambiguously measured by inertial measurement units. Strain sensing in the focus of this work does not intend to replace these units but rather complement attitude control and provide fast inner loop stability augmentation reflected in more stable inner loop states.

In this sense, strain feedback can provide this stability, albeit studies of modal impact will most likely have to be undertaken to guarantee that the strain controller will be able to not be affected by system vibrations. To this end, filtering could be necessary as well as tuning of the filter to the particular expected modal frequencies.

Gust mitigation literature review [3] suggests that the trend for more structurally efficient aircraft yields both lighter and more flexible aircraft which brings challenges in sensitivity to atmospheric disturbances. These lighter more flexible

aircraft face two significant challenges: reduced separation between rigid-body and flexible modes, and increased sensitivity to gust encounters due to decreased wing loading and improved lift-to-drag ratios.

Disturbances can be discrete or continuous, and are generally modeled as being isotropic in the real atmosphere. Discrete gusts are deterministic, continuous disturbances or turbulence is represented as a random variation of gust velocity with frequency spectra. This work mainly focuses on addressing disturbance rejection for discrete gusts based on structural inputs. The framework that will be presented however can be extended to frequency domain or time domain disturbances with some modifications.

Wing loading due to gusts can be idealized as one dimensional phenomena however it is actually a fully three dimensional phenomena. In this sense, the bioinspired mechanisms for gust rejection that will be presented take the three dimensional nature of gusts into account in that load balancing of control surfaces by means of strain associated signals can yield a wealth of information for stability augmentation. Albeit we are not measuring absolute forces, the strain measurements are a result of a combination of forces and moments on the aircraft.

1D and 2D theoretical approaches are proposed for stabilization by means of strain differentials or calculated force differentials, for implementation in fast reactive loops. Sensor placement techniques are applied to 1D and 2D cases as well and simulations are used in closed and open loop to test for these strain based mechanisms [4].

A high bandwidth inner loop was tested in hardware [5] [6] to use strain

able sensor network built by the SACL lab at Stanford University [8] and one which was instrumented with fiber optic sensors by Aurora Flight Sciences [7]. These wings are shown in Figure 1.3.

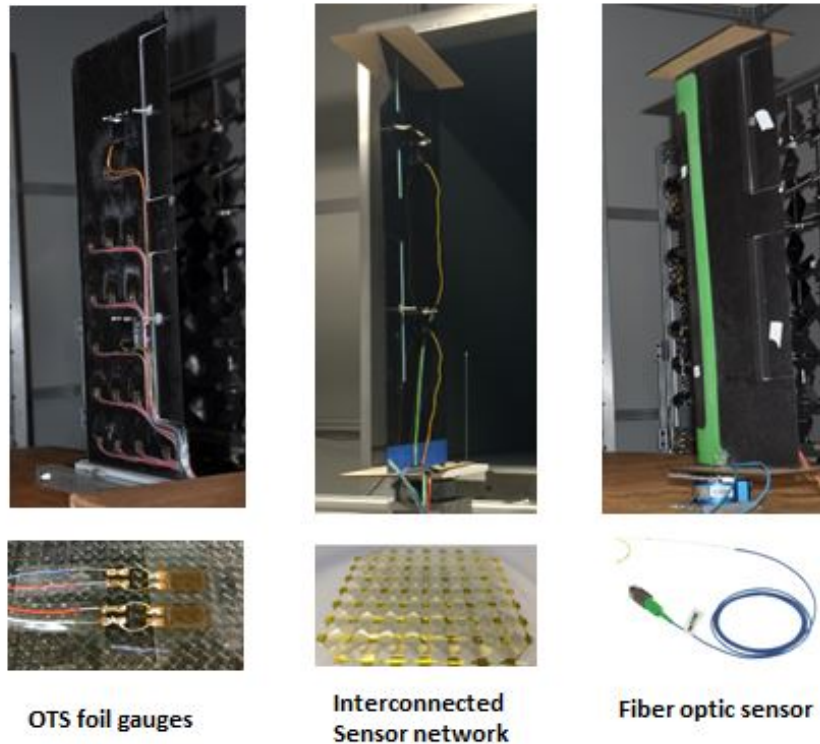


Figure 1.3: Pwings test articles for wind tunnel testing: UMD PWing (OTS foil gauges), Stanford PWing (Interconnected sensor network), Aurora PWing (fiber optic sensors)

The strain sensing implementation is presented in Chapter 3 with all the experimental results from open loop and closed loop tests in the presence of atmospheric disturbances.

1.1.4 Contributions in the perspective of the state of the art

- A bioinspired gust mitigation reactive mechanism was analyzed and implemented. This is a different methodology altogether from the conventional approach where gust alleviation is based on estimation of gust states or rigid body state disturbances. In the proprioceptive perspective of this work, the focus is on the relative strain measurements within the body of the aircraft and how they can be used to aid in gust alleviation.
- In the theory and analysis aspect, this work contributes a differential strain/force balance theoretical approach for pitch, roll and vertical force, where stability is achieved by monitoring the balance of forces on the corresponding controls surfaces.
- It also proposes another theoretical approach where if the forces and moments are empirically correlated to the strain sensing patterns i.e. by least squares regression methods, then stability can be achieved by monitoring the 6-DOF force differentials at the root of each wing.
- Another theoretical development is the wide field integration for strain as applied to disturbance rejection. A wide field integration for one dimensional wing was implemented in simulation producing successful gust rejection.
- Eigenstrains can be weighted according to the expected directionality of the gusts according to calculated mass participation factors or MPFs. These directional 2D weighting patterns can be considered to be basis functions for strain

measurements where a set of gains can be calculated to extract the different types of gusts. In this work, it was found that the MPF weighted patterns are strongly correlated to the observability Grammian, with the added directionality feature. Therefore the 2D energy weighting pattern which encodes six different types of gusts can be considered to be a directional Grammian. The basis functions for the strain wide field integration can be considered to be directional Grammians.

- In terms of hardware, bioinspired strain sensor networks were implemented on different platforms. These include a quadrotor, a UAV carbon fiber wing section and a full carbon fiber wing for a small UAV for flight testing. Bioinspired strain sensing had not been previously applied to UAS platforms for reflexive disturbance rejection in prior art. Previous developments had used strain sensors mainly for monitoring of loads for health monitoring, vibration suppression, wing shaping, among others.
- A MIMO multidegree of freedom framework was formulated with the proposed strain dependent output matrices. The uncertainty in the output matrix and estimation matrix can be modeled as either a structured uncertainty or an unstructured uncertainty by tuning the weighting functions related to the C matrix multiplicative uncertainty. This is such that the system will be nominally stable, have good performance characteristics such as good tracking and good disturbance rejection, and can be robustly stable and have robust performance amid the uncertainties. This is typically done through minimization

of the maximum singular value of the corresponding transfer function.

1.1.5 Organization of the dissertation

This work is organized as follows. An introduction is provided in the first chapter as an overview of the entire dissertation.

In chapter 2, the theoretical framework is presented. It begins with the proprioceptive bioinspired approach that was applied to the force disturbance sensing and rejection mechanisms. Then it presents some mechanisms found in insects when they use their wing strain sensors, or sensilla, to sense cuticle strain for many different purposes, including flight control. Then the most relevant gust models are presented as well as disturbance rejection mechanisms that have been used in the literature. After this is presented, a theoretical framework of the state of the art is introduced and after that, the theory and analytical model for the force and moment disturbance rejection. It presents the general intended framework in which all the strain feedback concepts are applied and it provides an overview of the general equations employed in the aeroelastic simulations used later on in chapter 2. The robust controller framework is also introduced for output matrices with uncertainties.

Also in chapter 3, the theoretical aspect of strain feedback is presented. These equations are based on the bioinspired approach presented in the previous chapter. A wide field integration for roll is presented for a 1D case. After this, the sensor placement analysis and results are presented for a 1D case. Gust simulations in open loop for the 2D CFD/structures simulation is presented as well as the closed inner

loop full 6-dof linear aeroelastic gust simulation obtained using ASWING. For a 2D case, the results are presented and applied to the PWings (Proprioceptive wings) test section and flight wing section.

In chapter 4, the experimental section and analysis is presented. A small UAS glider, a mini quadrotor, a wing section and a full wing were outfitted with strain gauges, results and analysis are provided. These platforms were tested under sharp disturbances including an actuator disturbance, a 1-cos disturbance, a turbulent wind disturbance, and a discrete finite gust disturbance. All these platforms which had strain sensing reactive mechanisms showed good disturbance rejection properties.

In chapter 5, a summary of all the tests and results is presented and some conclusions, as well as future work related to the developments of this work are envisioned.

Chapter 2: Theoretical Framework

This section introduces the bioinspired motivation for strain sensing as applied to flight control of fixed wing aircraft.

Bioinspired sensory mechanisms have shown to have multiple applications in ground navigation [9] as well as for UAS aircraft [10]. Feedback laws motivated by biological approaches can be used to reject gusts. Biological systems have natural strain gauges to aid navigation and stability [11]. These are triggered by stimuli caused by locomotion, changes in posture and external events. Examples of sensing encoders found in nature include the campaniform sensilla of insects and the slit sense organs of arachnids [12]. Insect wings have cuticular sensors which help them respond to environmental inputs. Campaniform sensilla, the load/strain sensors of insects, can induce a response in muscles that is an order of magnitude faster than that achieved by the vision system. These stress/strain sensors are directly connected to dendrites of the primary afferent neurons allowing a quick reflexive response [13]. The possibility of a low latency response is the initial motivation to use strain feedback for gust rejection. We will refer to strain feedback and force/torque/moment feedback interchangeably throughout this work.

In this work we not only explore the conventional approach to sensor place-

ment but also a wide field integrated approach [9] based on structural inputs. This approach is motivated by the mechanisms observed in nature. Strain, stress and load sensing mechanoreceptors are found in all species for navigation and motor control. Examples of sensing encoders found in nature include the cuticular sensors of insects and the slit sense organs of arachnids [12]. In insects, the stress/strain sensors are directly connected to dendrites of the primary afferent neurons allowing them to have a quick reflexive response [13]. The cuticle of the spider has a large number of slit sense organs, which respond to forces causing strain in the cuticle. These slits are connected to bipolar neurons which reflexively transmit the chemical synaptic potentials directly to the central nervous system [14]. A low latency response is possible by feedback of structural quantities which are directly correlated to higher order states. A distributed sensing approach can reduce the error covariance in the measurements while reducing feedback latency [9].

Strain sensing found in nature can be imitated by constructing sensing mechanisms of maximal desired output. A method of sensing strains, that may encode force information, based on the campaniform sensilla was developed by [?] and [15] to be embedded in space structures. Controllers based in these strain mechanisms have also been proposed and simulated for attitude control augmentation [16].

2.1 Bio-inspired approach and distributed sensing

The present work aims to harness the bio-inspired mechanisms of proprioception both in function and in functional morphology. Proprioception in biological

entities is a constantly running natural function which determines the body's position and the way it is moving through space. This mechanism allows for the brain to determine the body's state of motion and position. For a better understanding of the concept of proprioception, this overview will go through the corresponding mechanisms found in humans and will then translate and compare to the mechanisms found in insects and small fliers.

2.1.1 Proprioception in nature

2.1.1.1 Proprioception in humans

Proprioception, from the latin propius, is the perception of ones own motion. It is the sense of the relative position of body segments in relation to other body segments. Proprioceptive organs provide the central nervous system with information about the relative position and movement of body parts [17]. Proprioception allows for indication of whether the body is moving with the appropriate effort and where the various segments of the body are located in relation to each other [18]. It allows for the understanding of where each joint is at that moment in time. This relative position sensing is different from exteroception which entails sensitivity to stimuli originating outside of the body and it is different from interoception which is sensitivity to stimuli originating inside of the body. Conscious proprioception or kinesthesia allows the brain to bring to a conscious or knowing level where the body is in 3D space. Unconscious proprioception allows the brain and more specifically the cerebellum to know unconsciously where the body is in 3D space [19]. Much

of the afferent information generated by self-initiated movements does not reach consciousness.

Kinesthesia usually refers to the perception of one's own motion whereas proprioception not only entails the perception of movement but also awareness of the body's orientation in space [20]. This cognitive ability is channeled from the different proprioceptive receptors through neuronal afferents to the central nervous system, as shown in Figure 2.1. Spinal reflexes only travel to the spinal chord and back and are therefore subconscious. Reflexes are different from reactions, which are voluntary responses to stimuli from the environment. The reflex time, or the time between the onset of a stimulus and action of the effector, is determined mainly by the conduction time in afferent and efferent pathways. The conduction velocities of human nerve fibers are given by the speed at which a given electrochemical impulse propagates down a neural pathway [21]. In humans, the reaction times vary depending on which one of the senses is participating in the reflex and on a number of other biological factors. On average, the reflex time for visual inputs is 0.2 seconds [22].

The reflex arc is mainly composed of the elements shown in Figure 2.1.

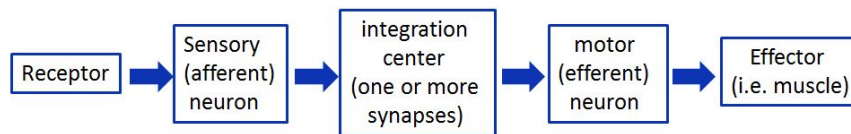


Figure 2.1: Spinal reflex order and components [23]

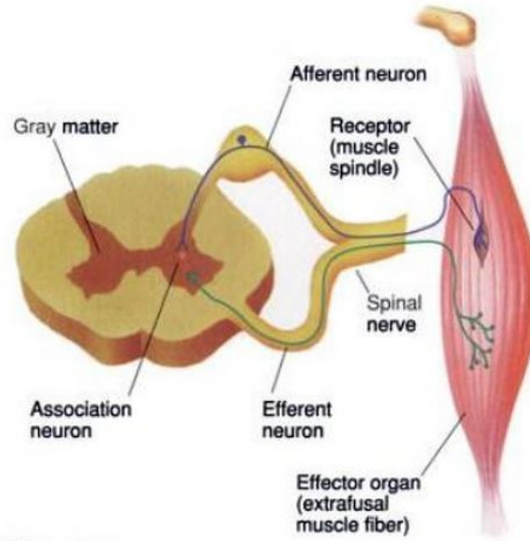


Figure 2.2: Spinal reflex in the human body, in particular with stretch proprioceptive receptors and corresponding afferent/sensory neurons [23]

Figure 2.2 shows the components of a reflex arc through muscle stretch proprioceptive receptors. The receptor is the organ that responds to the stimulus by converting it into a neural or electrical signal. Then the afferent neuron carries the signal to the central nervous system and encounters either association neurons (interneurons) or efferent neurons. The outcome of the signal transfer depends on the complexity of the reflex mechanism [23]. The output neurons or efferent neurons then carry the electric signal to the organ that is to respond to the stimulus. Receptors convert all the sensory information into action potentials or impulses which are ultimately relayed to the cerebellum.

In humans, the proprioceptive organs entail the muscles, joint capsules, ligaments, tendons, skin and the internal ear. These organs provide the central nervous system with information about the position and movement of body parts. The two

types of muscle receptors are the muscle spindles and the Golgi tendon organs, as shown in Figure 2.3. Muscle spindles are the principal proprioceptors [20], these are receptors which provide feedback information on the degree of muscle stretch for the muscle reflex mechanism. They can sense muscle length (limb position) and rate of length change (velocity or sense of movement) by means of the primary endings or afferents. Golgi tendon organs are receptors located at the junction of muscle and tendon and provide mechanosensory information to the central nervous system about muscle tension. Joint kinesthetic receptors are located within and around the articular capsules of synovial joints. They provide feedback information on the degree and rate of angulation of a joint. They act as limit detectors in that they operate mainly at the extremes of the normal range of biologically possible joint angles. Skin receptors have a similar function to that of muscle spindles. Skin mechanoreceptors are activated when the skin suffers rotation or compression. Proprioceptors in the internal ear function for equilibrium.

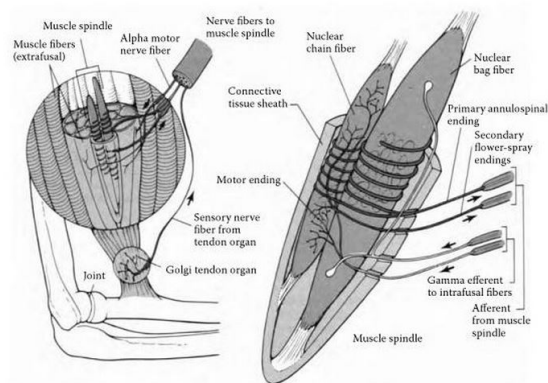


Figure 2.3: Stretch proprioceptive sensors in humans: a. muscle spindles and b. Golgi tendons [24]

Information about limb position and movement however is not generated by individual sensing receptors but by populations of afferents [20]. Afferent signals are generated during motion and are processed to encode limb endpoint positions. The afferent inputs are then referred to a central body map to determine the spatial location of the limbs. Afferent nerves are peripheral nerves that transmit to the spinal cord and ultimately the brain. These nerves therefore carry out a sensory function. Injuries to these may decrease proprioception as well as diseases of the neurologic system.

Proprioception also entails the ability to reposition a joint to a predetermined position. It gives an estimation of the relative position of parts of the body as well as the effort being employed in movement [17]. Proprioceptive senses include the senses of position and movement of limb the sense of effort, sense of tension or force and the sense of heaviness and the sense of balance [20]. These are always associated to motor commands. In the normal limb tendon organs and possibly also muscle spindles contribute to the senses of tension or force and heaviness. In particular, we would like to apply the mechanisms for the sense of force and balance in the present work.

2.1.1.2 Proprioception in birds

Birds also possess a number of mechanoreceptors, some of which have proprioceptive functions. These are located near the follicles of feathers allowing birds to detect turbulence [25], as well as in muscles for flight control. In avian flight, birds

and bats, possess modified forelimbs which contain muscles that control wing shape by moving the bones of the arm and hand (Figure 2.4).

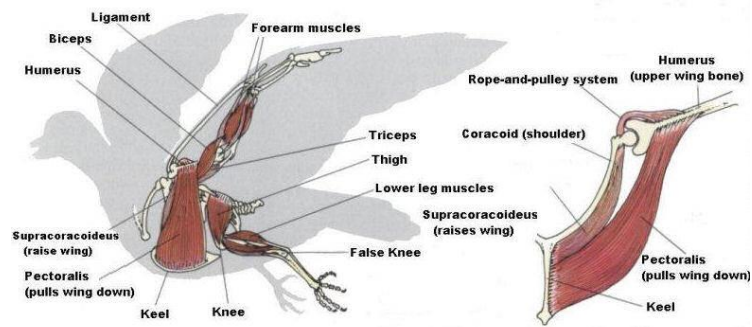


Figure 2.4: Avian muscles for flight control [26].

Wing receptor types in birds can be free nerve endings or encapsulated endings. Free endings sense temperature and pain, while encapsulated endings are mechanoreceptors or sensory corpuscles. Kestrels for instance, can withstand elevated levels of turbulence while hovering and maintaining a spatial reference posture. There are a number of corpuscles, out of which the Herbst and the Ruffini corpuscles have a flight control function in addition to other functions. Herbst corpuscles are widely distributed in the skin and are associated with feather follicles and with the muscles of the feathers. Ruffini corpuscles are axon endings in close contact with collagen fibers, probably serving as stretch receptors and numerous in-joint capsules [27].

Herbst corpuscles sense vibrations and are directionally sensitive. These are clustered in the leading edge of birds wings and the alula, or the freely moving first

digit. These organs are tuned to certain wind frequencies, which is also observed in insects and their analogous proprioceptive mechanoreceptors. It has been suggested that this frequency is a way to measure airspeed. Flight steering muscles of birds are controlled not only indirectly via neck reflexes but also in parallel, directly by the central nervous system. This combination of direct and indirect control of wing and tail muscles can be coordinated or switched off [28]. Stretch receptors in limb muscles are also potential load sensors and could be auxiliary to the cutaneous receptors in determining gust induced displacements of the wing. Feather displacements are also detected by additional sets of mechanoreceptors.

2.1.1.3 Proprioception and strain sensing in insects

This work is inspired in the proprioceptive mechanisms of humans and other vertebrates as mentioned in the previous sections, but finds most of its inspiration in the fast reflexive mechanisms observed in insects. In particular, those mechanisms which use wing mechanosensory information for flight stabilization. Insects are not limited by the cellular biophysics muscle contraction limits. Insects have simpler neurological mechanisms as compared to vertebrates and also have been observed to have faster reflexes. For instance, the visual startle reflex of a *Condylostylus* fly has been measured in the order of 5 ms [29].

Insects receive and respond to a wide variety of mechanical stimuli, they are sensitive to physical contact with solid surfaces, they detect air movements, including sound waves and they have a gravitation sense [30]. Some of these mechanisms

are exteroceptive, interoceptive and some proprioceptive. Proprioception in insects has a different structure altogether as compared to humans and birds, mainly due to the different physics associated to smaller scales. This information is gathered by a spectrum of mechanosensilla. These are sense organs that are able to respond continuously to deformations and stresses in the body, providing the insect with posture and position information. They send information to the insect central nervous system about mechanical strains in the cuticular exoskeleton [31].

Mechanoreceptors can be found in many places on the surface of an insects body Figure 2.6. These receptors are innervated by one or more sensory neurons that fire in response to stretching, bending, compression, vibration or other mechanical disturbance [32]. Arthropod mechanoreceptors are divided into two morphological groups: type 1 or cuticular and type 2 or multipolar. Type 1 are ciliated receptors, associated with the cuticle and have their nerve cell bodies in the periphery close to the sensory endings, they can be subdivided into three major groups: Hair-like receptors, campaniform sensilla, and chordotonal organs. Type 2 are nonciliated neurons whose central cell bodies have many fine dendritic endings. Other types of sensing mechanisms are also present in insects, including chemosensors. Sensilla can be both exteroceptive as well as proprioceptive.

Five types of proprioceptors occur in insects: hair plates, campaniform sensilla, chordotonal organs, stretch receptors, and nerve nets [30]:

(a) Hair plates:

Sensory hairs (sensilla trichoidea) occur on all parts of the insect body, however are found in greatest concentration on parts of the body which come into contact with the targeted sensing object. In its simplest form a sensillum comprises a rigid, poreless hair set in a membranous socket and four associated

sensing cells. Hairs differ in sensitivity, long hairs respond to small forces and pressure changes, whereas shorter thicker hairs (sensilla chaetica) respond to larger stimuli. Hair plates on the legs contribute to the insects gravitational sense.

(b) Campaniform sensilla:

A campaniform sensillum is similar to a tactile hair but has a dome shaped plate of thin cuticle instead of the hair shaft. The plate may be slightly raised above the surrounding cuticle, flush with it, or recessed but in all cases it contacts the neuron and serves as a stretch or compression sensor. This plate can be round or elliptical depending on the species. The elliptical plates have a stiffening rod of cuticle along the longitudinal direction on the ventral side of the plate. The plate has directional sensitivity to stress that is perpendicular to the longitudinal axis of the rod. Sensilla are typically arranged in groups with directional arrangements, i.e. such that rods are perpendicular.

(c) Chordotonal organs:

also known as scoloporous sensilla or scolopidia, are another widely distributed form of proprioceptor in insects. These differ from campaniforms in that there is no specialized exocuticular component. They are associated with the body wall, internal skeletal structures, tracheae and structures in which pressure changes occur. They exist as strands of tissue that stretch between two points. A change in length will produce stretching or bending of the dendritic membrane and will stimulate the sensing cell. Chordotonal organs of arthropods mediate resistance reflexes that are similar to stretch reflexes of vertebrates [33].

(d) Stretch receptors:

A multipolar neuron whose dendrites terminate in a strand of connective tissue or a modified muscle cell, which is then connected to a body wall, intersegmental membranes and muscles. If the terminals of the neuron are stretched, the receptor is stimulated. These provide information about rhythmically occurring events within the insect, like breathing.

(e) Nerve nets:

Interconnected nerve fibers and cells are connected together to form a nerve net. A nerve net provides a simple level of coordination. Most insect's nerve cells are clustered into groups which are called ganglia. Ganglia are interconnected by nerve cords and receive impulses from sense organs and direct them to other parts of the body, particularly muscles. Insects have multiple nerve chords, this contrasts with humans and other vertebrates, as these only have a single tubular one [34].

Amongst these types of proprioceptors, which involve insect organs which are superficial and non-superficial, insects have a number of cuticular sensilla Figure 2.5.

Table 2.1: Some insect mechanoreceptors

| Mechanoreceptor | Description | Function | Location |
|-------------------------|-----------------------------------|----------------------------------|--|
| Trichoform sensilla | Hairs | Tactile, motion | Behind head , on legs, near joints |
| Campaniform sensilla | Flattened oval discs | Flex receptors | Exoskeleton, legs, base of wings |
| Stretch receptors | Multipolar neurons | Stretch receptors | Interseg. membranes, muscular walls |
| Pressure receptors | Hair like structures | Pressure detectors | Tracheal system |
| Chordotonal organs | Subjenual, Tympanal, Johnstons | Vibration,acoustic, resonance | Legs, thorax, pedicel of antenna |

The cuticle is mostly superficial, however it's also layered into endo-, meso-, and exo- cuticle, with the tougher layer being the most external layer. The exocuticle is very strong under compressive forces but comparatively weak under tension. The endocuticle is flexible and is able to resist tensile forces. The cuticle is usually characterized by surface patterns which reflect the arrangement of cells beneath them. Sensilla found in the cuticle are the basic functional and structural units of cuticular mechanoreceptors and chemoreceptors.

The different types of cuticular sensilla are found in Figure 2.5. These illustrate the mechanoreceptor contraptions of insects which use these organs to sense tensile and compressive forces for survival and navigation. An example of the various functions of these types of insect sensors is found in Figure 2.6, where different

types of sensilla serve different proprioensing purposes by functional location on the insect's body and by orientation within the locations. There are groups of campaniform sensilla on the trochanter, a group proximally on the femur and another on the tibia, and a small number on the dorsal surface. These are typically accompanied by other types of proprioceptors, as discussed above. Probably the major function of campaniform sensillum is to register stresses produced by the weight of the insect's body on the limbs, the forces caused by the muscles on the cuticle, and external stimuli [31].

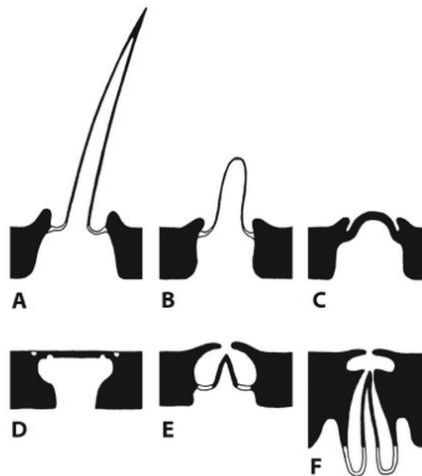


Figure 2.5: Different types of cuticular sensilla. a. sensillum trichoideum (hairs), b. sensillum basiconium, c. sensillum campaniformium, d. sensillum placodeum, e. sensillum coeloconium, f. sensillum ampullaceum, [35].

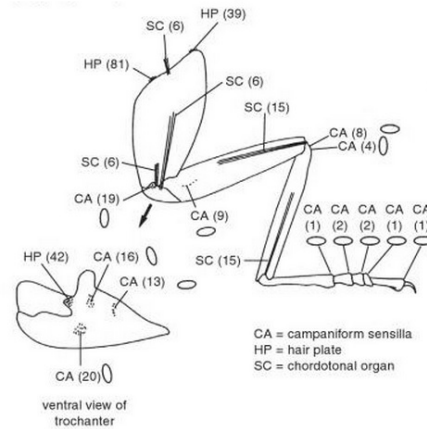


Figure 2.6: Proprioceptors of the foreleg of periplaneta. The numbers in brackets show the number of sensilla in each group. Ellipses show orientations of campaniform sensilla [36].

2.1.2 Location and distribution of proprioceptors

Insect platforms have different performance requirements. Proprioceptive organs in insects are located in many different places along the insects body, grouped around regions which will produce maximal outputs, i.e. grouping around a joint. Stretch proprioceptive organs are typically found near regions of maximal strain, as in the case of the stick insect trochanter where the campaniform sensilla are located at the leg joint Figure 2.7. In particular, stretch and stress sensors are found along insect bodies and wings.

Insects distribution of proprioceptive sensors is different from that of humans. In humans, the stretch sensors lie on skeletal muscle fiber and tendons. These move with the limbs to generate motion and adapt to different situations. For natural fliers, the muscle function however gets to be modified in actuating wings

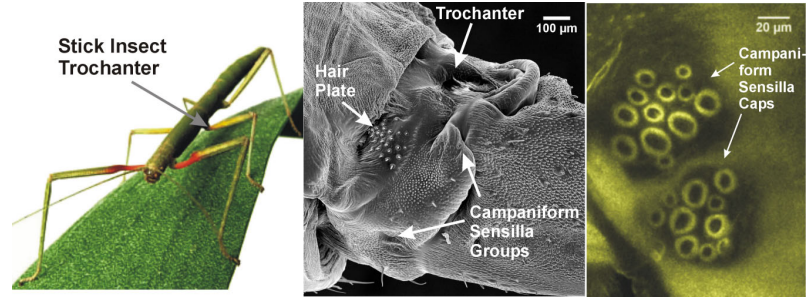


Figure 2.7: Distribution of camaniform sensilla in the stick insect's body [37].

for flapping and gliding.

The muscles of insect wings are however less complex than those of birds and do not extend beyond the axilla, which is the point at which thoracic muscles are attached to the insect wing and therefore control of shape must be exerted remotely. That is, they transmit forces via rigid wing components such as veins and areas of thickened membrane which act as levers. However, active muscular forces cannot entirely control then insect wing shape in flight. The muscular forces interact dynamically with the aerodynamic and inertial forces that the wings experience during flight and they also interact with the wings structural properties. The effects of these interactions are determined by the architecture of the wing itself, its planform and relief, the distribution and local mechanical properties of the veins, the local thickness and properties of the membrane as well as the position and form of the lines of flexion [38].

2.1.3 Proprioception in insect wings and flight control

Insect wings are muscularly driven aerodynamic surface that generate lift and propel the insect through the air. However, the wing is also a sensory surface, with a variety of sensory organs. Many of these sense mechanical and chemical inputs. They can detect relative movement between wing and body and mechanical deformation of the wing cuticle [39]. Similarly, as the sensilla distributed on the body (Figure 2.6), the sensilla on the wings is also composed of hairs, campaniform sensilla and chordotonal organs. The hairs are sensitive to external forces, the campaniform and chordotonal organs are sensitive to self motion of the insect. Campaniform sensilla are sensitive to cuticular deformation, and the chordotonal sensilla act as stretch sensors, therefore providing proprioceptive information.

Wings also possess a variety of surface structures mainly for sensing purposes [38]. These include tactile and proprioceptive sensilla, scales, microtrichia, a variety of spines and papillae, among others. Sensilla on insect wings have been reported previously in various species . Another insect organ that is well populated with campaniform sensilla is the haltere. This is an organ that serves as a gyroscope. Any departure from level flight will produce torques on the bases of halteres at twice the vibration frequency [31]. The unique flight control equilibrium sense is provided by the sensilla at the base of the halteres. This sense is a robust equilibrium reflex in which angular rotations of the body elicit compensatory changes in both the amplitude and stroke frequency of the wings [40]. Halteres encode the angular velocity of the body by detecting the Coriolis forces that result from the linear

motion of the haltere within the rotating frame of reference of the fly's thorax.

On wings, arrays of campaniform sensillae monitor the rate and extent of local bending. These sensory receptors are found in arrays which are concentrated near the front of the wing and at the wing base where stiffness and bending moments are highest. The high surface density of campaniform sensilla and their direct neural connections with central locations of flight control suggest that these sensors monitor cyclical wing motions. Their spanwise topographical arrangement suggest a role in monitoring progression of torsional waves during wing rotation [41]. On fly wings, the campaniform are tuned to the wing beat frequency. Campaniform also respond to deflections if camber is actively imposed to the wing, for instance during the upstrokes and downstrokes. A correlation between number of wing sensillae and flight maneuverability has been proposed.

Location of sensilla is species dependent. Grasshoppers, in particular the *Melanoplus sanguinipes*, have groups of campaniform sensilla on the proximal area of the subcostal vein of both fore and hind wings. These monitor the degree of wing twisting. Figure 2.8 shows the veins and distributed sensilla along the wings of a grasshopper. These figures show the number and distribution of sensilla on a representative fore wing (left) and hind wing (right) of a grasshopper (*Melanoplus sanguinipes*). The primary veins are: Sc, subcostal, R, R1, Rs, radius; M, Ma, Mp, media, Cu, cubitous [42]. In each wing, the main nerves follow the primary veins and their branches [42]. The intervenal nerve nets are formed by axons from surrounding sensilla, as these join to form the nerve branches of the main nerves. Both wings of the grasshopper have trichoid and campaniform sensilla, which is identified as

chordotonal. These groups of campaniform sensilla are responsible for reflex control of wing twisting, which is required for normal flight as well as body orientation and stability during flight [31].

Campaniform are also present in the wings of a number of other insect species such as *Drosophila* and *Calliphora*, as shown by Dickinson [43]. In *Drosophila*, the distribution of campaniform is somewhat along specific veins near the leading edge of the wing, this is shown in Figure 2.9. In the Dipteran wings shown, the campaniform sensilla lies exclusively on two branches of the radial vein $R1$ and R_{4+5} . These are used for flight control and wing coordination.

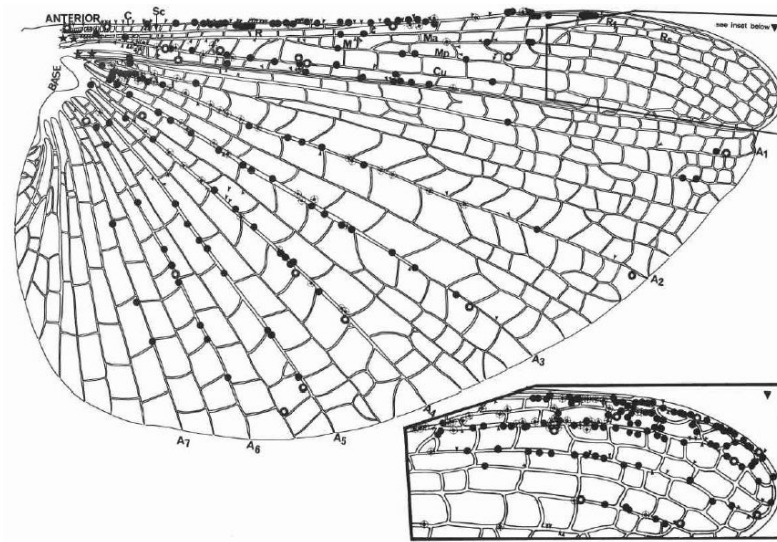


Figure 2.8: Campaniform sensilla on grasshopper wings

2.1.3.1 Location and distribution of sensilla on wings

In insect wings, sensilla are typically located near veins, as these are the structural support of the wing and therefore encode bending and torsion.

Veins are typically cuticular tubes which contain hemolymph and often tracheae and nerves. Hemolymph is the circulatory fluid of arthropods and is analogous to blood and lymph in vertebrates. There is a distinction between main or longitudinal veins which radiate from the base and cross-veins, which link the longitudinal veins. These main veins can also contain trachea, nerves, and can also conduct oxygen and sensory information. Aside from vital functionality they act as supporting members, preventing rips from spreading across the membrane. Many longitudinal veins are essentially beams, principally experiencing bending and twisting forces. Like typical man-made cantilevered beams, their diameter tends to decrease from the base to the tip, reflecting the fact that the bending moments on them do the same. This span wise tapering has two other functions; it reduces the moment of inertia, and hence the energy required as well as stresses generated during oscillation. It also makes the wing-tip more flexible and more easily deflected by excessive inertial forces and unpredictable impacts. Junctions between veins vary depending on the level of rigidity required for the function of the joint.

The location and distribution of sensilla is species dependent. It was shown that campaniform sensilla is placed at specific locations on the wing of *Drosophila* for the maintenance of control and phase relationships between the two wings. This allows the insect to steer and turn as well [43]. The presence of sensilla on the wings

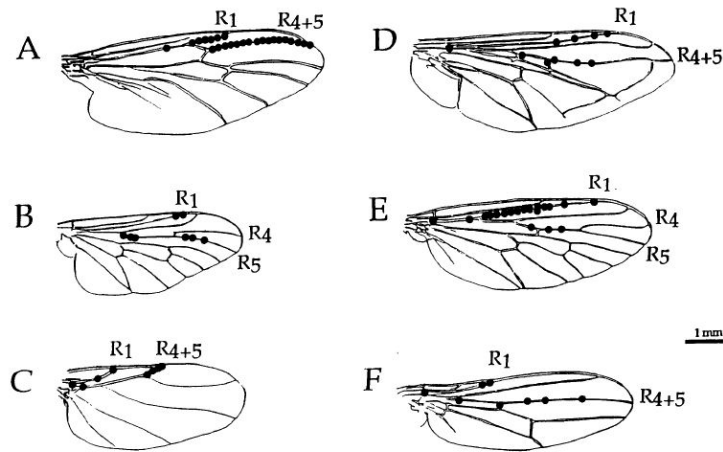


Figure 2.9: Distribution of campaniform sensilla on the wingblases of flies of different families of Diptera [39].

to control wing motion is common across all insect species. For the grasshopper wings, sensilla is located near the proximal end of both fore and hind wings. These are used for monitoring the degree of wing twist.

Campaniform sensilla occur in veins and in intervenal membranes. Those in membranes are surmounted by dome shaped plaques, those in veins have a less pronounced dome. Both types are innervated by a single neuron with a large soma and a short dendrite. The dendrite is inserted centrally inside the dome. Chordotonal sensilla were noted at the base of both wings [42] of the grasshopper. In both wings, the sensilla are concentrated along the longitudinal veins, only a few are on transverse veins and in membranous areas. On the fore wing, the sensilla are generally evenly distributed along the length of the wing, except for the wing tip. Heavier concentrations occur along the trailing margin of the wing. Hair and campaniform sensilla were observed mostly on the top surfaces of both wings of the

grasshopper Figure 2.8. Similarly for Diptera, the sensilla were mainly located near principal longitudinal veins.

Campaniform sensilla are situated primarily in the membranes of the wings, but always close to veins. Campaniform sensilla undoubtedly monitor the degree of cuticular stress with changes in air pressure at various locations on the wings. They are suitably located for this function on or near major veins and in clusters at the base of the hind wing. These sensilla in the hind wing are essential in regulating fore wing twisting during locust flight.

Venation patterns have an effect on the flexural stiffness of wings [44]. It has been found that spanwise flexural stiffness is 1 to 2 orders of magnitude larger than chordwise flexural stiffness. It has also been observed that there is an increased density of veins towards the leading edge, which causes anisotropy. This anisotropy would serve to strengthen the wing in bending while allowing chordwise bending to generate camber. This could also facilitate spanwise torsion, which is seen in many species during supination. Some insects have wings that are stiffer in both directions, for instance dragonflies, hawkmoths, flies and bumblebees have wings that are stiffer than expected for their size, whereas damselflies, crane flies and lacewings have more flexible wings than expected.

2.1.4 Distributed sensing in natural fliers

It is in the perspective of strain sensing and its bioinspired functionality that this dissertation is constructed upon. Similar to the Golgi tendons and joint recep-

tors in humans, as well as the sensilla organs, in particular those which sense in plane tension. Strain sensors were installed in the proprioceptive perspective such that they are able to sense relative motions of the aircraft. The location of the sensors and their distributed nature resembles that of insect wings, in morphology and in function. It has been shown that rapid reaction times can be achieved by means of fast integration of distributed sensors, such as in the fly's compound eye [9].

In the insect wings, natural stretch sensors are placed along wing venations, or the structural components of insect wings. They are typically distributed along the leading edge of the wings and concentrated around certain wing veins.

2.1.5 Wave propagation

This work is inspired not only in the proprioceptive mechanisms of nature but also in the physics of propagation of mechanical disturbances. As discussed earlier, some insects use the campaniform sensilla to sense the propagation of torsional waves through their wings for flight control [41].

Mechanical wave propagation has not been explored for disturbance rejection in the UAS aeronautical field, as typically not much information is obtained from the aircraft structure itself while on flight. Studies by [45], have measured and modeled the propagation of mechanical waves on a free free beam structure [46] by means of accelerometers.

Strain sensing was used for impact testing [46] and measurement of wave propagation related quantities Figure 2.10. The bimaterial beam shown is made of strips

of aluminum and epoxy. The impactor consisted of a steel ball which was dropped from a short height on one end of the bimaterial beam.

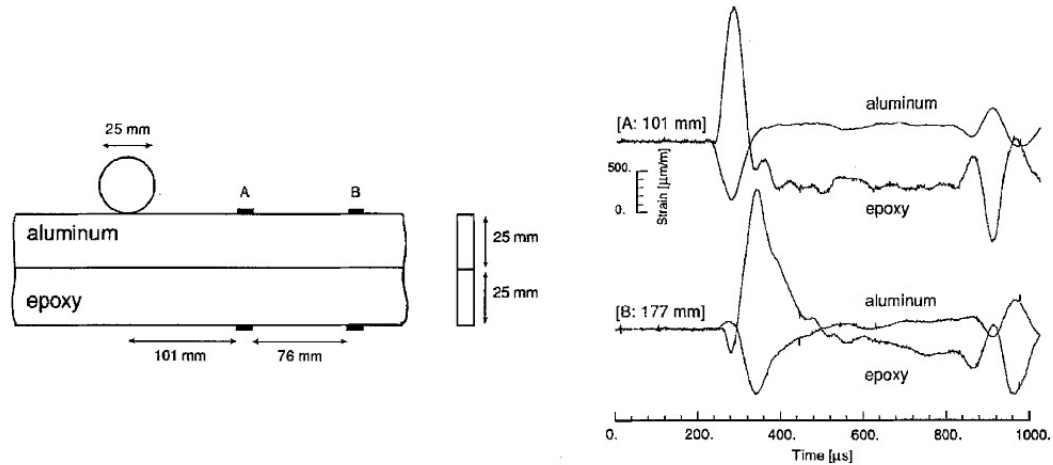


Figure 2.10: Wave propagation measured with strain gauges: bimaterial beam (left) and experimentally recorded strain histories (right) [46]

The propagation times depend on the material properties of the beam or wing. The time difference from the maximum peak on strain gauge A and the maximum peak of strain gauge B is the time of travel between the two points. In this case, the propagation times are in the order of tens of microseconds as the material for the beam is aluminum, which is very dense, rigid and therefore would yield fast propagation speeds. Computational models have been built to study force propagation, mainly for health monitoring purposes [45].

This work is based on anticipation of the rigid body motion by early detection of disturbance propagation, used in a proprioceptive way. The following diagram depicts the order of response to a disturbance in a fixed wing aircraft. First, discrete

or continuous disturbances will hit the wings, second, the mechanical disturbance will propagate throughout the structure until it finally reaches the fuselage, where IMUs will typically be recording rigid body motion. With strain feedback, anticipation is gained in the mitigation of the disturbance as reaction can occur before causing the fuselage to be affected, or at least completely affected. Anticipation times were measured for the glider experiments of Section (4.1.1).

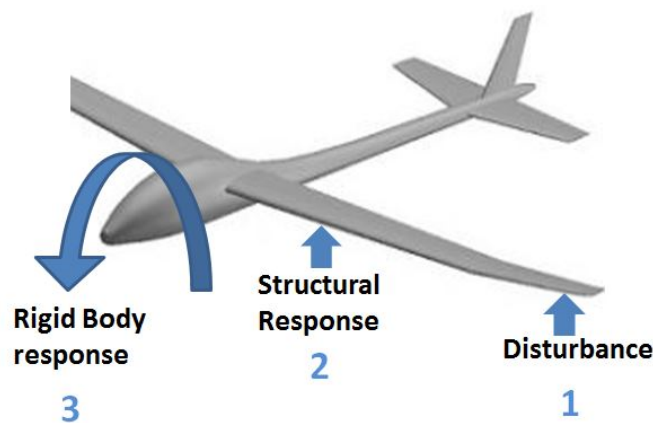


Figure 2.11: Order of timescales in disturbance sensing

2.2 State of the art

Relevant state of the art is presented in the context of strain sensing as applied to atmospheric disturbance rejection.

2.2.1 Atmospheric disturbances

Atmospheric phenomena is of many different origins Figure 2.12. Turbulence producing phenomena can be due to sharp thermal changes, convection changes, clear air turbulence, low level terrain induced turbulence, mountain wave turbulence, cloud induced or convective induced turbulence, cumulus clouds, and in-cloud turbulence [47], [48]. Thunderstorms produce the most severe type of turbulence. Tip vortices from other aircraft may also produce air turbulence in the vicinity of their flight path.

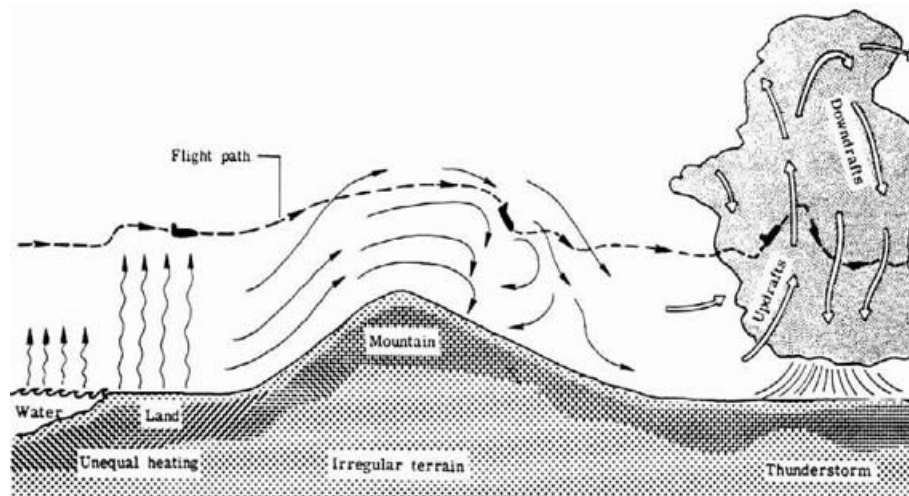


Figure 2.12: Turbulence production in the atmosphere [49]

Atmospheric wind can be considered a superposition of three types of flow: mean wind, waves and turbulence [3]. The variation time of mean winds is a few hours, for waves is tens of minutes and the timescales of turbulence range from seconds to minutes.

Disturbances can be categorized into two ideal categories: discrete and continuous, and are generally modeled as being isotropic in the real atmosphere. Discrete gusts are deterministic and have defined forms. Three forms of discrete gusts are of interest: step gusts or sharp-edged gusts, ramped gusts and 1-cosine gusts, which capture the form of a solitary gust. Two typical 1-cosine gust shapes are shown in Figure 2.13.

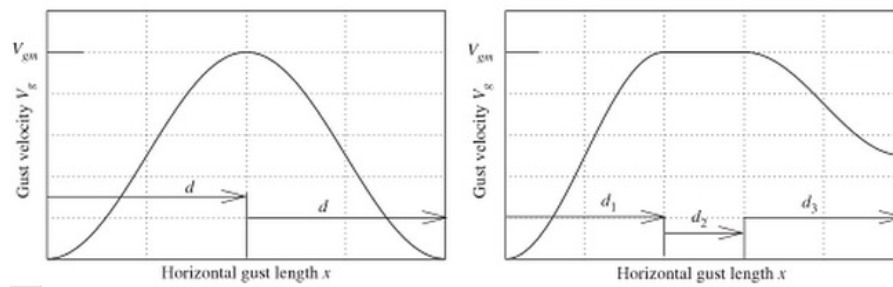


Figure 2.13: Typical 1-cos gust shapes [50]

Continuous disturbances or turbulence is represented as a random variation of gust velocity with frequency spectra due to the irregular and anisotropic nature of these wind variations. Dryden and von Karman distributions are two common continuous turbulence distributions. Their spectral representation can be used to generate turbulence by filtering band limited white noise with an appropriate shaping filter [51]. Figure 2.14 shows a ratio of the psd functions of the Von Karman and dryden continuous gust models. Both of these distributions are defined by characteristic scale wavelength which is a function of altitude in the atmosphere and the root mean square velocity. The von Karman distribution is often regarded

as a more accurate description of measured atmospheric distributions however the Dryden distribution is simpler to implement in the time domain.

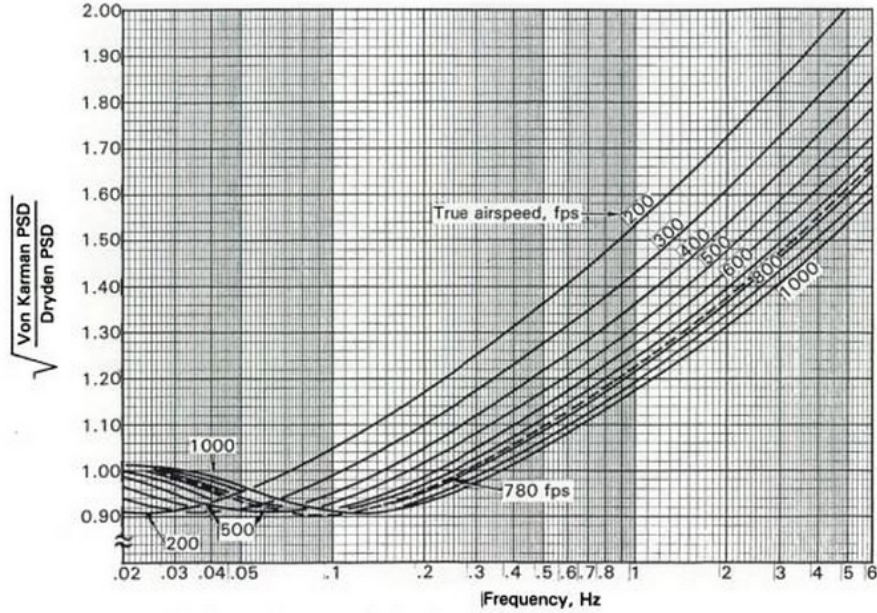


Figure 2.14: Ratio of Von Karman and Dryden PSD functions [52]

If uniform gusts are considered, the lift changes as a function of the angle of attack induced by the gust for lateral and vertical uniform gusts. For head on gusts, the change is in the dynamic pressure. These changes in lift are shown in Equation (3.43), from [52].

$$\begin{aligned}
 \Delta L &= \frac{\rho}{2} V_{\infty}^2 S C_{L\alpha} W_g & \text{gust}_{vertical} \\
 \Delta L &= \frac{\rho}{2} V_{\infty}^2 S C_{L\alpha} V_g & \text{gust}_{lateral} \\
 \Delta L &= \rho V_{\infty}^2 S C_{L\alpha} U_g & \text{gust}_{longitudinal}
 \end{aligned}
 \tag{2.1}$$

Where ρ is the air density, V_∞ is the freestream velocity, S is the planform area, and U_g , V_g , W_g are the longitudinal, lateral and vertical gust velocities. $C_{L\alpha}$ is the lift curve slope and C_L is the lift coefficient.

Wing loading due to gusts can be idealized as one dimensional phenomena. However, it has been shown that important effects arise from 3D modeling of gusts. For instance, a comparison of 3D and 1D gust load modeling on the C-5A Galaxy aircraft (Lockheed Martin, Bethesda, Maryland) showed that 3D gust modeling reduces wing loads and increases tail loads increased during turbulence. This was verified through flight test experiments [3]. In addition to this, uniform spanwise gust distributions can predict larger loads than non-uniform gust distributions.

In nature gust rejection is effectuated by means of visuals [53], tactile feedback, and other types of mechanosensory feedback. Halteres for instance keep the angular momentum to act as a gyro [?]. In visual disturbance rejection, principles of optic flow and neuronal integration produce patterns of motion which can be matched to the different visual cues. This highly reactive mechanism uses low bandwidth sensing organs in flying insects to quickly map out the nature of the disturbance.

2.2.2 Gust alleviation

Many different types of gust mitigation mechanisms have been devised and investigated. These mechanisms include, amongst others, passive and active mechanisms. Passive gust mitigation mechanisms are incorporated at the design phase. For instance adding wing dihedral adds roll stability and therefore mitigates gust

disturbances indirectly. Wings which have been designed to dampen out oscillations from gusts are another type of passive solution to the gust problem. Other mechanisms have modified wings which passively react to gusts, decreasing the load on the overall structure. An example of a passive mechanism includes having rotating mid-sections which can let vertical gusts pass by [54].

Other mechanisms that have been proposed consist of cutting out sections of the wing [55], enhancing spoilers, and varying the dihedral angle through wing geometric changes. Articulated wings by means of passive wing deflection [56] and inclusion of additional control surfaces such as winglets [57].

Active controls for gust mitigation can be grouped into three distinct groups: operational aircraft, flight test experiments, and wind tunnel experiments [58].

Examples of operational aircraft active controls include: Active lift distribution control (ALDCS), which uses wing tip accelerometers to determine wing bending and torsional motion. Similarly the Active control system (ACS) [59] used wingtip and fuselage forward and aft vertical accelerometers as well as fuselage pitch gyroscopes, for load alleviation.

Structural mode control has been widely explored. Structural vibration suppression can be found in many embodiments. One of them, the one implemented on the B-1 Lancer, which actively suppresses the unfavorable motion at the pilot station using dedicated active canard-like control surfaces and a co-located accelerometer. Flutter suppression has also widely been explored [60].

Wing morphing is another approach to vibration suppression [61] as well as adaptive controllers for recursive estimation of vibration modes [62]. Vibration

suppression can also be achieved by geometry changes of the airfoil [63]. Optimal and adaptive controllers for gust alleviation have also been developed to achieve gust mitigation [64]. Another method entails the measurement of the angle of attack computed as the difference between the measured angle of attack and the inertially derived angle of attack [65], [66].

Gust load alleviation surfaces can be implemented in out of phase configurations to damp out unwanted modes. Other methods actively control the rudder and elevators to increase the fuselage damping response. Trailing edge flaps can also be used to actively suppress the effect of gusts [67].

Optics mechanisms have also been proposed, such as LIDAR gust anticipations by measuring the flow properties of the wind ahead of the aircraft [68] as well as LIDAR variants such as the ultraviolet Doppler LIDAR for higher altitudes.

Wind tunnel experiments for gust alleviation have been similar to some of the flight testing methods.

Most of the methods in the literature use inertial loading measurements for gust alleviation, ride quality, and fatigue life extension of the aircraft.

The loading due to gusts is an important airworthiness requirement and is regulated by the FAA, FAR [3], [52]. Requirements on discrete, sharp gusts as well as continuous turbulence can be found in [58].

2.2.3 Static and dynamic loading of wing

Aircraft are subjected to different forces while on flight, causing the airframe to undergo structural deformations and internal loads. The total force is a summation of the inertial loads, the aerodynamic forces and the forces introduced by atmospheric disturbances such as gusts and turbulence. In the case of gust induced structural response, its flexibility will depend on either the amount of energy transferred from the gust disturbance to the structural bending modes or if energy is absorbed from the gust, the dissipation of that energy by some form of damping.

One dimensional wing static loading models can be developed as a function of Lift based on the available literature. Under the right assumptions, a wing can be modeled as a cantilever beam and the strains generated by Lift and other forces can be incorporated into a static force model.

A correlation of the strains produced by gusts and the gust characteristics will allow the necessary control surface corrections to account for the lift changes produced by the gust. Therefore gust disturbances can be aeroelastically correlated to strain profiles in the wing structure. In the simple case of a vertical gust W_g .

$$\text{If } \varepsilon = f(W_g) \text{ and } W_g = g(L) \rightarrow \epsilon = F(L_{aero}, P_{inertial}) \quad (2.2)$$

Where $L_{aero} = L_g + L_m$ is the total lift or total aerodynamic loading, corresponding to the gust and the motion generated lift, respectively. Coriolis and Centrifugal forces and their effect on the wing strain, are neglected for this initial

analysis.

If the wing is sufficiently slender, then strip theory can be applied and the force per unit span due to the gust velocity encountered by the airfoil's leading edge at the instant $t=sb/U$ can be calculated as follows [69], [70]:

$$L_g = 2\pi\rho Ub \int_0^s W_g(\sigma) \psi'(s - \sigma) d\sigma \quad (2.3)$$

Where U is freestream velocity. The distance traveled in semichord lengths is defined as $s = U * t/b = U * t/b$, with b a reference chord value which equals b for a uniform distribution. This expression assumes an equal spanwise chord length. If the gust distribution is made constant instead of arbitrary, then the lift produced by a sharp gust disturbance is an integral function of the Kussner's function ψ .

$$L_g = 2\pi\rho Ub W_g \int_0^s \psi'(s - \sigma) d\sigma \quad (2.4)$$

The second part of the aerodynamic loading, L_m can be calculated as a function of normal coordinates which represent the vibratory bending modes of the wing and the Wagner functions for indicial lift ϕ [69]. Therefore,

$$L_m = f(\varepsilon_i, \phi_i), i = 1, 2, \dots, n \quad (2.5)$$

Inertial terms can also be calculated in terms of these two parameters, the

integrand corresponding to inertial loads in a vibrating wing corresponds to:

$$I_{loads} = \left(\sum_{i=1}^n \phi_i(\eta) \varepsilon_i''(s) \right) m(\eta) \quad (2.6)$$

Using Euler-bernoulli assumptions for the wing approximated in its mechanical behavior to that of a beam, the calculation of strain at a vertical distance z from the neutral axis and at a distance x from the root of the wing or the center line can be calculated as follows:

$$\varepsilon_x = \frac{z}{EI_y} M = \frac{z}{EI_y} \int_x^l [L_g + L_m - I_{loads}] (\eta - x) d\eta \quad (2.7)$$

Where E is the Young's modulus of the wing, I_y the moment of area in the y direction at the centerline and l the length of the wing. This static output equation is based on the nature of the loads that the wing experiences and can be implemented in a feedback loop to account for the gust disturbances. If dynamic effects are considered, the state vector for longitudinal motion now depends on the truncated bending modes. It can be defined as follows, i.e. for the first two modes [71]:

$$x = [\alpha, q, \varepsilon_1, \dot{\varepsilon}_1, \varepsilon_1, \dot{\varepsilon}_1], \quad (2.8)$$

And the output is a function of the modified state vector and the measured strains. This state vector would then be formulated in the setting of an aeroelastic system of equations, as shown in Section (2.2.4). Another option for this calculation

consists of a quasistatic force analysis for the duration of the gust.

The forces on a beam produce stresses and strains. Assuming that the wing can be modeled as a simple cantilever, the lift per unit span would equal the shearing force per unit span on the beam. The lift per unit span on a finite wing of wing length L and a total wingspan of $2L$ is:

$$L' = \rho_{\infty} V_{\infty} \Gamma_0 \sqrt{1 - \left(\frac{x}{L}\right)^2} \quad (2.9)$$

The lift is elliptical due to the effects of the downwash created by finite behavior of the flow over a finite wing. V_{∞} is the freestream velocity and ρ_{∞} is the density of the freestream. Γ_0 is the circulation at the root of the wing and is equal to:

$$\Gamma_0 = \frac{V_{\infty} S C_L}{\pi} \quad (2.10)$$

Integrating the lift per unit span or shearing force per unit span q to get the total shearing force as a function of wing span x :

$$\frac{\partial F_s}{\partial x} = q \quad (2.11)$$

$$\frac{\partial F_s}{\partial x} = L' \quad (2.12)$$

Integrating to get the shearing force caused by the elliptical lift distribution:

$$F_s = \rho_\infty V_\infty \Gamma_0 \int \left(1 - \frac{x^2}{L^2}\right)^{\frac{1}{2}} dx \quad (2.13)$$

$$F_s = \rho_\infty V_\infty \Gamma_0 \left(\frac{x}{2} \sqrt{1 - \frac{x^2}{L^2}} + \frac{\log \left(x \sqrt{\frac{-1}{L^2}} + \sqrt{1 - \frac{x^2}{L^2}} \right)}{2 \sqrt{\frac{-1}{L^2}}} \right) \quad (2.14)$$

Using this expression of the shearing force, the bending moment can be found.

The shearing force is the rate of change of bending moment:

$$F_s = \frac{dM}{dx} \quad (2.15)$$

where the bending moment is:

$$M(x) = \int F_s dx \quad (2.16)$$

and the bending strain is calculated using:

$$\epsilon_x = -z \frac{M(x)}{EI} \quad (2.17)$$

2.2.4 Aeroelastic models

The coupling of structural and aerodynamic forces acting on can be described by aeroelastic models. These can be non linear, linear, dynamic, static or servoeelastic

[70].

Aeroelastic models are fundamented in a system of equations which consist of rigid body dynamics and structural dynamics. This system of equations is shown in Figure 2.15. In this equation A_R, B_R, C_R, D_R are the linearized rigid body equations of the aircraft and A_E, B_E are the linearized structural dynamics equations. All these matrices contain stability derivatives which can be identified with analytical or numerical methods. The elastic degrees of freedom correspond to the modes associated to each eigenfrequency.

$$\begin{array}{l}
 \text{Rigid Body Dynamics} \left\{ \begin{array}{l} \dot{x}_R = A_R x_R + B_R u_R \\ y_R = C_R x_R + D_R u_R \end{array} \right. \quad x_{R, long} = \begin{Bmatrix} u \\ w \\ q \\ \theta \end{Bmatrix} \quad x_{R, lat} = \begin{Bmatrix} v \\ p \\ r \\ \phi \end{Bmatrix} \\
 \\
 \text{Aeroelastic Dynamics} \left\{ \begin{array}{l} \dot{x}_E = A_E x_E + B_E u_R \end{array} \right. \quad x_E = \begin{Bmatrix} \eta_1 \\ \dot{\eta}_1 \\ \eta_2 \\ \dot{\eta}_2 \end{Bmatrix} \quad \begin{array}{l} \text{Vibration} \\ \text{modal} \\ \text{coords.} \\ \text{and} \\ \text{Rates} \\ \text{(1st, 2nd} \\ \text{modes)} \end{array} \\
 \\
 \text{EOM of} \\
 \text{Elastic degrees} \\
 \text{Of freedom} \left\{ \begin{array}{l} \ddot{\eta}_i + 2\xi\omega_i\dot{\eta}_i + \omega_i^2\eta_i = \frac{f_i}{m_i} \quad \text{For } i = 1,2 \end{array} \right.
 \end{array}$$

η_i is the modal coordinate associated with the i^{th} vibration mode

Figure 2.15: State space equations for rigid body motion and structural dynamics

The fully coupled 6-DOF aeroelastic equations are presented in Figure 2.16, in these equations, the elastic to rigid body aerodynamic coupling matrix is A_{ER} and the rigid body to elastic aerodynamic coupling matrix is A_{RE} .

ASWING is an aeroelastic simulation environment developed by [72]. In this

Coupling of RB
And Structural
Dynamics

$$\begin{aligned} \dot{x}_R &= A_R x_R + B_R u_R + A_{ER} x_E \\ \dot{x}_E &= A_E x_E + A_{RE} x_R + B_E u_R \end{aligned}$$

*Elastic to Rigid
Aerodynamic
coupling*

*Rigid to Elastic
Aerodynamic
coupling*

State variable
Model
For Elastic
Vehicle

$$\begin{cases} \dot{x}_R \\ \dot{x}_E \end{cases} = \begin{bmatrix} A_R & A_{ER} \\ A_{RE} & A_E \end{bmatrix} \begin{cases} x_R \\ x_E \end{cases} + \begin{bmatrix} B_R \\ B_E \end{bmatrix} u_R$$

$$y_R = [C_R \quad 0] \begin{cases} x_R \\ x_E \end{cases} + D_R u_R$$

Note: A_{RE} and A_{ER} include aeroelastic stability derivatives

Figure 2.16: 6-DOF coupled aeroelastic equations

package, A fully nonlinear Bernoulli-Euler beam representation is used for all the surface and fuselage structures, and an enhanced lifting-line representation is used to model the aerodynamic surface characteristics. The lifting-line model employs wind-aligned trailing vorticity, a Prandtl-Glauert compressibility transformation, and local-stall lift coefficient limiting to economically predict extreme flight situations with reasonable accuracy. ASWNG also allows for linear models to be constructed about reference flight condition points generated from a list of possible reference points.

2.2.5 Strain sensing

Strain gauges have been used for load calibrations [73]. These calibrations permit the measurement in flight of the shear or lift, the bending moment, and the torque or pitching moment on the principal lifting or control surfaces, landing-

gear structures, and relatively complex built-up wing and empennage assemblies. This investigation did not use these signals for control, but rather to monitor loads during flight with the objective of monitoring structural integrity demonstrations, and aiding developmental flight testing.

Many applications have strain bridges have been used to measure bending and torsional loads on the wing [74]. These however are only monitoring the bending and torsion of the wing and not used in feedback gust alleviation, an accelerometer was used in the active control of the full scale model instead.

Several wind tunnel models have been fitted with strain gauges for load monitoring. A feedback implementation is realized by [75] where a wind tunnel airfoil model was fitted with strain gauges at the root of an airfoil. Then a PID controller used measuring strain as a control input and the flap acceleration as the controller output .

Wind turbine blades have also been fitted with strain gauges to study fatigue load reduction potential when applying trailing edge flaps. Strain gauges are used as input for the flap controller such that local small fluctuations in the aerodynamic forces can be alleviated by deformation of the airfoil flap [76].

Wing shape control is another field where strain gauges are used. It was shown by [77] in a numerical simulation study, that the shape of the wings can be changed by integrated strain actuators. This allows for tasks such as gust load alleviation (i.e., disturbance rejection), flutter and vibration suppression (i.e., plant regulation), and maneuver enhancement (i.e., command following) and redistribution of maneuver loads. This approach albeit requires special piezoelectric actuation. Other strain

actuation applications include induced strain actuators, such as piezo ceramics and electrostrictives [78], which directly deform the structure through electromechanical coupling terms that appear in the actuator constitutive relations. Other aeroelastic wings have used strain gauges in closed loop to activate flaps [79] in wind tunnel settings for gust load alleviation.

Aeroelastic controls have been extensively explored [80]. Control laws applied to aeroelastic gust alleviation and flutter suppression include both MIMO [79], SISO laws [75], as well as PID [81], LQG [79], LQR [82], H_∞ controllers [83], among others.

2.3 Strain feedback and controller framework

Previous work related to the measurement of structural parameters of flexible aircraft [84] has had a variety of goals and applications, i.e. enhance aircraft performance, decrease loads and reduce vibrations [85]. In particular, the estimation of flexible structural motion for gust load alleviation has been implemented in the form of adaptive and non-adaptive control technologies [62]. Control laws associated to these systems relate the motion of control devices to measurements taken on the vehicle [86]. The various schemes found in the literature utilize different structural motion measurements to activate control devices through the proper control laws [87]. Most of these techniques focus on the aeroelastic and aeroservoelastic interactions of aircraft and typically aim to suppress vibrations and prevent the onset of flutter [62]. In UAV's these effects are much more critical due to the relative

closeness of the rigid body modes and the structural modes [88]; flexible UAV's have a much more agile flight potential as compared to large aircraft [84]. However, most of these approaches address vibration suppression. In this work we do not aim to suppress structural vibrations but rather use structural signals to generate a reflexive reaction to gusts. Reflexive strain feedback has not been widely explored. Strain measurements can influence the attitude control design [16]. For instance, regulation of the actuation commands sent to the control surfaces through augmentation of the attitude controller. A second way in which strain measurements can be implemented is to directly use them to detect angular acceleration to potentially obtain a more optimal tracking response [16].

Figure 2.17 shows a load feedback loop to optimize the attitude controller and reject disturbances.

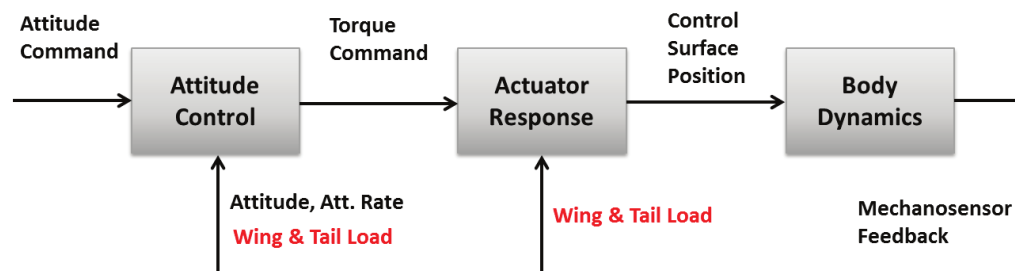


Figure 2.17: Augmented attitude controller: load feedback to optimize the responsiveness of the attitude controller and to reject disturbances and errors in actuated body torque (excerpt from Thompson et al. [16]).

2.3.1 Strain feedback

In this work, strain is measured in order to provide an estimation of the forces and moments acting on the aircraft. Strain measurements are taken with metal film strain sensors. These measurements are then projected or wide field integrated [9] to obtain the actual force state estimations. Given our main focus is the extraction of the force states, we will assume a quasi-static approach. To illustrate the state extraction procedure a 1D cantilever beam model is used. For a simple cantilever beam the second order ode shown in Equation (4.10) describes the behavior of the displacement with respect to span x .

$$\frac{d^2}{dx^2}(EI \frac{d^2y}{dx^2}) = Q \quad (2.18)$$

where EI is the bending rigidity, y is the vertical displacement and Q is the applied force. If Q is a uniformly applied force, then the strain as a function of span location x is given by Equation (4.12):

$$\varepsilon(x) = \frac{z}{2EI} * f(x) * Q \quad (2.19)$$

And z is the distance from the neutral axis, L is the wing semi-span. At the root, of the right wing for instance, the strain simply becomes Equation (4.13):

$$\varepsilon_R = \frac{zL^2}{2EI} * Q \quad (2.20)$$

The uniform vertical force applied to the wing can be calculated as Equation (4.11):

$$Q = \frac{2EI}{zL^2} * \varepsilon_R = C * \varepsilon_R \quad (2.21)$$

Therefore, the vertical force F_v acting at the root of the wing is calculated by simply scaling the strain sensor output. In the case of a fixed wing aircraft and assuming no inertial considerations, the total force on the aircraft rigid body becomes:

$$F_v = 2Q = 2C\varepsilon_R \quad (2.22)$$

$$F_{v_{levelflight}} = 2C\varepsilon_R = 2C\varepsilon_L \quad (2.23)$$

$$F_v = 2C(\varepsilon_R - \varepsilon_L) = C_w * \Delta\varepsilon \quad (2.24)$$

Where $2C$ equals the integrated output or wide-field integrated constant C_w . For level flight the left and right total strain output is approximately the same. An imbalance in forces produced by a gust disturbance is then proportional to the difference between the corresponding strains. The force/torque calculation is proportional to the strain differential. This basic calculation can be extended to encompass a chord wise structural response as well as to describe the extraction of

the remaining forces and moments. An implementation of the strain feedback is shown in Figure 2.18.

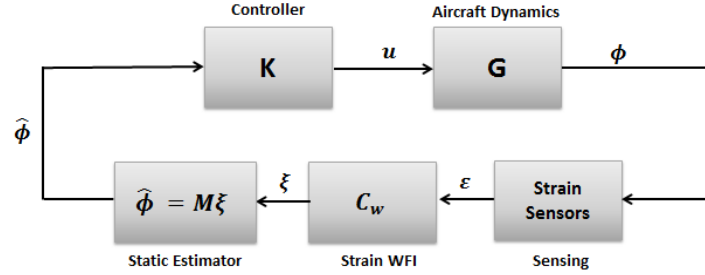


Figure 2.18: Strain Feedback implementation.

2.3.2 Robust controller framework

A robust control scheme is proposed in Figure 4.26. In this proposed multi-variable control scheme, the input disturbance on the plant output can be mitigated. Therefore, the disturbances are absorbed by the inner loop before they reach the plant. This controller was demonstrated for accelerometer and strain on a quadrotor by [6] in correcting roll and heave perturbations.

This feedback improves tracking of requested controls in the presence of disturbances by regulating errors between desired torques and actual torques. Thus the system is simultaneously capable of rejecting external disturbances, such as gusts, and internal disturbances, such as actuator variations.

In order to quantify the performance of this controller, robust analysis is used. The performance is quantified by means of input and output transfer functions

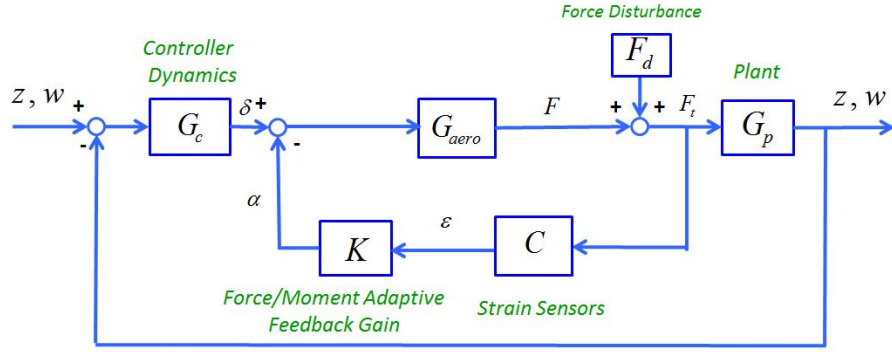


Figure 2.19: Fast inner loop for disturbance rejection

between the different signals of interest. Typical signals of interest include input and output disturbances, measurement noise, control commands, and states.

In the robust control framework, most signals live in bounded energy spaces, such as the Lebesgue space, which is the space of signals $f(t)$ with finite or bounded energy, as shown in Equation (2.25).

$$L_2^n(-\infty, \infty) = \{f : (-\infty, \infty) \rightarrow \mathbb{R}^n, \int_{-\infty}^{\infty} \|f(t)\|^2 dt < \infty\} \quad (2.25)$$

If a topological relationship is given to the Lebesgue space a number of spaces can be defined, among these, the Hilbert space. This is a space which has an inner product defined and is complete, meaning that the Cauchy sequences all converge within the space. The inner product has an induced norm, which gives a measure of the size of elements and in this case, of the gain of a particular transfer function. The Lebesgue space induced norm is defined as follows from Equation (2.26), where

the inner product is defined in Equation (2.27).

$$\langle f(t), g(t) \rangle = \int_{-\infty}^{\infty} \|f(t)\|^2 dt < \infty \quad (2.26)$$

$$\|f(t)\|_2 = (\langle f(t), f(t) \rangle)^{1/2} \quad (2.27)$$

Now applying the previous structures to a space of transfer functions we will obtain a transfer function space with bounded energy. This space is the \hat{L}_∞ space, which is a space of transfer functions that maps signals from $L_2(-\infty, \infty)$ to $L_2(-\infty, \infty)$.

$$\hat{L}_\infty = \{G : \|G\|_\infty < \infty\} \quad (2.28)$$

For a stable real rational transfer function G , with input \mathbf{w} and output $\mathbf{z} = G\mathbf{w}$, we may represent the induced operator norm in L_2^n of G as:

$$\|G\|_{L_2 \rightarrow L_2} = \sup_{\mathbf{w} \neq 0} \frac{\|\mathbf{z}\|_{L_2}}{\|\mathbf{w}\|_{L_2}} = \sup_{\mathbf{w} \neq 0} \frac{\|G\mathbf{w}\|_{L_2}}{\|\mathbf{w}\|_{L_2}} \quad (2.29)$$

This represents the input energy to output energy gain. This norm is equivalent to the infinity norm, which is defined as the supremum of the maximum singular value over all frequencies ω . The induced norm in L_2^n relates to the H_∞ norm $\|\cdot\|_\infty$

as

$$\|G\|_{L_2 \rightarrow L_2} = \|G\|_{\infty} = \sup_{\omega} \bar{\sigma}[G(j\omega)] \quad (2.30)$$

where $\bar{\sigma}[G(j\omega)]$ is the maximum singular value of G as a function of frequency ω .

The H_{∞} space is a subset of the \hat{L}_{∞} space, in that the transfer functions need to be real, and therefore stable, as well as rational. The norm of the H_{∞} space is then defined as:

$$\|G\|_{\infty} = \sup_{\omega} \bar{\sigma}[G(j\omega)] \quad (2.31)$$

where $\bar{\sigma}$ is the maximum singular value .

Thus the input signal energy to output signal energy gain may be represented via the maximum singular value $\bar{\sigma}$, and we may further note that the worst case scenario input energy to output energy gain is given by the H_{∞} norm, or equivalently $\sup_{\omega} \bar{\sigma}$.

In a MIMO setup, the effect of the input and output disturbances on the plant output can be quantified by means of different transfer functions. These transfer functions can be defined from block diagrams which describe the systems being modeled. In a general scenario, the block diagram for a system with input disturbance, output disturbance, and measurement noise is described by the diagram shown in Figure 2.20.

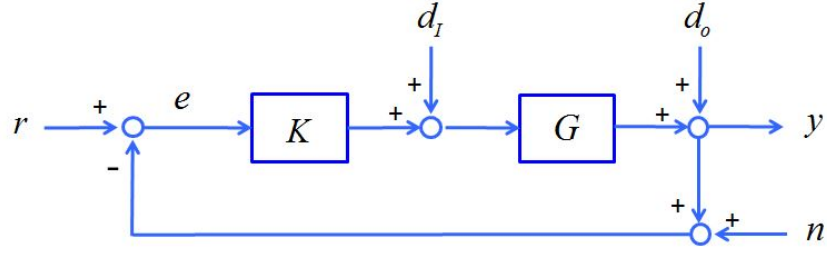


Figure 2.20: MIMO general case with input and output disturbances and noise

From this diagram the following equations for the output y and controller input u can be obtained:

$$\begin{aligned}
 y &= T_o \mathbf{r} + S_o G \mathbf{d}_I + S_o \mathbf{d}_o - T_o \mathbf{n} \\
 u &= K S_o \mathbf{r} + S_I \mathbf{d}_I - K S_o \mathbf{d}_o - K S_o \mathbf{n}
 \end{aligned} \tag{2.32}$$

where the open loop transfer functions depend on where the loop is broken, as in MIMO systems the transfer functions do not commute (Equation (2.33)).

$$\begin{aligned}
 L_o &= GK \quad S_o = (I + L_o)^{-1} \quad T_o = (I + L_o)^{-1} \quad break_{output} \\
 L_I &= KG \quad S_I = (I + L_I)^{-1} \quad T_I = (I + L_I)^{-1} \quad break_{input}
 \end{aligned} \tag{2.33}$$

When quantifying the performance of a MIMO system in terms of the qualities of the transfer functions in Equation (2.34) the norm of these transfer functions is

considered for desirable qualities. The maximum singular value $\bar{\sigma}$ and the minimum singular value act as collective gains of the MIMO system at every frequency ω and can be used for controller design. The singular values are also interpreted as a ratio of the input signal energy over the output signal energy, for each corresponding case.

The desired range of values for the transfer functions associated to good tracking and disturbance rejection are described as follows in Equation (2.34):

$$\begin{aligned}
 y &= S_o G \mathbf{d}_I && \rightarrow \bar{\sigma}(S_o G) && \text{small} \\
 y &= S_o \mathbf{d}_o && \rightarrow \bar{\sigma}(S_o) && \text{small} \\
 y &= -T_o \mathbf{n} && \rightarrow \bar{\sigma}(T_o) && \text{small} \\
 u &= K S_o \mathbf{r} && \rightarrow \bar{\sigma}(K S_o) && \text{small} \\
 e &= S_o \mathbf{r} && \rightarrow \bar{\sigma}(S_o) && \text{small}
 \end{aligned} \tag{2.34}$$

The first expression in the collection of partial dependencies as shown in Equation (2.34) requires that the maximum singular value of $S_o G$ be small for the frequencies of interest in order to have attenuation of input disturbance over the output y . The second expression needs the maximum singular value of S_o be small for attenuation of output disturbances on the output. Similarly, for the third expression, the max. singular values of the complimentary output sensitivity function need to be small in order for the measurement noise to have less of an impact at desired frequencies. This analysis applies as well to other signals, such as the last expression which allows for avoidance of large control signals due to reference commands.

In this framework, we would like to introduce strain feedback in a high band-

width inner loop, as show in Figure 2.21. In this fast loop, which is emphasized with a red dotted box, we use the structural response scales which are faster than the rigid body scales. Strain patterns encode instantaneous forces and moments being applied to the vehicle. Spatial weightings improve the signal to noise ratio by means of least squares estimated higher order states. The latency is reduced and no dynamic filtering is required. This feedback loop ensures that what is applied at the vehicle is what the controller asks for in the presence of disturbances.

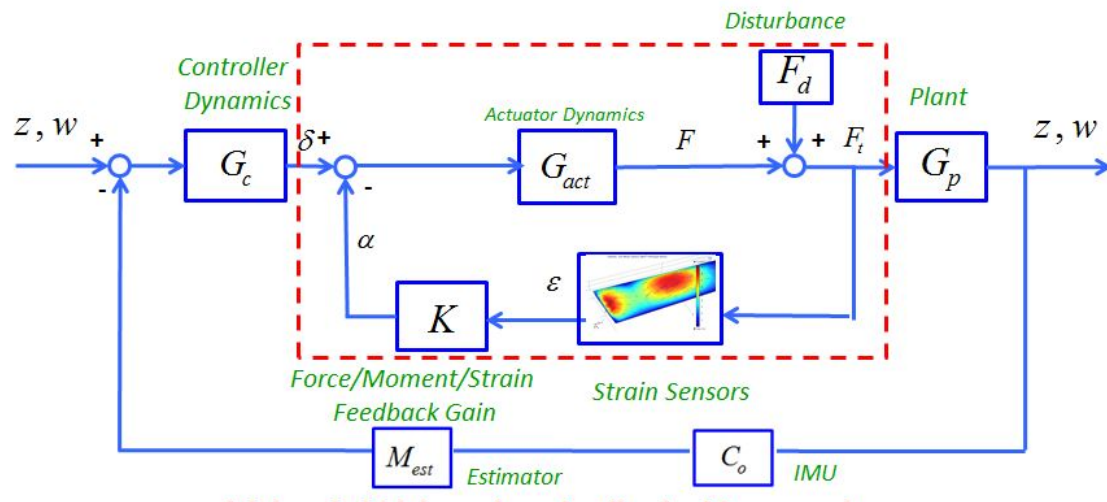


Figure 2.21: High bandwidth inner loop strain feedback

This controller is different from conventional ones in that the fast inner loop precedes the plant and absorbs input disturbances to the plant, preventing the plant from receiving highly perturbed inputs. This approach however also reduces commanded inputs, albeit one way to correct for this is to feedforward the commanded inputs to ensure that they will be properly fed to the plant. This approach was proposed by [89] for implementation in a quadrotor platform.

Chapter 3: Theoretical considerations, Sensor placement and simulations

A quasistatic one dimensional approach based on strain sensing is an approach to gust rejection, detecting imbalances to correct for disturbances.

The forces on the airplane's fuselage are a result of the applied forces on the aerodynamic and control surfaces. These forces propagate along the material out of which the wings and empennage are made. The speed of propagation of these mechanical inputs is given by the composition of the aircraft. A mechanical wave traveling on a softer material will take more time than one traveling in a material with high stiffness. Wave propagation is a natural phenomena which some insects use for flight control, like the diptera. Wing twist propagation is detected by clusters of campaniform sensilla, as it was shown in the previous chapter.

The quasistatic approach basically needs to obtain the distributed sensing profiles and match filter the wide field integrated constants to a particular flight mode. Disturbances will then be rejected when the interrelated strain parameters go beyond certain thresholds. This is a proprioceptive approach in that differences among different sensors allow for a disturbance rejection mechanism.

3.1 Theoretical approach to strains vs disturbance force differentials

3.1.1 Roll Moment

Assuming we can model the wings of the aircraft as a one dimensional cantilever beam, we have that the strain at any point x along the wingspan can be calculated as:

$$\varepsilon(x) = \frac{z}{EI}M(x) \quad (3.1)$$

If we have a set of strain measurements distributed along the wingspan we can calculate the discrete bending moments at each point:

$$M_i = \frac{EI}{z}\varepsilon_i \quad (3.2)$$

Using the static Euler beam equation we can relate the moment and shearing force applied locally at every sensor position:

$$\frac{d^2}{dx^2}(EI \frac{d^2w}{dx^2}) = q(x) \quad (3.3)$$

And since the moment can also be calculated as follows and considering only changes in the x -direction:

$$M(x) = EI \frac{d^2w}{dx^2} \quad (3.4)$$

we have that:

$$\frac{d^2}{dx^2}(EI \frac{d^2 w}{dx^2}) = \frac{d^2}{dx^2}(M(x)) = \frac{EI}{z} \frac{d^2 \varepsilon(x)}{dx^2} = q(x) \quad (3.5)$$

And therefore calculate the force per unit span that generates each strain:

$$q_i = \frac{d^2 M_i}{dx^2} = \frac{EI}{z} \frac{d^2 \varepsilon_i}{dx^2} \quad (3.6)$$

Each load can be calculated as follows by using the strain at three points by using the following numerical scheme, which is a result of applying the three point central difference formula for the approximation of the second derivative of a function at a given point [90].

$$\frac{d^2 \varepsilon_i}{dx^2} = \frac{\varepsilon_i(x+h) - 2\varepsilon_i(x) + \varepsilon_i(x-h)}{h^2} \quad (3.7)$$

Therefore the load at each point i can be calculated as:

$$q_i(x) = \frac{EI}{z} \frac{\varepsilon_i(x+h) - 2\varepsilon_i(x) + \varepsilon_i(x-h)}{h^2} \quad (3.8)$$

Where the load at x is calculated by measuring the strain at three different locations on the beam centered at x . The value of h depends on the hardware constraints in terms of connections and space required to attach each sensor to the wing surface. By calculating the bending moments on each sensor location and calculating the shear force per unit span, a distribution of the shear force per unit

span can be obtained as shown in Figure 3.1. In order to calculate the moment produced by the calculated point loads q_i and considering a discrete set of n sensors:

$$M_T = \sum_{i=1}^n q_i x_i \quad (3.9)$$

Where x_i indicates the position of the sensors along the wing span. This distance has an offset equal to half the width of the fuselage if the moments are calculated with respect to the center of gravity of the aircraft. If the fuselage has width $2a$, the moment arm to the center of gravity becomes:

$$x_i' = x_i + a \quad (3.10)$$

and the moment becomes:

$$M_T = \sum_{i=1}^n q_i (x_i + a) \quad (3.11)$$

In the case of having four strain sensors, the moment on one wing can be calculated as:

$$M_T = \sum_{i=1}^4 q_i (x_i + a) = q_1 x_1 + q_2 x_2 + q_3 x_3 + q_4 x_4 + a * (q_1 + q_2 + q_3 + q_4) \quad (3.12)$$

In the case of 6 sensors per wing then this equation becomes:

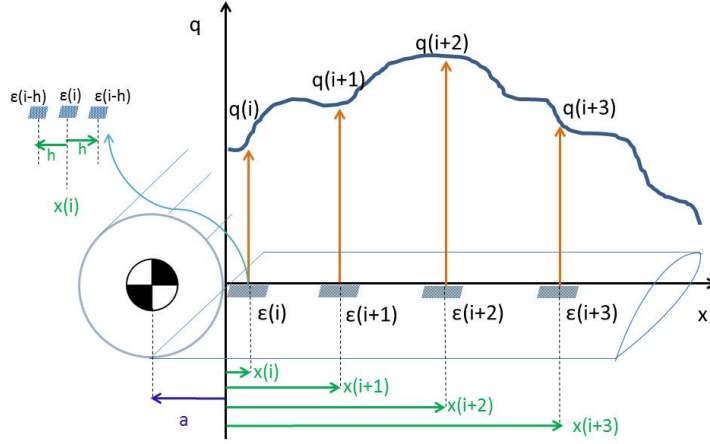


Figure 3.1: Calculation of wide field integrated constants

$$M_{L,R} = \begin{bmatrix} M_L \\ M_R \end{bmatrix} = \begin{bmatrix} C_{q1}^L & C_{q2}^L & C_{q3}^L & C_{q4}^L & C_{q5}^L & C_{q6}^L \\ C_{q1}^R & C_{q2}^R & C_{q3}^R & C_{q4}^R & C_{q5}^R & C_{q6}^R \end{bmatrix} \begin{bmatrix} q_1 \\ q_2 \\ q_3 \\ q_4 \\ q_5 \\ q_6 \end{bmatrix} \quad (3.13)$$

Where the wide field integration matrix (Section (3.2)) becomes:

$$C_w = \begin{bmatrix} C_{q1}^L & C_{q2}^L & C_{q3}^L & C_{q4}^L & C_{q5}^L & C_{q6}^L \\ C_{q1}^R & C_{q2}^R & C_{q3}^R & C_{q4}^R & C_{q5}^R & C_{q6}^R \end{bmatrix} \quad (3.14)$$

and its components can be calculated depending on the chosen locations along

the wingspan of each wing x_i and the local distance to the fuselage a_i :

$$C_w = \begin{bmatrix} a1 + x1 & a2 + x2 & a3 + x3 & a4 + x4 & a5 + x5 & a6 + x6 \\ a7 + x7 & a8 + x8 & a9 + x9 & a10 + x10 & a11 + x11 & a12 + x12 \end{bmatrix} \quad (3.15)$$

In this case we have considered that the first sensor location is at the wingtip of the left wing. The application of the output matrix allows for calculation of the resulting moment on each wing and therefore the differential rolling moment of the aircraft or disturbance rolling moment is given by:

$$L_d = M_L - M_R \quad (3.16)$$

An equivalent C matrix can be obtained to extract the rolling moment differential from the measured strains. Figure 3.2

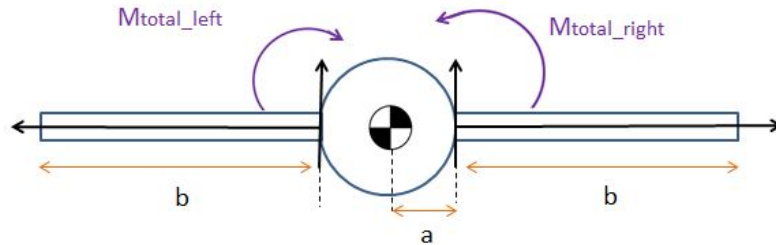


Figure 3.2: Balance of bending moments for calculation of disturbance roll moment

The sensors will then be placed in a strain feedback loop using proportional gains and weighted using the wide field integrated constants that were derived. A

more elaborate controller using H-infinity analysis can also be implemented for roll.

3.1.2 Pitch Moment

Assuming we can model the torsional properties of an aircraft fixed wing by means of the shear strain on the surface of the wing, we can calculate the total pitching moment applied to the center of mass of the aircraft. For simplicity purposes we will assume that the cross section of the wing is uniform and that it has a uniform second moment of area along the span wise direction. The wing is also assumed to have no sweep angle or dihedral. In this case the torque at any point of the wing (beam) can be calculated as shown in Equation (3.17).

$$T = GI_p \frac{d\theta}{dx} \quad (3.17)$$

Where G is the shear modulus of the beam at a particular location $x = L$ and θ is the shear deflection angle at every location x . This equation is related to the shear strain at that particular location by means of Equation (3.18).

$$T = GI_p \frac{d\theta}{dx} = GI_p \left(\frac{\gamma}{r} \right) \quad (3.18)$$

Where γ the shear strain and r is is an approximate torsion radius about a torsion axis. In the case of a wing, this axis is also known as the moment elastic axis. There are more detailed formulations of this mechanism; however, we will focus on the simpler approach in this discussion. The pitching moment induced by aircraft

controls has an immediate effect on the structural strains of the aircraft wings. This effect is time dependent but it can be approached in the way of a quasi-static torque balance. This pitching moment which starts at the center of mass of the aircraft, generates a torque pattern on the aircraft wings. The quasi-static solution entails the summation of the torques generated along the wingspan.

Conversely, if these torques are measured along the wingspan, then the variation in the pitching moment can be calculated using shear strain sensors at specific locations. In the case of a pure pitching motion, the total torque will be equivalent in both wings. However, this balance may not apply for combined motions such as pitch-yaw motions or pitch-roll motions.

Considering one wing, the total pitching moment applied corresponds to Equation (3.19):

$$M = T1 + T2 + T3 + TN \quad (3.19)$$

In the case of N shear sensors distributed at locations x_i along the wingspan. Where each torque is described by Equation (3.18).

If these torques are measured by shear strain sensors then the total pitching moment will be given by Equation (3.20).

$$M = T1 + T2 + T3 + \dots TN = \frac{GI_p}{r_{eq}} * (\gamma_1 + \gamma_2 + \gamma_3 + \dots \gamma_N) \quad (3.20)$$

It is worth mentioning that shear strain sensors need to be setup in pairs

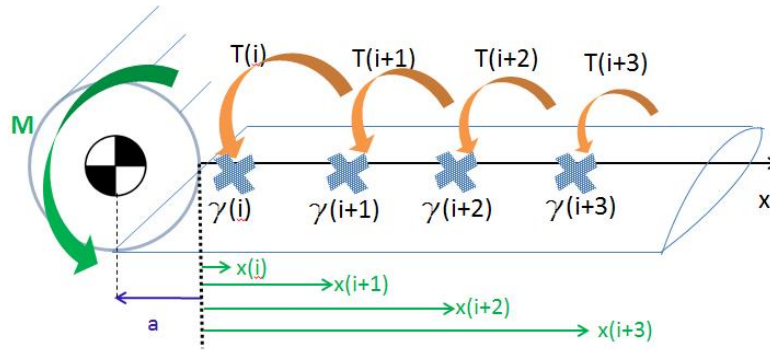


Figure 3.3: Pitching moment at root of aircraft as a function of shear stresses along the wings

of strain sensors at angles of 45 degrees. This setup however will depend on the structural and geometric properties of the wing. The location of the bending and torsion elastic axis will determine the exact location of these sensors.

In the case of a pure pitching motion, the total pitch moment on each wing will be identical and $M_L = M_R$.

However in the case the aircraft is undergoing combined motions, this may not apply. For instance, if the aircraft is undergoing a right turn while pitching: $M_L > M_R$, and if it is undergoing a left turn $M_L < M_R$, due to the increased loading on the inner turning wing.

The time propagation of the torque is described by the wave equation, therefore the temporal displacements will follow harmonic oscillations. The time dependent study however needs to take into account the appropriate initial conditions, which may vary during flight.

In general the total pitching moment applied to the center of mass of the

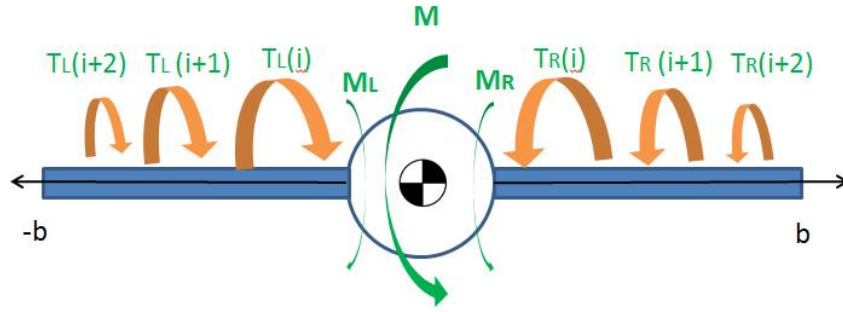


Figure 3.4: Different pitching moments at root as a consequence of maneuver or external inputs

aircraft will then be:

$$M_{LorR} = \sum_i^n \frac{GI_{pi}}{r_i} * \gamma_i = \tau_{LorR} \quad (3.21)$$

In case of uniform cross section, composition and straight wings for pure pitching motion:

$$M_{L=R} = \frac{GI_p}{r_{eq}} \sum_i^n \gamma_i = M_d \quad (3.22)$$

Where M_d is the pitch moment disturbance. An alternative approach to calculating the difference in pitching moment of the aircraft by means of strain measurements entails the use of bending strain sensors on the wings as well as on the aircraft empennage horizontal stabilizer.

If we have that the vertical force on the wings in a one dimensional simplified

approximation, if the wings can be modeled by a beam with appropriate cross-sectional characteristics:

$$Z_{wings} = 2 * F_s = 2 * \sum_{i=1}^n q_i = 2 * \sum_{i=1}^n q_i = 2 * \sum_{i=1}^n \frac{\varepsilon_i(x+h) - 2\varepsilon_i(x) + \varepsilon_i(x-h)}{h^2} \quad (3.23)$$

Where ε corresponds to the bending strains at sensor locations i spaced by a distance h . In a similar way, the total load can be calculated on the horizontal stabilizer of the aircraft:

$$Z_{horiz} = 2F_{sh} \quad (3.24)$$

Such that the combined strain measurements on the wings and empennage will yield a qualitative nose up or nose down pitch moment estimate, and will allow for rapid difference calculations. After a certain threshold a compensator should engage to reject the disturbance.

$$\begin{aligned} Z_{wings} &> Z_{horiz}, \text{ pitch up motion} \\ Z_{wings} &< Z_{horiz}, \text{ pitch down motion} \end{aligned} \quad (3.25)$$

And it can also yield the total disturbance pitching moment:

$$M_d = Z_{wings}d_w - Z_{horiz}d_h \quad (3.26)$$

Where d_w is the distance between the wings effective center of force to the aircraft center of mass and d_h is the distance between the horizontal stabilizers effective center of force to the aircraft center of mass. Ideally these will be co-planar on the plane defined by the center of mass of the aircraft, which divides the aircraft in symmetric halves along the nose axis.

3.1.3 Vertical Force

Similarly, based on Equation (3.23), a vertical force disturbance can be calculated as:

$$Z_d = 2 * F_s - mg \quad (3.27)$$

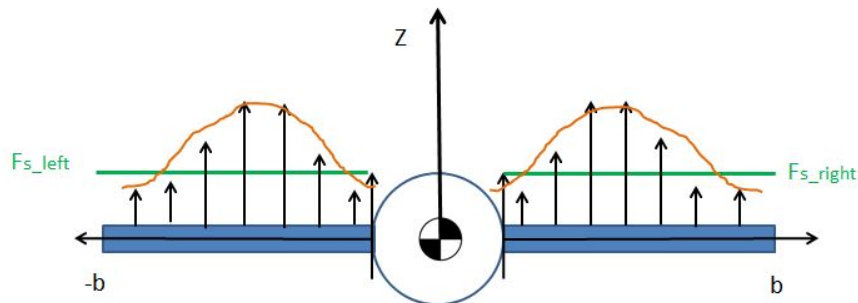


Figure 3.5: Vertical force on aircraft and shear forces on the wings

The disturbance vertical force calculation may assume that the shearing force on each wing is balanced for steady wings level flight Figure 3.5. However this can

be modified for a set tolerance for different maneuvers, i.e. steady turns, where the shearing force on the left wing to the right may have a defined ratio.

The disturbance rejection mechanism based on these static strain comparisons can be posed in different ways. One dimensional wide field integration constants can be obtained for each sensor location and maneuver.

3.1.4 6-DOF model

Using results from the Roll, Pitch, and vertical roll formulations, a controller which regulates the balance of forces by means of strain measurements can be formulated in the fast inner loop discussed in Section (2.3.2) .

$$\begin{aligned}
 L_d &= M_L - M_R = \delta, \text{ Roll disturbance with bending strain} \\
 M_d &= \tau_L - \tau_R = \delta, \text{ Pitch disturbance with shear strain} \\
 M_d &= Z_{wings}d_w - Z_{horiz}d_h = \delta, \text{ Pitch disturbance with bending strain} \\
 Z_d &= 2 * F_s - mg = \delta, \text{ Vertical force disturbance}
 \end{aligned} \tag{3.28}$$

Where δ is either zero or some calculated or measured value for steady wings level flight or steady turns. A 6-DOF model can be obtained by obtaining the remaining balancing equations, in rejection of larger values of δ . This is a somewhat de-coupled method.

A coupled 6-DOF model can be obtained by computing least squares calculations on system identified matrices. It is proposed that the forces and moments at the root of each wing need to balance out with respect to the center of gravity. By

parallel theorem this is only a constant away for rotational inertias of interest.

In this way, if a set of sensors has been system identified with respect to their corresponding wing forces and moments, then a simple force balance of the forces calculated by the regression matrices can be computed fast, if the matrices are previously obtained by experimental load tests. In this sense a MIMO controller can be formulated and built to regulate the following relationship:

$$\hat{F}_{rootleftwing} - \hat{F}_{rootrightwing} = \Delta \quad (3.29)$$

A diagram of the method is illustrated in Figure 3.6.

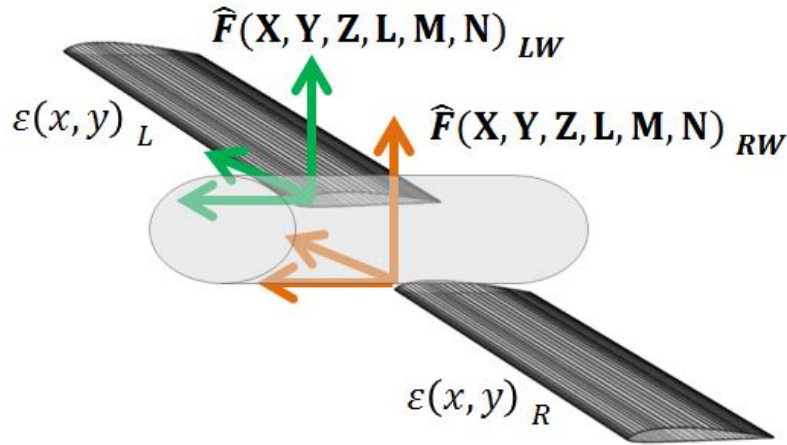


Figure 3.6: 6-DOF coupled model for force/strain feedback

A formulation of the MIMO controller based on results from the theoretical considerations is found in Figure 3.7 and Figure 3.8.

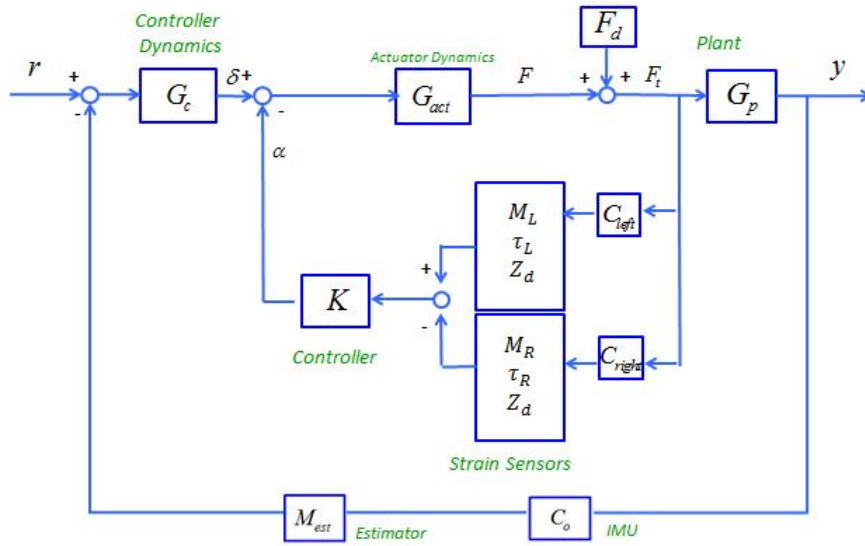


Figure 3.7: Formulation for the strain feedback MIMO controller based on SISO strain balance

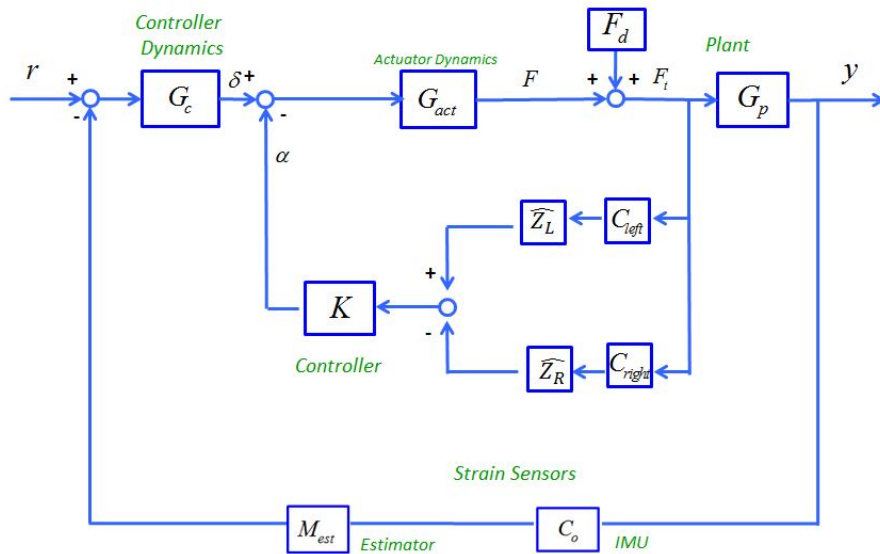


Figure 3.8: 6-DOF formulation for the strain feedback MIMO controller based on system identified output matrices

Multiplicative uncertainty in the proposed output C matrices can be formulated as shown in Figure 3.9. In this diagram the output matrices and the force estimation matrices have been clustered into a single block. Techniques from robust control can be then applied to synthesize the model based controller. A generalized plant needs to be derived based on generalized inputs w, generalized outputs z. For the uncertainty case a similar linear fractional transformation can be calculated using block diagram manipulations. Uncertainty in the C matrix will yield a family of uncertain plants which will make the closed loop stable depending on the stability margins found for the MIMO system. Weighting transfer function matrices can be tuned for better closed loop response.

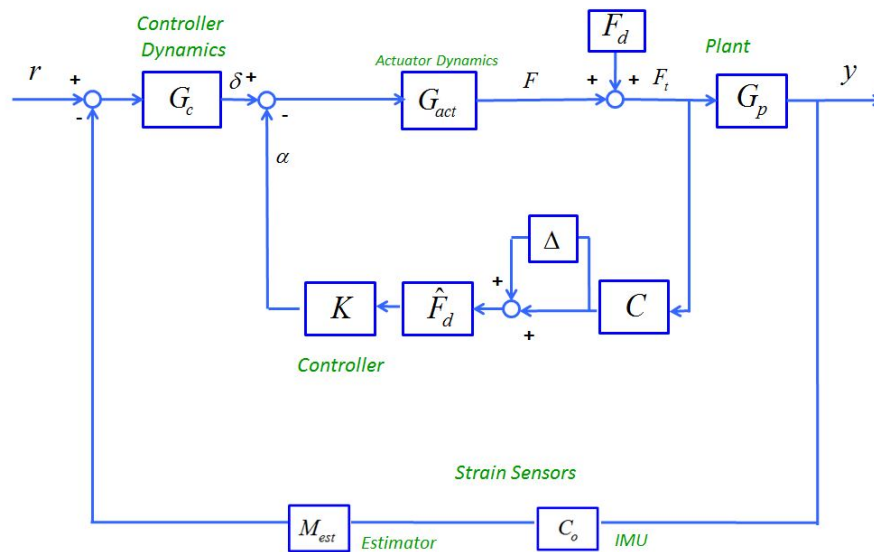


Figure 3.9: 6-DOF formulation for the strain feedback MIMO controller with uncertainty in the C matrix

3.2 Strain based wide field integration (WFI)

3.2.1 1D strain WFI

Considering the static Euler Bernoulli beam models for the wing, which were presented in Section (2.2.3), a one dimensional wide field integration can be formulated based on the expected strains as a function of wingspan.

Alternatively, using the trigonometric substitution $x = L\cos\theta$ to get a simpler form of the shearing force for an elliptic lift distribution from Equation (2.13):

$$F_s = \rho_\infty V_\infty \Gamma_0 \int \left(1 - \frac{x^2}{L^2}\right)^{\frac{1}{2}} dx = -L\rho_\infty V_\infty \Gamma_0 \int (\sin^2 \theta) d\theta \quad (3.30)$$

Where L is the length of the wing and $\theta = \arccos \frac{x}{L}$. Carrying out another implicit integration, back substituting and expanding in Taylor series up to the third degree:

$$F_s = -L\rho_\infty V_\infty \Gamma_0 \int (\sin^2 \theta) d\theta = L\rho_\infty V_\infty \Gamma_0 \cdot \frac{(6L^2x - 3\pi L^3 + x^3)^3}{648L^9} \quad (3.31)$$

Truncating this expression to the fourth term, the shear force becomes:

$$F_s = -L\rho_\infty V_\infty \Gamma_0 \cdot \left(\frac{\pi^3}{24} - \frac{\pi^2 x}{4L} + \frac{\pi x^2}{2L^2} - \frac{x^3}{3L^3} \right) \quad (3.32)$$

Using this expression of the shearing force, the bending moment can be found.

The shearing force is the rate of change of bending moment:

$$F_s = \frac{dM}{dx} \quad (3.33)$$

and the moment is:

$$M(x) = \int F_s dx \quad (3.34)$$

Using the approximation found for the shear force, the moment is:

$$M(x) = -L\rho_\infty V_\infty \Gamma_0 \int \left(\frac{\pi^3}{24} - \frac{\pi^2 x}{4L} + \frac{\pi x^2}{2L^2} - \frac{x^3}{3L^3} \right) dx \quad (3.35)$$

$$= L\rho_\infty V_\infty \Gamma_0 \left(\frac{x^4}{12L^3} - \frac{\pi^3 x}{24} + \frac{\pi^2 x^2}{8L} - \frac{\pi x^3}{6L^2} \right) \quad (3.36)$$

and the corresponding strain is calculated using:

$$\varepsilon_x = -z \frac{M(x)}{EI} \quad (3.37)$$

using the approximation found for the moment, the strain is:

$$\varepsilon_x = \frac{-zL\rho_\infty V_\infty \Gamma_0}{EI} \cdot \left(\frac{x^4}{12L^3} - \frac{\pi^3 x}{24} + \frac{\pi^2 x^2}{8L} - \frac{\pi x^3}{6L^2} \right) \quad (3.38)$$

which is the strain produced by an elliptical span wise aerodynamic lift. This contribution of strain needs to be added to the contribution produced by the other flight dynamics variables for a complete calculation.

$$\varepsilon_x = \varepsilon_{xnominal} + \varepsilon_{xgusts} \quad (3.39)$$

where the nominal strain for an elliptic lift distribution corresponds to Equation (3.38):

$$\varepsilon_{nominal} = \frac{-zL\rho_\infty V_\infty \Gamma_0}{EI} \cdot \left(\frac{x^4}{12L^3} - \frac{\pi^3 x}{24} + \frac{\pi^2 x^2}{8L} - \frac{\pi x^3}{6L^2} \right) \quad (3.40)$$

Assuming that the young's modulus and second moment of area are constant or can be reduced to a single equivalent value for the beam model of the wing. The strain due to uniformly distributed gusts, is a summation of the strains produced by

With the strain defined at each point of the cantilever, a set of coefficients for each linearly independent term can be calculated when passed through an inner product of orthogonal polynomials. Some of the possible polynomials which are orthogonal in the -1 to 1 value range for the spanwise coordinate x are: Legendre polynomials (from 0 to 1), Chebyshev polynomials, Laguerre polynomials. For instance, the Laguerre polynomials:

$$L_0 = 1, L_1 = x, L_2 = \frac{1}{2}(3x^2 - 1), L_3 = \frac{1}{2}(5x^3 - 3x), L_4 = \frac{1}{8}(35x^4 - 30x^2 + 3) \quad (3.41)$$

where x goes from -1 to 1. Therefore, we have to normalize the span by dividing by L . In this case, if we set $y = x/L$ the normalized strain equation which can be integrated in an inner product is:

$$\varepsilon_x = \varepsilon_{nominal} + \frac{z}{2EI} \rho_{\infty} V_{\infty} S \left(U_g C_L + \frac{U_w}{2} C_{L\alpha} + \frac{U_v}{2} C_{L\alpha} \right) \quad (3.42)$$

Where the added expression is calculated under the assumption that the gusts are impacting the aircraft uniformly and therefore the lift differential can be expressed according to Equation (2.1).

Lift differentials can be calculated based on a nominal expression for lift such that any differences are due to gust perturbations. Coefficients can be calculated via inner product due to the orthogonality of the polynomials in the range from $x=-1$ to $x=1$. This approach can also be regarded as a one dimensional wide field integration by means of basis functions. In a later chapter the WFI constants will be derived based on the physics of the formulation.

Similarly, basis functions can be chosen based on the eigenstrains obtained from the finite element calculations. Based on the type of gust affecting the structure, the patterns change according to mass participation factors.

3.2.2 2D strain WFI

Eigenstrains on the surface of the wing can be used as basis functions to generate a 2D eigenstrain pattern as well as weighting matrices. A general formulation of strain field integration is shown in Figure 3.10.

Strain WFI $\left\langle \Delta\varepsilon, \Phi_i \right\rangle = \int_0^S \Delta\varepsilon(x, S, X_R, X_E) \Phi_i dx = C_{RE} \begin{Bmatrix} X_R \\ X_E \end{Bmatrix}$

Measured Strains and Dynamic Modes $\varepsilon(x, t) = \sum_{i=1}^2 \frac{1}{2} \left(\frac{\partial \psi_i(x)}{\partial x} + \left[\frac{\partial \psi_i(x)}{\partial x} \right]^T \right) \eta_i(t)$

Integrated C matrix (pointing to C_{RE})

Basis Functions based on wing geometry (pointing to Φ_i)

i-th FE eigenmode (pointing to $\eta_i(t)$)

Figure 3.10: Strain wide field integration

In particular, if the MPF weighted directional eigenstrains are used as basis functions:

$$\begin{aligned} \int \varepsilon \Phi_M P F_v & , V_{gust} \\ \int \varepsilon \Phi_M P F_u & , U_{gust} \\ \int \varepsilon \Phi_M P F_w & , W_{gust} \end{aligned} \quad (3.43)$$

and if the sensors are a discrete set, then they are appropriately weighted by:

$$\int \varepsilon_{discrete} \Phi_i \quad (3.44)$$

A weighting function which would capture the three types of gusts would then be given by:

$$\int \Phi_{MPF_v} \Phi_{MPF_u} \Phi_{MPF_w} = M \quad (3.45)$$

3.3 Sensor placement

3.3.1 Sensor placement techniques

Optimal location of sensors can be a determining factor in both state estimation and disturbance rejection. These methods are usually limited to energy and modal analyses. In this work we not only explore the conventional approach to sensor placement but also a wide field integrated approach [9] based on structural inputs.

Sensor placement methods have been explored for a wide variety of purposes including vibration suppression, actuator effectiveness, and active control [91]. These methods can be deterministic or heuristic. Heuristic methods typically require a cost function to be minimized or a performance function to be maximized. Deterministic methods use more stringent conditions to find the optimal set of locations. A mapping between the design variables and the physical sensor locations is required for both. Some of these methods are appropriate for large undefined sets whereas other methods require a small set of possible locations around local minima or maxima. For instance, some of the methods are based on neighbor search of locations while others focus on selecting a location from widely scattered possible locations. Genetic algorithms (GA) are effective at finding optimal solutions that are widely scattered throughout the design space. The algorithm is initialized by generating a large number of random subsets which are combined and mutated to search for improved subsets.

Some of the most common methods will be described in what follows. Exhaustive search looks at all the possible sets of sensor locations to determine the best; this can turn out to be computationally expensive. Local neighbor search or Tabu Search (TS) uses less computational resources by keeping memory structures that describe the visited solutions of a provided set of rules. Another method which uses pre-selected locations is the Neural Network approach where sensor location are discarded based on each sensor contribution to the optimization criteria. Similarly, Simulated Annealing entails a nearest neighbor search based on optimization of subsets which are selected upon improvement of the cost function. Energy methods include: maximization of the modal kinetic energy (MKE) of a sensor configuration, selection of a set with the highest entropy and maximization of the modal strain energy (MSE) [92].

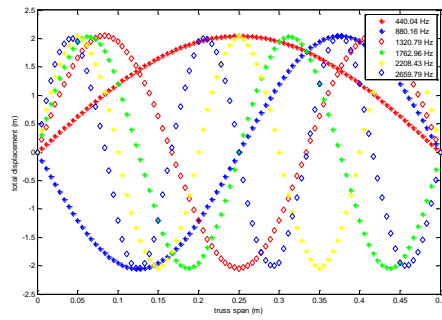
Modal techniques for sensor placement are yet another subcategory of techniques. Driving point residue method (DPR) [93] [94] is a modal participation factor methods where the sensors are placed based on the highest average response over all of the target modes. The eigenvalue product method (EVP) forms an indicator consisting in the absolute value of the product of every eigenvector. The best locations are those with the highest product value. Singular value decomposition (SVD) of a given candidate set of sensor locations can also be used to find an optimal set.

Effective independence (EFI) [95] is a heuristic ranking scheme that attempts to maximize the determinant of the Fisher information matrix (FIM) [96] or equivalently, maximize its minimum eigenvalue. The FIM is directly correlated to the error covariance, which gets minimized in the process. The Fisher information ma-

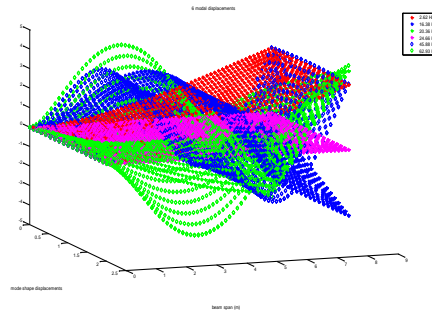
trix is also the inverse of the observability Grammian of sensor locations [97]. The observability Grammian is used as an assessment of the contribution of the individual modes. Each contribution should be high in order to warrant high observability in a specific set of sensor locations. In this work we will be focusing on three approaches: mass participation factor weighting, effective independence /observability Grammian and wide field integrated strains.

As a first approach to identifying the best sensor solutions using the EFI methodology, we set up an Aluminum 1D beam with free-free boundary conditions and carried an eigenfrequency analysis. The first 6 modeshapes that resulted from the finite element simulation were extracted. Figure 3.11 shows the results of the modal displacements of such beam and the corresponding eigenstrains. These are symmetric due to the boundary conditions. The same technique applies to cantilever beams and wings. The results of the Comsol structural mechanics eigenvalue solver yielded the numerical solutions shown in Figure 3.11. This technique will be used in following analyses of 1D and 2D wings.

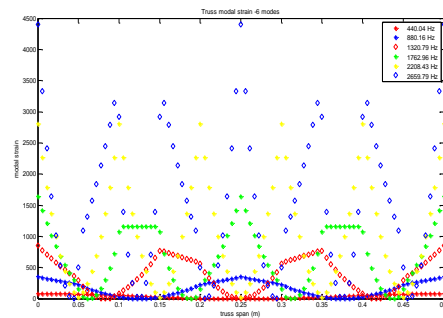
The optimization of sensor locations techniques can be applied to any structure, and in particular to the aircraft wings. By customizing the cost function to be a performance metric, one can tailor the locations to best observe the quantities of interest, i.e. Forces and Moments, gust forces, etc... The performance metrics may also include observability and controllability metrics.



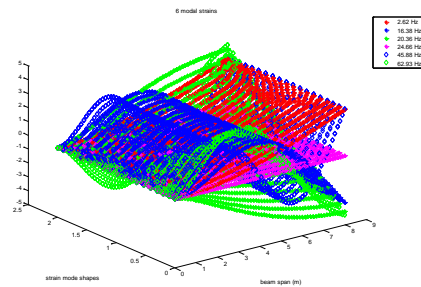
(a) First 6 modal displacements of free-free 1D beam (truss)



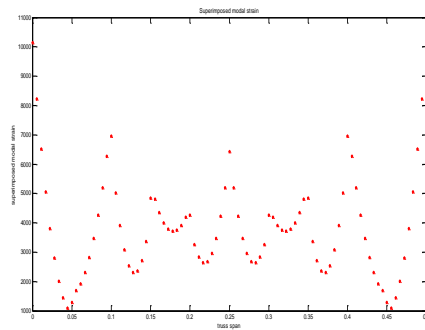
(b) First 6 modal displacements of cantilevered 2D beam



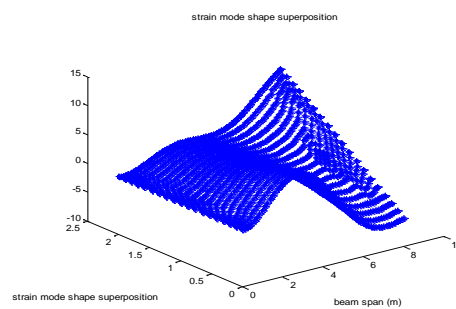
(c) First 6 modal strains of free-free 1D beam (truss)



(d) First 6 modal strains of cantilevered 2D beam



(e) Eigenstrain superposition



(f) Eigenstrain superposition

Figure 3.11: 1D dimensional aluminum beam eigenstrain superposition (left) and 2D aluminum beam eigenstrain superposition (right).

3.3.2 Theoretical Framework EFI and Grammian

A variety of methods can be applied; however, we have chosen to combine the most representative ones based on the nature of our application. A wide field integrated approach will also be pursued; it includes physics that are not normally considered for sensor placement. In this sense, the conventional approaches can define the local subsets of maxima based on energy and structural considerations. Then a physical approach can determine sensor output weightings for an estimated maximal output. Sensor locations can be first identified by using mass participation factors. These coefficients provide a method for judging the significance of a vibration mode. That is, modes with higher factors can be readily excited whereas ones with lower factors cannot. This is an appropriate analysis for an aircraft wing in that it undergoes different types of loads during flight which may produce deformations and strains. It allows a study of the more significant impacts of the loads on the wing, which produce strains. There is a participation factor for every available degree of freedom.

In addition to mass and energy considerations, an effective independence approach is useful in that it allows for the error covariance to be minimized, or equivalently for the observability Grammian to be maximized over a range of possible sensor locations. It is also useful in the sense that a modified cost function can be applied. This function entails not only the modal participation factors but can also contain information about the flight dynamics in a closed loop strain feedback

configuration. In EFI, the output equation can be expressed as:

$$y_s = \Phi_{fs}q + w \quad (3.46)$$

In this equation, y_s is a vector of sensor outputs at a large candidate set of sensor locations. Φ_{fs} is a matrix of FEM target modes which have been Φ_f partitioned to the corresponding sensor location degrees of freedom. This partitioning refers to the removal of the targeted sensor location to evaluate its contribution. The target mode response vector is q in normal coordinates. The noise is represented by w , and it is assumed to be a stationary random observation disturbance possessing zero mean and covariance intensity matrix satisfying the expectation operator. Estimate error covariance matrix for q is found to be the inverse of the Fisher information matrix Q [95] and equivalent to the observability Grammian Y_o :

$$E[(q - \hat{q})(q - \hat{q})^T] = [(\Phi_{fs})^T R \Phi_{fs}]^{-1} \quad (3.47)$$

Maximizing determinant of the FIM will maximize the spatial independence of the target modal partitions as desired and maximize the signal strength of the target modal responses in the sensor output. This results in the best estimate of the modal response. Sensors should be placed such that Q is maximized or equivalently such that Y_o is maximized. The Effective Independence Distribution vector can be

used as the cost function.

$$E_D = [\bar{\Phi}_{fs}\Psi]^2(\Lambda)^{-1}\mathbf{1}_k \quad (3.48)$$

Where Ψ is the matrix of eigenvectors of Q and Λ is the corresponding matrix of eigenvalues. $\mathbf{1}_k$ is a k -dimensional column vector of ones. Each term within vector E_D represents the contribution of the corresponding candidate sensor location to the rank of the information matrix and thus the linear independence of the target modes. Another equivalent calculation of the effective independence vector [98] is found from:

$$E_D = \text{diag}[\bar{\Phi}_{fs}(\Phi_{fs}^T\Phi_{fs})^{-1}\Phi_{fs}^T] \quad (3.49)$$

A ranking of candidate sensor locations can be calculated by:

$$E_{D_i} = \frac{\det(Q) - \det(Q_{T_i})}{\det(Q)} \quad (3.50)$$

and $0 < E_{D_i} < 1.0$ is the range of possible values of the ranking of candidate sensor locations. A zero value indicates that the corresponding candidate sensor location will contribute nothing to the identification of the target modes. Additional cost functions can be implemented in a closed loop entailing the entire set of sensor measurements, weighted by wide field integrated constants.

3.4 1D Sensor Placement Analysis

3.4.1 Wing FEM model

A typical UAS plane was used for the aeroelastic simulations and sensor placement analysis. The wing types used in these one dimensional linear structural models is a unidirectional carbon fiber with typical Young's modulus and material characteristics. The wing was modeled using Comsol Multiphysics Figure 3.12 with slender beam elements and had an aspect ratio of approx. 7. The mesh consisted of nearly 1000 elements in two dimensions. An eigenfrequency analysis was performed without considering geometric nonlinearities. A parallel sparse direct solver was used to solve the system of equations. The wing root was modeled as a fixed constraint whereas the wing tip was modeled as a free constraint. The eigenvalue analysis shows that the first six bending eigenfrequencies are: 0.69 Hz, 4.37 Hz, 12.44 Hz, 24.95 Hz, 42.5 Hz, and 65.95 Hz. These frequencies were obtained with the assumption of a uniform cross-section and may vary depending on the internal structure refinements such as ribs, spars, etc.

The following sensor placement analysis will be based on the modal results rendered by the finite element model. Two approaches will be presented. The first approach considers a modal energy approach complimented by the gradient, and the second approach entails a measure of the information matrix as provided by each sensor location. This second approach is equivalent to computing the observability matrix, which is also a measure of the effective independence of the targeted modal

strains.

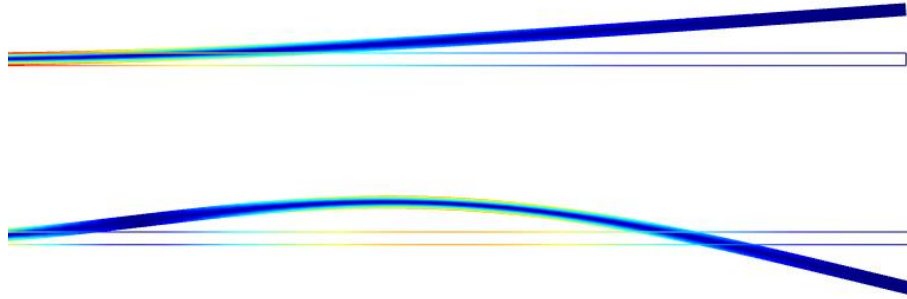


Figure 3.12: First and second finite element eigenmodes of UAS wing

3.4.2 Sensor placement using MPF/gradient and EFI/Grammian

Each eigenmode has an associated eigenstrain shape. From Figure 3.12 the associated stresses and strains can be seen around the contour of the eigenmode. The eigenstrains were normalized with respect to wing length L_w and with respect to maximum strain, as shown in Figure 3.13. They directly correspond to the eigenfrequencies in the same corresponding order. A complete set of finite element eigenfrequencies and mass participation factors is shown in table 3.1. Participation factors in the normal direction are called MPFv and in the axial direction are named MPFu. In particular we are interested in the influence of structural and energy characteristics in the vertical or normal direction since this is the direction most impacted by gusts. The different magnitude scales of mass participation factors can be seen from 3.1 which shows that lateral loading doesn't have much of an

impact on bending modes and therefore chordwise bending moment which is directly proportional to strain.

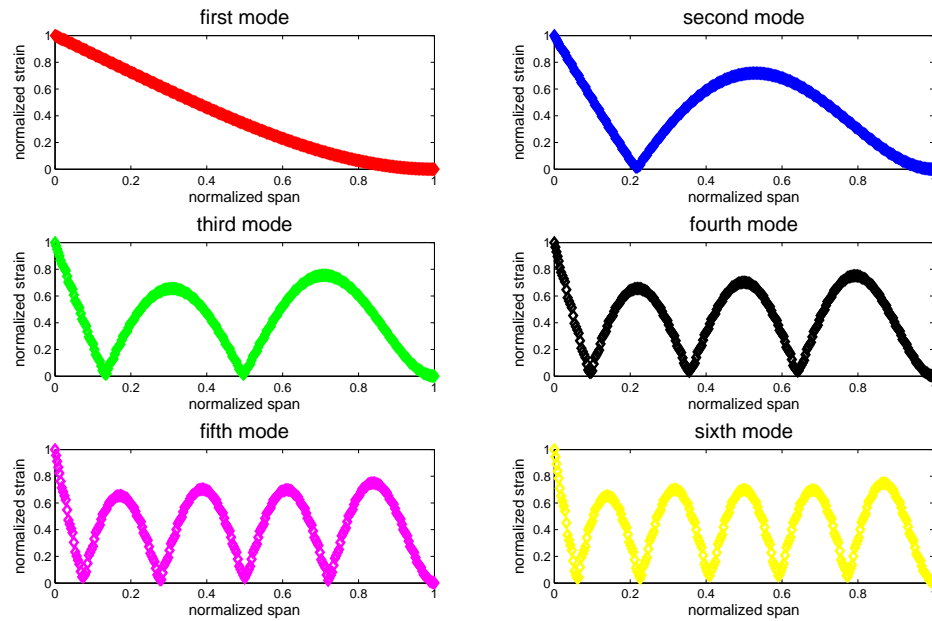


Figure 3.13: UAS normalized eigenstrains from finite element simulation

Table 3.1: Mass participation factor results for 2D model of wing

| Eigenfrequency (Hz) | MPF u | MPF v | Total Strain Energy (J) |
|---------------------|-----------|-------|-------------------------|
| 0.69 | -7.35E-13 | 1.35 | 4.72 |
| 4.37 | -4.30E-12 | 0.74 | 189.17 |
| 12.44 | -9.17E-12 | 0.43 | 1529.18 |
| 24.95 | -1.60E-11 | 0.30 | 6144.57 |
| 42.50 | -2.30E-11 | 0.23 | 17828.18 |
| 65.95 | 6.15E-10 | 0.18 | 42927.74 |

The mass participation factors in the vertical or normal direction are used to weigh each of the six modes. This will give a relative indication of how well a particular mode is excited from a given degree of freedom. A comparison between linearly weighted eigenstrains and MPF weighted strains can be seen from Figure 3.14. It is noticeable that the mass participation factors dramatically modify the expected areas of maximal sensor outputs, or areas where the absolute value of strain is expected to be larger. A comparison of the calculated gradients for both the linearly weighted and the MPF weighted strain distributions can be seen from Figure 3.15.

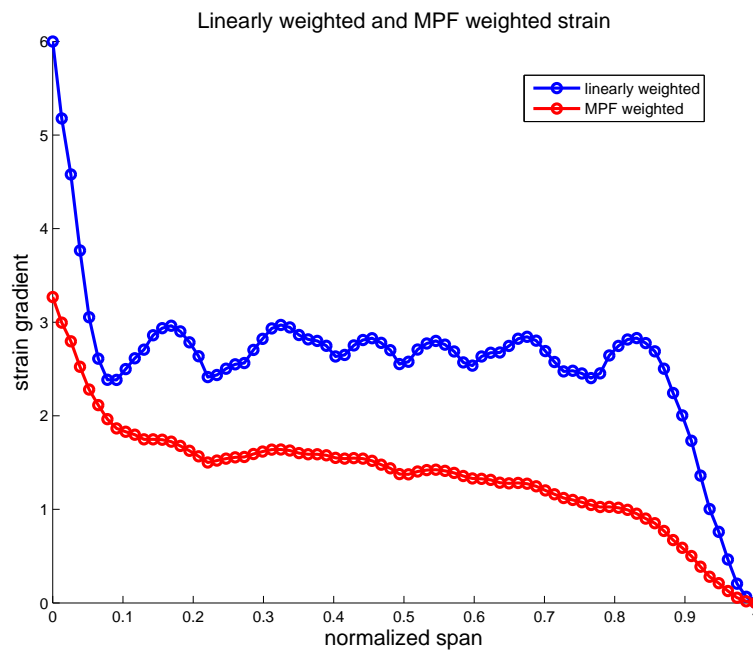


Figure 3.14: UAS normalized weighted eigenstrains using equal weights and MPF

The MPF weighted eigenstrain curve can be combined with its corresponding gradient to avoid locations of fast strain rate. This normally depends on the sensor

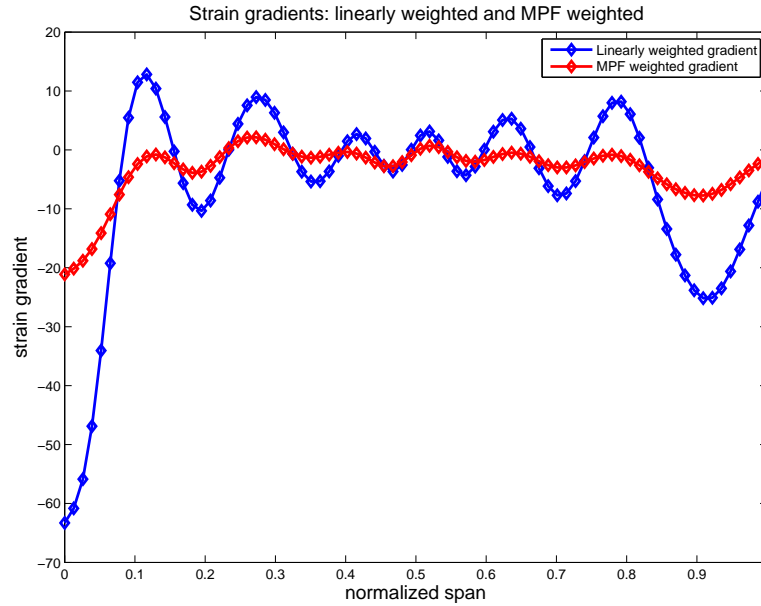


Figure 3.15: Linearly weighted and MPF eigenstrain gradients

location targeted application but typically areas of fastly changing strain need to be avoided due to increased risk of measurement nonlinearities. These areas of sharply changing strain can induce noise and increase possible debonding, in the case of conventional strain gauges. The MPF weighted curve and its corresponding gradient are shown in figure 5. Sensor placement that results from this analysis is depicted with shaded columns. A stronger colored column indicates a higher expected overall strain value whereas a fading one indicates the strain value is not expected to be as high. The columns intersect areas of higher strain and constantly increasing gradients, avoiding gradient peaks.

A similar analysis was performed using EFI/Grammian analysis based on the finite element results for eigenshapes. The fisher information matrix was calcu-

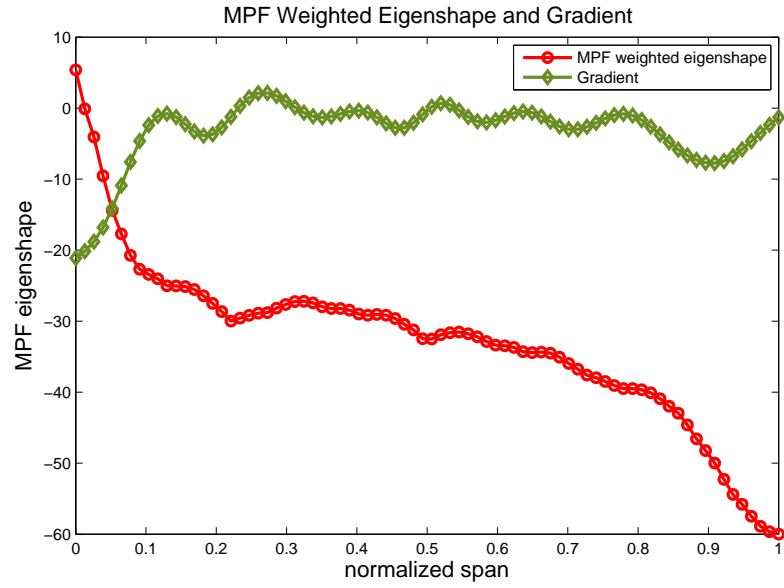


Figure 3.16: UAS wing MPF based sensor placement using weighted eigenstrains and gradient

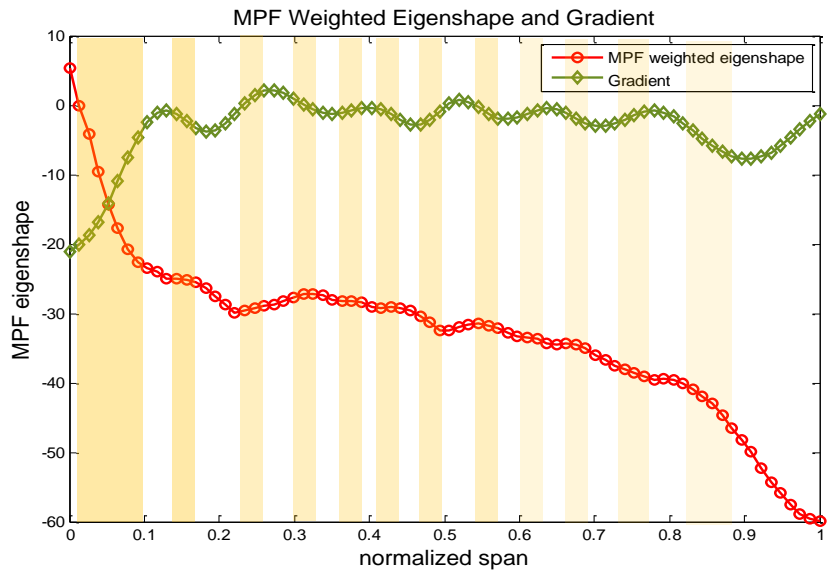


Figure 3.17: UAS wing MPF based sensor placement using weighted eigenstrains and gradient

lated using six eigenstrains. Then the effective independence distribution vector was calculated by obtaining the diagonal of the matrix in (3.49). Each term in the vector represents the contribution of the corresponding candidate sensor locations to the rank of the Fisher matrix and therefore the linear independence of the target eigenstrains. The resulting independence vector E_D was calculated as a function of normalized span, as shown in Figure 3.18.

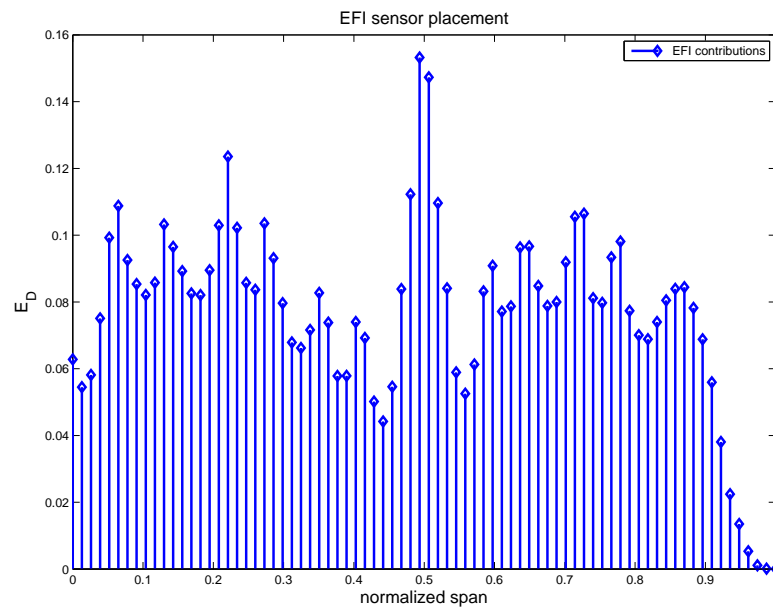


Figure 3.18: UAS wing EFI/Grammian sensor placement

The first ten locations with higher contributions to the observability Grammian are found in table 3.2. These values were picked such that they would correspond to rather distributed areas as opposed to being in close proximity. The table is arranged from higher to lower values of the effective independence vector.

A comparison of results obtained between the energy method of mass partici-

Table 3.2: Distributed sensor locations with higher EFI contribution

| Normalized span | EFI contribution |
|-----------------|------------------|
| 0.4935 | 0.1532 |
| 0.2208 | 0.1236 |
| 0.06 | 0.1088 |
| 0.72 | 0.1065 |
| 0.2727 | 0.1035 |
| 0.1299 | 0.1032 |
| 0.05 | 0.0992 |
| 0.6494 | 0.0966 |
| 0.1429 | 0.0965 |
| 0.2857 | 0.0931 |

pation factors with gradient considerations and the effective independence/ observability Grammian method are presented in Figure 3.19. It can be observed from this figure that the observability metric allows for more potential sensor locations while the energy weighted modal strain approach provides an emphasis of the areas of higher energy for the chosen direction of the participation factor. In this case, this MPF corresponds to the direction normal to the span/chord wing plane, which is the direction in which gusts would have a greater impact. Other MPF factors can be calculated and applied to the mass weighting method based on the intended sensing application.

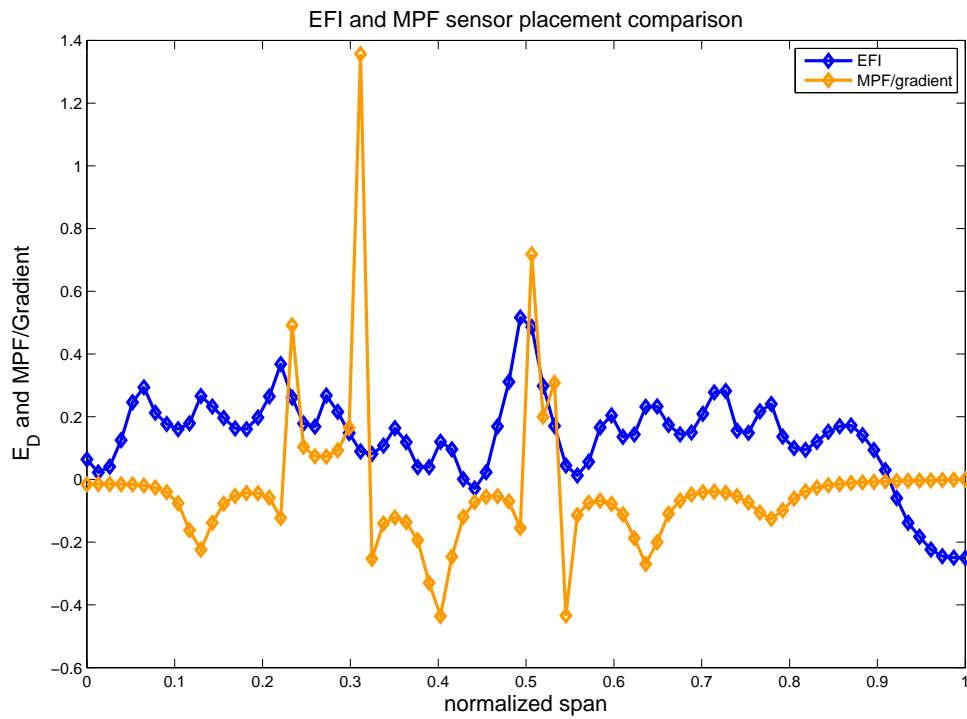


Figure 3.19: Comparison of EFI/Grammian and MPF/Gradient sensor placement methods

3.5 Gust simulations

3.5.1 ASWING aeroelastic model simulation

An aeroelastic model of the UAS was implemented in ASWING [72] to evaluate the strain wide field integration approach presented in section 3.3.2 as well as to look for the impact of sensor placement considerations from section 3.4. ASWING allows for fully non-linear aeroservoelastic simulations where lifting line theory is used for aerodynamic computations and is coupled with non-linear Euler Bernoulli beam elements for structural computations (Figure 3.20). Control surfaces can be defined within the model geometry as well as full 3D gust fields.

The aircraft model used in the simulations is consistent with the wing beam model used for finite element analysis of section 3.43.4.1. It consisted of four beams, fuselage and wing planform, vertical and horizontal stabilizer, as can be seen in Figure 3.21. Each beam had structural properties as well as aerodynamic properties such as lift and drag coefficients. The propeller can be modeled as a point mass with thrust vector properties. Sensors can be placed at different locations on the wing to measure both aerodynamic (i.e. angle of attack) and structural properties (i.e. strains). A large number of coupled aeroelastic modes as well as typical rigid body dynamics can be obtained from the fully non-linear simulation. These can be reduced if the system is linearized about a trim condition. A reduced order model was obtained about a specific flight condition, namely steady wings level flight at a constant speed of approximately 15 m/s. This linear time invariant model allows

for extraction of rigid body states as well as structural dynamics states associated to bending of the wing. A coupled dynamics matrix was obtained and used for extraction of the strain outputs at particular locations on the wing. Sensors can only be placed at 12 locations at a time in ASWING, therefore a different geometry needs to be executed for every change in sensor location. The linear reduced order model implemented around the steady wings reference flight condition had 6 displacement sensors on each wing, for a total of 12 sensors. The strains were also calculated along the span of the wing.

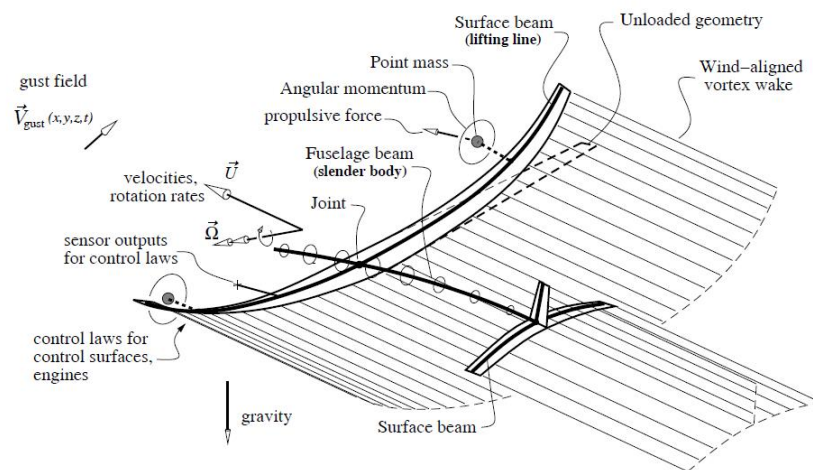


Figure 3.20: ASWING definitions (excerpt from reference [72])

3.5.1.1 ASWING nonlinear simulation -3D gust

A heuristic non-linear simulation was implemented in ASWING using the UAS model described in the previous section. The aircraft was set to interact with a 3-D gust field of two different gust intensities. The simulation was set such that the

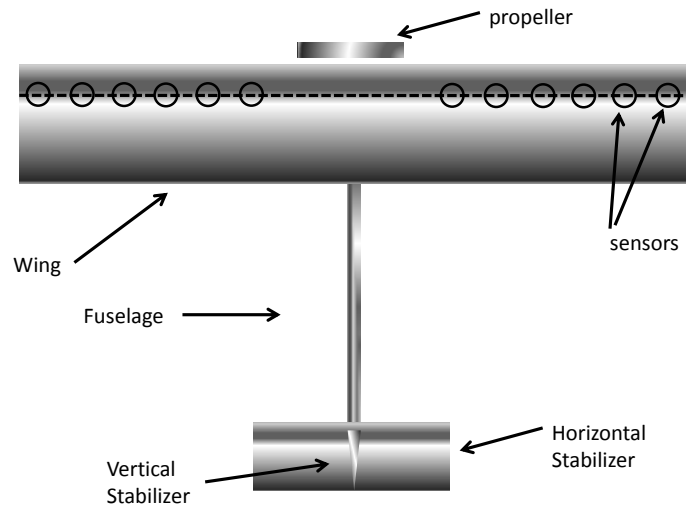


Figure 3.21: Top view of aircraft model for ASWING simulation

aircraft would follow a straight path and then encounter a vertical gust field. This produced a disturbance of the rolling angle and other rigid body states, as can be observed from the time histories of the bank angle. Initial gust simulation results are shown in Figure 3.22, where there is a measurable impact of gust vertical velocity on the vehicle's flight states .

3.5.1.2 ASWING linear simulation -1D gust

In the reduced order model, a similar roll gust effect was obtained by injecting a disturbance in the left most aileron. The impact of this disturbance on the linear model can be seen in Figure 3.24. This artificial roll disturbance has a similar effect on the roll angle as that observed in the fully non-linear case, where the aircraft was

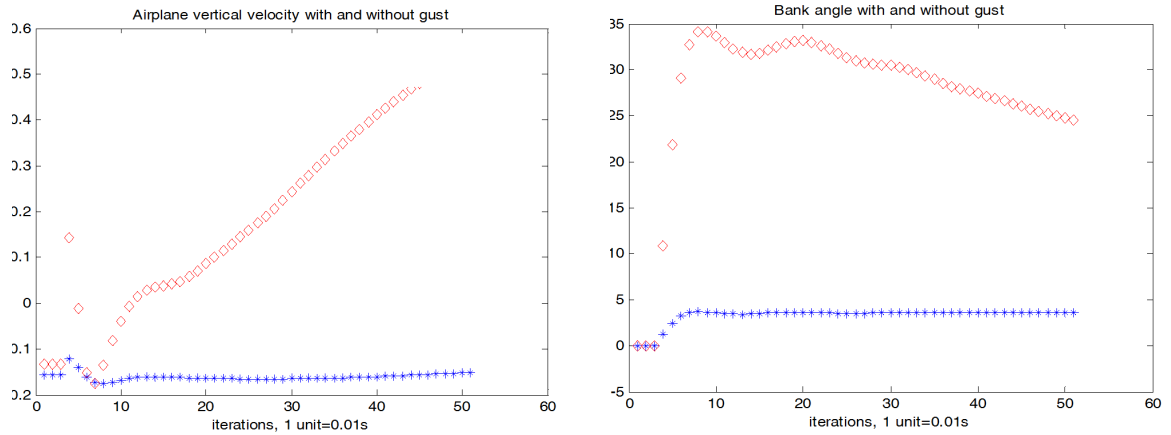


Figure 3.22: Airplane vertical velocity and bank angle with and without gust, nonlinear ASWING simulation

set to fly over a simulated gust field.

Strain wide field integration was implemented in closed loop feedback by obtaining the strains from each sensor location (Figure 3.21) and weighting them using the output C_w matrix. The calculated actuator command was then fed back to the symmetric aileron on the right wing, to account for the effect of the roll disturbance generated by the aileron on the left wing. The strain feedback loop however was only implemented for roll disturbance rejection in the way of an inner loop (Figure 3.23). There were no additional outer loop controllers in place for further attitude stabilization, therefore the simulations only evaluated the performance of strain feedback alone. The simulated disturbance consisted on rapidly changing the left aileron angle by a few degrees for one second after one second of flight. The effect of the simulated roll disturbance on the vehicle states can be observed from Figure 3.24. In this figure, it can be observed from the roll angle time history that

the roll disturbance causes the roll angle to increase over time. Other states also become unstable as a consequence of the disturbance. The roll disturbance has an impact on the wing strains, this can be observed from Figure 3.25. This information is used in the strain feedback loop.

A combined set of sensor locations from EFI and MPF calculations were used and the impact on the closed loop in the presence of a roll disturbance was observed. The C_w matrix was calculated using these locations and used in closed loop to weigh the values of strain coming from each sensor. These EFI/MPF sensor locations were then compared to the performance of random sensor locations to mitigate the roll disturbance. The random set produced instabilities in the rigid body states, therefore the EFI/MPF sensor locations were conserved. A PID controller was implemented in the strain feedback loop using the EFI/MPF locations and at different gains, higher gains enable a more effective strain feedback control, as can be seen from Figure 3.26.

Inner loop stabilization by means of bioinspired mechanisms was demonstrated for a one degree of freedom roll disturbance case. Distributed strain sensing showed to be effective in counteracting roll disturbances. The weighting patterns in the output matrix are crucial to the bioinspired reactive mechanism which addresses the disturbance at higher order states before they propagate onto lower order states. A physics based weighting pattern was implemented and it showed to be useful in roll disturbance mitigation. This pattern was obtained by means of force and moment considerations.

Sensor placement is also a fundamental part of distributed sensing arrays.

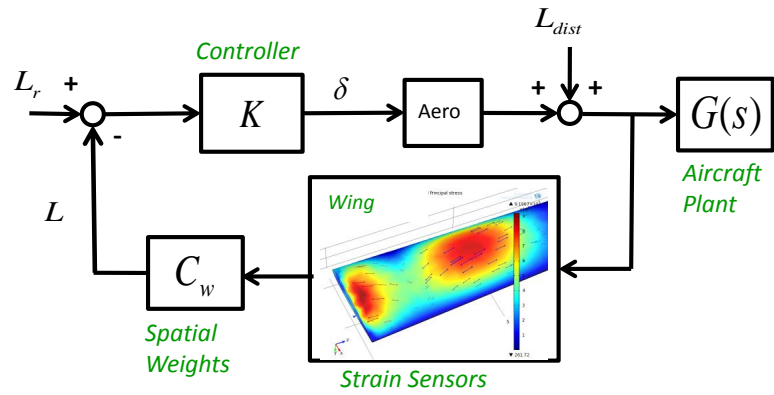


Figure 3.23: Strain feedback used in ASWING reduced order simulation

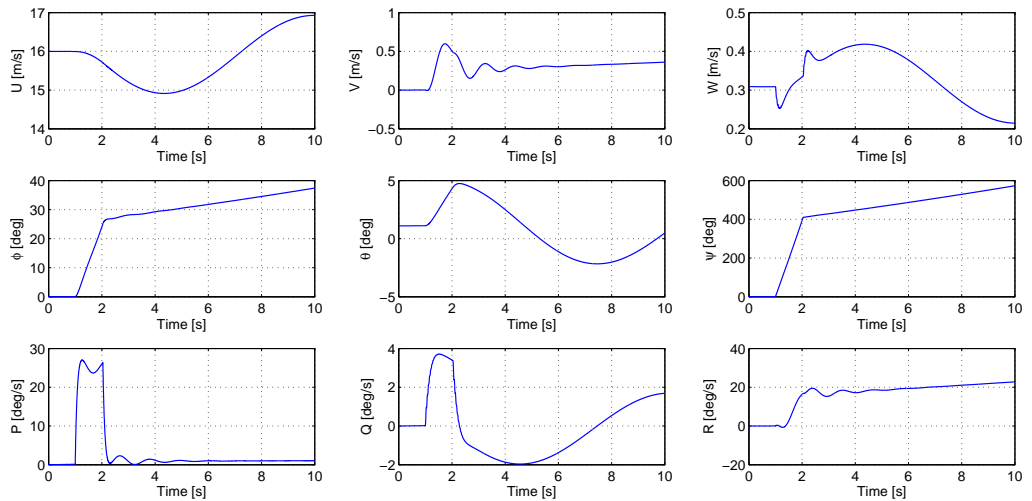


Figure 3.24: Roll disturbance on aircraft states

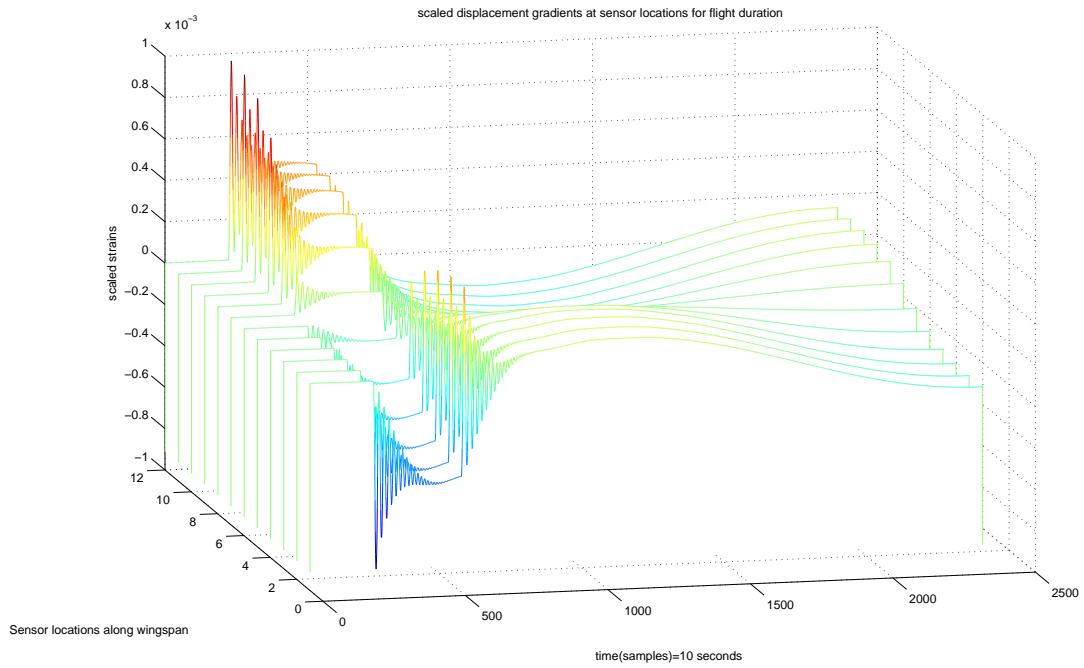


Figure 3.25: Impact of roll disturbance on sensors

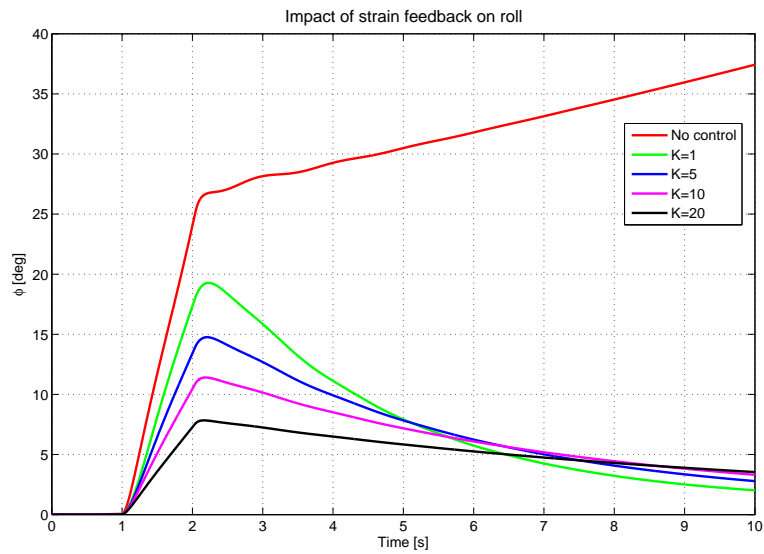


Figure 3.26: Roll angle at different strain feedback proportional gains K , with derivative $D=1$ and integral $I=2$ gains.

Two methods were explored, one based on system observability (EFI/Grammian) approach and the other one based on modal energy superposition with gust directionality (MPF-v). A combined approach using these two methods yielded sensor locations which were used in conjunction with the calculated output matrix. These provided disturbance mitigation results which were compared to those of a random sensor location set. It was observed that the randomly placed sensors did not produce a reduction in the roll disturbance. It was also observed that the optimal sensor locations in the closed loop case may have been close to the ones calculated in the open loop case. Symmetric sensor locations seemed to have consistently shown some improvement in roll disturbance rejection. A PID controller was implemented in the strain feedback loop. It was observed that roll disturbance rejection increased at higher proportional gains and relatively small derivative and integral terms.

Robust controllers based on strain feedback can be implemented for higher degree of freedom systems by means of higher order reactive loops. A closed loop sensor location optimization can be used to compare to locations predicted by energy and observability calculations.

3.5.2 Fluid structure interaction simulations- Static Aeroelastic (Comsol)

A static aeroelastic simulation was built using the FSI or fluid structure interaction module in Comsol Multiphysics. The module combines fluid flow with solid mechanics to capture the interaction between the fluid and the solid structure. The

fluid structure interaction couplings appear on the boundaries between the fluid and the solid. The fluid structure interaction interface uses an arbitrary Lagrangian Eulerian or ALE method to combine the fluid flow formulated using an Eulerian description and a spatial frame with solid mechanics which has been formulated using a Lagrangian description in a material reference frame.

The fluid flow is described by the Navier Stokes equations which yield a solution for the fluid velocity field. The fluid exerts a force on the boundary of the solid, which is given by the negative of the reaction force on the fluid [99]. This reaction force is given by:

$$f = n \cdot \left(-pI + \left(\mu(\nabla u + (\nabla u)^T) - \frac{2}{3}\mu(\nabla u)I \right) \right) \quad (3.51)$$

where p is the fluid pressure, n is the outward normal to the boundary, and I the identity matrix. Since the Navier stokes equations are solved in the spatial and therefore deformed frame and the solid mechanics interfaces are defined in the undeformed frame, a transformation of the fluid force on the solid is necessary. This transformation scales the mesh elements in both frames to come up with a mesh ratio. This ratio is defined by the spatial element factor dv and the material element dV . f is the force on the fluid, defined in the spatial frame and F is the force defined in the material frame.

$$F = f \frac{dv}{dV} \quad (3.52)$$

The solid mechanics counterpart entails the structural velocities to act as a moving wall for the fluid domain. These bidirectional couplings allow for the fluid structure interaction simulation. The mesh is free to move inside the fluid domains and adjusts to the motion of the solid walls. The geometric change of the fluid domain is automatically accounted for in Comsol.

The static aeroelastic simulations were set in the way of a wind tunnel test scenario Figure 3.27. This approach therefore consists of a simulated wind tunnel environment. There is an inlet upstream of the leading edge of the wing and an outlet downstream of the trailing edge of the wing and four non-slip surfaces. This scenario was chosen due to the computationally expensive nature of CFD computations and due to the purpose of the simulations which is to observe the interactions of the fluid and the wing, and the produced strains and stresses on the surface of the wing.

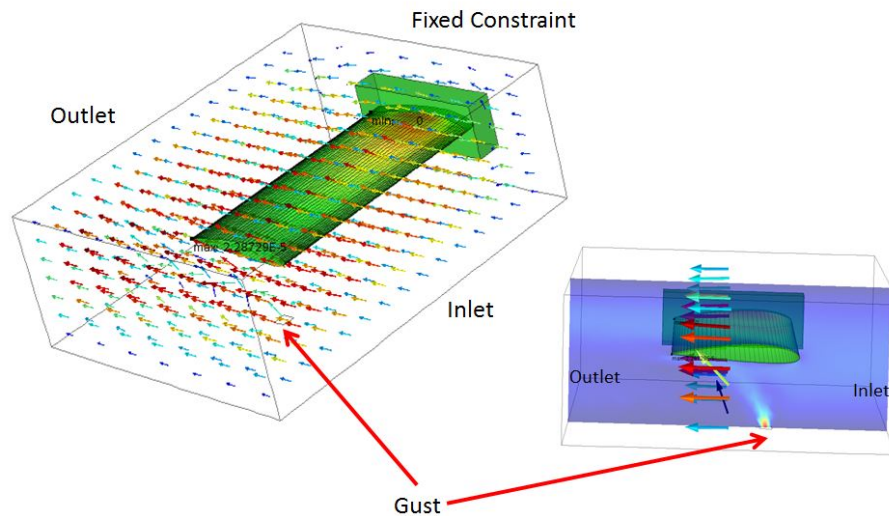


Figure 3.27: Wind tunnel simulation of fixed wing with impinging vertical gust

An acrylic wing was used for these simulations. The mesh elements used in the simulation were tetrahedral elements in the order of 450000, as well as triangular surface elements in the order of 30000 and about 9000 edge elements. The length of the box was made shorter than typical virtual tunnel CFD simulations due to the computational requirements, as it allowed to observe the interactions of the wing material and the fluid.

A vertical gust was included in the simulation with the purpose of observing the effects on the wing strains. Results from these simulations are shown in Figure 3.28. The speed of the tunnel was varied from 0 to 30 m/s and the gust velocities varied from 0 to 15 m/s, which are a bit unrealistic but were mainly for heuristic purposes. Correlations of gust velocities, wind speeds and surface strain maps can be drawn from different simulation cases.

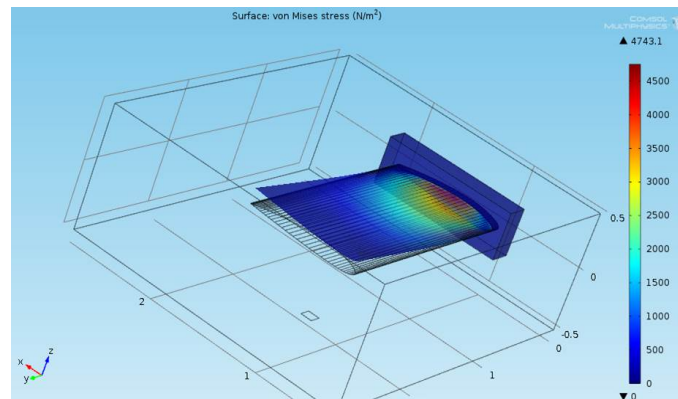


Figure 3.28: Wind tunnel simulation of fixed wing with impinging vertical gust, strains are produced as a result of the impinging vertical gust

Another interesting simulation setup which was implemented consists of a

rotational gust. This gust was simulated by placing gusts on opposite sides of the wing. The fluid pressure profiles can be observed from Figure 3.29. The resulting strain profile is quite different from the one observed for an impinging unidirectional gust from Figure 3.28.

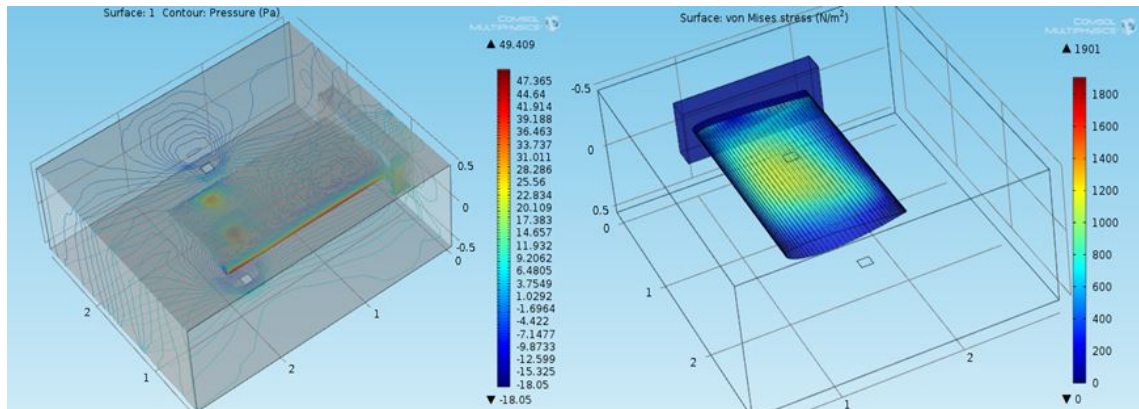


Figure 3.29: Wind tunnel simulation of fixed wing with impinging rotational gust:
Fluid pressure profiles (left) and wing strains (right)

From these simulations another important result was observed. The principal strains and stresses are a function of the gust directions. These quantities vary depending on the direction in which the fluid is interacting with the wing structure. Further simulations will be conducted in other works to study and model this interaction in depth. These directions can be observed from Figure 3.30. In these figures, the stress surface is superimposed and the arrows show the first principal stress in the wing due to the gust.

Time dependent simulations can also be undertaken to study dynamic aeroelasticity effects, however, these are extremely computationally expensive with the

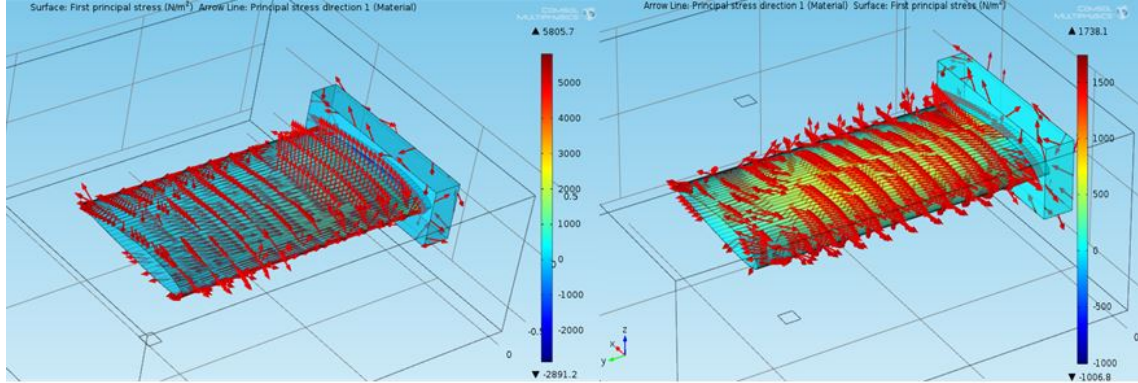


Figure 3.30: Principal strains for different impinging gusts: vertical gust (left) and torsional gust (right)

current computational platform and will be left for further study. A single one second simulation took approximately 8 days to successfully run. Another important study that will be left for further study is the FSI validation. Comsol has several CFD validation models and structural models, however these have not been validated jointly in the FSI module. These need to be verified as part of the well understood CFD and simulation requirements [100], [101].

3.6 2D sensor placement analyses (Comsol)

3.6.1 PWing test section

3.6.1.1 Wing FE model and sensor placement analysis

A wing section was used to test the concepts from the energy based sensor placement approach. This approach was shown to have similar results to those provided by the Grammian analysis for a vertical gust. The technique is now applied

to the surface of a three dimensional wing to find the best sensor locations to give best outputs amidst vertical gusts.

The software used for the finite element simulations was COMSOL Multiphysics. The wing was an unswept wing with airfoil profile AG-35 manufactured by Borealis Composites [102]. It was constructed such that the torsional compliance is much larger than the bending compliance. The layup configuration consisted of foam core, 1k carbon fiber weave placed at ± 45 degrees with respect to the lengthwise axis and one layer of ± 90 degree fiberglass cloth as the outermost layer. The wing geometric characteristics are shown in Figure 3.31 and Table 3.5. The aerodynamic properties are calculated based on the approximate characteristics of the NACA 2408 airfoil.

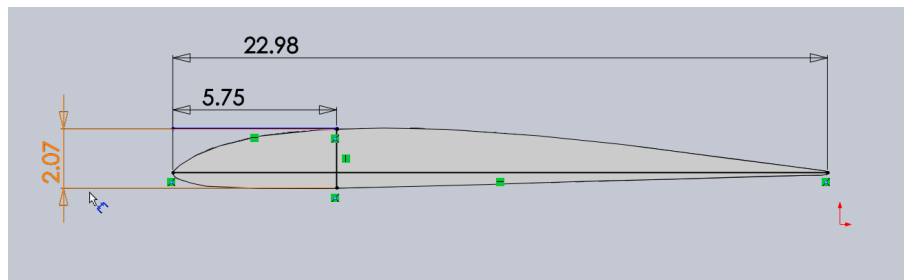


Figure 3.31: Airfoil geometric characteristics

The wing also had two ribs, one at the root and one at the tip made out of wood. These however are not carrying any significant loads. There are no ribs or spars, therefore the entirety of the loads is carried by the carbon fiber shell. For a simplified model, a carbon fiber at 0 degrees shell with extruded styrofoam core was considered. The behavior of the composite is mostly unidirectional, therefore this

Table 3.3: Wing geometric characteristics

| Wing characteristics | Value | Wing characteristics | Value |
|-----------------------|---------------------------|----------------------|--------|
| Chord length | 22.98 cm | Approx. NACA | 2408 |
| Quarter chord | 5.75 cm | Lower flatness1 | 93.0% |
| Max. thickness | 2 cm | Max. CL1 | 0.953 |
| Max. Camber | 4 mm | Max.CL angle1 | 13.5 |
| Wing length | 62 cm | Max. L/D 1 | 41.453 |
| Shell thickness | 0.0528 cm | Stall angle1 | 2.5 |
| Second moment of area | 5.9748e-08 m ⁴ | Zero Lift angle1 | -2.0 |
| Dihedral | 0 deg. | Ailerons | 2 |

approximation was made.

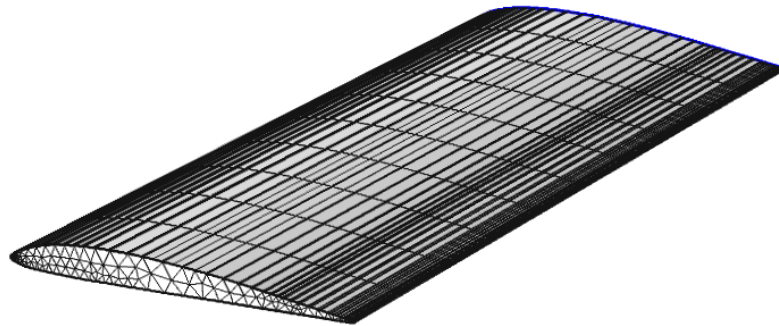


Figure 3.32: Normal element size mesh of carbon layup wing

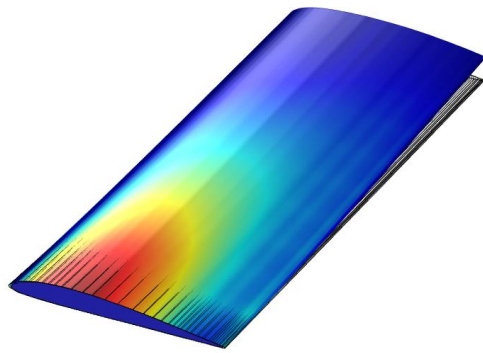
The solvers used to solve for the eigenmodes is the MUMPS (or Multifrontal Massively Parallel sparse direct Solver) [103]. This solver is a variant of Gauss elimination which builds a LU or Cholesky matrix decomposition of the sparse matrix and then solves it one subset, or front, at a time. The multifrontal approach refers to the usage of parallel cores to process different frontals simultaneously. This solver uses several reordering algorithms to permute the columns for prearrangement.

The eigenmodes obtained are in-vacuo and with cantilevered boundary conditions. The finite element results are shown in Figure 3.33. The frequencies of these eigenstresses are, respectively, 53.682 Hz, 166.65 Hz, 184.66 Hz, 235.80 Hz, 286.05 Hz, 325.02 Hz.

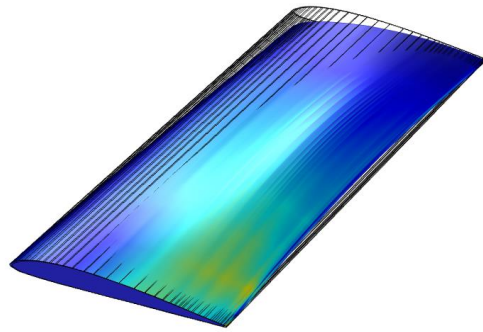
A top view of the 3D wings gives an idea of the 2D eigenstresses in the same modes. This is shown in Figure 3.34.

Using these first six modes, we proceed now to weighting them and superimposing them by means of mass participation factor coefficients. These coefficients provide a method for judging the significance of a vibration mode. That is, modes with higher factors can be readily excited whereas ones with lower factors cannot. This is an appropriate analysis for an aircraft wing in that it undergoes different types of loads during flight which may produce deformations and strains. This allows a study of the more significant impacts of the loads on the wing, which produce strains.

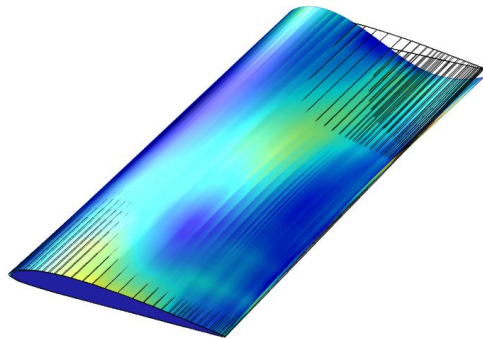
The following mass participation factors were also calculated in the finite element solver and are used for weighting the modes and combine them into a linearly superimposed eigenstrain profile. The resulting profile is used for the sensor place-



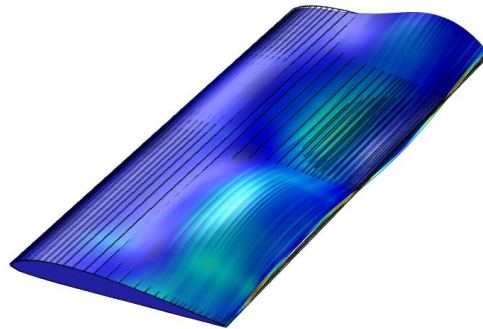
(a) First eigenstress mode



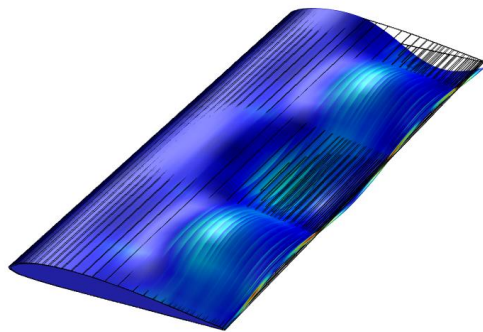
(b) Second eigenstress mode



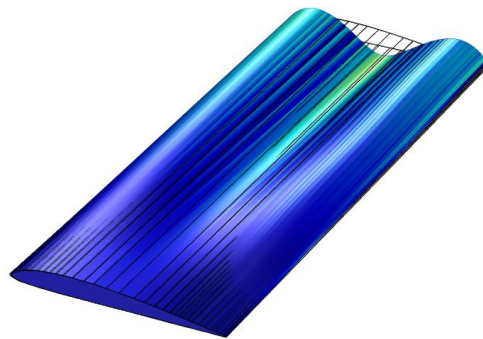
(c) Third eigenstress mode



(d) Fourth eigenstress mode

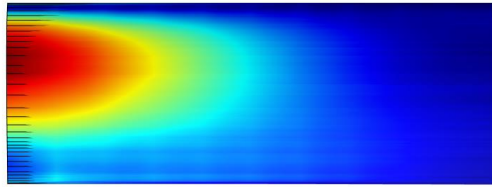


(e) Fifth eigenstress mode

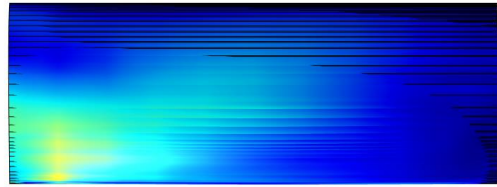


(f) Sixth eigenstress mode

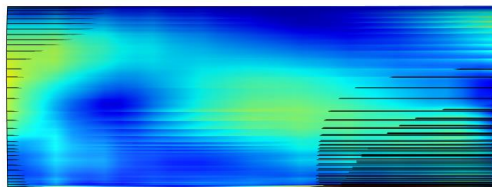
Figure 3.33: First six eigenstresses of carbon fiber wing



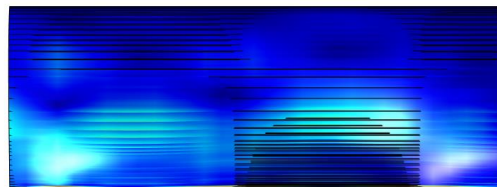
(a) First eigenstress mode



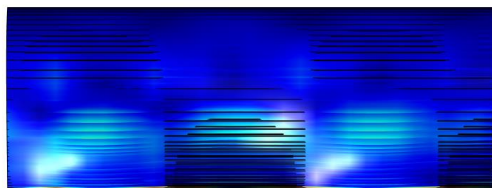
(b) Second eigenstress mode



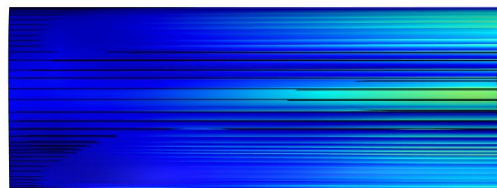
(c) Third eigenstress mode



(d) Fourth eigenstress mode



(e) Fifth eigenstress mode



(f) Sixth eigenstress mode

Figure 3.34: 2D view of first six eigenstresses of carbon fiber wing

ment study. The resulting mass participation factors are shown in Table 3.6.

Table 3.4: Mass participation factors of carbon fiber wing

| Eigenfreq. | MPF-u | MPF-v | MPF-w |
|------------|-----------|---------|-----------|
| 53.68259 | -0.00297 | 0.34194 | -7.62E-05 |
| 166.6564 | -0.011898 | 0.07544 | -5.04E-05 |
| 184.6618 | 0.00843 | 0.11441 | 1.95E-04 |
| 235.8009 | -0.00412 | 0.05275 | -1.30E-04 |
| 286.0515 | -0.0026 | 0.03837 | 1.07E-05 |
| 325.0233 | 0.00675 | -0.0038 | 2.35E-04 |

The eigenstrain profiles are calculated for two cases of linear superposition of modes. One case with equal weighting coefficients and the other one with the mass participation factor MPF weighted eigenstrains in the v-direction, which for purposes of the simulation corresponds to an out of plane displacement, or displacements which are produced by loads that are normal to the wing, i.e. lift. The resulting eigenstrains are shown in Figure 3.35.

In this figure, the root of the wing is at zero wing length and the trailing edge is at the zero chord line. In this figure, the areas of maximal stress are in red and the areas of minimal stress are in dark blue. The equal weighting mode superposition gives a very different strain field from that of the MPF-v weighted eigenstrains. It can be observed from the graphs that the areas of maximal stress are rather close to the trailing edge, this is probably due to a higher bending moment in thinner sections of the wing, as the moment of area goes down in these regions. The areas of

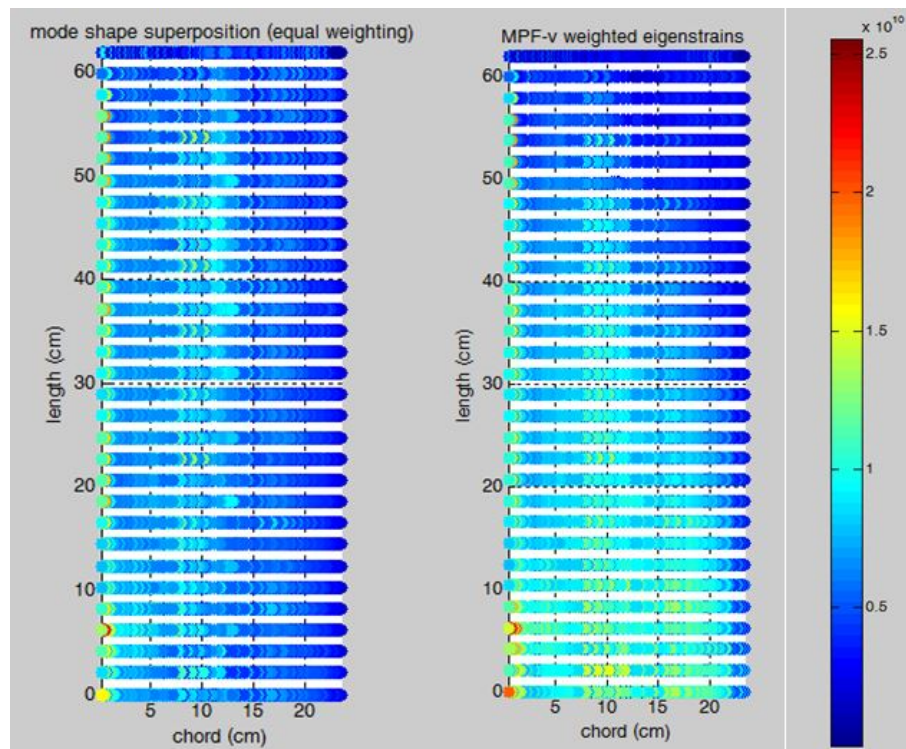


Figure 3.35: Superposition of first six eigenstress modes (top view)

maximal strain which are suitable for placing strain gauges are those which have not so high gradients. This combination will yield better results at the implementation phase because the areas of larger strain gradients can cause the strain gauges to detach and or produce rapidly changing signals.

The possible number of sensors and sensor arrangements depends on the available sensor platforms. These platforms will be presented in the following chapter. One of the sensor platforms that were used was provided by the structures and composites laboratory at Stanford University [8]. This platform consists of a stretchable sensor network, where the strain gauges and interconnections are microfabricated into a single stretchable mesh. The constraint of this network entails a maximum of 15 sensors with 5 x 9 possible sensor locations in a grid which has an adjustable length. A maximum of three sensors per lengthwise row could be chosen at a time. Possible scenarios and distributions based on these constraints and the analysis shown in Figure 3.35 are shown in Figure 3.36.

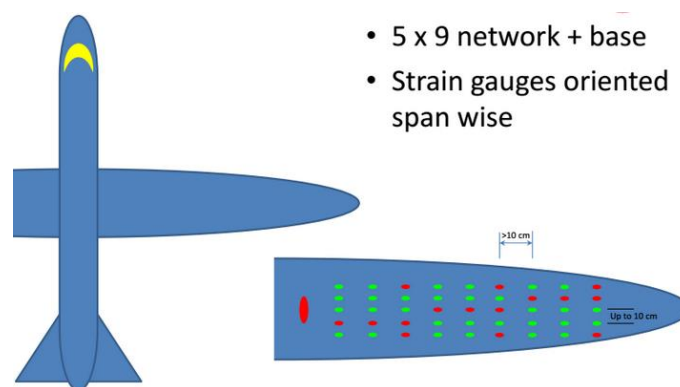


Figure 3.36: Strain gauge stretchable network in spanwise orientation (Structures and Composites Lab SACL, Stanford University) [8]

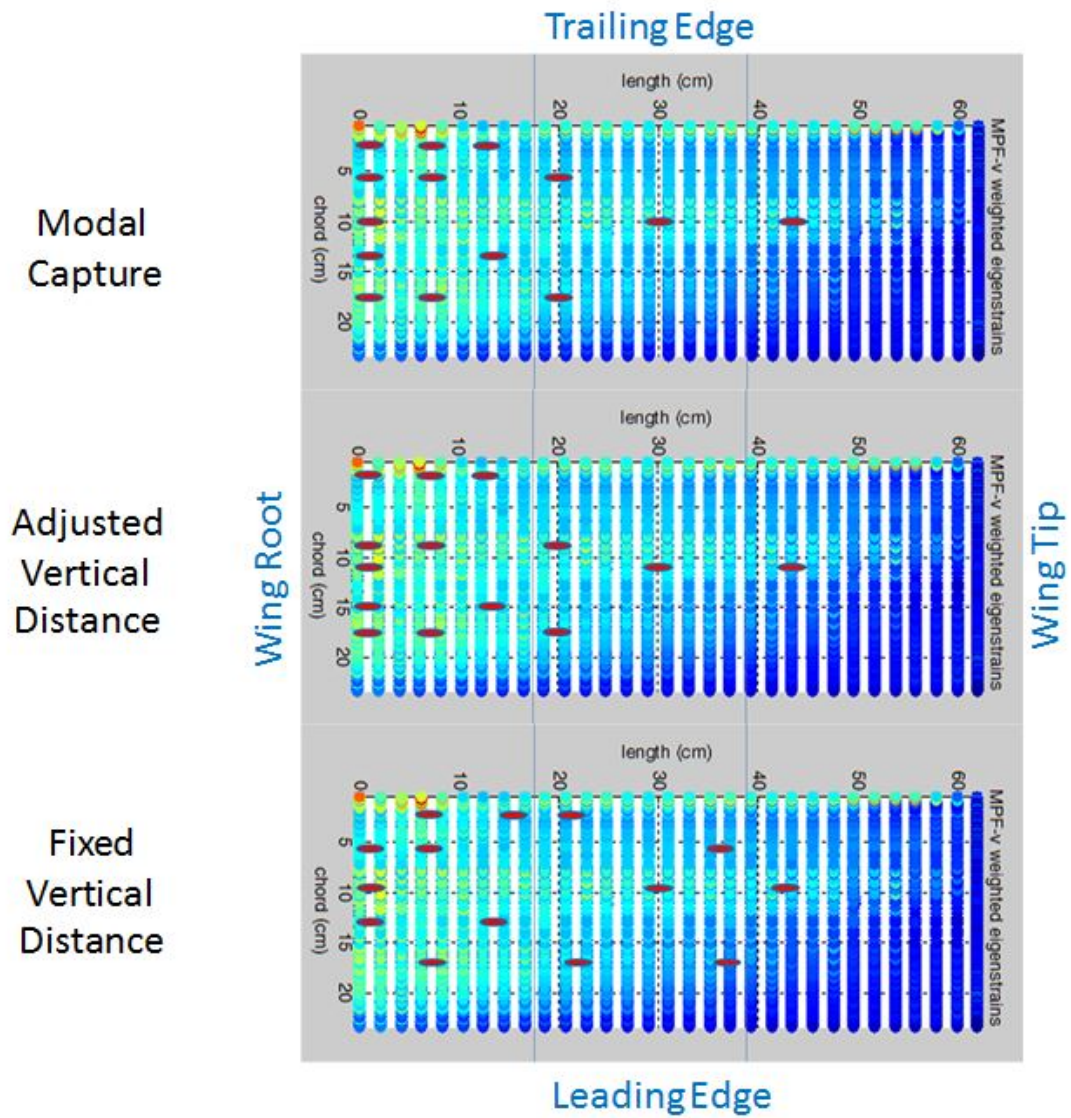


Figure 3.37: Sensor distributions based on SACL lab stretchable sensor network

The three scenarios presented in Figure 3.37 were chosen based on the intended measurements. The first scenario is a somewhat uniform vertical distance modal capture distribution, as it covers most of the areas of maximal stress and lower gradients. The second scenario also intends to capture most of the modal strain, however with an adjusted vertical distance to look for more convenient areas for sensor locations. The fixed vertical distance scenario is a distribution that may also allow for possibly capturing other phenomena or serving to validate assumptions during the modeling process.

Another important analysis feature is given by the sensor orientations. In nature, as it was seen in the bio inspired section of this work, strain sensors of animals are oriented depending on what their intended functionality is. Campaniform sensilla are elliptical and the major axes are oriented in the maximal strain output directions. In strain analysis, the orientation of the sensors is given by the principal stress directions. These are directions which are calculated to be the directions in which strain is varying the most, according to geometry and full 3D material properties. These orientations are also calculated in Comsol, and can also be weighted to find energy weighted patterns. These strain fields can also be superimposed according to the mass participation factors. However this procedure entails 3D vectorial summation to generate the superimposed vector field of principal stress/strain. Figure 3.38 are the principal directions for the first three modes of the wing.

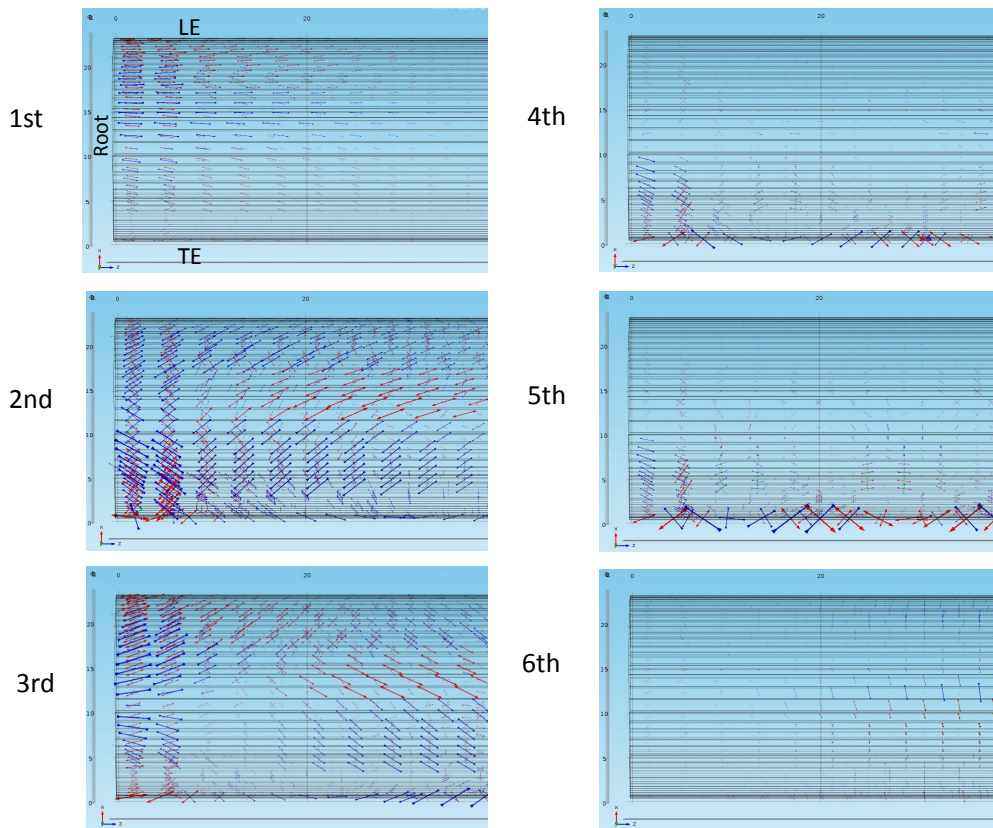


Figure 3.38: First six principal strain directions of carbon fiber wing

3.6.2 Flight test PWing

A similar approach was followed for the actual test flight wing, which is to be assembled with the Apprentice aircraft airplane.

The full wing for flight tests with the apprentice had a similar layup as compared to the first Pwings test section. It has dihedral and a similar carbon fiber and fiber glass layup. The wing characteristics are described as shown in the following table. The airfoil is the same profile AG-35 which can be approximately described by the NACA 2408. Figure 3.39 shows the geometric characteristics as designed by the manufacturer [102] and by Aurora Flight Sciences [7]. Figure 3.40 shows a set of two manufactured PWings without strain gauge instrumentation or servo motors.

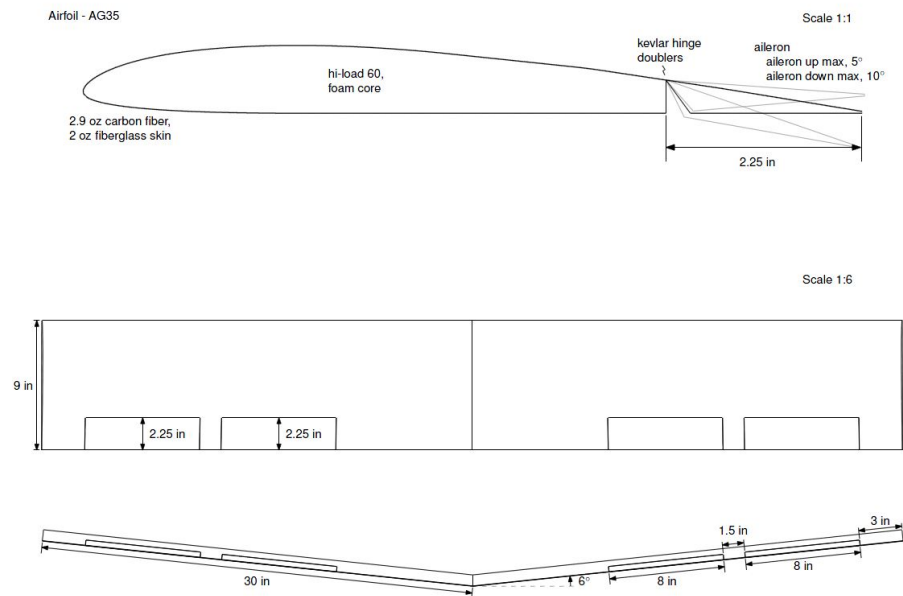


Figure 3.39: Pwing Airfoil and full wingspan geometry

Table 3.5: Wing geometric characteristics

| Wing characteristics | Value | Wing characteristics | Value |
|-----------------------|---------------------------|----------------------|--------|
| Chord length | 9 in | Approx. NACA | 2408 |
| Quarter chord | 2.25 in | Lower flatness1 | 93.0% |
| Max. thickness | 2 cm | Max. CL1 | 0.953 |
| Max. Camber | 4 mm | Max.CL angle1 | 13.5 |
| Wing length | 62 cm | Max. L/D 1 | 41.453 |
| Shell thickness | 0.0528 cm | Stall angle1 | 2.5 |
| Second moment of area | 5.9748e-08 m ⁴ | Zero Lift angle1 | -2.0 |
| Dihedral | 6 deg. | Ailerons | 4 |
| Ribs | 2 deg. | Small joining spar | 1 |

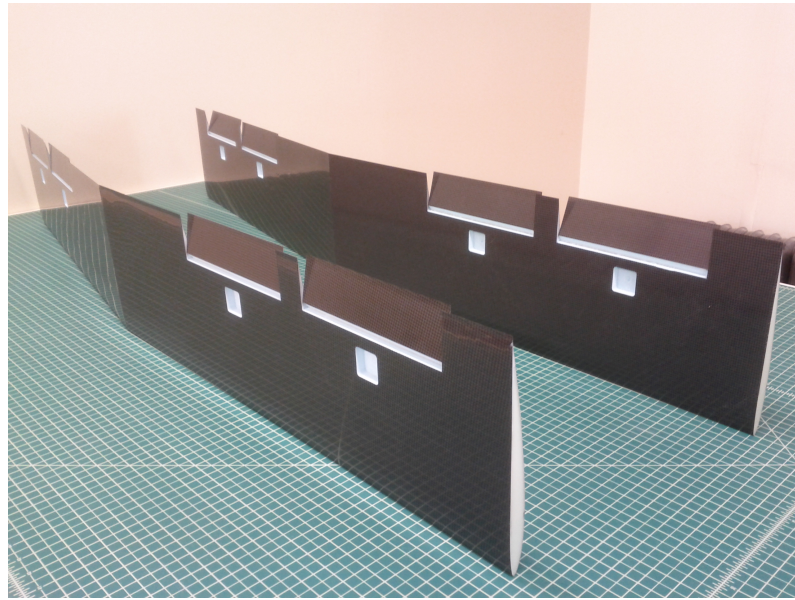
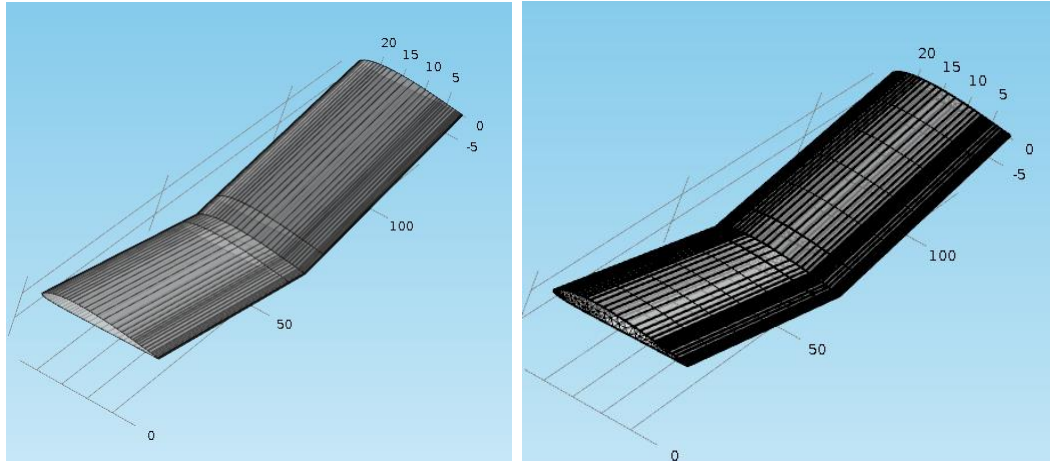


Figure 3.40: Flight Pwings for assembly with Apprentice Aircraft



(a) Comsol model

(b) FE mesh

Figure 3.41: FE model of flight test wing and meshed geometry

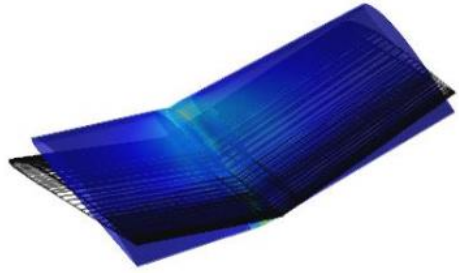
3.6.2.1 Wing FE model and sensor placement analysis

The finite element model was generated with a sweep mesh. The boundary conditions for the model were an elastic foundation at the section where the wing is attached to the fuselage.

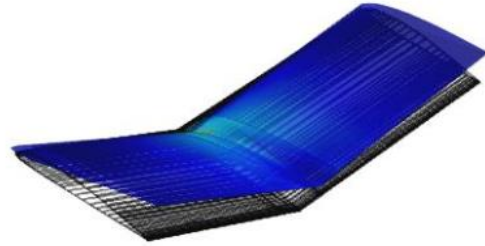
In this model, a spring foundation was used to model the actual attachment of the wing to the apprentice fuselage. The rubber bands provide a firm attachment to the wing, however the elastic foundation influences the eigenstrain modes found as a result of the finite element calculation. Some of the first few eigenstrains are shown in Figure 3.42.

Based on the first six modes, the equally weighted eigenstrain and the MPF-v weighted eigenstrain superpositions are shown in Figure 3.43.

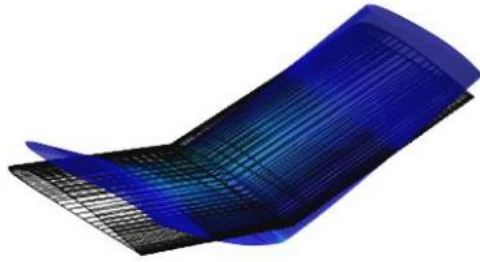
From this mapping, which uses the first low frequency damped modes, some



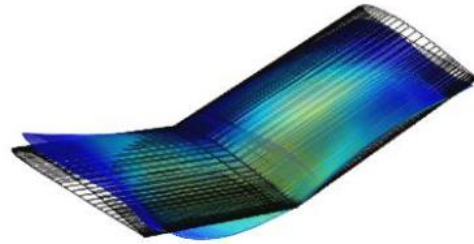
(a) First eigenstrain mode



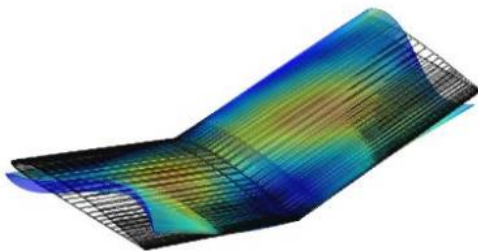
(b) Second eigenstrain mode



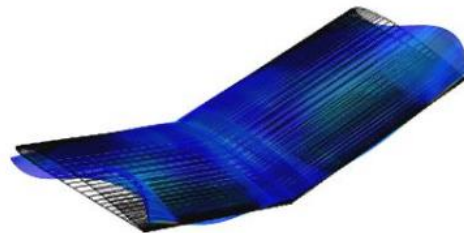
(c) Third eigenstrain mode



(d) Fourth eigenstrain mode



(e) Fifth eigenstrain mode



(f) Sixth eigenstrain mode

Figure 3.42: First few eigenstrain modes of flight wing

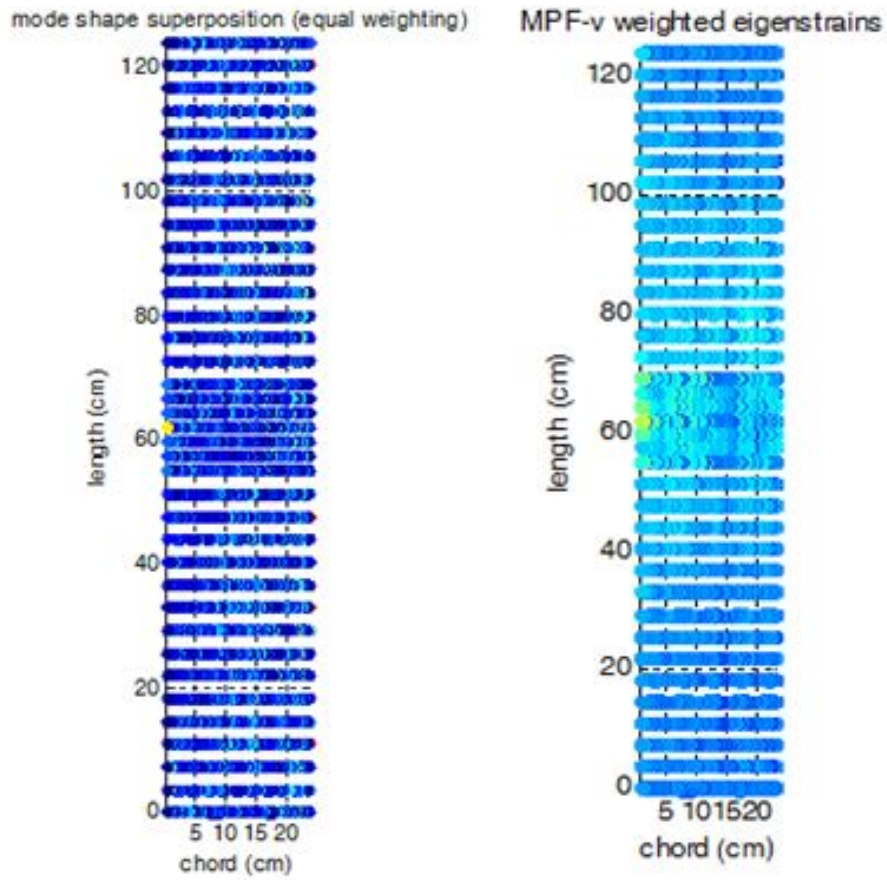


Figure 3.43: Eigenstrain modes of flight wing: linear weighting (left) and MPF-v weighted (right)

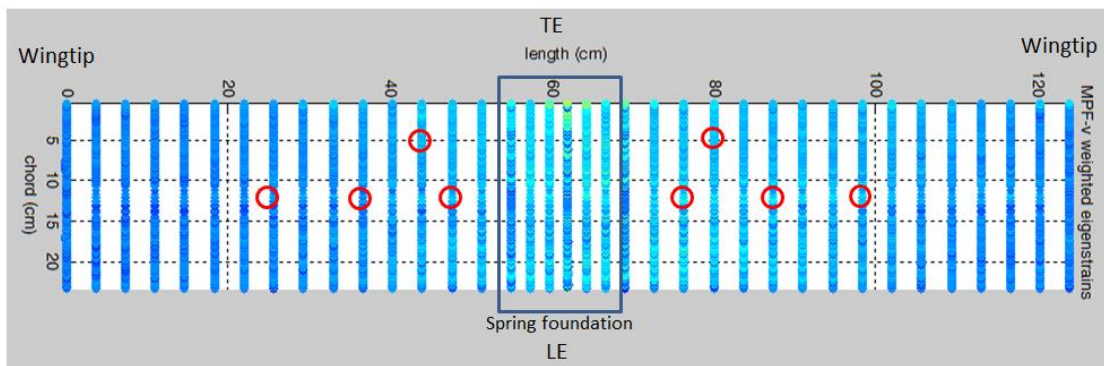


Figure 3.44: MPF-v weighted eigenstrain map for 8 sensors

asymmetry can be ignored, as this is an artifact of the damping mode structure of the FE solver. The sensor placement diagram based on these low frequency, damped modes, is shown in Figure 3.44. Other diagrams may be obtained depending on the number of modes that are going to be considered. Typically if 80 % of the model mass is accounted for in the mass of the modes used for the superposition then is a reasonable approximation. If however more mass needs to be accounted for, then possibly more energy considerations on the modes need to be made. This model also depends on the approximation of the spring foundation. It is worth noting that the dihedral reduces the observability of the vertical gusts on the surface of the wing. Another factor which reduces observability of the gusts is the spring foundation, as now the impact of the vertical gust disturbance is partially absorbed and damped by the rubber bands which hold the wing to the fuselage. The flight scenario is therefore more complex and more factors need to be taken into consideration for a reasonable approximation to be made. Figure 3.44 shows the sensor placement of 8 sensors, four on each wing, on the areas of maximum expected strain. A symmetric extension was made based on approximations made above. In this case, the placement is solely made on observability considerations. If wave propagation were going to be studied with the sensor setup, then most probably some sensors would need to go towards the tip of the wing.

Table 3.6: Mass participation factor v of carbon fiber wing

| Eigenfrequency | MPF- v |
|----------------|-------------|
| 0.01436i | 2.11168e-4 |
| 0.02834i | 1.02403e-5 |
| 0.01454 | -2.63717e-5 |
| 0.44147 | 4.48709e-5 |
| 2.9061 | 0.35438 |
| 4.01844 | 0.49673 |
| 72.96186 | -0.00189 |
| 159.43176 | -9.06982e-9 |
| 168.91207 | -1.16206e-8 |
| 200.00018 | 1.48484e-4 |
| 215.37157 | 5.81196e-5 |
| 226.2739 | -5.74395e-9 |
| 257.33485 | 8.38917e-5 |
| 278.86208 | -8.44229e-9 |
| 292.43694 | 1.53964e-9 |
| 300.08143 | 3.85717e-5 |
| 324.85174 | -1.41942e-9 |
| 326.8127 | -1.47191e-5 |
| 331.12235 | -1.0998e-9 |
| 340.1933 | -3.427e-9 |

Chapter 4: Experimental section and analysis

4.1 Glider experiments

4.1.1 Experimental Setup

A 1D strain feedback Glider experiment was conducted to test the feasibility of using strain feedback for gust alleviation. The one dimensional model used is found in Section (2.3.1).

The experimental setup intended to measure a glider's response to a vertical discrete gust while on flight. The setup was composed of a glider, rail launcher, a fan blower and a landing net (Figure 4.1). The rail launcher entails a sliding launching cradle pulled by a bungee cord. The launcher is compact and can be placed at different launching angles simply by adjusting the height at one end. An inelastic cord is used as a stopper for the cradle as well as for keeping the bungee cord under tension. The cradle is released from the receiver upon a transmitter command (Figure 4.1). The bungee cord then transfers its elastic potential energy to the launching cradle which then stops near the end of the railing giving its kinetic energy to the glider.

All the experiments were synchronized such that the Labview acquisition would

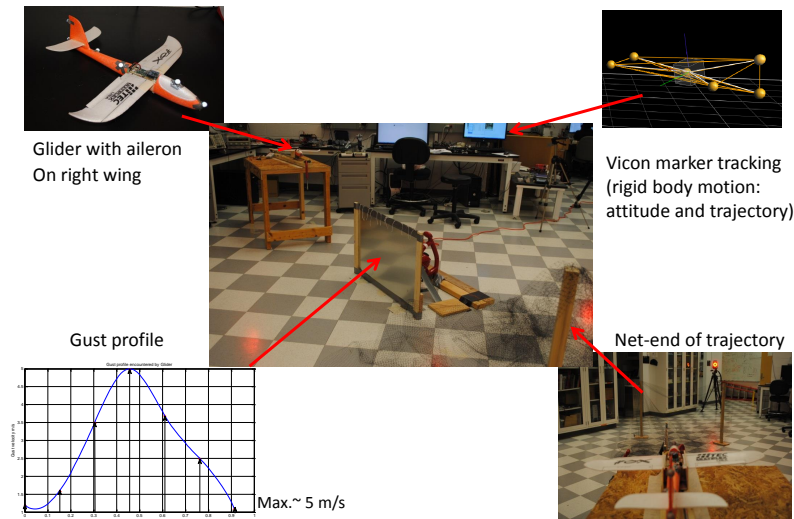


Figure 4.1: Experimental setup of glider and launching mechanism

start recording the glider trajectory upon launch. A MOTE transmitter was connected to Labview in order to have repeatable launches. The glider was consistently launched at a velocity of 0.6 m/s in the x-y plane (floor plane) in all the experiments as a result of this mechanism. The strain gauges were mounted onto two plate spars which were manufactured using a fast prototyping machine using Garolite (Figure 4.2). These spars were fitted with full bridge strain gauges. The wings were mounted onto a spar on each side of the central plate which also carried the processing unit and XBee transmitter. The strain gauges installed were of 1000 Ohms in full bridge per each wing, 2 in tension and 2 in compression.

The microcontroller system on board performs all of the A/D conversion, PWM generation and computation necessary for in flight feedback from up to 4 separate strain gauge channels to up to 4 separate PWM servo channels. The aileron

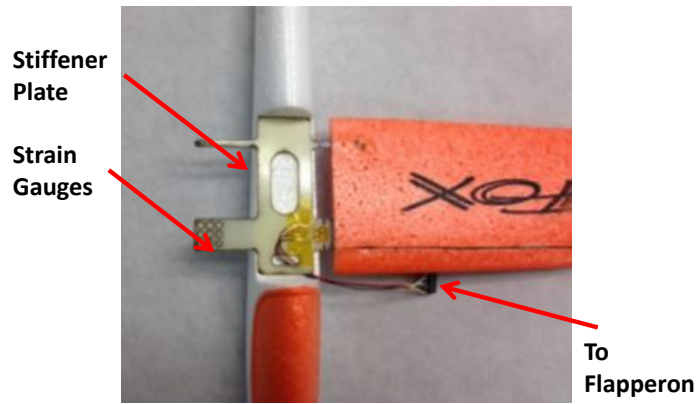


Figure 4.2: Glider plate and strain gauges

servo was also connected to the microcontroller board. The connections were placed inside the foam to help maintain laminar characteristics around the airfoil.

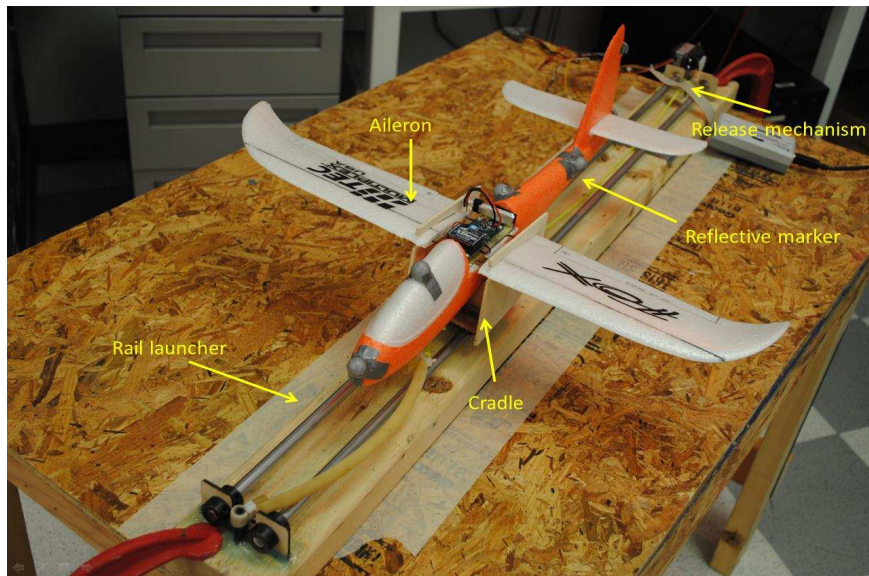


Figure 4.3: Experimental setup of glider and launching mechanism

The dynamics acquisition was implemented in Labview using VICON marker

data. All experimental results were obtained using the VICON motion capture system of the Autonomous Vehicle Lab at the University of Maryland College Park campus. The VICON motion capture system records position, attitude and orientation by triangulating marker points Figure 4.4. In the case of the glider, the markers were distributed along the fuselage to avoid any error due to local deformation. This would have been the case had the markers been placed on the flexible wings. A calibration of the VICON system was required before collecting the data and needed to be recalibrated often to avoid errors due to marker displacements produced during vehicle landings. The calibration included defining the vehicle's marker setup as well as defining the axes in a north, east down system such that the positive x-direction corresponded to the direction in which the glider was launched and the positive y-direction entailed the right hand side of the testing area. Adjustments due to this nomenclature were accounted for in the data presented in this work.

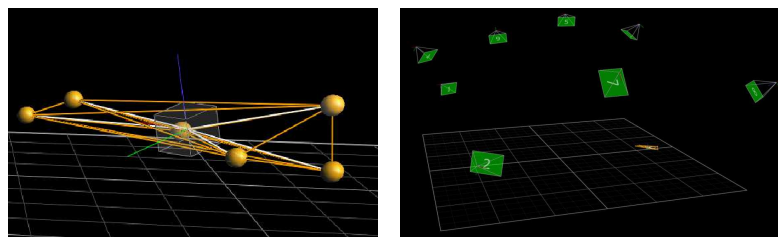


Figure 4.4: VICON Setup: Vehicle marker setup(left) and VICON camera setup and vehicle (right)

Roll dynamics were measured mainly for three sets of flight cases; free flight, flight under gusting conditions and flight under gusting conditions using strain feedback. In particular the experiments focused on the effect of the application of strain feedback to regulate roll. Different proportional gains were applied to investigate the effects of strain feedback on the rolling motion of the glider under gust conditions. The strain feedback results were also compared to classical controllers which were implemented off board using the VICON system/Labview setup to send updated aileron commands.

In order to achieve a good gust setup a couple of possibilities were evaluated. First, a box fan was set as the gust source and the glider projected path directly over it. This however doesn't provide a sharp edged gust which is desired to generate a strong rolling motion. Then a plate was incorporated to shape the gust. In this case the flow was not strong enough and the air stream near the plate was turbulent. Finally a leaf blower fan placed next to the plate was chosen for its more laminar qualities and strength. Tufts were used to heuristically determine the orientation of the flow field. The gust and plate were placed at 40 inches from the launch point. Figure 4.5, shows the gust contour utilized for the tests. It resembles a 1-cos gust, which is a commonly used gust model type. The measurements of the flow field were obtained using a hand anemometer. The gust had an approximate peak value of 5 m/s. After passing through the sharp gust, the glider would roll and land on a net set ahead of the gusting region. The VICON flight dynamics and trajectories were recorded for each flight.

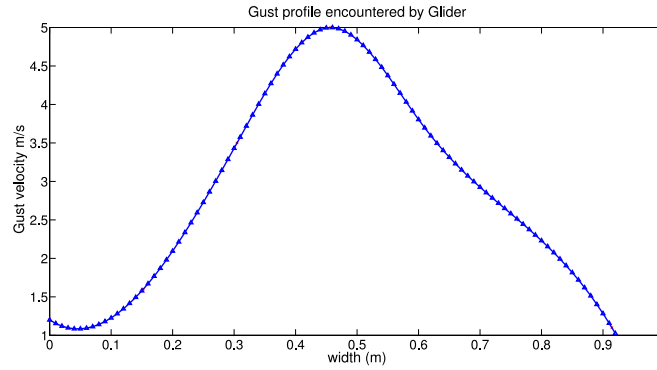


Figure 4.5: Gust encountered by glider.

4.1.2 Controls Setup

The controls implemented for the strain feedback closed loop tests is shown in Figure 4.6. It entails a combination of off-board calculations and an on-board

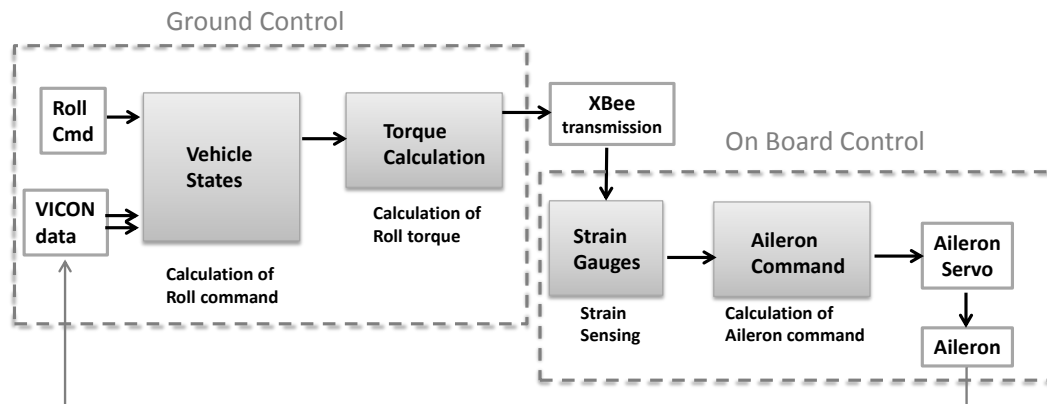


Figure 4.6: Controls used in strain feedback tests.

Figure 4.6 shows the controls used in strain feedback tests. A reference roll command is defined in the ground control which uses data from VICON. This in-

formation is used in the calculation of a desired roll torque which is sent via Xbee to the on board controller. Once the desired torque has been transmitted to the on-board controller, a calculation for the aileron command ensues. Finally this value reaches the servo and changes the aileron angle, producing changes in the vehicle's states, which are being recorded in VICON at all times.

In order to compare the results obtained using strain feedback, a couple of flights using classical controllers were undertaken. The classical controllers are classical in the sense that they use the recorded rigid body dynamics to calculate an aileron response. For these tests, the controls scheme utilized is shown in Figure 4.7. A comparison is shown later on in the experimental results section.

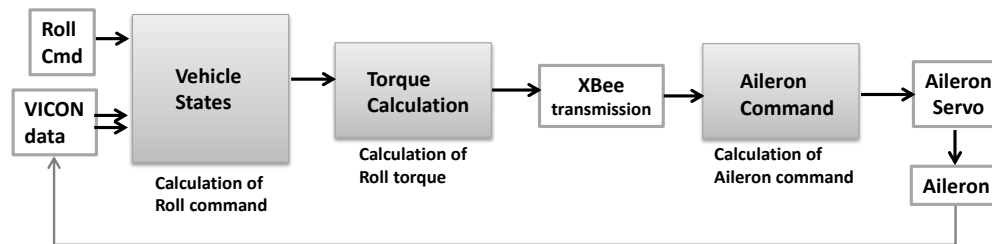


Figure 4.7: Classical controller used for controller types comparison.

4.1.3 Experimental Results

4.1.4 Force/Strain Feedback using Proportional Gains

The experimental results are presented in this section. Ten roll curves were recorded in VICON for each case. Figure 4.8 a shows the free flight history of the Glider. In this graph the four distinct flight phases are shown. First, the glider

remains on the launcher cradle (smooth horizontal region) after which it is launched and the roll angle increases as the trajectory advances. The short flight ends when the glider hits the net, generating scattered data points. These points however are discarded for calculations. The free flight data set is used later on in this work as a baseline for comparing the effectiveness of the structural feedback controller.

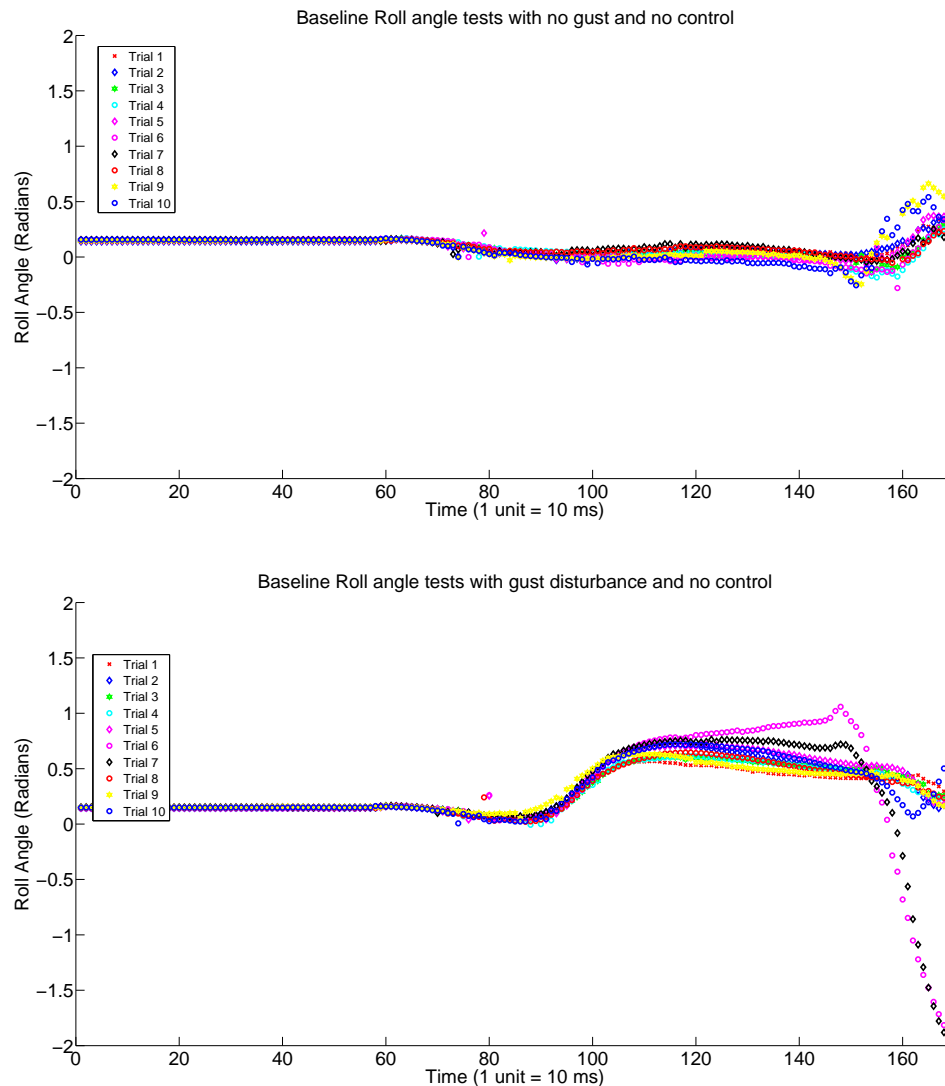


Figure 4.8: Glider baseline roll angle curves: with no gust perturbation (top), and under a vertical asymmetric gust (bottom).

A similar test was carried out for the case where no feedback control was applied in the presence of the sharp gust. The gust produces a maximum roll angle in the order of 45 degrees. These tests are shown in Figure 4.8. The effect of the gust can be clearly seen from Figure 4.8 (bottom). In Figure 4.9, each curve represents an average of the 10 flights for each case; free flight and with gust perturbation.

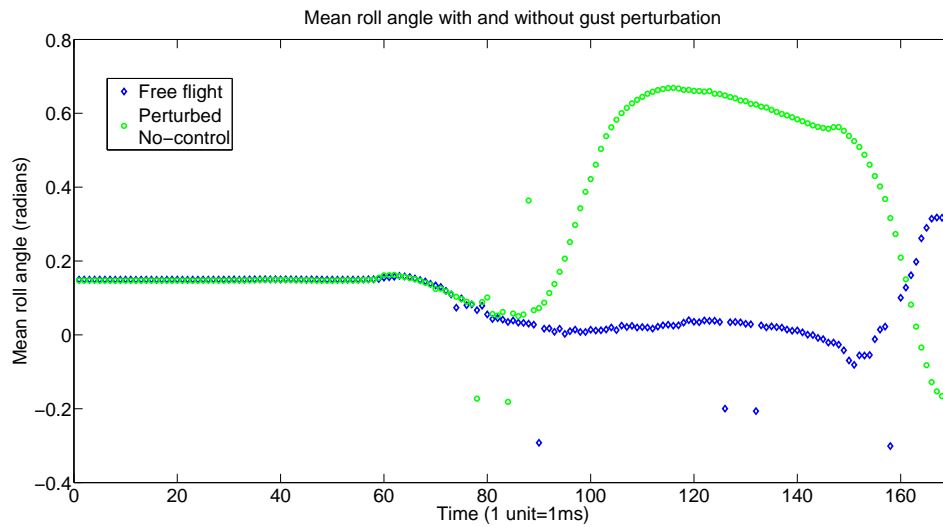


Figure 4.9: Glider mean roll for free flight and with vertical gust perturbation.

After measuring the impact of the gust on the glider’s roll angle a structural feedback controller was implemented. The controller intends to bring the roll angle back to an unperturbed baseline behavior. The major impact of the structural feedback correction of the roll angle can be seen towards the end of the graphs due to the shortness of flight duration. Figure 4.10 shows the effect of the controller at different proportional gains. Each one of the curves shown in these figures is an average of 10 to 20 flights. The effect of the structural feedback controller is shown to be higher at higher gains.

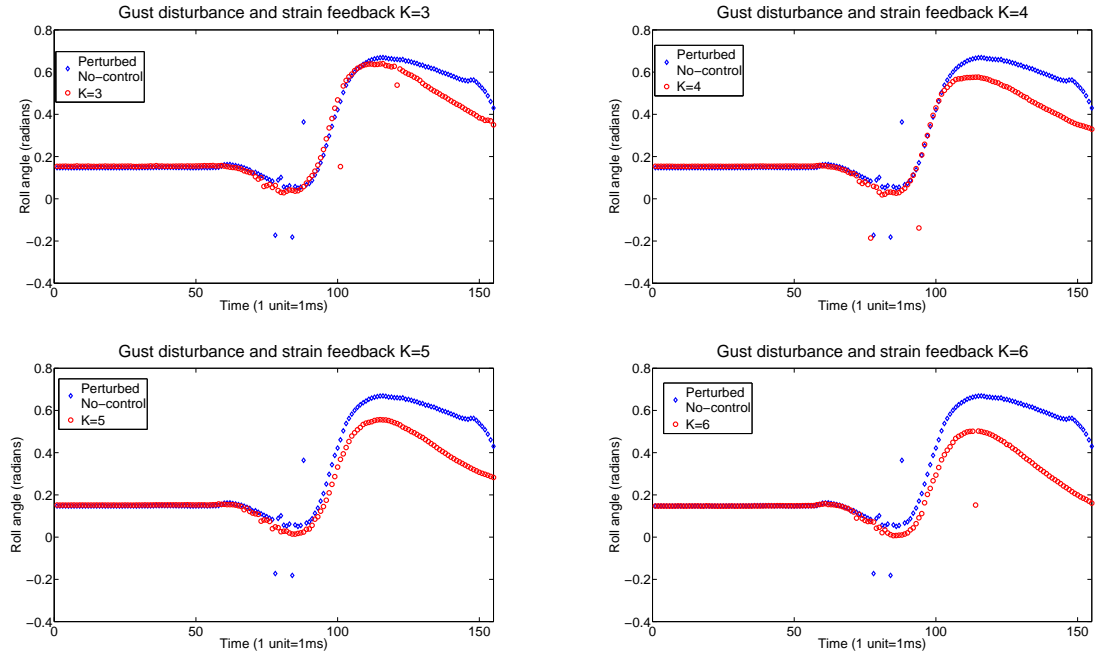


Figure 4.10: Glider mean roll for proportional gains $K=3$, $K=4$, $K=5$, and $K=6$

Figure 4.11 shows a summary of the applied gains and compares it to the baseline curves. This figure shows that when the gain is increased, the maximum perturbed roll angle is reduced and the roll angle decreases faster.

The effectiveness of the structural feedback can be quantified using different metrics. We have chosen the D2 metric for this purpose. The D2 metric provides a summation of the differences in the trajectories of the glider for the perturbed case with no applied control and the case where the controller is applied. Figure 4.12 shows that the D2 metric increases with the applied structural gain. This implies that the glider roll angle will increasingly stay away from the roll angle corresponding to the perturbed case.

As a way to compare strain feedback with classical controllers, we conducted

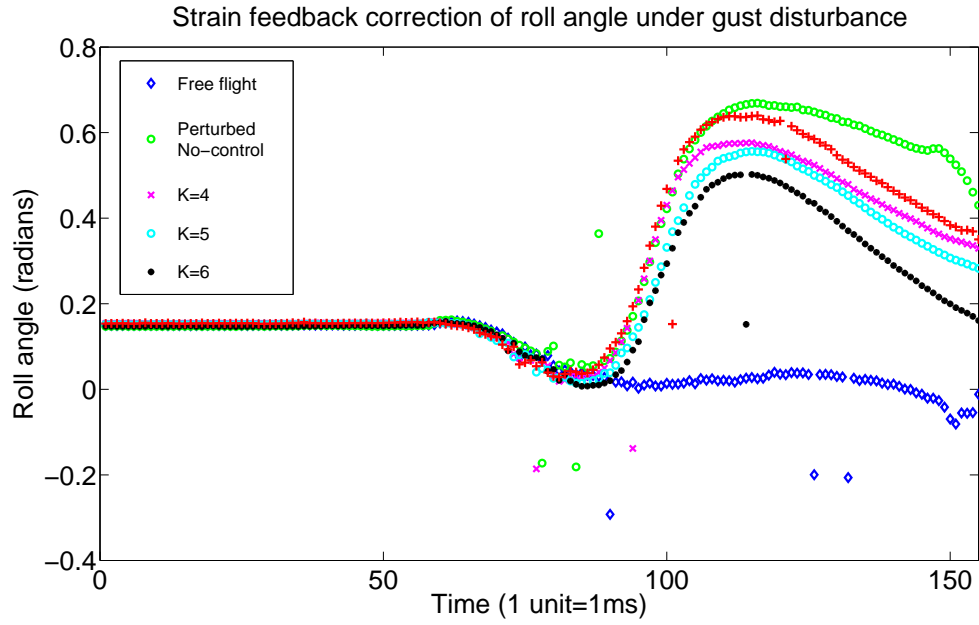


Figure 4.11: Glider roll angle and strain feedback at gains $K=3, 4, 5, 6$ and baseline flight.

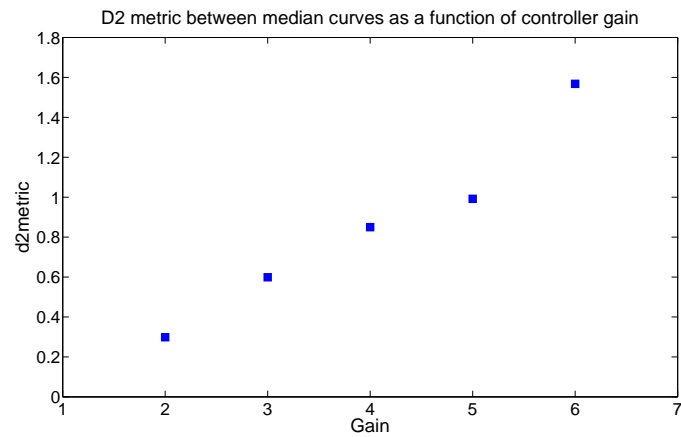


Figure 4.12: D2 metric between the perturbed data with no applied control and the one with applied strain feedback.

four tests. The first two tests included a classical controller where VICON provided the feedback and the following two tests included on board strain feedback. From Figure 4.13 we can see that the two controllers with strain feedback are more effective than the ones based on classical state feedback.

The effect of applying strain feedback can also be observed in the planar trajectory followed by the glider (Figure 4.14). This graph shows a representative curve of the x-y plane directional velocity evolution of the glider for three cases: under no gusting conditions, under gusting conditions and under gusting conditions while using strain feedback.

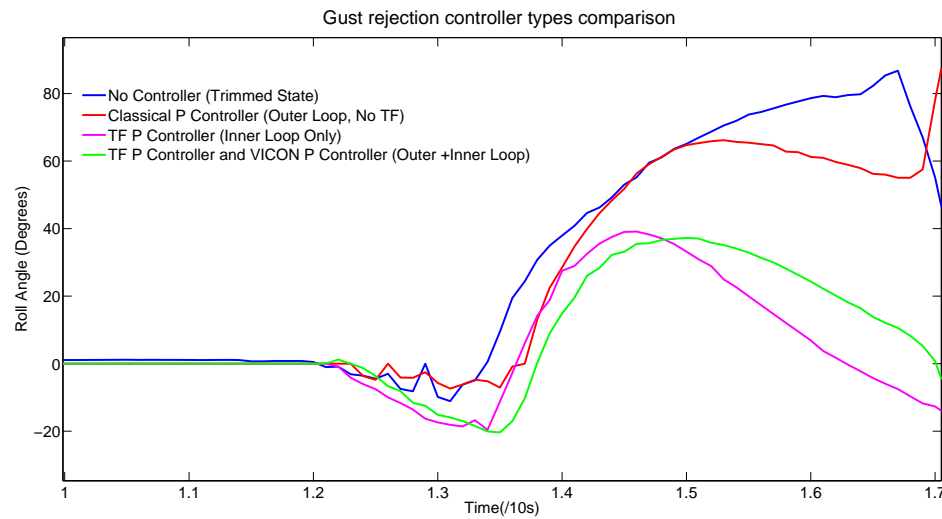


Figure 4.13: Controller comparison for roll gust rejection. TF= torque feedback, P=proportional.

Weights were attached to the fuselage of the glider. They were placed near the center of mass and in a way that they would not affect the aileron mechanism or produce any additional imbalance. The roll angle behavior was observed by testing



Figure 4.14: Glider trajectories: in free flight, under the influence of a gust and using strain feedback.

the glider without the gust disturbance, with the disturbance and with both the disturbance and strain feedback to measure controller effectiveness. The following graphs correspond to the three vehicle weights.

Each curve represents the average of ten runs of the glider. The two following graphs amount to forty glider flights (Figure 4.15). These results show that strain feedback is robust to small payload alterations. As an observation, the weights add a different roll time history behavior, which is consistent within each weight. Another trend observed is that at higher loads, the effect of the proportional controller seems to be decreasing.

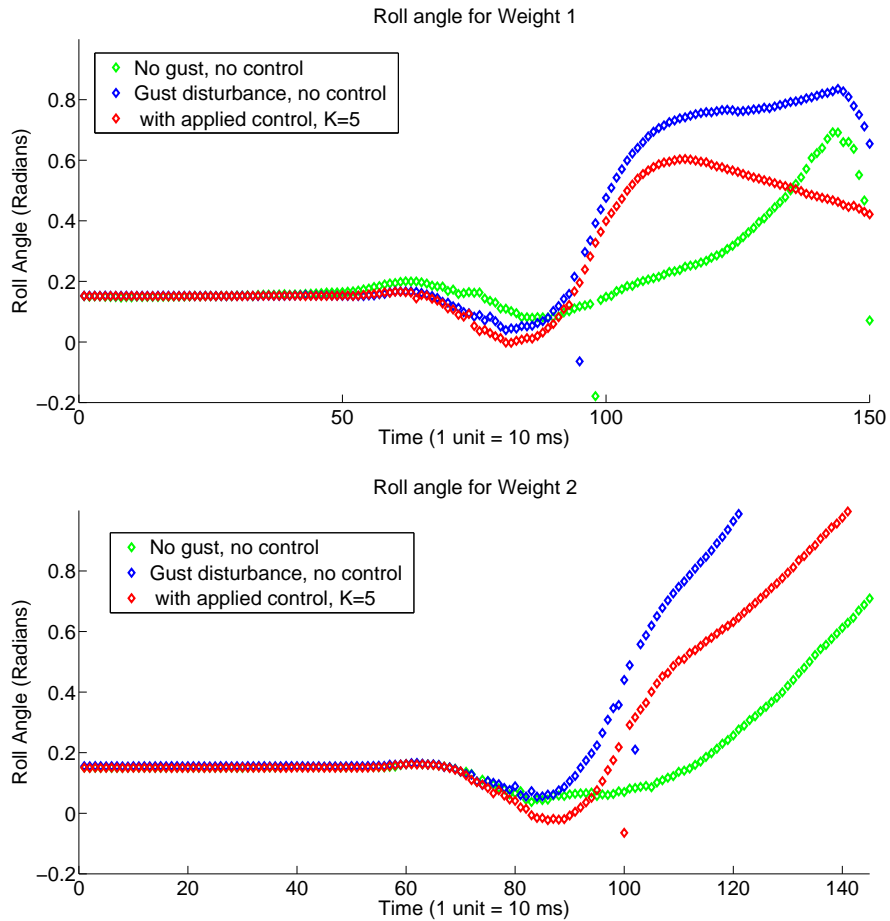


Figure 4.15: Impact of weight on glider roll angle: Roll angle for glider weight and a payload of 4.4 grams (top) and Roll angle for glider weight and a payload of 10.9 grams (bottom)

4.1.5 Aileron System Identification

4.1.6 Static Proportional Model

A static proportional model for the aileron can be generated by providing step inputs to the wing and recording the corresponding aileron deflection outputs. The glider was placed on a solid surface and two of the vicon cameras were brought up closer for increased resolution of the motion of wing and aileron relative to the fuselage. For this purpose a three rigid body marker setup was devised in order to record the corresponding angles of each (Figure 4.16).

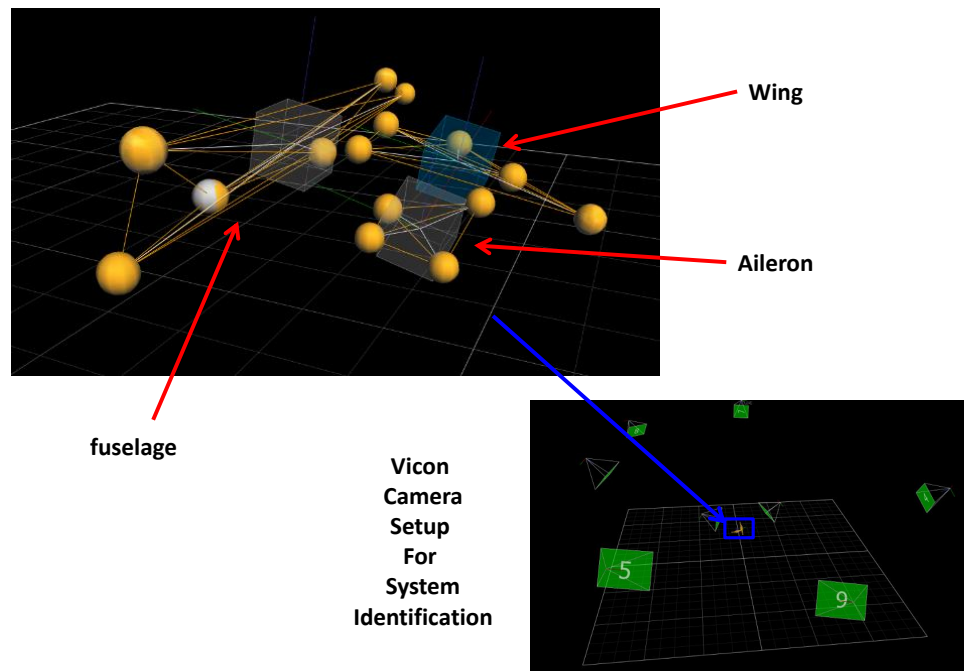


Figure 4.16: Vicon camera setup for system identification

Figure 4.17 shows the raw VICON data for a strain feedback gain of $K=1$. It depicts a series of step inputs of wing deflections and their corresponding output of aileron angular deflections. A static model was derived from these tests by taking an average of values for each step of aileron deflection and correlating it to the wing angular deflection.

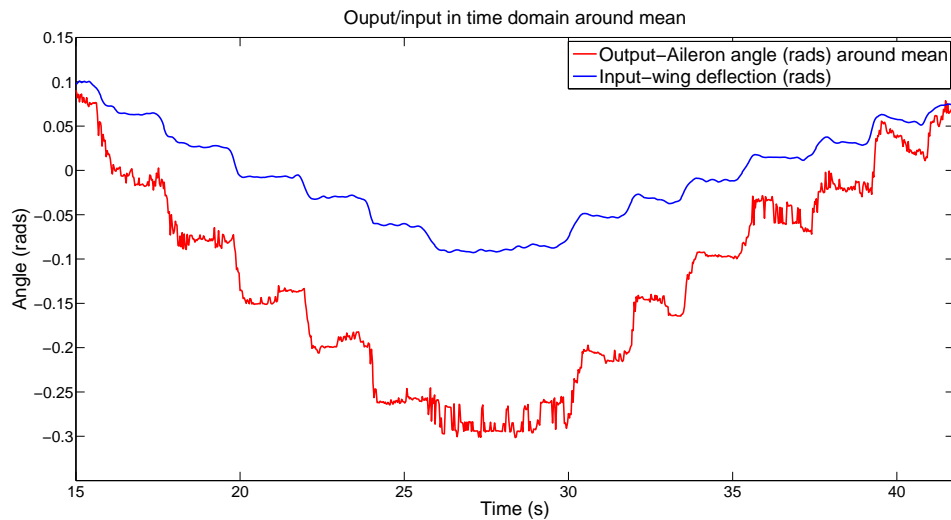


Figure 4.17: Step input of wing deflections and corresponding output of aileron deflections.

The static model is shown in Equation (4.16). It provides a direct correlation between the input wing deflection and the output aileron deflection by means of proportional constants. There is a different model for every strain feedback gain K . A gain of $K=1$ had less error produced by oscillations in the servo than those seen on higher gains such as $K = 3, 4, 5$. The model results for gains $K=1$ and $K=3$ are

shown in Table 4.4 and Table 4.2.

$$\Delta Wing = C * \Delta Ail + C_o$$

$$\Delta Ail = \frac{1}{C} \Delta Wing + D_o = D * \Delta Wing + D_o \quad (4.1)$$

$$C = 5.7429, C_o = 0.4090, D = 0.1734, D_o = -0.0711$$

A fit for the raw data and the comparison with the extracted data points is shown in Figure 4.18 for K=1. These values however depend on the method used for data reduction.

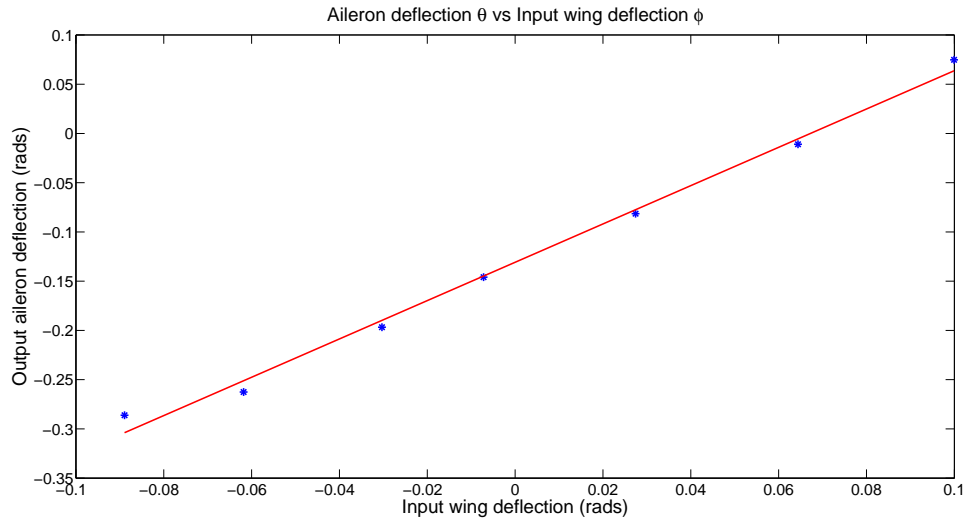


Figure 4.18: Aileron deflection vs wing deflection for K=1. Each point is the result of averaging local points that correspond to the duration of the step input.

Different methods were applied to obtain the model parameters. An average, filtered and smoothed roll angle history was used in order to obtain the four con-

starts. The filter applied is a second order Butterworth with a sampling frequency of 33 Hz which is the VICON data rate and a cut-off frequency of 10 Hz. The smoothing algorithm applied was a local regression using weighted linear least squares and a 1st degree polynomial model. A comparison of the model fit parameters of interest using different data processing methods is shown in Table 4.4 for K=1. Similar results and method comparison are shown in Table 4.2 for K=3.

Table 4.1: Comparison of linear fit with different processing methods for static model and K=1.

| Parameter | θ | θ mean | θ filtered | θ filtered mean | θ smooth | θ smooth mean |
|-----------|----------|---------------|-------------------|------------------------|-----------------|----------------------|
| C | 1.9237 | 1.9237 | 1.9231 | 1.9231 | 1.9459 | 1.9459 |
| Co | 0.1139 | -0.1291 | 0.1139 | -0.1290 | 0.1148 | -0.1308 |
| D | 0.5171 | 0.5171 | 0.5172 | 0.5172 | 0.5106 | 0.5106 |
| Do | -0.0589 | 0.0667 | -0.0589 | 0.0667 | -0.0586 | 0.0668 |

Table 4.2: Comparison of linear fit with different processing methods for static model and K=3.

| Parameter | θ | θ mean | θ filtered | θ filtered mean | θ smooth | θ smooth mean |
|-----------|----------|---------------|-------------------|------------------------|-----------------|----------------------|
| C | 5.7429 | 5.7429 | 5.7531 | 5.7531 | 5.8142 | 5.8142 |
| Co | 0.4090 | 0.2022 | 0.4093 | 0.2025 | 0.4039 | 0.1974 |
| D | 0.1734 | 0.1734 | 0.1730 | 0.1730 | 0.1690 | 0.1690 |
| Do | -0.0711 | -0.0352 | -0.0710 | -0.0352 | -0.0689 | -0.0340 |

4.1.7 Dynamic Model

A dynamic model was obtained for the input wing deflection as a function of the output aileron deflection. Inputs of different frequencies were provided to the wing in order to characterize the aileron in its frequency response. Figure 4.19 shows the aileron angle and corresponding wing deflection time histories measured in VICON.

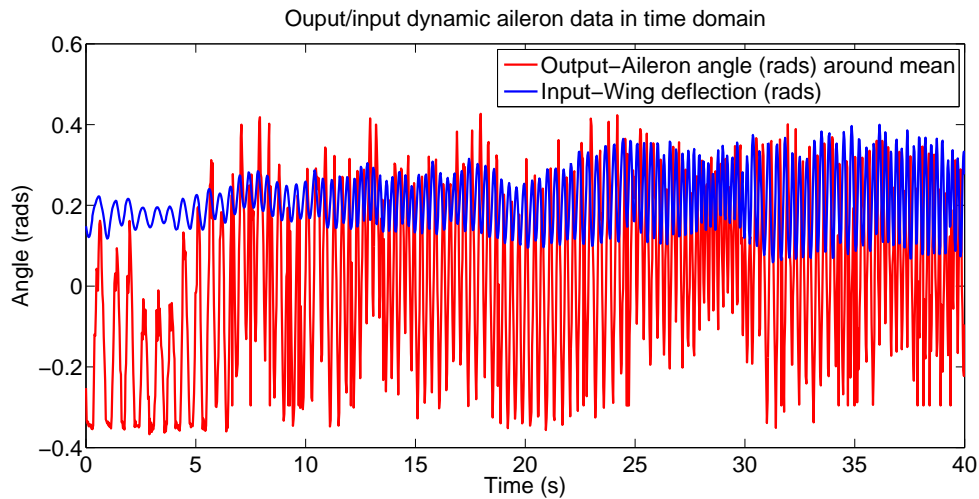


Figure 4.19: Filtered data, where aileron output has been drawn around its mean value

A system identification of the aileron dynamics was obtained using the following model which includes a delay term and one pole.

$$H(s) = \frac{K_p}{1 + T_p s} * e^{-T_d s} \quad (4.2)$$

Where $H(s)$ is the transfer function that relates wing deflection to aileron

deflection:

$$H(s) = \frac{\text{Output}}{\text{input}} = \frac{\Delta Aileron}{\Delta Wing} \quad (4.3)$$

For the filtered data, the following coefficients were obtained for the model shown in Equation (4.17)

$$Kp = 1.5564$$

$$Tp = 0.0224$$

$$Td = 0.0869 \quad (4.4)$$

$$\text{Lossfunction} = 0.01306$$

$$FPE = 0.01309$$

For completeness and to enable simulation capabilities of the current system, a state space model was generated using a Pade approximation of order n=1 for the delay term:

$$e^{-T_d s} = \frac{1 - T_p s}{1 + T_p s} \quad (4.5)$$

Thus, the following model can be used for the aileron transfer function by using the approximation in Equation (4.5) and into Equation (4.17):

$$H(s) = \frac{K_p}{1 + T_p s} * \frac{1 - T_p s}{1 + T_p s} \quad (4.6)$$

For this transfer function a time domain model can be obtained by applying an inverse Laplace transform, where the variables of interest are Φ , or the wing deflection angle and Θ , or the aileron deflection angle. The differential equation that relates the aileron and wing deflection can be written as shown in Equation (4.6).

$$K_p * \Phi(t) - \frac{T_d}{2} * \frac{d\Phi(t)}{dt} = \Theta(t) + \left(T_p - \frac{T_d}{2}\right) * \frac{d\Theta(t)}{dt} - \frac{T_d T_p}{2} * \frac{d^2\Theta}{dt^2} \quad (4.7)$$

A state space representation can also be obtained for the model with delay:

$$A = \begin{bmatrix} -\frac{2}{T_d T_p} * \left(\frac{T_d}{2} + T_p\right) & -\frac{2}{T_d T_p} \\ 1 & 0 \end{bmatrix}, B = \begin{bmatrix} 1 \\ 0 \end{bmatrix}, C = \begin{bmatrix} -\frac{K_p}{T_p} & \frac{2K_p}{T_d T_p} \end{bmatrix}, D = [0] \quad (4.8)$$

Or numerically for the last case of filtered data:

$$A = \begin{bmatrix} -2.5403 & -0.7678 \\ 1 & 0 \end{bmatrix}, B = \begin{bmatrix} 1 \\ 0 \end{bmatrix}, C = \begin{bmatrix} -0.0201 & 0.0449 \end{bmatrix}, D = [0] \quad (4.9)$$

The delay terms show that the aileron is fast enough to be used in conjunction with the fast strain based loop. The delay constant is of the same order of magnitude as the observed time required to turn the rigid body of the glider after a gust input. A faster servo could decrease the overall system reaction time if the choice of strain sensors and substrate conserve their high bandwidth.

The time scale of the structural response is much less than that of the rigid

body response. This time scale was measured using high speed videos of the glider passing over the gust. The fuselage starts to turn roughly 0.03 seconds after the gust hits the left wing and it levels out completely at 0.06 seconds. Thus, demonstrating the advantage of using structural feedback as a way to achieve reflexive control. This enables the implementation of a faster inner loop configuration. This loop can be implemented before the plant dynamics, in a way that it absorbs unknown inputs and disturbances. An inner loop force adaptive feedback approach.

Strain force feedback is demonstrated using a small UAV under a sharp gust condition. The vehicle was instrumented with strain gauges which were sensitive to vertical gust disturbances. The sensor output was used in a fast inner loop for reflexive reaction to gusts. Linear strain measurement weightings or wide field integrated strain can provide force state estimations which can be used in these fast inner loops. This feedback is much more effective at higher proportional gains in the case of a strain/force proportional controller. Less deviation in the roll trajectories was observed by means of the D2 metric as the gain was increased. Structural feedback is also robust to small payload additions, affecting the roll rate but conserving the fast reaction characteristics. Structural feedback also demonstrated to be more effective than classical rigid body dynamics controllers. The classical controllers were based on VICON state feedback of the rigid body states, which would be equivalent to on board IMU's attached to the core of the fuselage. A system identification of the aileron dynamics showed that the time constant is of the same order of magnitude as the time that it takes for the disturbance input to propagate to the rigid body. A faster servo would probably show a faster response to correct for disturbances, albeit

it also depends on the magnitude of the disturbance. Aileron dynamics were fast enough for the employed combination of gust speed and roll correction. The aileron was sufficiently fast to respond to the structural feedback inner loop. Structural feedback using wide field integrated constants is a promising mechanism for UAV's to reject gust disturbances as they allow a faster reaction than conventional control mechanisms.

4.2 Quadrotor experiments

A similar bio-inspired approach to strain sensing-based gust rejection can be applied to quadrotor vehicles. In this case, the sensors and the underlying structure, or quadrotor arm, need to be designed for such purpose. In quadrotors there are added challenges such as additional and varying motor vibration as well as aerodynamic phenomena present during flight and as a consequence of the rotor induced aerodynamics. A quad strain sensing arm was developed to be used in gust mitigation, as shown in Figure 4.20.

In the case of strain sensing for a quadrotor, design and characterization of substrate/sensor pairs is required in order to obtain optimal measurements. This refers to the best locations, surface dimensions and geometries that can be used for installation of strain gauges. A natural selection of these locations is found in nature, these locations correspond to areas of high density of surface stresses or areas of higher stimuli inputs. Given the small time scales of the structural responses as compared to rigid body responses, a structural feedback scheme can be proposed

to reject gust disturbances. Moderately flexible quad arms are needed while also preserving the control authority of the motors. This flexibility allows for encoding of the forces and moments being exerted on the quad arms in the form of strains and stresses.

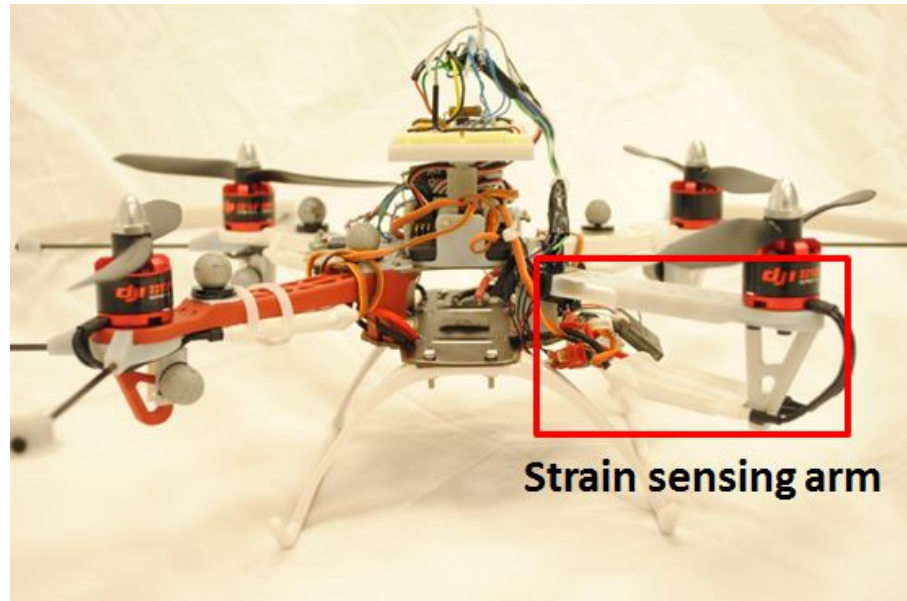


Figure 4.20: DJI Flamewheel quadrotor with strain sensing arm

The forces and moments anticipate and precede the rigid body motion of the quadrotor. Therefore, the mapping between forces and strains enables the implementation of a fast inner loop which can be used for disturbance rejection. The resulting strain measurements are functions of the position and orientation of the sensors, the structural modes of the airframe, and the forces and torques, which may be externally applied or commanded. Assuming the structural loads are primarily on the quadrotor arms, a network of strain sensors can be used to anticipate the quadrotor rigid body rotations and displacements. In this section, a heave perturbation to

the quadrotor is encoded in a set of strain gauges. The strain information associated to encoded forces is used in a fast inner loop which corrects for the disturbance before it reaches the quadrotor rigid motion states. That is, it allows for a correction of the disturbance before it propagates to lower order states. Strain sensing has not been explored for quadrotor UAVs, partially due to size, weight and power constraints but also due to the complex structural effects it endures during flight. The quadrotor arms are subjected to a number of forces, both aerodynamic [104] and inherently mechanic. The four motors introduce not only mechanical vibrations but also generate turbulent air patterns [104] which are constantly hitting the quadrotor arms. The effects also vary depending on whether the quadrotor is close to the ground, near a wall, or if it has forward velocity. Other effects inherent to rotor motion such as feathering, flapping and lead-lag can also affect the strain time history. Atmospheric disturbances will also introduce additional force components which will also be seen in the strain measurements.

4.2.1 Strain Sensing

Structural deformations are gradients of three dimensional displacements. For linear regimes shear deformations can be neglected allowing for a simpler formulation. A quadrotor arm can be thought of as an Euler Bernoulli beam type of structure cantilevered at the center plate. The fixed condition however is not entirely met due to the flexible nature of the center plate, designed mainly to robustly host electronics and batteries. As would be expected, the locations of higher strains

for an isolated beam are close to the root, or the clamped end. These higher strain regions are mainly due to the nature of the predominant influence of thrust vectors produced by the rotors, which are typically perpendicular to the plane formed by the quadrotor arms. A one dimensional beam formulation can approximately model the strains produced by the thrust vector forces. In a quasi-static formulation, the displacement w at any location x along the arm spanwise direction produced by applied forces P is described by:

$$\frac{d^2}{dx^2}(EI \frac{d^2w}{dx^2}) = P(x) \quad (4.10)$$

And the bending moment is given by:

$$\frac{d^2}{dx^2}(M(x)) = P(x) \quad (4.11)$$

This uniaxial approximation is made for simplicity, as the actual strains are produced in all directions within the material. The larger strains however are along this axial or spanwise direction. This formulation also becomes complex when considering beams with varying cross-sections and stiffenesses. The neutral axis becomes a function of the axial coordinate and a piecewise formulation is then more appropriate.

In particular, for a beam of uniform cross-section and a force applied at a location x on the quad arm of length L , the force and strain are related to each other by means of

$$\varepsilon(x) = \frac{z_l}{EI} * P(x) \quad (4.12)$$

where the force is a function of lengthwise location of the force and z_l refers to the distance from the neutral axis of the surface at which the strain is being recorded. If the strain is to be evaluated at a location L_0 from the fixed end of the arm, then the strain at this point becomes

$$\varepsilon(L_0) = \frac{z_l}{EI} * P * (L_0 - L) \quad (4.13)$$

where P is the magnitude of the applied force. Similarly, the associated bending moment at the location L_0 can be calculated as

$$M(L_0) = \frac{EI}{z_l} * \varepsilon(L_0) \quad (4.14)$$

Biased values of strain are present due to different factors which include: weight, flight maneuvers or certain flight conditions. These however can be subtracted so that the measurement vector, or vector of measured strains can be calculated as in Equation (3.1) and Equation (3.2), as presented in [6]:

$$\mathbf{y}_\varepsilon = C_\varepsilon \mathbf{x}_\varepsilon \quad (4.15)$$

The dimension of the output y is related to the number of independent measurements of strain. The absolute state vector x_ε is the force and moment associated to all the forces and moments being exerted on the quadrotor at any given time:

$$\mathbf{x}_{\varepsilon T} \equiv \begin{bmatrix} P_x & M_x \end{bmatrix}^T \equiv \begin{bmatrix} P(L_0) & M(L_0) \end{bmatrix}^T \quad (4.16)$$

If we apply the bias, then the state vector directly correlates to the heave disturbance, for this particular implementation.

$$\mathbf{x}_{\varepsilon} \equiv \begin{bmatrix} \Delta P & \Delta M \end{bmatrix}^T \quad (4.17)$$

and the output matrix C_{ε} is a function of the location L_0 of the strain gauges:

$$C_{\varepsilon} = \begin{bmatrix} \frac{EI}{z_l} \frac{1}{L_0 - L} \\ \frac{EI}{z_l} \end{bmatrix} \quad (4.18)$$

Such that the states related to the heave disturbance can be estimated as:

$$\hat{\mathbf{x}}_{\varepsilon} = M \mathbf{y}_{\varepsilon} = (C_{\varepsilon}^T C_{\varepsilon})^{-1} C_{\varepsilon}^T \mathbf{y}_{\varepsilon} \quad (4.19)$$

or equivalently:

$$\begin{bmatrix} \hat{\Delta P} \\ \hat{\Delta M} \end{bmatrix} = C_{\varepsilon} \hat{\mathbf{x}}_{\varepsilon}, \quad (4.20)$$

These states can be used in force feedback to attenuate the effect of distur-

bances and return the system to the unperturbed states. Distributing sensors on more locations along the quadrotor arm may yield better estimations of the states associated with the disturbance.

4.2.2 Sensor design for quadrotor arm

Sensor design and associated substrate optimization need to be considered in order to achieve higher sensitivities to the targeted disturbances. In addition to this, the overall bending stiffness of the quadrotor needs to be kept close to the one of the original DJI quadrotor arm. This trade of between strain sensitivity and stiffness was observed during design iterations. First, the possible loads on the quadrotor arm were determined. This amounts to the loads due to gravity and the loads due to flight maneuvering. Five maneuver tests, ranging from sharp turning to normal hover, were recorded in VICON motion capture system. Analysis of the rigid body states showed that the forces do not exceed approximately 0.2 N per arm. This force range was utilized in the design of the quadrotor arms to maximize load sensitivity.

Characteristics of the DJI quadrotor arm are presented in table 4.3. The bending stiffness characteristics were measured using an MTS machine and a three point bending setup. In this procedure the quadrotor arm was placed evenly on top of two supports. The loading point is found half way between the two supports. Force and displacement data are recorded by means of a load cell and a displacement gauge, respectively. The test was carried in a destructive way such that the yield stress will also be measured. In the linear region of the graph, a direct relationship

is found between the force and displacement and this value is proportional to the bending stiffness if the cross-section characteristics are known. It was interesting to observe that by design, the lateral bending stiffness of the quadrotor is larger than the longitudinal bending stiffness.

Table 4.3: Comparison of quad arm characteristics of Original DJI arm and prototyped arm.

| Parameter | Original DJI Arm | RP Quad Arm |
|------------------------|------------------------|--|
| Composition | Thermoplastic | Photopolymer |
| Young's Modulus | 15000 MPa | 2000-3000 MPa |
| Tensile strength | 160 MPa | 50-65 MPa |
| Density | 1370 kg/m ³ | 1170 kg/m ³ |
| Bending Stiffness (EI) | 1.61 Nm | 2.48 Nm (solid), 1.43 Nm (I-beam), 1.32 Nm (hollow) |

Once the bending stiffness was measured, quadrotor arms of different cross sections were built using rapid prototyping (Figure 4.23). The material used was a photopolymer with medium stiffness properties. Static properties of the rapid prototyped arm and sensors were obtained by means of a tip loading and unloading set of tests at the Rotorcraft Center [105]. The setup is shown in Figure ???. Hysteresis was observed in the measurements. The creep behavior of the photopolymer of the RPM material was also observed. The creep scale however was larger than the expected time scales for our experiments. Results from these tests are found in Figure 4.22.

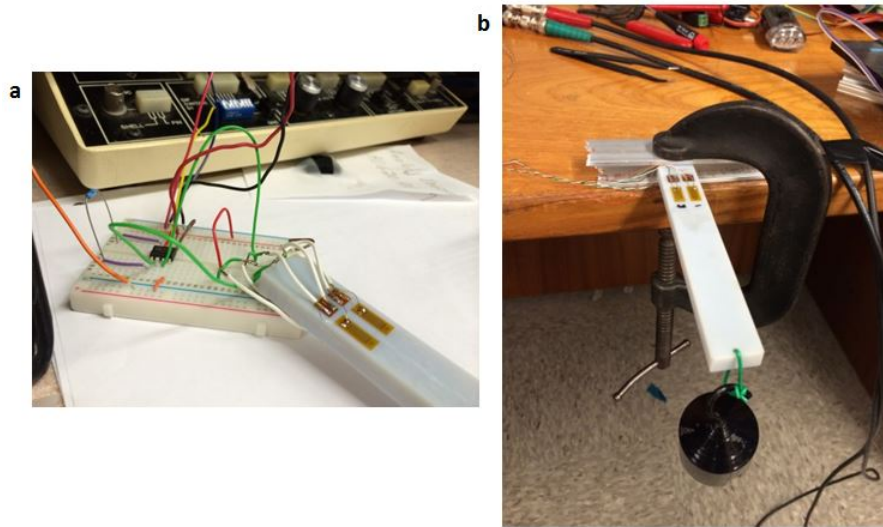


Figure 4.21: (a) Quad arm with amplifier circuit, (b) Static testing of RPM quadrotor arm

A series of tests with different cross-sections were performed until a good candidate was found for maintaining good weight to strength ratio. Initially a solid cross-section was used, this however did not yield good sensor sensitivity to loading. Therefore a second part of the substrate optimization encompassed a local cross-section optimization.

This local optimization was carried by means of finite element simulations of the rapid prototyping material with different geometrical parameters. In order to increase the strain output a local increase in strain needed to be generated without reaching the material yield stress. This was achieved by matching high strain levels and not so large stress surface distributions. It was observed that the best characteristics were achieved by using an almost elliptical hollow section. Three of the cross section designs are shown in figure 4.24. The best sensor locations were shown

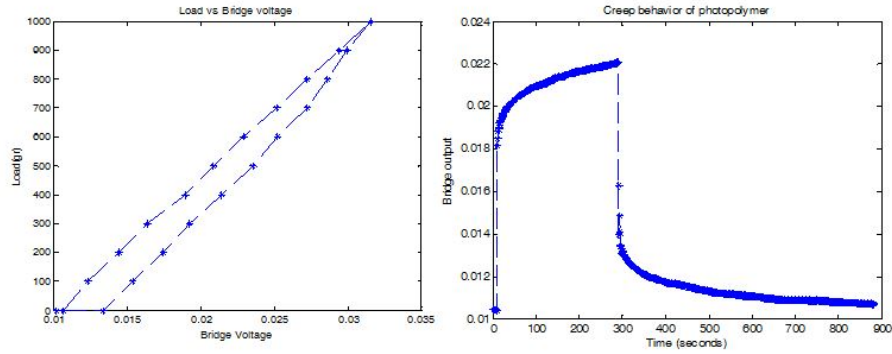


Figure 4.22: (a)Hysteresis at a loading and unloading cycle, (b) Creep behavior of RPM quad arm

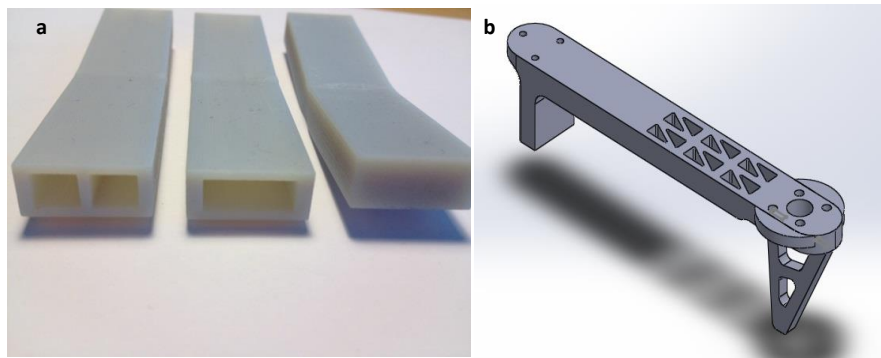


Figure 4.23: (a) Photopolymer prototyped arm sections for MTS testing and (b) CAD model of the quadrotor arm without optimized cross-section

to remain close to the highest curvature point of the hollow section near the root.

After determining the proper locations for the sensors a proper grid size and backing material were chosen. The sensors used in this implementation were Omega 1000 Ohms dual strain gauges. These sensors are typical foil gauges with a gauge factor of 2.02 and a tolerance of 0.3 %. These linear strain gauges were implemented in a wheatstone bridge configuration in tension/compression pairs, and bonded to the polymer substrate at the optimal locations. A surface treatment was necessary to match the foil backing material to the photopolymer surface. The photopolymer

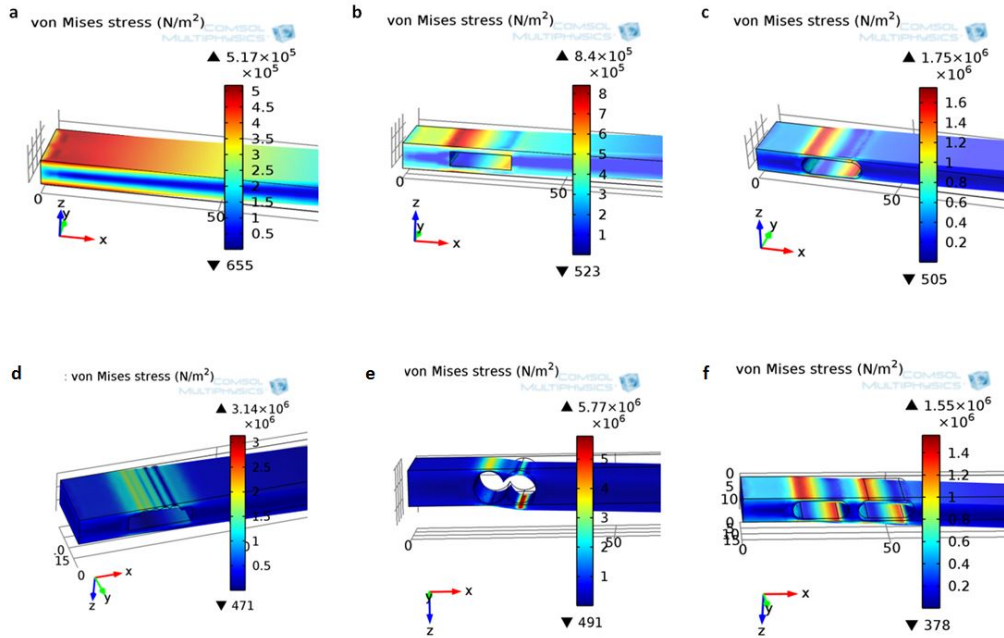


Figure 4.24: Finite element simulations of stress under maximum expected quadrotor load: (a) Solid cross section, (b) Square hollow cross section and (c) Smoothed square hollow section, (d) striated cross section, (e) load cell cross section, (f) bi-rectangular cross section

was susceptible to creep typical of plastics but was accounted for by using updated measurements. The bridge implementation is shown in figure 4.25. The bridge output was amplified at a biased voltage so that the measured values of strain can oscillate around a nominal value. Ground effects were observed in the strain measurements as well as high altitude effects, where the rotor downwash had an influence over the measurements.

It is worth mentioning that in this implementation there was a need to have landing gear to protect the prototyped arm from undergoing sharp and concentrated loads at the optimized sensor locations. The photopolymer loses strength over

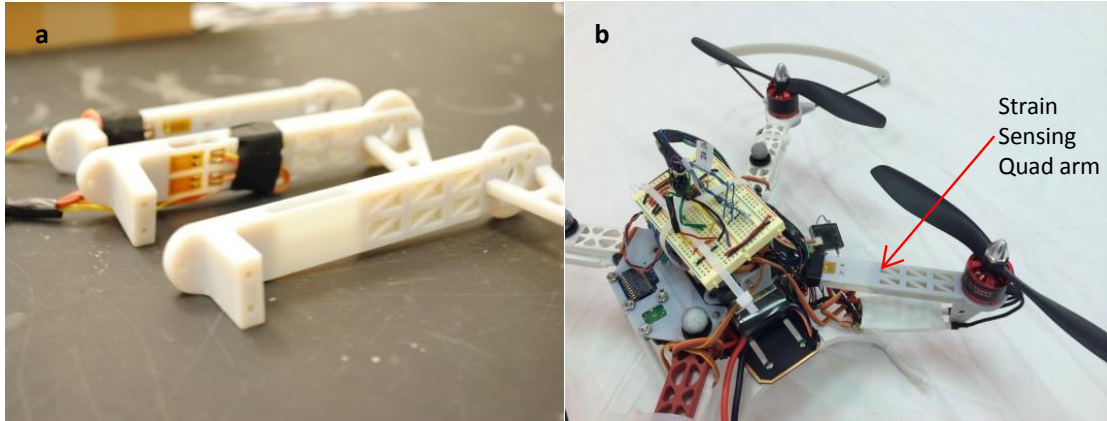


Figure 4.25: Strain sensing implementation: (a) Quad arms with different cross sections and (b) Quad arm vehicle implementation

time, increasing sensor output but also making the prototype prone to breakage. Therefore other material substrates can be considered to avoid these challenges, i.e. carbon fiber, fiber glass, aluminum shells, etc...

4.2.3 Heave disturbance rejection

A robust control scheme is proposed in Figure 4.26. This controller was used by [6] to demonstrate disturbance rejection with accelerometer data in correcting roll perturbations. In this proposed scheme, the disturbance gets to be mitigated way before it reaches the plant.

This feedback improves tracking of requested controls in the presence of disturbances by regulating errors between desired torques and actual torques. Thus the system is simultaneously capable of rejecting external disturbances, such as gusts, and internal disturbances, such as actuator variations.

An artificial heave gust was implemented as a collective motor perturbation,

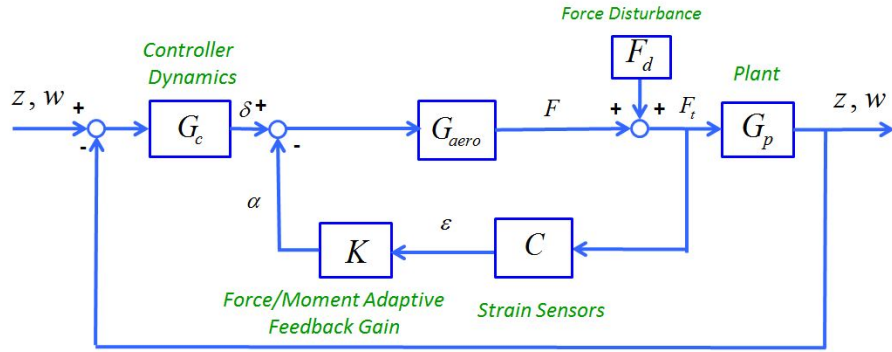


Figure 4.26: Fast inner loop for disturbance rejection

inducing the vehicle to lose altitude as might be experienced in a downdraft. An L1 norm was calculated for a sample of the perturbation intervals. The corresponding strain output and the nominal average strain were used for this calculation, which is shown in Figure 4.27.

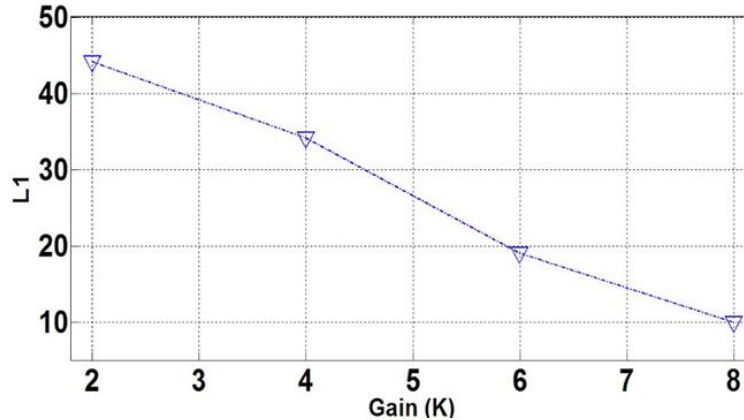


Figure 4.27: Strain feedback performance metric

A control augmentation feedback control from the strain gauge network affixed to the vehicle arm was implemented to return the vehicle to a previous strain state corresponding to hover and thereby reject the disturbance. The improvement in

maintaining altitude can also be observed from the time histories for the altitude and vertical velocity states for increasing feedback gains (Figure 4.28).

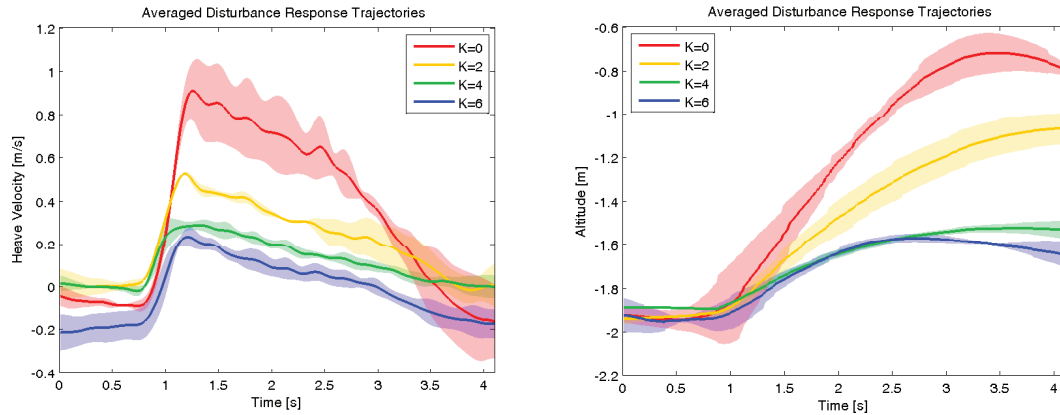


Figure 4.28: Heave Velocity and Altitude Time History for Impulse Heave Disturbance for Varying Feedback Gain from Strain Gauge Sensing

Using novel sensor implementations of strain and acceleration measurements, estimates of the forces and torques applied to a quadrotor sUAS were estimated. Furthermore, these estimates were provided through static linear combination of the raw measurements, yielding a computationally simple and analog implementable estimation architecture. The response of the systems was characterized in the presence of force and torque stimuli. Feedback from these estimates was used to mitigate the effect of motor perturbations in the roll and heave degrees of freedom. Two characteristics were observed from these feedback implementations. Undesirable exogenous disturbances, motor perturbations in this case, are attenuated in the output state of the vehicle. However, desired actuation forces are also attenuated, resulting in a slower reference tracking response. Future implementations of this feedback con-

control will account for this undesired attenuation by removing contributions from the intended actuator forces and torques in the control adaptation.

4.3 Wing structural properties testing

The carbon fiber wing described in Section (3.6.1.1) was manufactured by [102] with the Aurora PWings design [7], which follows an AG-35 airfoil and has the geometric characteristics shown in Table 3.5. The wing entails a foam core, no spars or ribs, and a layup of carbon fiber and fiber glass.

The wing was tested in its static structural properties. Bending and torsion tests yielded stiffness parameters for comparison with the finite element model. The Vicon tests for structural wing property measurements were conducted at the Rotorcraft center of the UMD, College Park [105]. The static load bending and torsion tests were conducted at Aerolabs, UMD, College Park [106].

4.3.1 Experimental setup

In order to measure the bending stiffness of the carbon layup wing, two main setups were used to measure vertical deflection and angular torsion. For bending, static tip deflection and section wise vicon deflections were used. For torsion, two methods were used, the mirror method and the angular displacement method.

The first setup consists of a height gage and a number of loads, as shown in Figure 4.29. The loads are placed at the wingtip and the vertical tip displacement is measured with the height gage. The maximum bending load was close to 1 kg,

therefore the weights used were only up to about 700 gr. It is worth mentioning that these measurements were subject to errors stemming from clamping method, loading speed, loading intervals, material creep from the wing and reading errors. The reading error is less than 5 % and the other errors can be considered systematic.

The second setup is shown in Figure 4.30 and it consists of a Vicon system, reflective markers and a number of loads. For the vicon marker placement the wing had to be divided into equal length spanwise sections. Three markers were placed at each spanwise location. The camera setup for the vicon test consists of four cameras that are rather close to the wing as the volume needed to be minimized. The surface of the wing had to be covered in non-reflective material, as the epoxy finish of the wing induced errors in the marker position estimation of the Vicon setup Figure 4.31.

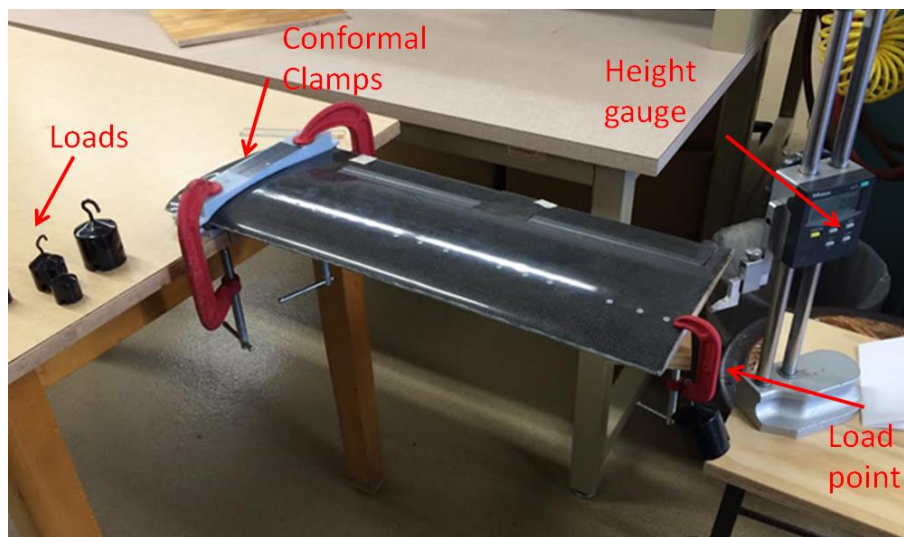


Figure 4.29: Height gauge setup for calculation of bending stiffness

Both setups used reinforced RPM conformal clamps. These are clamps which

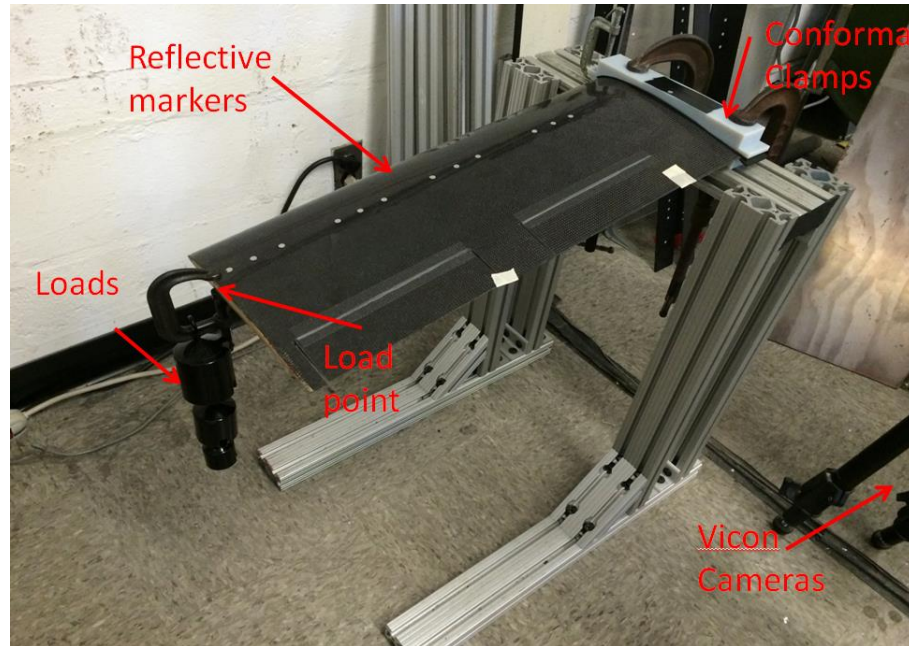


Figure 4.30: VICON setup for calculation of bending stiffness

have the exact airfoil shape to distribute the load evenly and provide appropriate boundary conditions. The conformal clamps were placed at the root with aluminum reinforcements, as the RPM material wasn't stable enough for the loads applied and produced artificially soft modulus results due to slippage. After the reinforcements were included, results were much better. Another conformal clamp with reinforcements was placed at the tip of the wing for torsion tests. The top reinforcement of the tip conformal clamp was much longer to be able to produce a long moment arm and therefore larger torsion. These clamps are shown in Figure 4.31. The angle measurements for the torsion tests were measured with an electronic protractor which was placed at the wingtip.

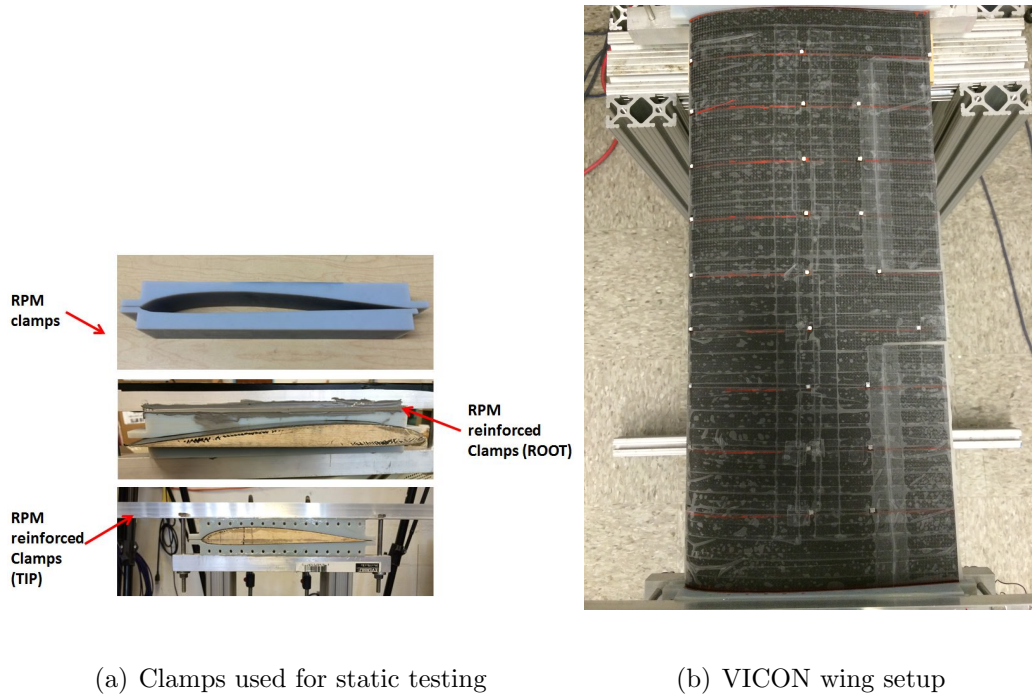


Figure 4.31: Clamps used for static testing and Vicon wing setup

4.3.2 Bending and torsion properties

The testing procedure for the first setup consisted of recording the vertical displacement of the tip of the airfoil under increasing load. For this purpose, the following formula was applied and a least squares estimation of the slope was generated to calculate EI. The results can be observed from Figure 4.32.

After averaging the estimated least squares slopes, the bending stiffness EI for each can be calculated using Equation (4.21).

$$EI = \frac{PL^3}{3w_t} \quad (4.21)$$

Where P is the applied load, L is the effective length of the cantilever and w_t

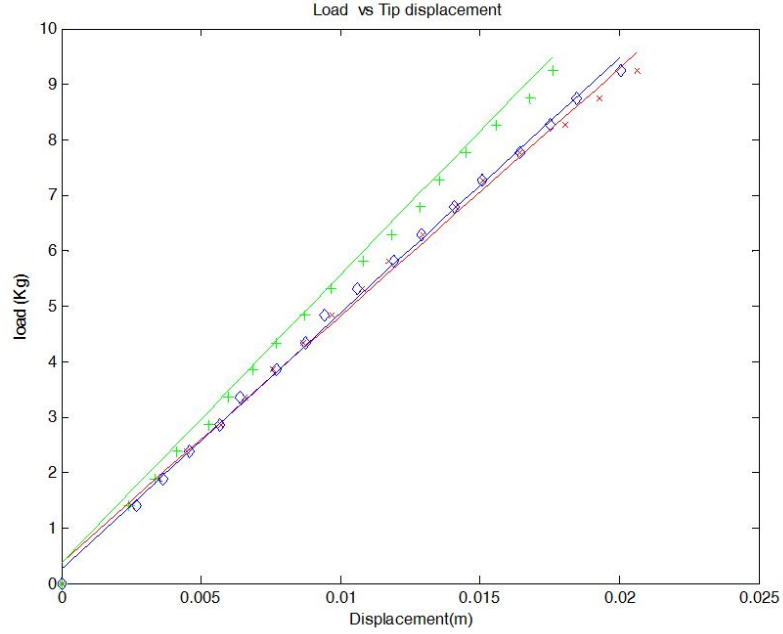


Figure 4.32: Load vs. tip displacement curves for estimation of EI with height gauge

is the tip deflection. The average calculated bending stiffness from the three curves is then calculated to be $EI = 25.4949Nm^2$.

The second setup entails a similar test in that loads are placed at the tip of the wing and the deflection evaluated. The deflection is now measured using Vicon nexus for deflection tracking [105]. Four sets of three markers are placed on the quarter chord along the length of the wing. These three points are used in a Lagrange polynomial to calculate the corresponding deflection. The bending stiffness is now calculated using position on the wing length and deflection slope. This can be calculated using Equation (4.22) which entails the deflection slope of the wing.

$$w' = \frac{P}{EI} * \left(Lx - \frac{x^2}{2} \right) \quad (4.22)$$

By using this formula on every three markers, we can get an approximation of the stiffness at the four different sections that the markers span. The thirteen marker positions are depicted in Figure 4.33. Each deflection value is an average of deflections taken by vicon at a 60Hz rate. The last three sets of markers had a lot of noise. This could mean that these last markers which were closer to the wing tip were probably not placed smoothly over the surface of the wing.

| Marker position | 188gr deflection | 388gr deflection | 688gr deflection | 988gr deflection | EI average |
|-----------------|------------------|------------------|------------------|------------------|------------|
| 0.145588 | 0.075921 | 0.108652 | 0.1605945 | 0.2541335 | ref. |
| 119.7357 | 0.569806 | 1.211286 | 2.2139625 | -3.414636 | 25.29337 |
| 146.9644 | 0.718225 | 1.499112 | -2.734751 | -4.204731 | |
| 176.3668 | 0.884063 | 1.830384 | 3.3374685 | -5.144669 | |
| 261.2144 | 1.404108 | 2.894021 | -5.295747 | -8.089334 | 34.2336 |
| 292.0368 | 1.605125 | 3.338317 | 6.1035945 | -9.316115 | |
| 325.1994 | 1.810825 | 3.802784 | -6.941435 | 10.612358 | |
| 389.3086 | 2.305745 | 4.788209 | -8.748306 | 13.294703 | 33.80149 |
| 419.5094 | 2.525592 | 5.148691 | 9.5778115 | 14.596308 | |
| 446.9116 | 2.756851 | 5.825108 | 10.623665 | 15.889816 | |
| 511.1241 | -3.26173 | 6.909894 | 12.449129 | 18.821159 | 43.778 |
| 542.0757 | 3.485234 | 7.321774 | 13.348956 | 20.206466 | |
| 567.7505 | 3.517541 | 8.018125 | 4.398712 | 21.683537 | |

Figure 4.33: VICON processed data

Taking into consideration the first three averaged bending stiffness values we can calculate an average of these, yielding $EI = 31.10949Nm^2$.

This value is very close to the one measured by the height gauge. The accuracy of the height gage might be better than the vicon measurements in that the markers used were not the optimal ones at that time. More accurate results can be obtained with smaller markers. The other possible sources of error besides marker visibility

are numerical approximations and small deflections near the root of the wing. This method has been vetted by comparing known material properties and actual results [105], therefore the approximations are reasonable. Given the aspect ratio of the wing, there might also be some error associated to the assumptions of the beam equations.

Alternatively one can construct a CLPT model to try and estimate the bending stiffness. Using a symmetric layup of perfectly bonded layers one can calculate reduced stiffness matrices based on the assumption of planar stress. These reduced stiffness matrices can be calculated for each layer, considering their orientation with respect to the axial or longitudinal axis. The symmetric layering assumption can be applied to chord wise sections of the airfoil, or panels. We can identify an effective set of geometric properties that produce the required bending stiffness. For an orthotropic laminate the reduced stiffness matrices in the material axes are shown in Equation (4.23).

$$Q_{mat} = \begin{pmatrix} \frac{E_1}{1-\nu_{12}\nu_{21}} & \frac{\nu_{12}E_1}{1-\nu_{12}\nu_{21}} & 0 \\ \frac{\nu_{12}E_1}{1-\nu_{12}\nu_{21}} & \frac{E_2}{1-\nu_{12}\nu_{21}} & 0 \\ 0 & 0 & G_{12} \end{pmatrix} \quad (4.23)$$

The following layup was used in the calculation of the rotated stiffness matrices: $Layup = [-90, +90, +45, -45, 0, 0, -45, +45, +90, -90]$ and the rotation matrix

used is shown in Equation (4.24).

$$T = \begin{pmatrix} \cos^2\theta & \sin^2\theta & -2\cos\theta\sin\theta \\ \sin^2\theta & \cos^2\theta & 2\cos\theta\sin\theta \\ \cos\theta\sin\theta & -\cos\theta\sin\theta & \cos^2\theta - \sin^2\theta \end{pmatrix} \quad (4.24)$$

Using the available information on the layer thickness of each component material, as well as the material properties specified for unidirectional fibers, placed at the corresponding angles. Once these stiffness matrices have been constructed, one can evaluate the generalized stiffness A, cross-coupling B and bending stiffness D matrices. The bending stiffness can be calculated from Equation (4.25).

$$EI = c * D(1,1) \quad (4.25)$$

Where c is the airfoil chord and $D(1,1)$ is the first entry of the resulting bending stiffness matrix. The calculated bending stiffness for the airfoil is then $EI = 25.4949Nm^2$.

This value is calculated based on a number of assumptions, however, the layup and the resultant effective thickness provides a calculation which is close to the measured results. Sources of error in this calculation are volume fractions of fibers to epoxy, possible out of plane orthotropic properties and airfoil shape approximate panel partitions. A better analytic calculation can be obtained from other methods.

4.4 Wind tunnel tests

The wing section described in Section (3.6.1.1) was instrumented with strain gauges and tested at the REEF wind tunnel of the University of Florida [107].

The sensor locations chosen were according to Section (3.6) for sensing vertical gusts. The wing sensor placement considerations were mainly for bending, however with the goal of extracting forces and moments by means of system identification tests done a priori.

4.4.1 Experimental setup

Fifteen locations were chosen for installing full bridges. The sensitivity of a full bridge is the best as compared to half a bridge or quarter bridge. Each Wheatstone bridge was set in bending configuration, that is a pair in tension and a pair in compression. The sensor network was amplified using a 5V voltage source and a National Instruments USB DAQ mass terminal was used to acquire the signals. The sensors had a nominal resistance of 350 Ohms each and have a temperature range of -100F to 350. The gauge factor as typical of constantan foil gauges on polyimide film was of 2.160. The wiring consisted of small gauge wire with low -weight cable jackets. A greater resolution is found by increasing the supply voltage to 10V, however increasing the risk for overheating and gauge delamination.

The wing had to be prepared for sensor installation by means of surfactants and abrasive removal of the superficial epoxy layer. Better adhesion and bond endurance is achieved when the gauges are bonded to textured surfaces. Soldering

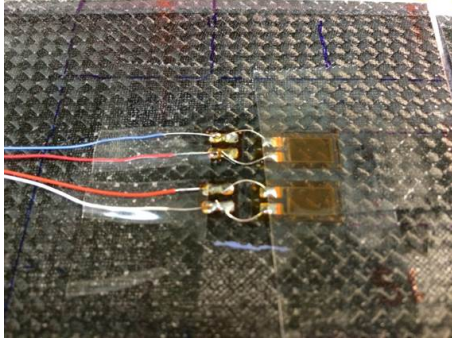


Figure 4.34: Strain gauge top half of full bridge

pads were used to add stability to the installations and prevent detachment of the gauges. The cables were carefully placed to try and avoid tripping the boundary layer. Although this may not be entirely the case, the streamlined configuration used is much better than random orientation of the connections. Servo motors were installed in the two ailerons.

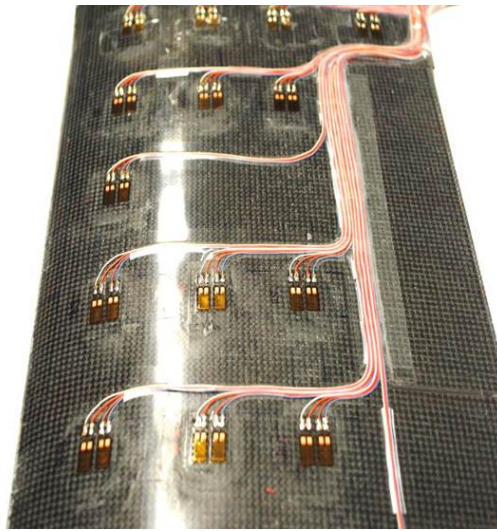
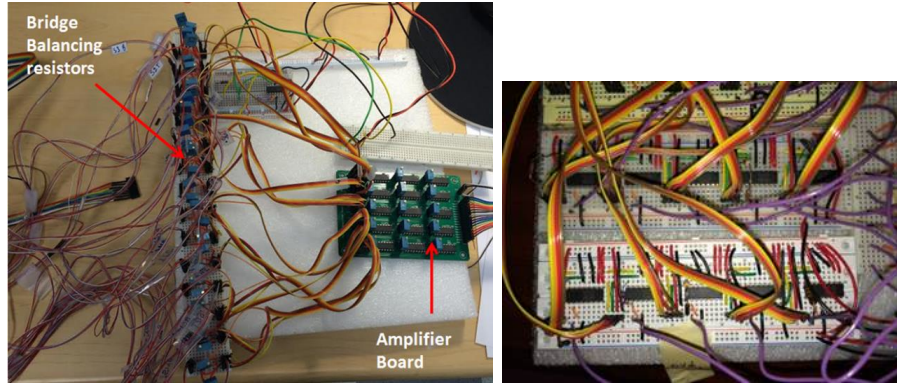


Figure 4.35: Wing with sensor network

An amplification PCB board was designed to reduce the cable volume Fig-



(a) PCB setup

(b) Prototype board setup

Figure 4.36: Strain gauge amplification electronics

ure 4.36. Initial tests however were performed with the prototyped amplification board. The hardware preparation consisted of tuning each sensor bridge with two trimming resistors. These produced a desired bridge output in the available voltage output range so that it would be evenly split for positive and negative directions of wing bending. Each bridge output was then connected to the PCB board with gain resistors which were tuned to yield a gain of approximately 100 times the incoming signals.

The data was then collected in labview for the open loop tests as well as the closed loop tests. For the closed loop tests the weighting matrices were coded in fast loops achieved with a compromise of sampling rate and samples sent to the ailerons. After tuning this loop the latency was minimized, albeit non comparable to an on-board processor with hard coded algorithms. Therefore the bandwidth seen with the labview DAQ setup for data sensor acquisition and actuator signal generation can be improved. For the closed loop both actuators were used simultaneously. The

tests entailed steady state as well as turbulence tests by means of an ATG or active turbulence grid, as developed by [108].

The wind tunnel is a low speed wind tunnel of open section type. Velocities can go up to 20 m/s. The overall length of the wind tunnel is approximately 45 feet while the inlet is a 10 by 10 ft area. The enclosure can hold large aerodynamic models. The commanded throttle is controlled via an analog voltage 0-10V and the airspeed inside the tunnel is monitored by a pitot probe.

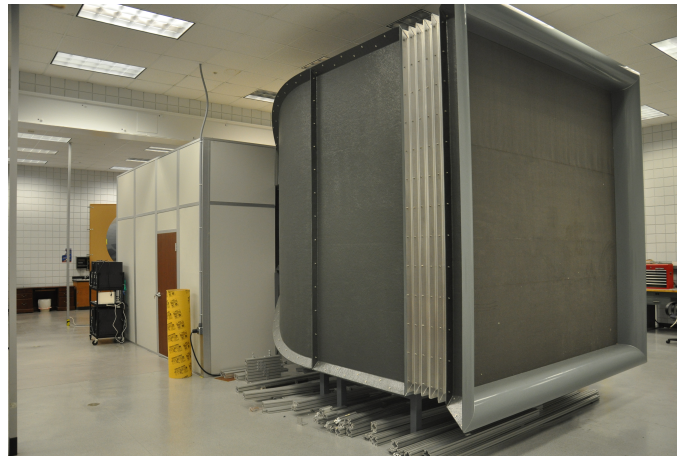


Figure 4.37: REEF wind tunnel

The wing was set about 68 inches downstream from the wind tunnel inlet. It was mounted on a six axis load cell Figure 4.39 and had a plywood floor which went from the inlet up until the location of the load cell. The mounting fixture consisted of an assembly of aluminum plates and c-channels. A load cell plate was adapted to the load cell bolts directly. Attached to this plate a wing adapter plate was fixed by means of four bolts. The wing adapter plate had two c-channels for wing positioning over the plate. Initially one c-channel was used, however it was observed that there

were some oscillations induced by the lack of stability on the opposite end of the fixture. Therefore the remaining tests were done using the additional c-channel which was mounted on the opposite end of the first one. On top of the c-channel there was the conformal reinforced clamps which clamped the wing. These clamps too were bolted together to firmly grasp the wing, however without exerting too much force and cause damage to the wing. The wing setup with the fixtures and the load cell is shown in Figure 4.38.

The instrumentation used consisted of a voltage supply, amplifying electronics, a DAQ board and a DAQ computer. This equipment was set close to the wing. The ATG was rolled over the inlet for the turbulence tests, as shown in Figure 4.40.

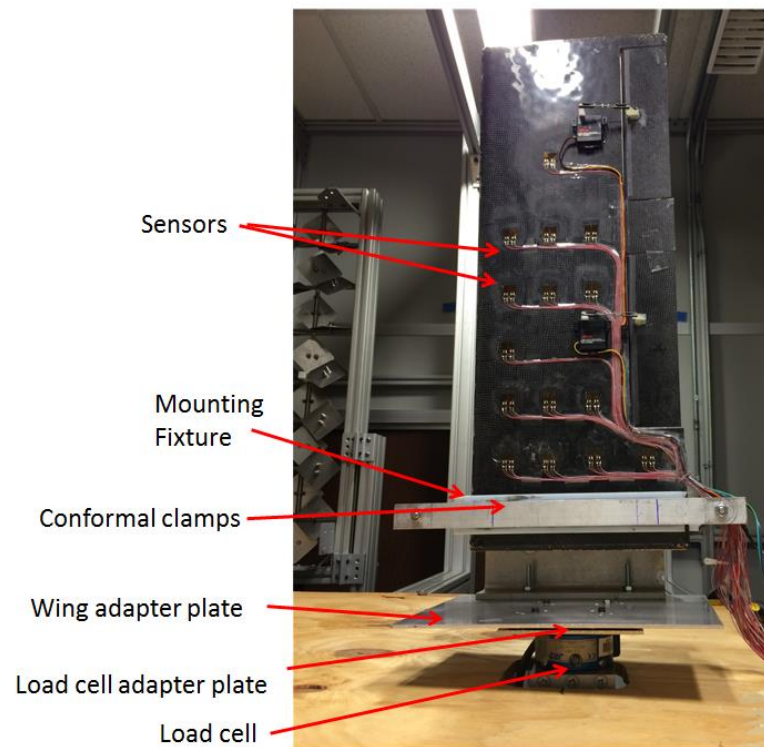


Figure 4.38: Wind tunnel wing setup

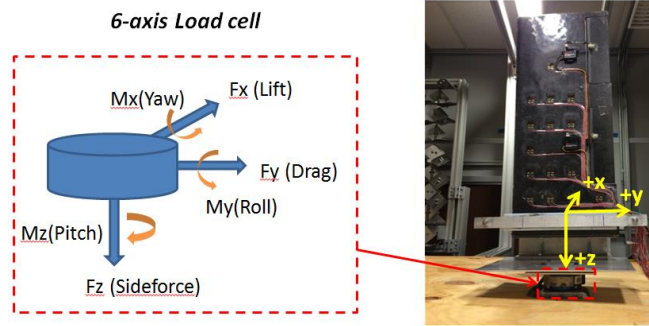


Figure 4.39: Load cell axes

For each of the tests described in Table, Figure ?? two sets of data were collected: first the data coming in from the wind tunnel and the data being recorded from the strain gauge sensors installed on the wing.

Table 4.4: Overview of initial wind tunnel tests

| |
|--|
| <p>Steady State: (2 Angles of Attack and 3 Speeds):</p> <p>AoA 0 deg: 5m/s, 7.716 m/s, 10.288 m/s, 12.861 m/s (4x2)</p> <p>AoA 5 deg: 5m/s, 7.716 m/s, 10.288 m/s, 12.861 m/s (4x2)</p> <p>AoA 0 deg, Ramp: 10.288 m/s, 12.861 m/s, 7.716 m/s, 10.288 m/s (x2)</p> <p>AoA 5 deg, Ramp: 10.288 m/s, 12.861 m/s, 7.716 m/s, 10.288 m/s (x2)</p> |
| <p>Turbulence Grid (AoA: 5 deg)</p> <p>Turbulence Grid (ATG): 4.73 m/s and 7.11 m/s (x2)</p> |
| <p>Turbulence Grid (ATG) at 7.11 m/s:</p> <p>Open loop (x1)</p> <p>Closed Loop using S1.S15, One Aileron (x15)</p> <p>Closed Loop using S1S15, Two Ailerons (x15)</p> <p>Open Vanes (x2)</p> |

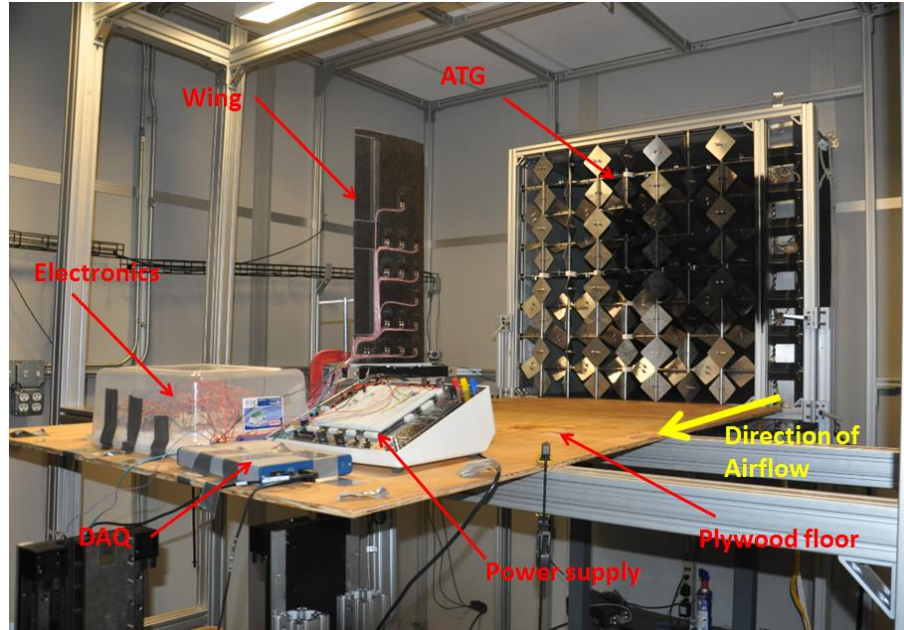


Figure 4.40: Test setup with ATG

The load cell data was collected at 2000 Hz and the strain gauge data was collected at 10kHz. For preliminary testing two DAQs were used, the load cell data was recorded using a NI-PXI system available at REEF whereas for the sensor data, a USB mass terminal DAQ was used. In order to synchronize the measurements coming out from the two DAQs a mechanical pulse was used, this is shown in Figure 4.42.

The voltage data was passed through a calibration matrix M for the JR3 load cell which was used so that the forces and moments produced were calculated in Newtons (Forces)and Newtons.meters (Moments), as $F = MV$. V are the available voltage values per channel. Each of the tests were approximately 2 minutes long, with a steady velocity approximate duration of 30 seconds. This area of steady flow for the steady tests can be seen from the flat portion of the signals. . In

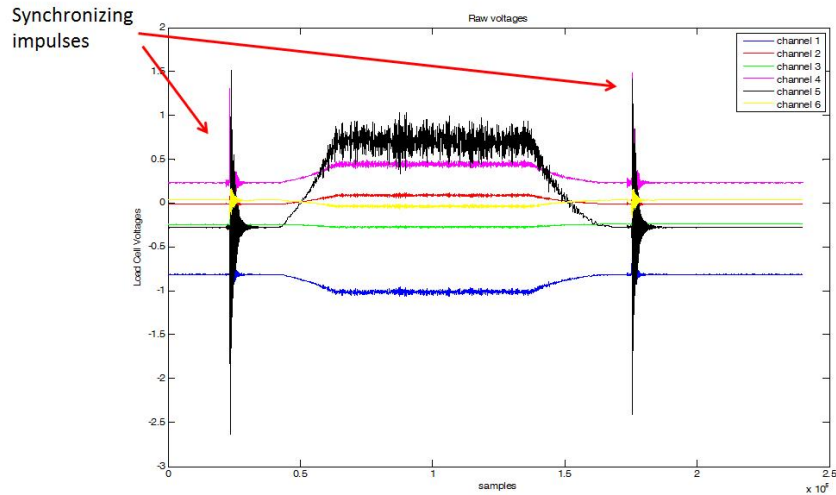


Figure 4.41: 6-axis sample data from load cell during steady test, mechanical pulses were used to synchronize data

In addition to the conversion to forces and moments, each voltage channel had an offset which translated to an offset in forces and moments. These offsets were due to gravity effects in the balance of the heavy aluminum fixture assembly. The JR3 load cell however had sufficient load capacity. These offsets were subtracted from the measurements to obtain the actual force and moment variations.

4.4.2 Experimental results

The frequency content of the wind tunnel data in both the steady and the turbulent tests can be analyzed in the perspective of vibration modes coming both from the wing structure, fixture structure and aerodynamic effects. It was observed that the oscillations of aerodynamic behavior did not produce divergent aeroelastic effects. It could also be observed that the Lift channel had the strongest impact of aeroelastic interactions of the wing. In order to gauge for proper airfoil trends,

i.e. lift increases with speed and angle of attack, the load cell data vs. steady wind tunnel speed is presented in Figure 4.42.

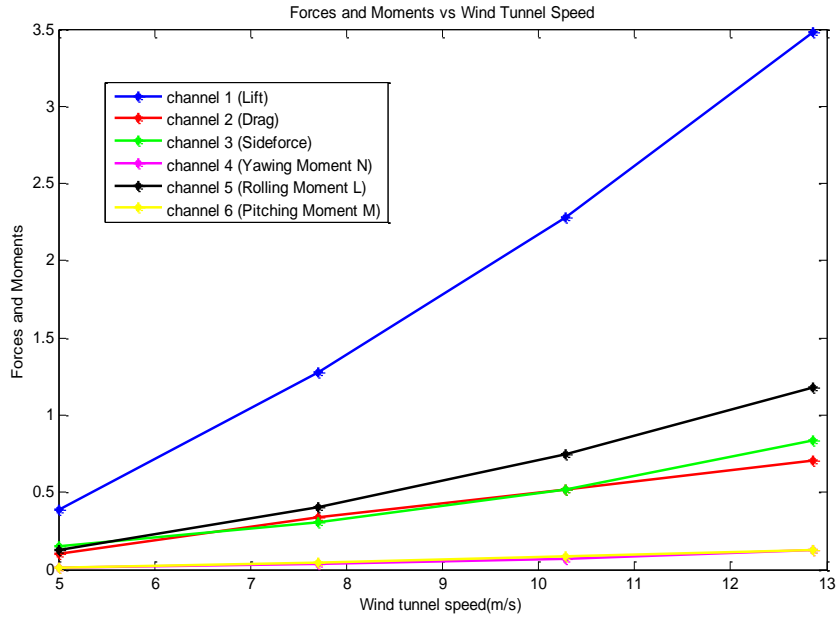
The lift coefficient was calculated for each case using the four speeds: 5 m/s (9.72 kts), 7.716 m/s (15 kts), 10.288 m/s (20 kts), 12.861 m/s (25 kts). The values in Figure 4.43 were calculated using a wing length of 0.555 m and air density of 1.2 Kg/m^3 at 20 Celsius (68 F). The Reynolds number was calculated using the chord as characteristic length and a dynamic viscosity of 1.8205E-5 $Kg/m.s$.

These results can be compared to the AG35 polar plots found in Figure 4.44 and the AG35 rotated airfoil, found in [109].

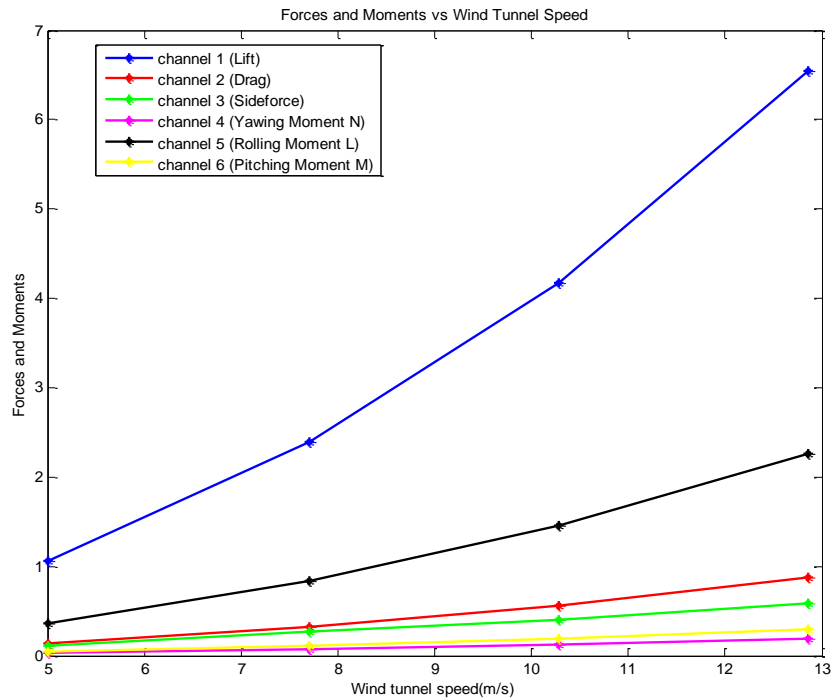
Even though the choice for a rotated airfoil to compare the results for CL and CD needs to be further verified, the rotation by 1.563 degrees to orient the chord line horizontally was very similar to what the UMD Pwings two point mount did. In addition to this, the values for CL and CD are in close proximity with those predicted by the low speed airfoil data of the rotated airfoil.

From the Lift coefficient graph in Figure 4.44, a zero degree angle of attack will produce a lift coefficient close to 0.2 and for a 5 degree AoA a lift coefficient close to 0.54. These values are in close agreement with experimental results. A similar comparison can be drawn for the drag coefficient, albeit the measured values seem to be in the same order of magnitude but higher than the results of the polar curve in [109].

A sustained gust test was performed to test how well the strain gauge sensors tracked the wind speed changes. Figure 4.45 shows the forces and moments as well as the strain signals coming from each bridge.



(a) Forces and moments AoA=0 deg



(b) Forces and moments AoA=5 deg

Figure 4.42: Calculated forces and moments vs wind tunnel speed for angle of attack)

degrees and angle of attack 5 degrees

| Angle of attack (0 deg) | | | | Angle of attack (5 deg) | | | |
|-------------------------|-----------------|--------|--------|-------------------------|-----------------|--------|--------|
| Wind tunnel speed (m/s) | Reynolds Number | CL | CD | Wind tunnel speed (m/s) | Reynolds Number | CL | CD |
| 5 | 72340 | 0.2052 | 0.0517 | 5 | 72340 | 0.5736 | 0.0750 |
| 7.716 | 116180 | 0.2818 | 0.0757 | 7.716 | 116180 | 0.5457 | 0.0726 |
| 10.288 | 154900 | 0.2839 | 0.0642 | 10.288 | 154900 | 0.5365 | 0.0700 |
| 12.861 | 193780 | 0.2765 | 0.0562 | 12.861 | 193780 | 0.5376 | 0.0699 |

Figure 4.43: Calculated lift and drag coefficients from wind tunnel data

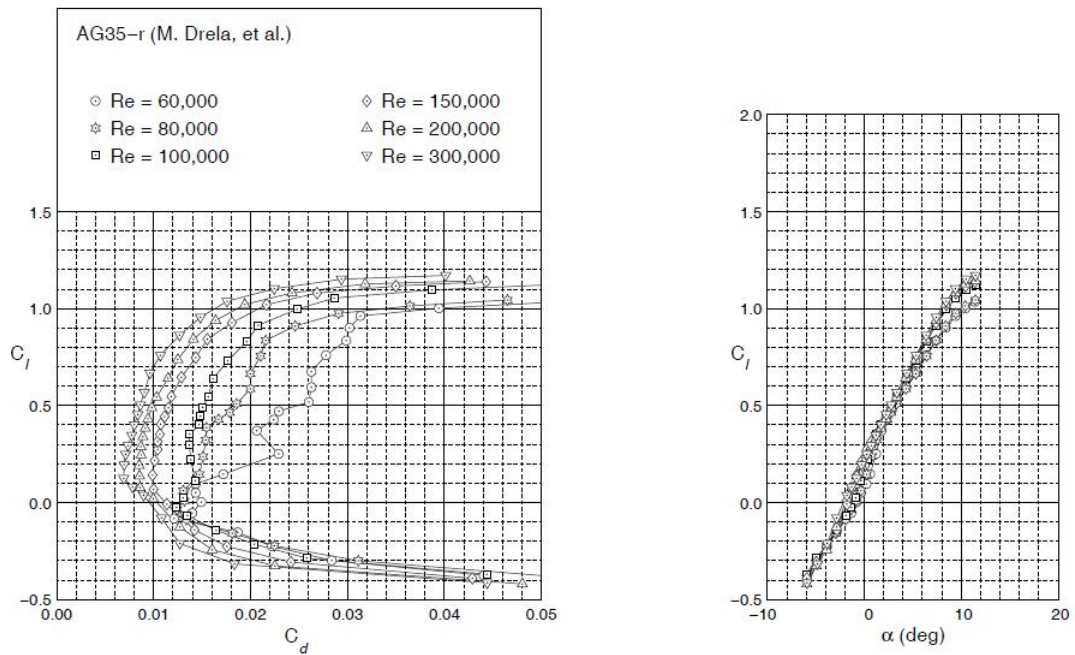
The rms level data collected from each bridge for each of the steady velocity tests was plotted in a pattern that conserves the distances between each bridge pair along the wing span. Interpolation of the bridge data renders a 3D surface of measured rms strains on the surface of the wing. Figure 4.46 shows a representative case where the higher strains are close to the root as expected. This map can be better built if more sensors are available. During the preliminary tests four sensors did not work properly and therefore had to be taken out of the set. If access is possible to more sensor locations, then the following figure would have more bridge points (hollow circles), as shown in Figure 4.46.

If a top view of these RMS calculated strains is taken, a similar pattern is shown for each case of increased angle of attack and increased wind velocity. These patterns are interpolations based on experimental measurements. The strains were calculated by means of the gauge factor and the bridge voltage. The 0 deg and 5 deg angle of attack cases are shown in Figure 4.47.

The maximum rms strains also increase with wind speed, as can be observed from a comparison of 3D interpolated rms strains at a zero angle of attack and low

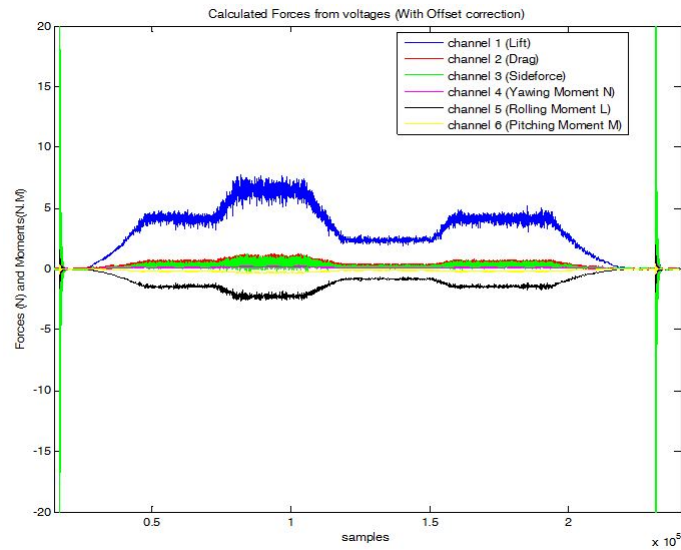


(a) Rotated airfoil

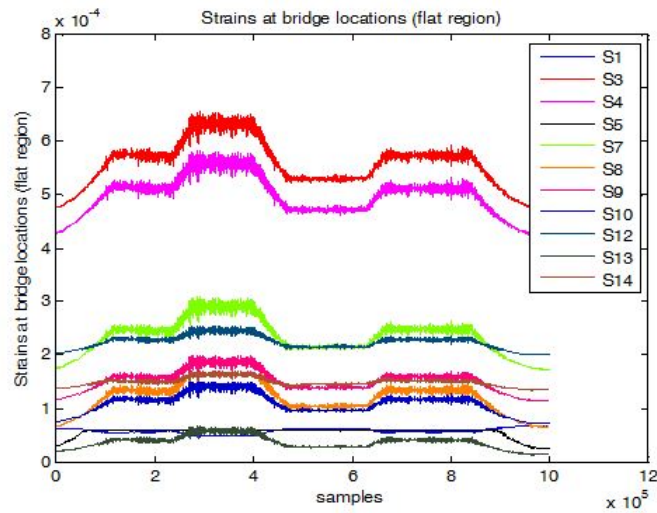


(b) Lift/Drag coefficients vs angle of attack

Figure 4.44: AG35-r Drela airfoil, from [109], rotated airfoil and lift/drag coefficients vs angle of attack.



(a) Forces and moments



(b) Strain sensor data

Figure 4.45: Ramp test to simulate sustained gusts (20 kts, 25 kts, 15 kts, 20 kts),

AoA =5 deg: load cell forces and moments and strain sensor data.

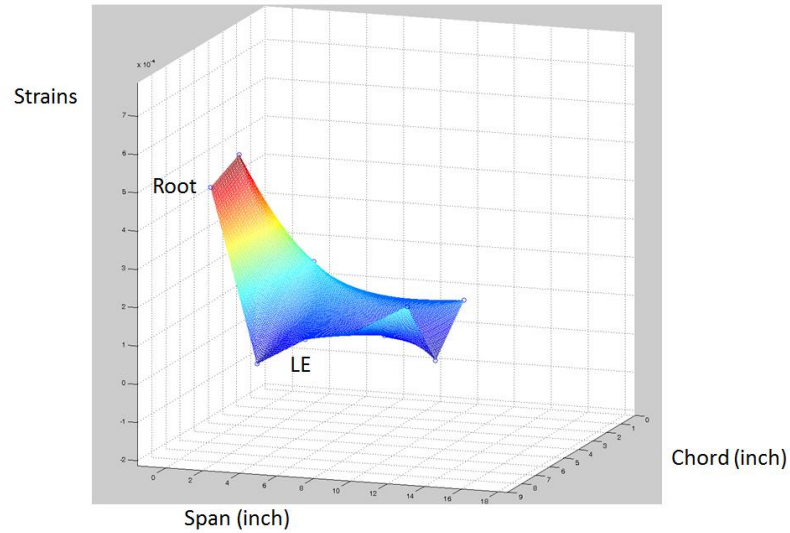
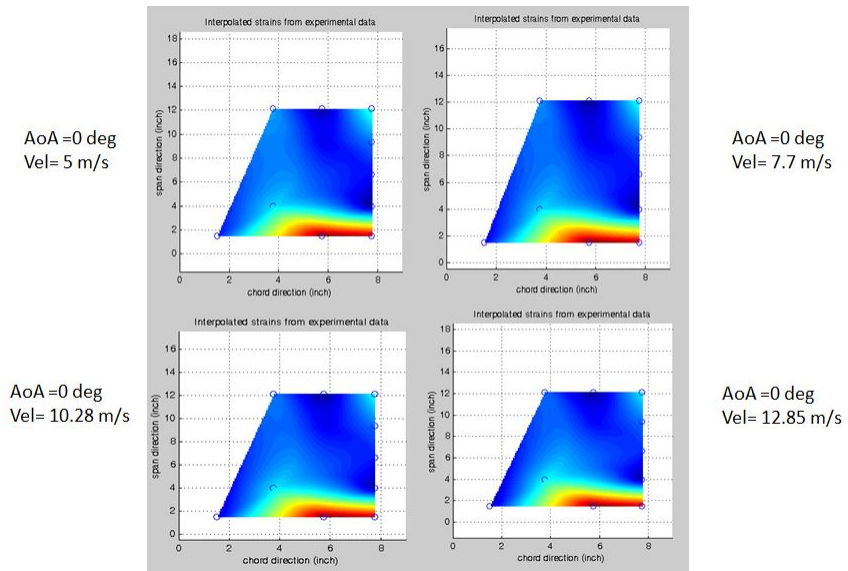


Figure 4.46: Representative of interpolated strain rms measurements for steady wind velocity

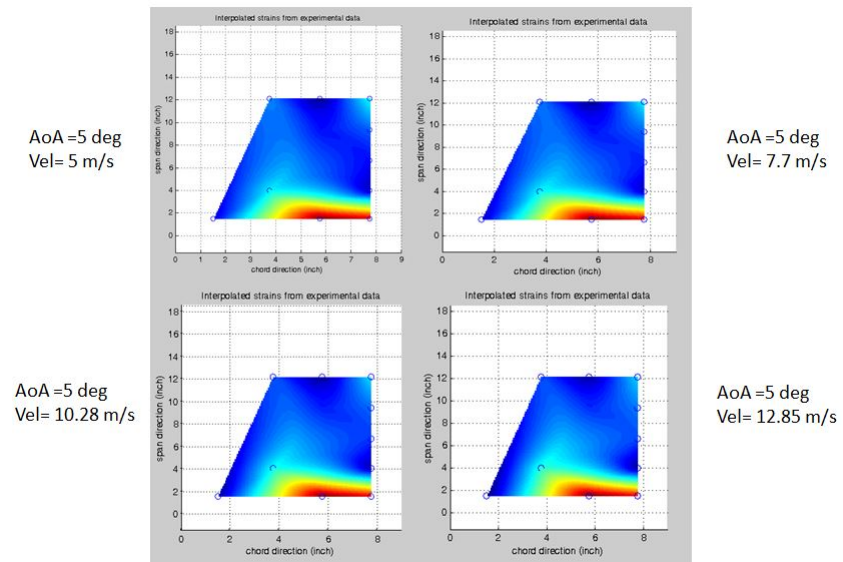
speed, with a 5 degree angle of attack and fastest speed. This comparison is seen from Figure 4.48, where the maximum strain goes from about $4.2 e^{-4}$ to about $6 e^{-4}$.

Wing tip static loading tests were also performed with tip loadings of 100 gr to 800 gr. Two of the tests are shown in the following graphs of Figure 4.50. It is interesting to observe that although strains are higher at the root some of the sensors contribute more in the steady wind dynamic case. This pattern is consistent with what is observed from the mass weighted strain simulation for the full wing.

Turbulence tests were carried by means of an active turbulence grid or ATG. It consists of two orthogonal grids of rotating vanes. Each vane consists of a shaft with attached winglets which are driven to rotate by a computer controllerd motor. This device is placed in the wind tunnel at the upstream end of the test section and the action of the spinning vanes causes the air flowing throught the device to



(a) Interpolated strains at AoA 0 deg



(b) Interpolated strains at AoA 5 deg

Figure 4.47: Interpolated strain rms measurements for steady wind velocity at AoA 0 deg and AoA 5 deg

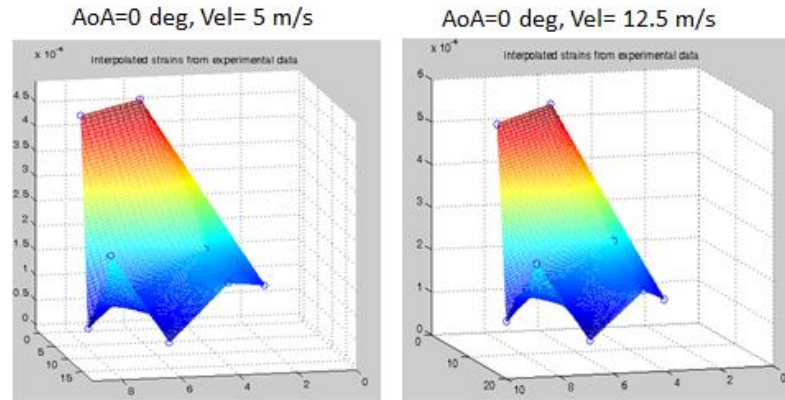


Figure 4.48: Comparison of max. rms strains during steady runs

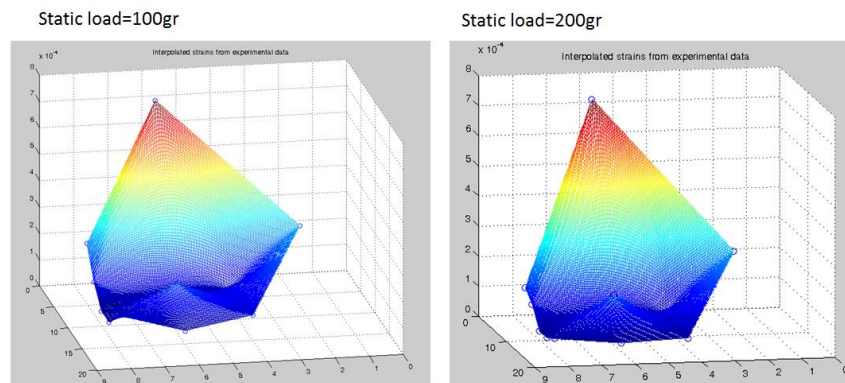


Figure 4.49: Comparison of strains produced with wing tip loadings of 100gr and 200gr

become highly turbulent.

Tests with the ATG grid on were carried using a core velocity of approx. 7.1 m/s. The random processes associated to this velocity have been characterized with a hot-wire probe in [1]. The percentage variation from a mean core velocity are attributed to external airflow events and do not impact the quality of the flow. Overall the baseline flow is very uniform. The ATG was shown capable of generating free stream turbulence intensities from 15 % to 35 %, with length scales on the

order of 0.6 m and with spectra approximating the von Karman model that showed a possibility for tonal or smooth behavior depending on run mode. The statistical characteristics of the ATG are given by the tables corresponding to $x/M=12.5$ and 43.5 % throttle. The statistical tables for the ATG are found in excerpts from [1] in Appendix B.

The turbulent data can only be analyzed with statistical metrics, given that this is a random process. The following graph shows the calculated Lift from load cell data without strain feedback and with strain feedback. The strain feedback gain used was $K=1$, both with one aileron and with two ailerons for feedback. Higher gains could not be tested due to experimental constraints in that the wind tunnel was available for limited amount of time.

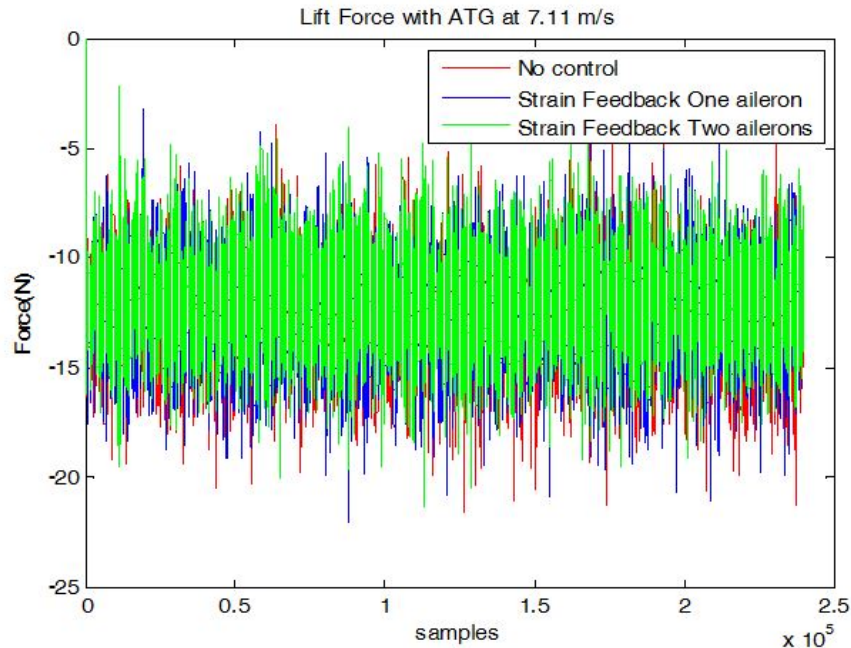


Figure 4.50: ATG produced Lift force with and without strain feedback

One way to quantify improvements of using strain feedback is to calculate the rms level of the measured lift force. Table 4.5 shows results of using strain feedback with a gain of $K=1$, feeding back from different bridges individually, where bridge 1 is S1, bridge 8 is S8, etc All the ATG tests were about 2 minutes on average, sampling at 2000 Hz.

Table 4.5: RMS lift using strain feedback at different strain gauge bridges

| Test Case | RMS level Lift Force (Newtons) |
|---|--------------------------------|
| No control, turbulent Lift | 12.9535 |
| Strain feedback using one aileron SFB at S1 | 12.6901 |
| Strain feedback using two ailerons at S1 | 12.0564 |
| Strain feedback using two ailerons at S8 | 11.2332 |
| Strain feedback using two ailerons at S9 | 11.1297 |
| Strain feedback using two ailerons at S12 | 11.0696 |
| Control Lift RMS two ailerons at S14 | 11.2330 |

4.4.3 System identification of output matrix

In the perspective of a bio inspired approach and to test the distributed sensing concept, we used system identification techniques to relate forces and moments to sensor measurements. If the set of measurements over a number of distributed sensors are weighted in the least squares sense they can be used for feedback control. The matrices can anticipate a force/moment measurement and enable the controller

to calculate an actuator command to anticipate impending rigid body motion. It has been shown in previous work by the UMD AVL lab that the weighting algorithm provides an improvement in bandwidth and allows for noisy sensor signals, if the noise is non-correlated [9]. Other techniques can be used to overcome this type of sensor noise.

For the system identification we used three methods to generate the loads and calculate output matrices. The output matrices correlate the forces and moments at the root of the wing -and therefore at the fuselage if there was one attached to the wing- with data from sensors which have been distributed over the surface of the wing. The following tests were carried for the system identification of output matrices.

The first test consisted of a static loading in the Lift direction. The wing was loaded at the wingtip and chordwise at the shear center by means of a pulley, string, and static weights. This was done at only zero angle of attack. The second test consisted of wind tunnel loading at different speeds and angles of attack. In this case the wing was uniformly loaded by the air stream at different velocities. Ten velocities and four angles of attack were used. In the third approach, static manual loading was exerted on the wing to produce coupled and decoupled forces and moments. The wing was randomly loaded to try and produce coupled and decoupled loads. Some loading directions were more challenging to obtain as can be expected, in particular the yawing direction and all the moments.

A second setup consisted of discrete gusts to test for strain feedback properties and flight envelope increase under near stall conditions. The main UMD goal

however was to test the effectiveness of the strain feedback controller in mitigating the gust disturbance.

The discrete gust test was designed to provide the wing with additional lift for a different duration of time. The gust generator (Figure 4.51) was designed and built by Aurora Flight Sciences [7] and it consisted of tubing, a fan and a latch mechanism to control the duration of the gusts injected into the air stream. The gust generator was placed upstream of the test section and it was adjusted in height such that it would produce an increase in lift that would make the wing stall. This additional objective had the purpose of demonstrating that the strain feedback was able to increase the flight envelope of the wing. This is an added benefit and application of the proposed sensing mechanism. For this setup the plywood tunnel floor was removed and the amplification electronics were placed underneath the wing.

Three wings were tested in this setup as well. The fiber optics wing, the stanford wing with a stretchable sensor network and the off the shelf UMD wing.

The stanford wing setup and amplification board are shown in Figure 4.52.

depicts a sample static forcing case to find the output matrices with coupled components. The coupled forces should yield matrices which are non-sparse and with coupled entries. The initial portion of the graph has small variations which are also encoded in the strain signals, although the graph doesn't show the scale of these variations.

Another set of tests entailed forcing the wing with static directional forces with the purpose of decoupling the forces and moments. Figure 4.54 shows the case for F_x , where the the lift direction or the x direction as well as the rolling moment are

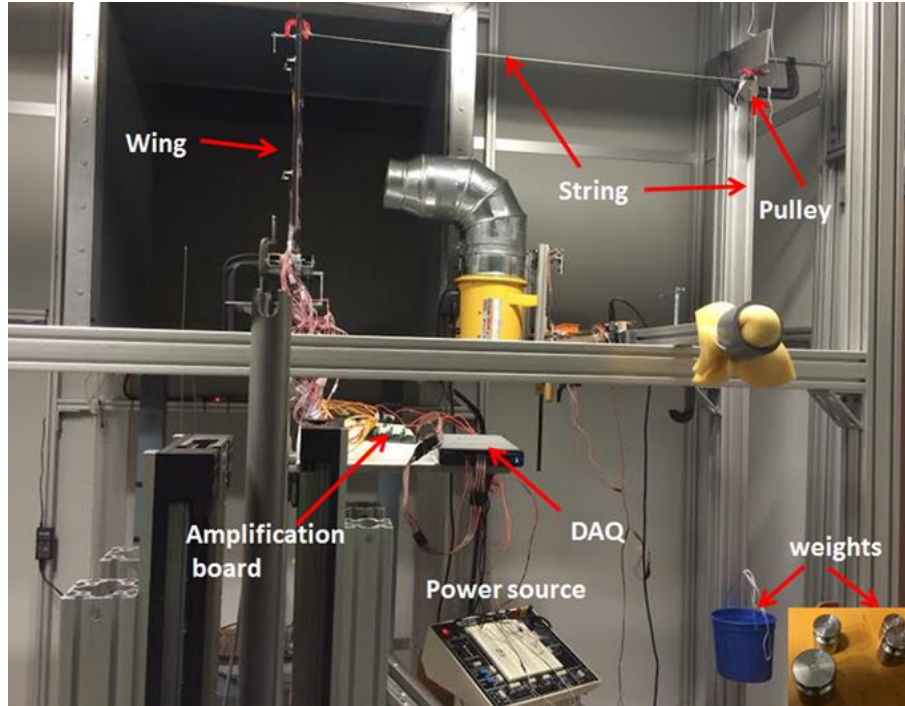
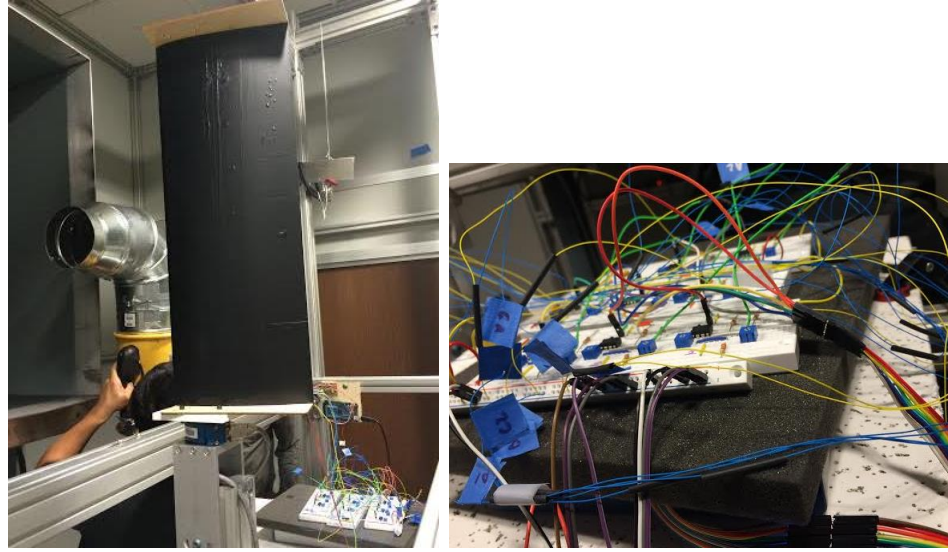


Figure 4.51: Setup for Static system identification in the lift direction

very pronounced. Figure ?? shows results for the data in Figure 4.54, Figure 4.55, and Figure 4.56.

The least squares estimator used a linear regression to calculate the dependencies of the overall strain field measured by the 15 sensing bridges and the forces and moments at the root of the wing. The Cmatrices for manual F_x , F_y , F_z calculated with least squares estimator and colored noise. These are shown in Figure 4.57.

For the gust tests, the following matrices in Figure 4.58 were calculated using least squares for the two particular design points which were described earlier. These matrices may be slightly different from those of the static case, due to possible excitation of modes that were not excited in the static tests.



(a) Stanford wing with stretchable sensor network (b) Stanford wing amplification board

Figure 4.52: Stanford wing wind tunnel gust setup

4.4.4 Discrete gust tests

In order to measure the impact of gusts over the wing, open loop and closed loop tests were carried at two specific design points. These design points were originally intended to drive the wing close to a stall at the moment the gusts were applied. However for the UMD wing the stall was not easy to set up or observe therefore the focus will be in an overall reduction of the impact of gusts.

For the case of 3 deg angle of attack and a wind speed of 20kts, the following impact on the wing forces and moments was observed, as shown in Figure 4.59.

As it can be observed from Figure 4.59, the impact of the upstream gusts on the forces is mainly observed with a shift from the steady state forces, along some oscillations due to aerodynamic and structural effects. Feedback was implemented

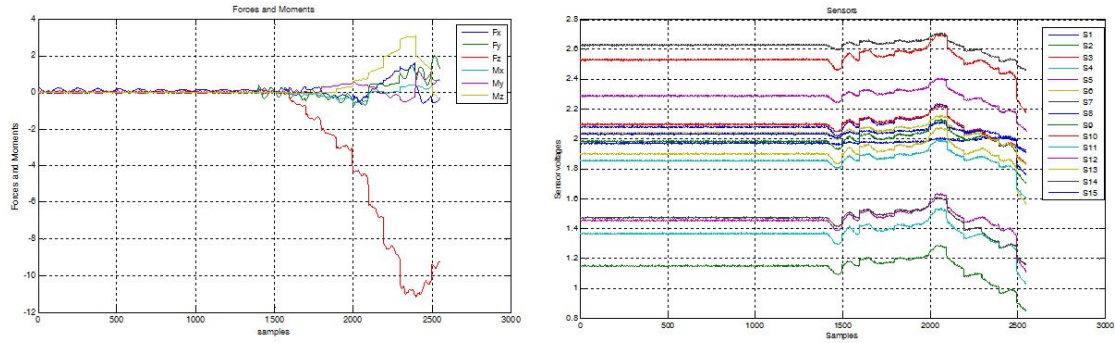


Figure 4.53: Static manual forcing with coupled components

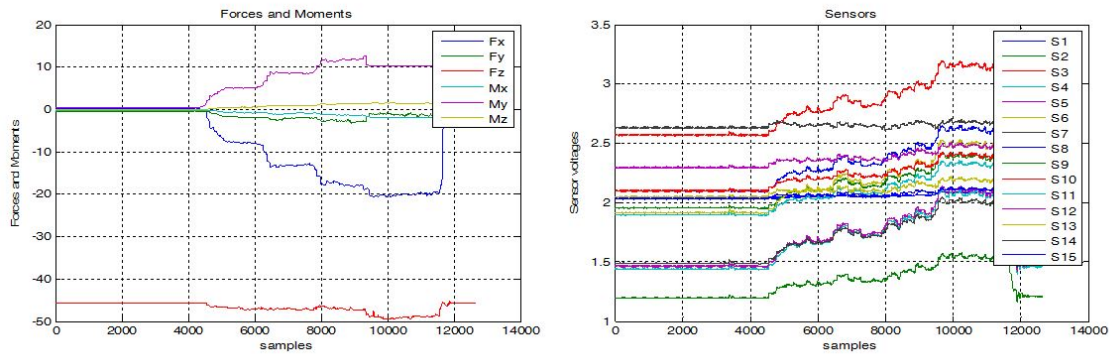


Figure 4.54: Static manual decoupled forces and moments F_x , forces and moments (left), sensor data (right)

by means of three methods: 1. Using only one sensor location (S2) for feedback, 2. Using an average Cmatrix, which kept an overall average of all the sensors at all times, 3. Using system identified output matrices. The results of the closed loop tests are shown in Figure 4.60, Figure 4.61 and Figure 4.62. For the feedback based on a single sensor location (Figure 4.60), a sensor near the root of the wing and far from the aileron was selected. This method shows that it produces some correction to the overall force shift due to the gusts. However it also shows that is prone to more oscillations due to sensor noise. The feedback which uses an average Cmatrix

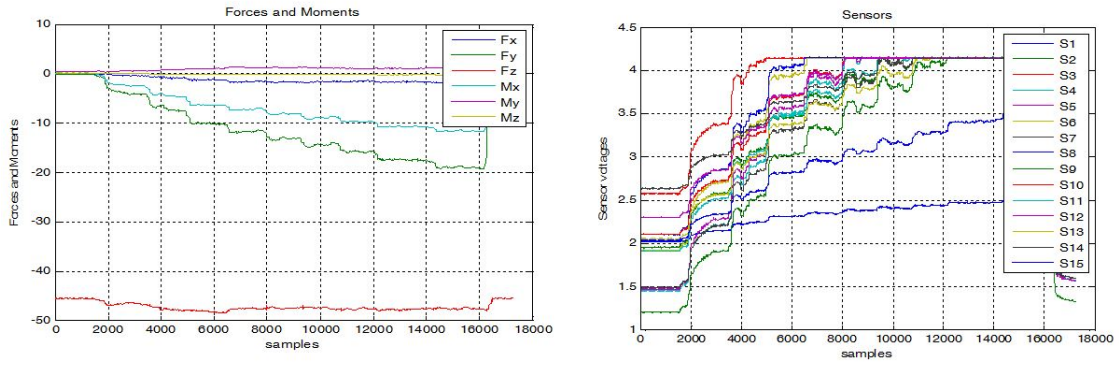


Figure 4.55: Static manual decoupled forces and moments F_y , forces and moments (left), sensor data (right)

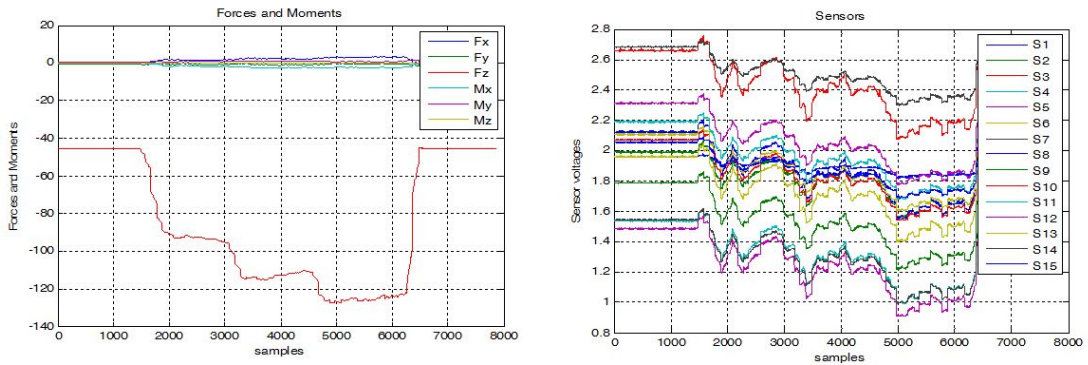


Figure 4.56: Static manual decoupled forces and moments F_z , forces and moments (left), sensor data (right)

to produce aileron commands, shows that it is able to correct for the overall shift and reduce the amplitude of the oscillations observed when the gusts are applied. The response shows that there is a good level of oscillation. Finally, with the I_d matrix the feedback is able to reduce the shift as well as reduce the amplitude of the oscillations while the gust is acting on the wing.

A moving average was used for generating Figure 4.63 and allow for evaluation of the improvement in counteracting the gust forces. From Figure 4.63 it can be

| | | | | | | | | | | | | | | | | | | | | |
|-----|---------|---------|---------|---------|---------|--------|-----|---------|---------|---------|---------|---------|--------|-----|--------|--------|---------|---------|--------|--------|
| C = | -0.0118 | -0.0033 | 0.0057 | -0.0080 | 0.0792 | 2.0295 | C = | -0.0524 | -0.0205 | 0.0568 | 0.0601 | -0.1861 | 2.0259 | C = | 0.0330 | 0.0044 | -0.1092 | -0.0172 | 0.1428 | 1.9554 |
| | 0.0068 | 0.0061 | -0.2303 | 0.0005 | 0.0214 | 1.9557 | | 0.0891 | -0.1176 | -0.3213 | 0.4074 | 0.7034 | 2.0209 | | 0.0560 | 0.0143 | -0.3382 | -0.0253 | 0.1907 | 1.9920 |
| | 0.0141 | 0.0086 | -0.3178 | 0.0049 | -0.0015 | 2.5707 | | -0.1213 | -0.2510 | 0.4349 | 1.1396 | -8.3086 | 2.6130 | | 0.0957 | 0.0200 | -0.4904 | -0.0360 | 0.4096 | 2.6514 |
| | 0.0291 | 0.0125 | -0.3893 | 0.0163 | -0.1108 | 1.4439 | | 0.0931 | -0.2215 | -0.3354 | 1.0592 | 1.3371 | 1.5495 | | 0.1039 | 0.0195 | -0.4950 | -0.0266 | 0.5226 | 1.5213 |
| | 0.0348 | 0.0132 | -0.4046 | 0.0191 | -0.1409 | 1.4660 | | 0.1459 | -0.2191 | -0.3700 | 1.1767 | 0.0028 | 1.5684 | | 0.0910 | 0.0196 | -0.4738 | -0.0282 | 0.3897 | 1.4792 |
| | 0.0289 | 0.0114 | -0.3736 | 0.0151 | -0.1233 | 1.9164 | | 0.0739 | -0.2970 | -0.1298 | 1.2565 | -1.9348 | 1.9838 | | 0.0930 | 0.0191 | -0.4679 | -0.0300 | 0.4062 | 1.9534 |
| | 0.0310 | 0.0102 | -0.3406 | 0.0183 | -0.1431 | 1.4916 | | 0.0751 | -0.1651 | -0.3681 | 0.4869 | 1.9761 | 1.5735 | | 0.0883 | 0.0179 | -0.4252 | -0.0288 | 0.3433 | 1.5377 |
| | 0.0445 | 0.0118 | -0.3967 | 0.0267 | -0.2504 | 2.0967 | | 0.0342 | -0.3109 | -0.0433 | 1.1659 | -2.2141 | 2.1543 | | 0.0971 | 0.0190 | -0.4568 | -0.0307 | 0.3946 | 2.1168 |
| | 0.0478 | 0.0006 | -0.3722 | 0.0350 | -0.4102 | 1.1982 | | -0.0743 | -0.1763 | -0.2287 | -0.0021 | 3.5743 | 1.2522 | | 0.0974 | 0.0180 | -0.4241 | -0.0347 | 0.3878 | 1.7814 |
| | 0.0406 | 0.0006 | -0.3232 | 0.0295 | -0.3514 | 2.1002 | | 0.0897 | -0.1694 | -0.2454 | 0.9042 | -0.0098 | 2.1802 | | 0.0897 | 0.0168 | -0.3933 | -0.0337 | 0.3580 | 2.0648 |
| | 0.0506 | 0.0132 | -0.3704 | 0.0306 | -0.3007 | 1.8995 | | 0.0386 | -0.1517 | -0.2595 | 0.5257 | 1.6287 | 1.9837 | | 0.0881 | 0.0159 | -0.3723 | -0.0327 | 0.3788 | 2.1831 |
| | 0.0410 | -0.0071 | -0.2893 | 0.0341 | -0.4345 | 2.2969 | | 0.0785 | -0.1421 | -0.2304 | 0.7675 | 0.2234 | 2.3707 | | 0.0919 | 0.0161 | -0.3702 | -0.0381 | 0.3812 | 2.3065 |
| | 0.0390 | -0.0095 | -0.2690 | 0.0342 | -0.4414 | 2.0471 | | 0.0070 | -0.1268 | -0.2560 | 0.0665 | 2.5346 | 2.0905 | | 0.0855 | 0.0151 | -0.3449 | -0.0346 | 0.3558 | 2.1020 |
| | 0.0303 | -0.0161 | -0.1951 | 0.0319 | -0.4239 | 2.6312 | | 0.0354 | -0.0911 | -0.2141 | 0.1864 | 1.4610 | 2.6719 | | 0.0662 | 0.0115 | -0.2631 | -0.0271 | 0.2725 | 2.6779 |
| | 0.0212 | -0.0065 | -0.1552 | 0.0191 | -0.2551 | 2.0337 | | -0.1482 | -0.0388 | 0.0863 | -0.0376 | 0.9334 | 2.0272 | | 0.0627 | 0.0101 | -0.2233 | -0.0314 | 0.2814 | 2.0502 |

Figure 4.57: Cmatrices for manual Fx, Fy, Fz calculated with least squares estimator and colored noise

| | | | | | | | | | | | | | |
|-----|---------|---------|--------|---------|---------|--------|-----|---------|---------|--------|---------|--------|--------|
| C = | -0.0036 | -0.0063 | 0.0161 | -0.0055 | -0.0193 | 2.0396 | C = | -0.0023 | -0.0018 | 0.0070 | -0.0100 | 0.0048 | 1.9931 |
| | -0.0041 | -0.0054 | 0.0175 | -0.0101 | -0.0203 | 2.0668 | | -0.0153 | -0.0080 | 0.0439 | -0.0673 | 0.0305 | 2.1011 |
| | -0.0254 | -0.0369 | 0.1152 | -0.0565 | -0.1282 | 2.9835 | | -0.0203 | -0.0098 | 0.0581 | -0.0899 | 0.0455 | 2.7997 |
| | -0.0194 | -0.0246 | 0.0862 | -0.0413 | -0.1013 | 1.8944 | | -0.0196 | -0.0096 | 0.0567 | -0.0902 | 0.0479 | 1.6750 |
| | -0.0220 | -0.0298 | 0.0991 | -0.0466 | -0.1112 | 1.7311 | | -0.0190 | -0.0091 | 0.0554 | -0.0841 | 0.0444 | 1.5424 |
| | -0.0209 | -0.0258 | 0.0928 | -0.0414 | -0.1067 | 2.2394 | | -0.0181 | -0.0091 | 0.0530 | -0.0834 | 0.0427 | 2.0619 |
| | -0.0183 | -0.0240 | 0.0823 | -0.0385 | -0.0959 | 1.7705 | | -0.0157 | -0.0075 | 0.0461 | -0.0724 | 0.0359 | 1.5979 |
| | -0.0180 | -0.0230 | 0.0814 | -0.0366 | -0.0962 | 2.3272 | | -0.0154 | -0.0072 | 0.0461 | -0.0695 | 0.0370 | 2.1627 |
| | -0.0143 | -0.0177 | 0.0643 | -0.0243 | -0.0719 | 1.4048 | | -0.0123 | -0.0051 | 0.0372 | -0.0530 | 0.0341 | 1.2759 |
| | -0.0126 | -0.0168 | 0.0575 | -0.0230 | -0.0628 | 2.2167 | | -0.0108 | -0.0048 | 0.0330 | -0.0471 | 0.0315 | 2.1143 |
| | -0.0124 | -0.0152 | 0.0560 | -0.0225 | -0.0655 | 2.0729 | | -0.0108 | -0.0051 | 0.0327 | -0.0463 | 0.0277 | 1.9566 |
| | -0.0095 | -0.0121 | 0.0432 | -0.0137 | -0.0510 | 2.4041 | | -0.0082 | -0.0033 | 0.0254 | -0.0330 | 0.0236 | 2.3309 |
| | -0.0089 | -0.0121 | 0.0412 | -0.0157 | -0.0500 | 2.0622 | | -0.0076 | -0.0026 | 0.0237 | -0.0294 | 0.0238 | 2.0026 |
| | -0.0067 | -0.0092 | 0.0305 | -0.0114 | -0.0371 | 2.6860 | | -0.0058 | -0.0027 | 0.0179 | -0.0240 | 0.0170 | 2.6336 |
| | -0.0038 | -0.0063 | 0.0184 | -0.0065 | -0.0196 | 2.0654 | | -0.0032 | -0.0010 | 0.0098 | -0.0121 | 0.0079 | 2.0371 |

Figure 4.58: Cmatrices for design points: AoA 9 deg, V=15kts (left) and AoA 3 deg, V=20 kts (right).

observed that the overall shift from steady flight is reduced with strain feedback, which was applied using three methods. The red curve represents the impact of gusts on Fy without any feedback. The blue curve represents the correction achieved using only S2 for feedback, which yields a good correction, although with some oscillation. The magenta curve was obtained using a C average matrix, again the oscillation is observed mostly during the application of the gusts. The green curve was obtained by using the sys id matrix. It can be seen that the sys id matrix improves both the shift and the amplitude of oscillations during the application of the gust. An increased bandwidth can reduce the shift even further. Other methods can be explored in order to continue to measure the improvement achieved when using

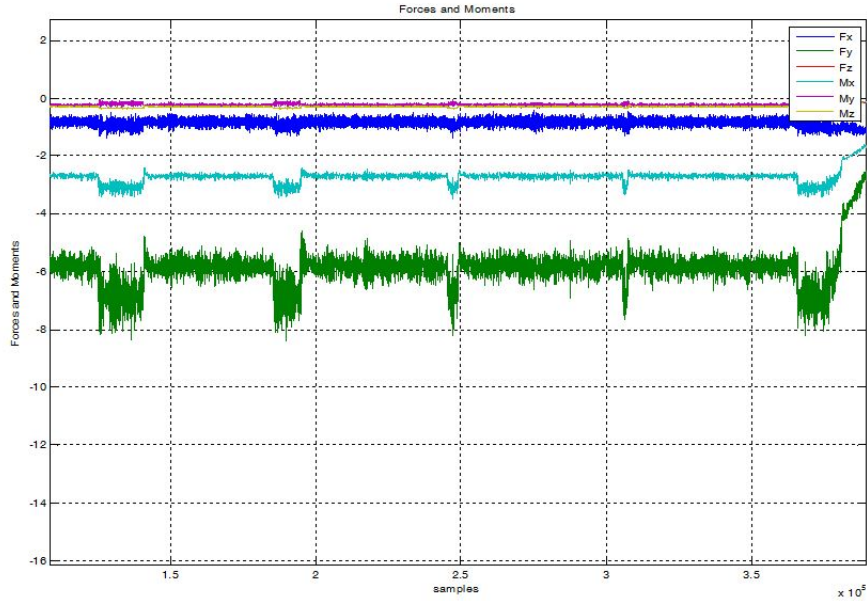


Figure 4.59: AoA=3 deg, V=20 kts, gusts, open loop

strain feedback and in particular the sensor to force and moment output matrices.

4.5 Flight testing

A similar wing to that of the wind tunnel tests was instrumented with strain gauges. The locations of the gauges were distributed based on MPF-v calculations from Figure 3.43. The outermost locations were chosen farther than the predicted areas of larger strains for observation of strain phenomena near the wing tips. The full wing was then assembled on top of the fuselage, with minor modifications to the original Apprentice. The modified aircraft with the strain gauge instrumented wing is shown in Figure 4.66.

Analog amplifiers were connected to the strain gauge bridges for signal output to the xbee transmitter. Signals were transmitted and sent off to a ground station

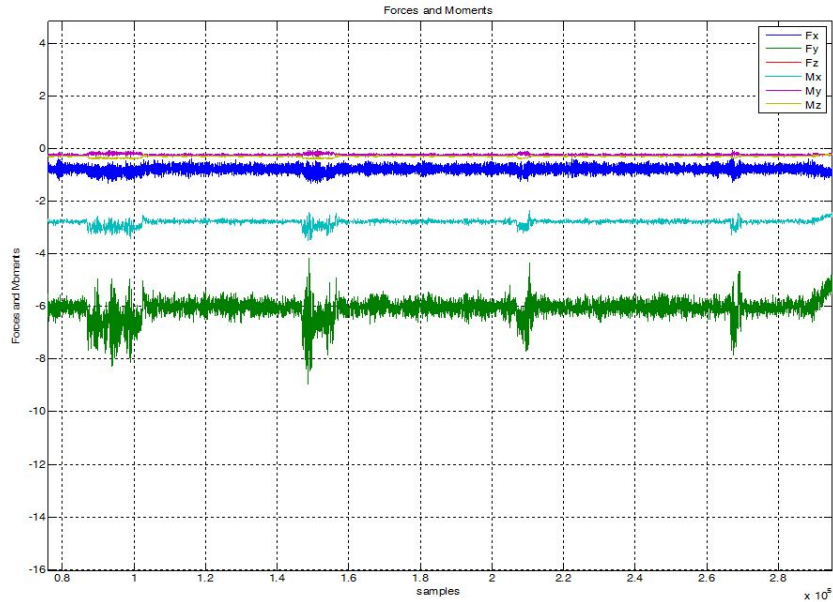


Figure 4.60: AoA=3 deg, V=20 kts, gusts, closed loop feedback S2

where they were also recorded. Signals from the strain gauges were also used in conjunction with the calculated Cmatrix for roll stabilization. This process is shown in Figure 4.67. During the flight trials, an autopilot was also tested, the APM 2.6. This setup will however require a multiplexer to input all the strain signals into the APM for processing and output to the ailerons and other controls surfaces. Two lipo batteries were used. One to power the ESC to the propeller throttle, or the main power, and another one to power the strain gauge amplification board and processor on board.

The voltage signals were obtained by the ground station and seemed to follow the stages of the flight in open loop. This is shown in Figure 4.68, where the ground data is clearly distinct from the flight data. In the flight data portion, several observations can be made. First, the level of strain from each sensor bridge is

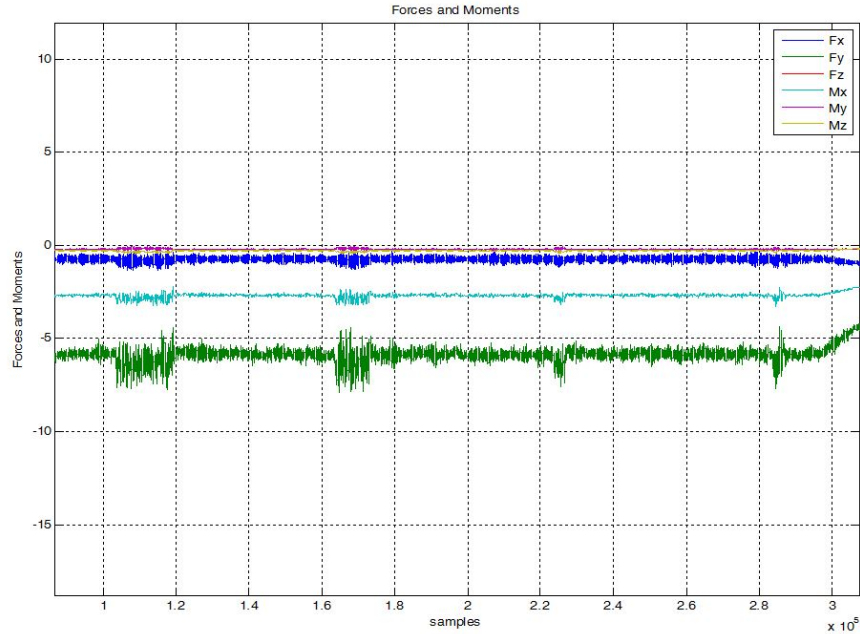


Figure 4.61: AoA=3 deg, V=20 kts, gusts, closed loop feedback C average

expected. The bridges closer to the wing tips, 1 and 8 have less strain response than those closer to the root of the wing, 3,4,5,6. Strain gauges 2 and 7 have less of a response as well although higher than than 1 and 8, also expected. Some channels were filtered and others were not, this allows for observation of the actual strain data being collected and the processing required.

After a few open loop flights, strain feedback was implemented with the output matrix from the physics based approach. This matrix had proportionality of expected forces and moments as well as strain signal intensity. The open and closed loop sections chosen correspond to those where the strain differentials have similar values. The open loop data and corresponding roll rate is shown in Figure 4.69 and the closed loop data is shown in Figure 4.70.

Overall, it is noticeable that the roll rate decreases in magnitude when the

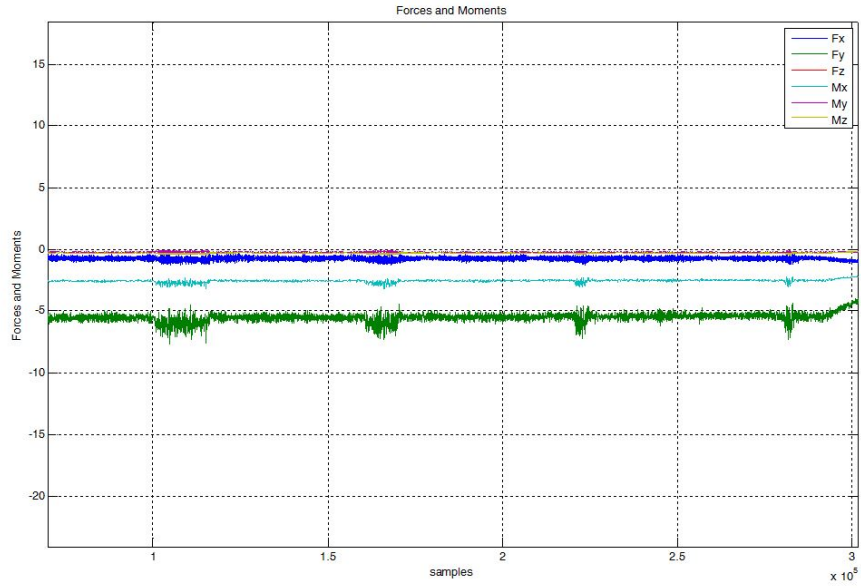


Figure 4.62: AoA=3 deg, V=20 kts, gusts, closed loop feedback C matrix (sysID)

closed loop strain feedback is enabled. A comparison of these for a single roll angle oscillation is found in Figure 4.71.

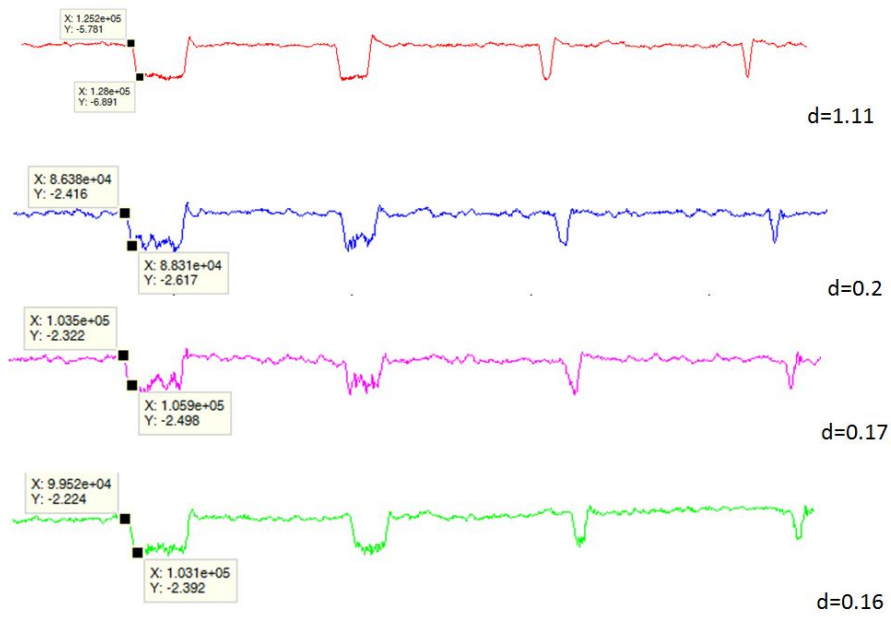


Figure 4.63: Filtered AoA 3 deg, $V=20 F_y$ data to measure performance of feedback loop, d represents a decrease in the shift for the first gust which is proportional to the shift observed in the other gusts

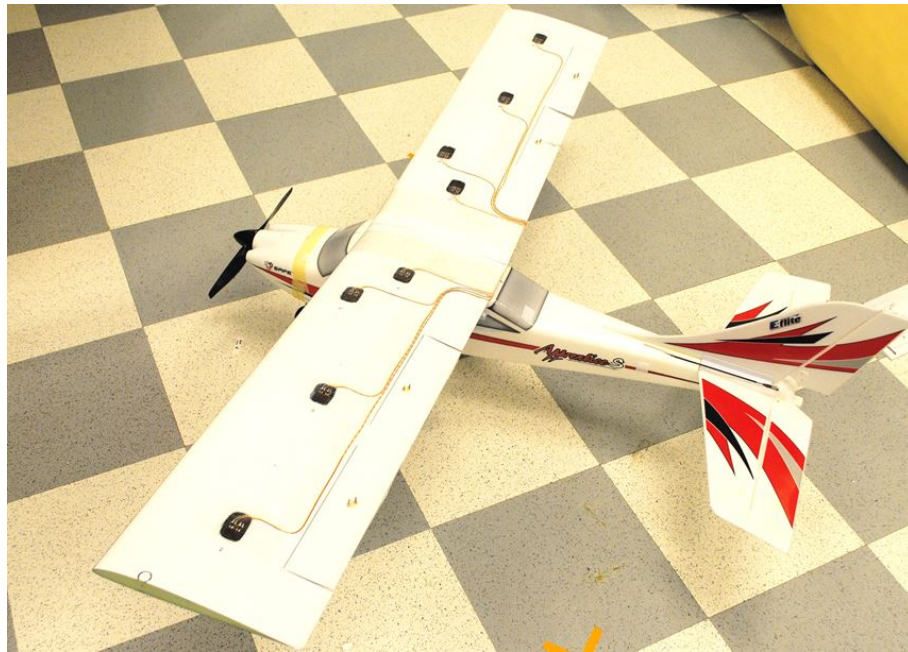


Figure 4.64: Apprentice aircraft with modified instrumented wing

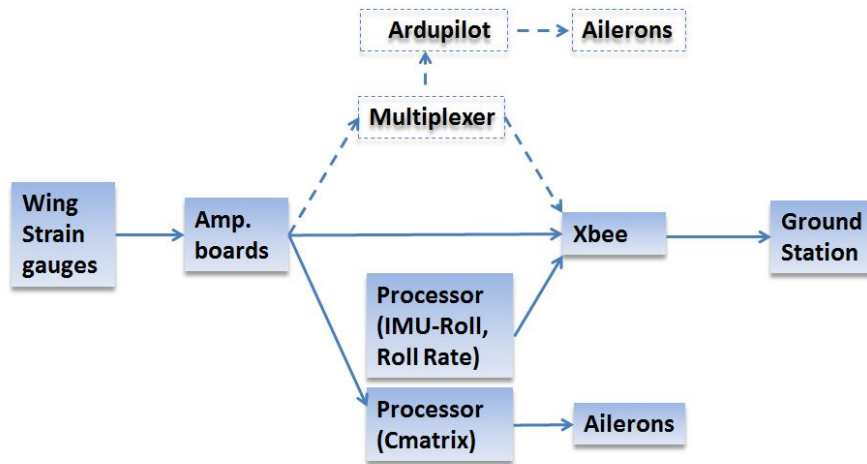


Figure 4.65: Strain signals and IMU recording and feedback for flight tests.



Figure 4.66: Apprentice aircraft and ground station during flight test preparation



Figure 4.67: Apprentice flight tests

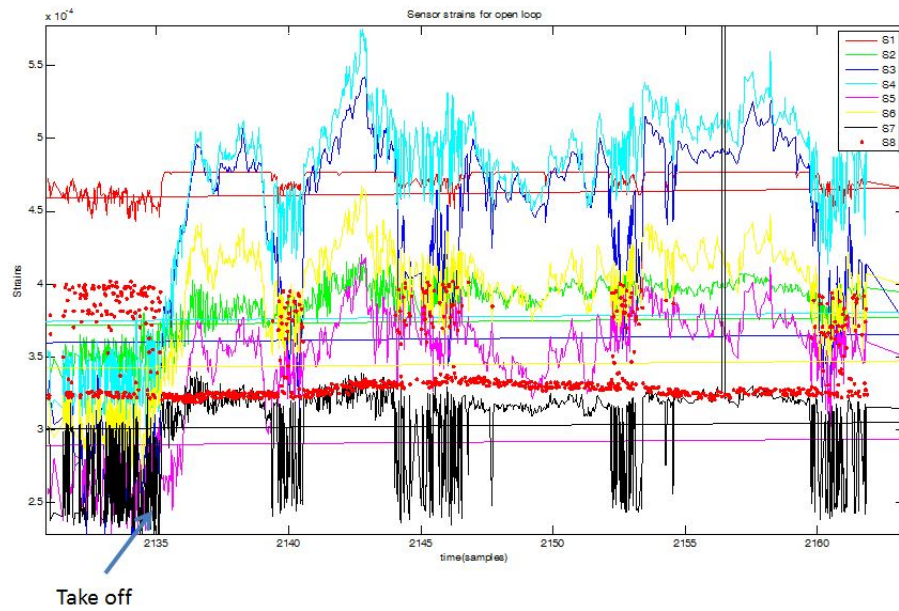


Figure 4.68: Open loop flight data, eight bridges, 32 sensors

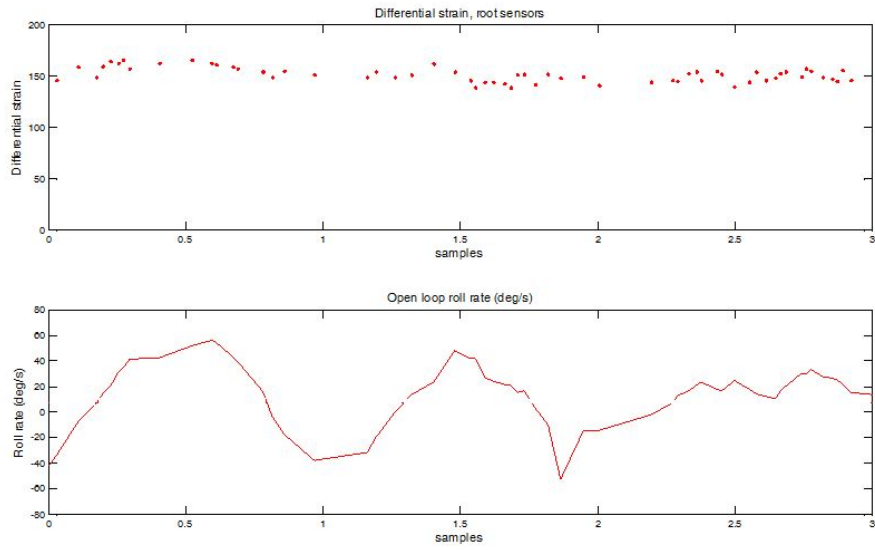


Figure 4.69: Flight data open loop, differential strain for sensors 4 and 5 and aircraft roll rate

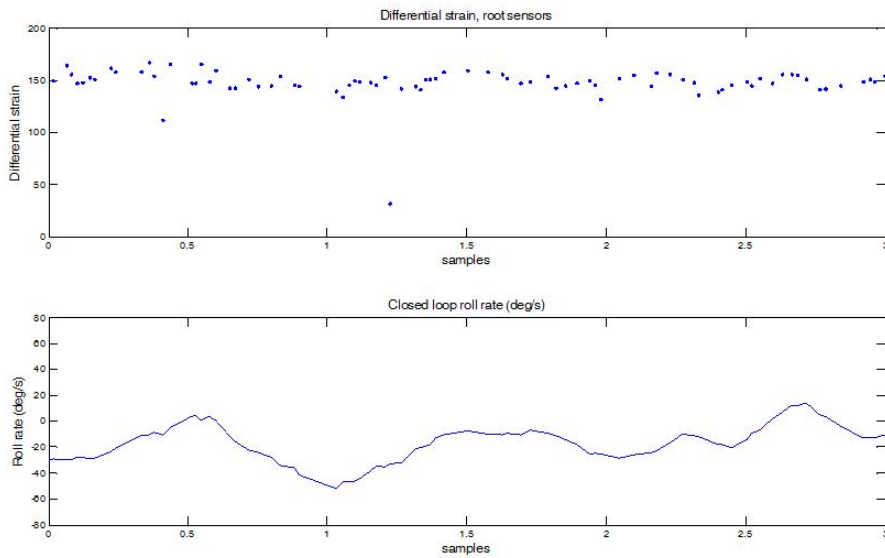


Figure 4.70: Flight data closed loop, differential strain for sensors 4 and 5 and aircraft roll rate

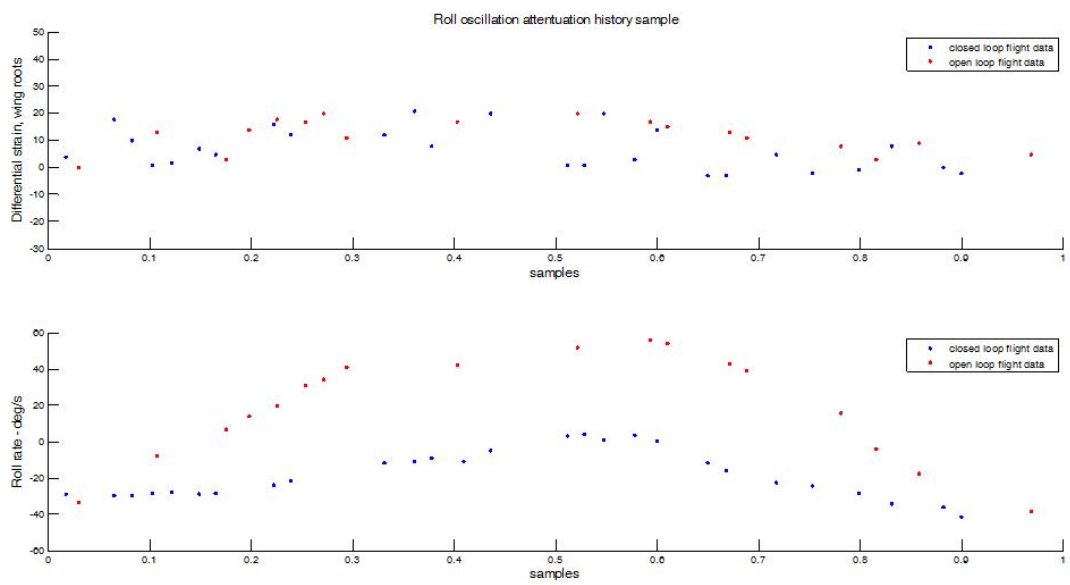


Figure 4.71: Flight data closed loop, differential strain for sensors 4 and 5 and aircraft roll rate for flight section.

Chapter 5: Summary and Conclusions

5.1 Summary

Bioinspired mechanisms of force/strain feedback were investigated and applied to small unmanned aircraft platforms. Regulation of the differential disturbance force was used in the high bandwidth inner loop for gust mitigation.

Using a small glider UAS, it was verified that the structural time reaction scale is much smaller in magnitude than that of rigid body motion, as it was observed in footage of the glider's flight. The rigid body motion lagged by roughly 0.03 seconds but was enough time for the strain sensors to activate the servo motor and react to the sensed gust disturbance before it actually turned the fuselage. The glider was instrumented with strain gauges [7] at the root of each wing and was successfully flown in closed strain feedback loop. Therefore, strain/force feedback was demonstrated using a small UAV under a sharp gust condition. The gust which was used for the experimental tests resembled a 1-cosine gust. Strain sensing output was successfully used in a fast inner loop for reflexive reaction to gusts. Aileron dynamics were fast enough for the employed combination of gust speed and roll correction.

Linear strain measurement weightings or wide field integrated strain can pro-

vide disturbance force state estimations which can be used in these fast inner loops. It was observed that this feedback is much more effective at higher proportional gains in the case of a strain/force proportional controller. Less deviation in the roll trajectories was observed by means of the D2 metric as the gain was increased. The structural feedback controller also demonstrated to be more effective than classical rigid body dynamics controllers, as it was compared using vicon and xbee transmission as the IMU.

A quadrotor platform was also used to demonstrate strain feedback. One of the arms of the quadrotor was instrumented with strain gauges, and was used in closed loop to correct for a heave gust condition. The heave disturbance was imparted by artificially injecting a motor disturbance and after the disturbance had been generated, the strain feedback compensator was activated. Material creep and therefore sensor creep was accounted for by carrying a parallel strain signal to which the controller resorted to when the disturbance was activated. In this mechanism, there can be sensor drift to a certain extent, as the loop is constantly updating the measurement of level flight. This feedback is much more effective at higher proportional gains in the case of a strain/force proportional controller. Less deviation in the roll trajectories was observed by means of the L1 metric as the gain was increased. Motor dynamics were fast enough for the employed combination of artificial gust and heave correction. A robust controller was implemented using strain feedback on the quadrotor, albeit in the case of the strain controller it was only for one degree of freedom [6].

In the perspective of all the aeroelastic models, static and dynamic, three

methods for strain feedback compensation were developed. These methods correspond to what would be more reasonable given the available degrees of freedom for sensor implementation.

First, a 1D static model is proposed for computing spatial weightings to translate strains into forces and moments. In this approach, the strain feedback provides a measure of the force imbalance on the lifting surfaces of the aircraft, and therefore proprioceptive. This approach can be implemented either with a single sensor on each control surface or it can be implemented using several sensors. One way of integrating the multiple sensor outputs is through wide field integration, in the sense that each sensor is weighted according to its expected physical contribution to the system in stabilizing a particular force. In this way, a one dimensional roll controller based on outputs weighted by physical constants was developed and was tested in a full 6-DOF dynamic linear aeroelastic simulation (ASWING). The controller roll tracking response was good, although the speed of response can be improved by adding outer loop stabilization. The principle however was demonstrated by closing the inner loop with strain feedback. The distributed 1DOF mechanism can also be used to detect disturbance propagation as insect wings such as the ones in drosophila can achieve by detecting torsional waves from the moment they begin at the wing tip onward.

Second, a wings only approach is presented as well, where a distributed sensor network is empirically correlated to the forces and moments at the root of the airfoil. This procedure was demonstrated by instrumenting a carbon fiber wing layup manufactured by [102] and implementing force feedback by means of a pseudoinverse

matrix, which had been calculated by a least squares regression. A closed loop improvement was observed for cases of discrete gusts of different durations as well as an improvement in the case of the turbulent wind tunnel tests.

Third, with a system identified strain map vs forces and moments at the root of the wing, estimations of the differential six degree of freedom forces can be made. This approach basically means that once the wing has been identified, all that needs to be done for control is to regulate the differences between the forces at the root of the wings. This approach would only need the main lifting wings as sensory surfaces for disturbance rejection. It is also a proprioceptive approach in that relative measures of detected forces and moments on each wing are constantly being compared and when any difference is detected it runs in the high bandwidth inner loop which may be robust as the calculated forces and moments are 6-DOF.

A Full aero elastic model can be developed by measuring aeroelastic stability derivatives through system identification or by aeroelastic simulation packages such as NASTRAN or COMSOL, with dedicated computational resources.

A framework for sensor placement using an FEM model of the wing was developed for open loop sensor placement. The observability map, which correlates well with the MPF-v weighted map that was obtained, relies only on the material properties of the wing. Closed loop sensor placement mechanisms can be used when a particular application is being targeted. Actual wing properties can be used to tune the model. Experimental measurements of static and dynamic wing properties were taken and it was found that the torsional stiffness of the wing is much larger than the bending stiffness. This behavior however is expected from the ± 45 degree

carbon fiber layout. Some error in the vicon estimation is made due to corrections in the Euler Bernoulli equations for a plate. A 2D wide field integration approach is presented for mapping of the impact of gusts on wing strain by means of the MPF weighted eigenstrains. A set of gains can be retrieved from the corresponding MPF weighted patterns and can be applied to any number of sets of sensors that are physically realizable. An integration of all the basis functions yield sensor locations which are sensitive to all the different types of gusts, that is, in the corresponding degree of freedom.

A CFD/structures gust framework is proposed to study the effect of gusts on wing structures and help in validation of sensor locations. The length of the control volume was not as long as it should be due to computational time constraints, however, it was shown that this is a useful tool to study the static aeroelastic interactions of fluid flow and wing structures. It was observed that the principal strains change during the interaction with the gusts.

With the wind tunnel tests it was also shown that the observability Grammian results for 2D sensor placement was coherent with the finite element simulation results. The rms strains showed to have energy patterns consistent with the mass participation factors. As extrapolated from the 1D analysis where the effective independence metric is proportional to the observability Grammian, these results produced similar to those produced by eigenstrain weighting using directional mass participation factors. This weighting produced best sensor location regions for best observation of vertical forces on the wing and therefore vertical gusts and perhaps lateral gusts if combined with another metric. Three estimation matrices were con-

structured with the linear regressors, they all produced improvements in the closed loop measured lift in the presence of gust disturbances.

It was also observed that wind tunnel load cell data contains frequencies corresponding to structural frequencies, aerodynamic frequencies, and noise. Sensor data also contains frequencies, although much less than the load cell data. Sensor data was shown to be consistent with open loop sensor placement. ATG data shows that strain feedback allows for a reduction in the average values of Lift force, at a proportional feedback gain of 1. ATG data shows that using two ailerons for structural feedback produce better results in reducing the average values of Lift force. The controller was only tested at $K=1$ but it produced a 10 % improvement over the rms lift disturbance produced by the rotating vanes upstream of the wind tunnel test section.

A flight test served to show that these principles work in actual flight, with the uncertainty caveats, as small UAS aircraft materials undergo thermal and structural changes. The sensor placement results depend on boundary conditions imposed on the sparse equation solver. Therefore changes in these boundary conditions will somewhat change the estimates for best observability. The extent to which these changes dramatically affect the performance of the closed loop controller during flight is a quantity that can be further studied.

5.2 Conclusions

From experimental work with four platforms as well as simulations of proposed mathematical mechanisms, it was shown that strain sensors can be used in fast inner loops for reflexive reaction to gusts. The mechanisms chosen in this work were bioinspired in proprioceptive qualities as well as distributed sensing features.

Structural feedback provides faster reaction times than IMUs alone, meaning that there indeed is an improvement by using signals coming from material deformations of the aircraft wings.

Strain feedback can be implemented in different types of small unmanned aerial platforms: glider, quadrotor, wind tunnel wing, flight test wing. It was effective in rejecting discrete roll disturbances of the glider, lift disturbances of the wind tunnel wing, roll disturbances of the flight wing, and heave disturbances of a quad rotor. In the case of the quadrotor, these were injected at the rotors to simulate the effect of the aerodynamic disturbances. For all the platforms, there is a certain degree of flexibility to obtain an adequate signal to noise ratio. In particular for the quadrotor, quad arms had to be designed to obtain a good signal to noise ratio without losing thrust power.

Effectiveness of the strain feedback mechanism heavily depends on the servo motor response, i.e. time constant. An ideal case would have the servo response be as fast as the strain sensor response, although typically, for off the shelf strain sensors this response is much higher by at least one order of magnitude.

Sensor noise is mitigated by using the least squares estimator. This estimator

considers that the noise has a zero mean and is uncorrelated. When the pseudo inverse is calculated it will correct for the noise in the sensor readings to the extent of the number of sensors. Sensor noise however still affects the measurements, especially if a reduced number of sensors are used. Analog filters and other faster response filters can be implemented to provide improvements.

Mass participation factors for sensor placement lead to an estimation of the observability Grammian in open loop, in the case of vertical gusts. This Grammian is directly related to the effective independence index-EFI, which is an engineering approach to mode targeting. It was observed that the MPF method produced more restricted sensor placement areas than the EFI approach. This analysis was carried in 1D and 2D. Wind tunnel experiments showed agreement of the strain sensor data with the areas predicted by the MPF map to be of higher rms output.

Strain sensor implementation at the selected locations based on placement analyses had good stability characteristics and was temperature compensated in a full bridge bending configuration. Gauge wiring seemed to be strong yet unobtrusive to the strain measurements. For the flight wing additional encapsulation options were pursued to avoid strong shear over the sensors and prevent damage to the sensors and wiring. Amplification and connections were customized for fast troubleshooting.

Different types of C-matrices were calculated. One proposed method entails an output matrix based on the physics of the different aircraft dynamics, i.e. roll. Another one entails output matrices that were system identified according to particular flight conditions, both static and dynamic. MPF maps can be used to construct

spatial maps which yield areas of more or less influence of the different types of gusts. Theoretical considerations produced a 6-DOF model for disturbance mitigation on the assumption that the output matrix which relates the forces and moments at the root of the wing has been identified. A 6-DOF decoupled model is also possible if considering differential balancing of strains on corresponding controls surfaces. These differentials form output matrices to be used in SISO and MIMO strain based controllers.

Closed loop linear aeroelastic simulations using both strain feedback and bioinspired Cmatrix based on the physics of the rolling motion, showed correction of the roll angle as well as of the overall trajectory.

Strain feedback was effective in reducing the peak rms lift disturbance produced by discrete gusts of different durations in wind tunnel tests. It also showed a promising correction to turbulent air with a core velocity of 7.1 m/s. Different C matrices were used to estimate the lift force at the root of the wing and feed the correction to the wing ailerons. All the matrices produced disturbance mitigation.

During flight tests, all the installed sensors showed a good response to different flight characteristics. A roll rate reduction during closed loop was observed as well. This would mean that the strain feedback was acting on the mitigation of roll disturbances. Further tests will be pursued where vertical force rms and lateral force rms will be measured for open and closed strain feedback loop. These are similar tests to those taken in the wind tunnel with the wing section.

A robust controller framework was formulated for output matrices with multiplicative uncertainty. The least squares estimator will give structured uncertainties,

however a worse case scenario can be chosen for the unstructured uncertainty formulation. The multi-degree of freedom case can be formulated in the forces and moments of the aircraft be it at the center of gravity or be it at the root of each wing for differential comparisons. In either event, the force estimations using strain sensors can be of a distributed nature or a discrete nature. Distributed systems benefit from least squares estimators as they provide a way to reduce noise in the individual components to enable fast inner loops as no further measurements need to be carried to estimate the states, in this case, force/strain differentials. The bandwidth limit is imposed by the strain sensor bandwidth which is very high for foil gauges, as compared to typical rigid body IMUs.

5.3 Future work

This work can be continued in many different directions as the strain platforms can be tested with many different controllers and under many different types of inputs.

Other modalities of strain sensing will also be explored in future work.

The CFD-structures or fluid structure interaction simulation can be extended to a dynamic case by inputting gusts with frequency content matching von Karman or Dryden profiles for a given altitude.

Closed loop sensor placement using minimization of the maximum singular value of the system and comparison with results from open loop placements. This procedure will allow for the closed loop to be optimized based on system require-

ments.

Implement the MIMO framework for the fixed wing system in the different theoretical approaches that were presented in the theoretical section. Exploring model uncertainties in the different parameters that were introduced is an important theoretical direction. Physical implementation of these controls algorithms is also an entire experimental area to be explored.

Appendix A: Strain sensors for aircraft wing applications

A number of off the shelf strain sensors can be used for aircraft applications. The choice of sensor depends on the performance requirements and the application goals. Different types of strain sensors can be applied to aircraft surfaces. These main types, among others are: piezoelectric, piezoresistive, DEAP and resistive, these are shown in Figure A.1.

Piezoelectric sensors use generated voltage which is produced on applied stress and is mainly for dynamic measurements due to electric current leakage. They are composed of piezoelectric materials such as Barium Titanate, cadmium sulfide, Quartz, PZT, PVDF, PVC, PMN-PT. A common type of material for piezoelectric applications is PVDF piezoelectric film due to its flexibility, high mechanical strength and dimensional stability. It also has a larger area than resistive gauges, which may make a difference in particular applications.

Resistive sensors or wire/metal strain gauges are typically made of constantan foil, although there are many other alloys used as well. These may or may not be temperature compensated but have a broad temperature range. They are typically based on a polyimide carrier and have a gauge factor of about 2. The maximum strain is not too large as it is mainly tailored to detect strains in the

micro-range. These need surface conditioning and are good for both dynamic and static measurements.

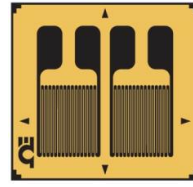
Semiconductor strain gauges are typically made of Silicon and Germanium. They have a higher unit resistance and higher strain sensitivity. The temperature effects are greater too and typically are non-linear. These can be customized using polymeric matrices and semiconductor fillers. These are also good for static and dynamic measurements. While the higher unit resistance and sensitivity of semiconductor wafer sensors are definite advantages, their greater sensitivity to temperature variations and tendency to drift are disadvantages in comparison to metallic foil sensors.

Electroactive polymers are another type of strain sensors which can be applied to an aircraft wing. They can be ionic or dielectric and possess greater flexibility. These also have actuator features and are versatile materials. The fine film allows for shape and size adaptation. The length is unrestricted which is a great advantage for some applications. The gauge factor typically depends on substrate stiffness. The maximum strain is greater than 100 %. These also allow for dynamic measurements although the bandwidth may vary with the different types of materials.

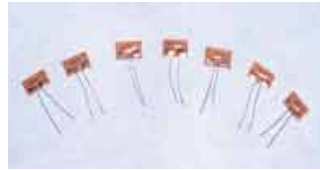
In general, the surface where the strain gauges need to be bonded require surface conditioning. This is to ensure a good physical and chemical bonding between the two surfaces. There will be surfaces resistant to any bonding agent. For this, a coating or abrasive method can be utilized to enable bonding. Solvent in bonding agent needs to be non-reactive with the wing surface material. A different type of glue may be used if this is the case. The impedance needs to match the moduli of



Piezoelectric film sensor



Resistive sensor



Piezoresistive sensor



Electroactive polymer sensor

Figure A.1: Strain sensors for aircraft wings

both materials as well as the shear modulus. The strain percentage on the surface of the wing needs to match the maximum sensor strain or be below the maximum value.

The installation requirements are such that for an airplane wing, the thickness of sensors and connections needs to be non-disruptive to the airflow. The signal conditioning and amplification is also very particular to each type of sensor installation, therefore light systems need to be kept in mind, especially for fiber optics strain sensing platforms. The ultimate sensor characteristics will depend on aircraft wing structural characteristics. These characteristics are compared using nominal representative values for each in Figure A.2. Other additional factors for a successful installation of strain sensors on aircraft wings include: effective encapsulation

for protection from humidity, electrical shielding and grounding, appropriate connectors and mechanical stability. If the wires connecting the strain gauges to the conditioning electronics are not protected against humidity a parasitic resistance created between the wires and the substrate to which the strain gauge is glued or between such wires. Acrylics adhesives, synthetic rubber resins, epoxies and cyanoacrylates are all frequently employed in lamination and assembly. An overview of the main advantages and disadvantages of these types of sensors is found in Figure A.3.

| Sensor Charact. | Resistive Foil gauge | Piezoelectric Piezo film | Piezoresistive Semiconductor | EAPs (DEAP) |
|----------------------|--------------------------|---|------------------------------|-------------------|
| Approx. Bandwidth | ~50 kHz | 0.001 Hz-10 ⁹ Hz | ~5Hz (substrate dep.) | ~1000Hz |
| Sensitivity | 2.0 ±5% Gauge factor | 12 x 10 ⁻³ V per microstrain | 150±5% Gauge factor | 1.46 Gauge Factor |
| Max. Strain/Force | 3% or 30,000 microstrain | 6-9 KgF (~) | 6000 microstrain | Up to 100% |
| Temperature Range | -75 to 200C | -40 to 100C | -50 -80C | -40 to 140C |
| Flexibility | Medium-low | Medium-High | High | High |
| Noise Sensitivity | Electrical noise and EMI | Susceptible to EMI when output is low | Medium-Low | Medium |
| Mechanical Stability | Good | Good | Medium | Low |
| Moisture Absorption | Medium-Low | Low, resistant to most chemicals. | Less than wire gauges | Medium |

Figure A.2: Strain sensors characteristics comparison chart

| Sensor Type | Resistive | Piezoelectric | Piezoresistive | EAPs |
|-------------|--|---|--|---|
| AVANTAGES | *Stability *Reliability *Linearity | *Higher frequency range *Micron scale films | *Higher sensitivity *Static and Dynamic measurements. | *Actuator properties, *Larger compliance *Increased max. strain |
| DISADVANT. | *Increased electrical noise *Not compliant enough for very flexible applications. | *Mainly Dynamic but quasistatic meas. are possible. *Films can be customized | *Stability, *Linearity, *Signal drift, *Temperature sensitivity | *Customization of components for each application. |

Figure A.3: Strain sensors advantages and disadvantages chart

Appendix B: ATG characteristics

The active turbulence grid at the university of Florida was developed by [1]. It consists of orthogonal rotating vanes, rotated by motors which rotate at a maximum frequency of 18Hz.



Figure B.1: ATG turbulence grid

The statistical characteristics of the settings used for the wing strain tests are found in Figure B.2. The ratio x/M is a key non dimensional parameter which

characterizes wind tunnel statistics and distance at which turbulence is developed downstream from the inlet. It is calculated based on the distance of the wing to the wind tunnel inlet upstream. In this case the distance was approx. 68 inch which divided by M, or the mesh size, gives a ratio of about 12.9, the closest chart that describes the characteristics of the flow is the one corresponding to a ratio of 12.5.

| $\frac{x}{M}$ | $\Omega \pm \omega$ | $U_\infty \pm 95\%CI$ | TI_X | TI_Y | TI_Z | ϵ | η | λ | Re_λ | $L_{11,c}$ | $Re_{L_{11,c}}$ | $L_{11,f}$ | $Re_{L_{11,f}}$ | I_{xy} | I_{zz} | I_{yz} |
|---------------|---------------------|-----------------------|--------|--------|--------|-------------------|--------|-----------|--------------|------------|-----------------|------------|-----------------|----------|----------|----------|
| | Hz | $\frac{m}{s}$ | % | % | % | $\frac{m^2}{s^3}$ | mm | mm | | m | | m | | | | |
| 12.5 | 2 ± 1 | 8.68 ± 0.26 | 19.1 | 18.5 | 18.0 | 5.68 | 0.16 | 10.5 | 1158 | 0.726 | 80464 | 0.456 | 50488 | 1.04 | 1.06 | 1.02 |
| 12.5 | 3 ± 1.5 | 8.46 ± 0.21 | 18.2 | 17.7 | 17.3 | 5.59 | 0.16 | 9.8 | 1002 | 0.587 | 60203 | 0.409 | 41943 | 1.03 | 1.05 | 1.02 |
| 12.5 | 4 ± 2 | 8.25 ± 0.19 | 17.6 | 16.5 | 16.4 | 5.23 | 0.16 | 9.5 | 921 | 0.526 | 50918 | 0.399 | 38574 | 1.07 | 1.07 | 1.01 |
| 12.5 | 5 ± 2.5 | 8.04 ± 0.18 | 17.1 | 16.1 | 15.8 | 4.91 | 0.16 | 9.3 | 858 | 0.481 | 44175 | 0.429 | 39474 | 1.07 | 1.08 | 1.02 |
| 12.5 | 4 ± 1 | 8.24 ± 0.19 | 17.4 | 16.4 | 16.5 | 5.28 | 0.16 | 9.4 | 897 | 0.504 | 48273 | 0.415 | 39681 | 1.06 | 1.06 | 1.00 |
| 12.5 | 5 ± 1.25 | 7.99 ± 0.18 | 16.8 | 15.8 | 15.8 | 4.91 | 0.16 | 9.1 | 808 | 0.440 | 39215 | 0.428 | 38217 | 1.06 | 1.06 | 1.00 |
| 12.5 | 6 ± 1.5 | 7.84 ± 0.22 | 16.2 | 15.1 | 14.9 | 4.55 | 0.17 | 8.9 | 759 | 0.408 | 34602 | 0.495 | 42014 | 1.07 | 1.09 | 1.02 |
| 12.5 | 0 ± 3 | 8.47 ± 0.31 | 20.7 | 19.0 | 18.5 | 5.84 | 0.16 | 10.9 | 1275 | 0.833 | 97462 | 0.557 | 65169 | 1.09 | 1.12 | 1.02 |
| 12.5 | 0 ± 4 | 8.25 ± 0.27 | 20.2 | 18.3 | 18.0 | 6.02 | 0.15 | 10.2 | 1134 | 0.694 | 77140 | 0.527 | 58650 | 1.11 | 1.12 | 1.02 |
| 12.5 | 0 ± 5 | 7.95 ± 0.25 | 19.3 | 17.4 | 18.2 | 6.09 | 0.15 | 9.3 | 956 | 0.535 | 54811 | 0.492 | 50349 | 1.11 | 1.06 | 0.96 |
| 12.5 | 0 ± 6 | 7.87 ± 0.25 | 19.4 | 17.3 | 18.1 | 6.08 | 0.15 | 9.3 | 945 | 0.527 | 53589 | 0.511 | 51998 | 1.12 | 1.07 | 0.95 |
| 12.5 | 0 ± 8 | 7.60 ± 0.25 | 18.6 | 16.5 | 17.2 | 5.79 | 0.16 | 8.8 | 833 | 0.441 | 41622 | 0.573 | 54107 | 1.13 | 1.09 | 0.96 |
| 12.5 | 2.5 ± 0 | 7.96 ± 0.20 | 18.4 | 17.3 | 18.3 | 6.33 | 0.15 | 8.7 | 852 | 0.446 | 43560 | 0.388 | 37822 | 1.06 | 1.01 | 0.95 |
| 12.5 | 5 ± 0 | 7.32 ± 0.20 | 17.1 | 15.2 | 16.5 | 5.65 | 0.16 | 7.9 | 661 | 0.314 | 26195 | 0.571 | 47724 | 1.13 | 1.04 | 0.92 |
| 12.5 | 8 ± 0 | 6.73 ± 0.31 | 17.2 | 14.2 | 15.2 | 4.50 | 0.17 | 8.2 | 631 | 0.310 | 23861 | 0.816 | 62940 | 1.21 | 1.13 | 0.93 |

Figure B.2: ATG turbulence statistics with wind tunnel throttle at 43.5 % and at $x/M=12.5$, from [1]

Measured percent variations from core for freestream velocity and different ATG run modes are shown in Figure B.3. This figure shows measured percent variation from the mean core velocity close to 7.1 m/s for U_{inf} , run mode $\Omega = 0$ and $\omega = 3$, as well as the measured percent variation from core for TIx at different percentages with the baseline flow [1]. TIx is a relative turbulence parameter which is calculated by dividing the square root of the flow velocity in the direction of the

freestream into the freestream velocity.

$$TI_x = \frac{rms(u)}{U_{inf}} \quad (B.1)$$

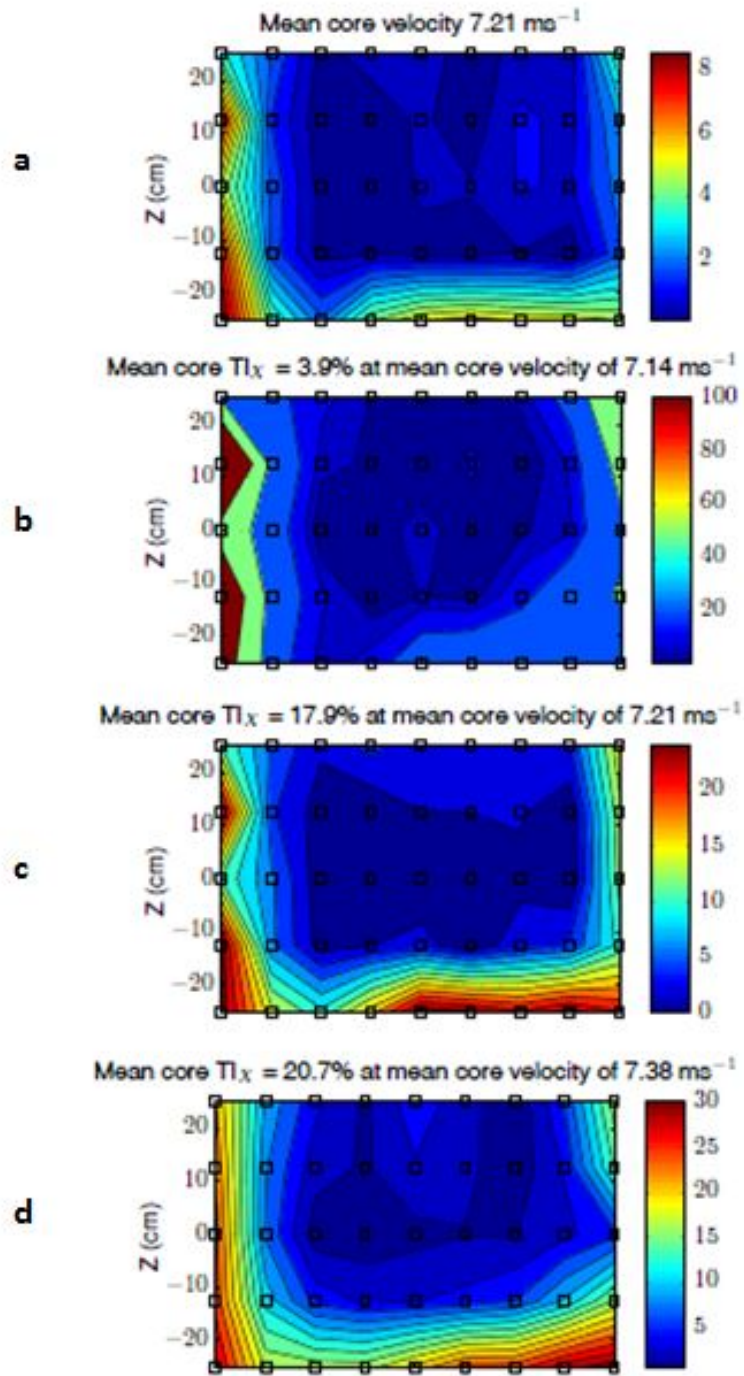


Figure B.3: ATG turbulence statistics mean core velocities: a. Mean core velocity at 7.21 m/s, b. Mean core velocity at $TI_x=3.9\%$, c. Mean core velocity at $TI_x=17.9\%$, d. Mean core velocity at $TI_x=20.7\%$

Bibliography

- [1] Michael J Sytsma. *Effects of turbulence on fixed wing small unmanned aerial systems*. University of Florida, 2013.
- [2] Michael Ol, Gregory Parker, Gregg Abate, and Johnny Evers. Flight controls and performance challenges for mavs in complex environments. *AIAA Paper*, 6508, 2008.
- [3] Christopher D Regan and Christine V Jutte. Survey of applications of active control technology for gust alleviation and new challenges for lighter-weight aircraft. Technical report, NASA/TM-2012 216008, Dryden Flight Research Center, Edwards, California, April: 1-15, 2012.
- [4] Lina M Castano, Simone Airoidi, Terrence McKenna, and J Sean Humbert. Wing sensor placement for gust disturbance rejection.
- [5] Lina M Castano, Simone Airoidi, Terrence McKenna, and J Sean Humbert. Gust rejection using force adaptive feedback for roll. In *AIAA Aviation Technology, Integration, and Operations Conference*. AIAA, 2014.
- [6] Gregory M Gremillion, Lina M Castano, and J Sean Humbert. Disturbance rejection with distributed acceleration and strain sensing. In *AIAA SciTech Conference*, 2015.
- [7] Aurora Flight Sciences. Research and development, 90 Broadway suite 11 Cambridge, MA 02142.
<http://www.aurora.aero/>. Last accessed: June 22 2015.
- [8] Fu-Kuo Chang. Structures and composites lab sacl.
<http://structure.stanford.edu/>. Last accessed: June 22 2015.
- [9] James Sean Humbert and Andrew Maxwell Hyslop. Bioinspired visuomotor convergence. *Robotics, IEEE Transactions on*, 26(1):121-130, 2010.
- [10] Nicolas Franceschini, Franck Ruffier, and Julien Serres. A bio-inspired flying robot sheds light on insect piloting abilities. *Current Biology*, 17(4):329-335, 2007.

- [11] Graham K Taylor and Holger G Krapp. Sensory systems and flight stability: what do insects measure and why? *Advances in insect physiology*, 34:231–316, 2007.
- [12] A Skordos, PH Chan, JFV Vincent, and G Jeronimidis. A novel strain sensor based on the campaniform sensillum of insects. *Philosophical Transactions of the Royal Society of London A: Mathematical, Physical and Engineering Sciences*, 360(1791):239–253, 2002.
- [13] Thomas Werner, Shigeyuki Koshikawa, Thomas M Williams, and Sean B Carroll. Generation of a novel wing colour pattern by the wingless morphogen. *Nature*, 464(7292):1143–1148, 2010.
- [14] Mikko Juusola and Andrew S French. The efficiency of sensory information coding by mechanoreceptor neurons. *Neuron*, 18(6):959–968, 1997.
- [15] Carlo Menon, Rebecca Brodie, Sally Clift, and Julian FV Vincent. Concept design of strain sensors inspired by campaniform sensilla. *Acta Astronautica*, 64(2):176–182, 2009.
- [16] Rhoe A Thompson, Johnny H Evers, and Kelly C Stewart. Attitude control augmentation using wing load sensing—a biologically motivated strategy. In *AIAA Atmospheric Flight Mechanics Conference*, 2010.
- [17] Joel A DeLisa, Bruce M Gans, and Nicholas E Walsh. *Physical medicine and rehabilitation: principles and practice*, volume 1. Lippincott Williams & Wilkins, 2005.
- [18] Physiopedia. Proprioception. <http://www.physio-pedia.com/Proprioception>. Last accessed: June 22 2015.
- [19] Brian Coles. *Essentials of avian medicine and surgery*. John Wiley & Sons, 2008.
- [20] Uwe Proske and Simon C Gandevia. The proprioceptive senses: their roles in signaling body shape, body position and movement, and muscle force. *Physiological reviews*, 92(4):1651–1697, 2012.
- [21] Robert F Schmidt and Gerhard Thews. *Human physiology*. Springer, 1983.
- [22] Robert J Kosinski. A literature review on reaction time. *Clemson University*, 10, 2008.
- [23] Sharon A Plowman and Denise L Smith. *Exercise physiology for health fitness and performance*. Lippincott Williams & Wilkins, 2013.
- [24] Scott Kline Powers and Edward T Howley. *Exercise physiology: Theory and application to fitness and performance*. 2007.

- [25] A Mohamed, S Watkins, R Clothier, M Abdulrahim, K Massey, and R Sabatini. Fixed-wing mav attitude stability in atmospheric turbulence part 2: Investigating biologically-inspired sensors. *Progress in Aerospace Sciences*, 71:1–13, 2014.
- [26] Paul Noll. Avian muscles. <http://www.paulnoll.com/Oregon/Birds/Avian-Muscle.html>. Last accessed: June 22 2015.
- [27] John J Videler. *Avian flight*. Oxford University Press, 2006.
- [28] Mark NO Davies and Patrick Green. *Perception and motor control in birds: an ecological approach*. Springer Science & Business Media, 2012.
- [29] Andrei Sourakov. Faster than a flash: the fastest visual startle reflex response is found in a long-legged fly, *condylostylus* sp.(dolichopodidae). *Florida Entomologist*, 94(2):367–369, 2011.
- [30] Cedric Gillott. *Entomology*. Springer Science & Business Media, 2005.
- [31] Robert B Northrop. *Introduction to dynamic modeling of neuro-sensory systems*. CRC Press, 2000.
- [32] Vincent H Resh and Ring T Cardé. *Encyclopedia of insects*. Academic Press, 2009.
- [33] SASHA N Zill. Plasticity and proprioception in insects. ii. modes of reflex action of the locust metathoracic femoral chordotonal organ. *Journal of experimental biology*, 116(1):463–480, 1985.
- [34] Brian S Beckett. *Beginning Science: Biology*. Oxford University Press, 1983.
- [35] Rolf G Beutel, Frank Friedrich, Xing-Ke Yang, and Si-Qin Ge. *Insect Morphology and Phylogeny: A Textbook for Students of Entomology*. Walter de Gruyter, 2013.
- [36] Reginald Frederick Chapman. *The insects: structure and function*. Cambridge university press, 1998.
- [37] Zill Lab Sasha N. Zill. Mechanoreceptors in stick insects. <http://www.marshall.edu/bms/2012/08/30/sasha-n-zill-ph-d/>. Last accessed: June 22 2015.
- [38] Robin J Wootton. Functional morphology of insect wings. *Annual review of entomology*, 37(1):113–140, 1992.
- [39] MH Dickinson, S Hannaford, and J Palka. The evolution of insect wings and their sensory apparatus. *Brain, behavior and evolution*, 50(1):13–24, 1997.

- [40] Michael H Dickinson. Haltere-mediated equilibrium reflexes of the fruit fly, *Drosophila melanogaster*. *Philosophical Transactions of the Royal Society of London B: Biological Sciences*, 354(1385):903–916, 1999.
- [41] Robert Dudley. *The biomechanics of insect flight: form, function, evolution*. Princeton University Press, 2002.
- [42] PJ Albert, RY Zacharuk, and L Wong. Structure, innervation, and distribution of sensilla on the wings of a grasshopper. *Canadian Journal of Zoology*, 54(9):1542–1553, 1976.
- [43] Michael H Dickinson, Fritz-Olaf Lehmann, and KG Gotz. The active control of wing rotation by *Drosophila*. *The Journal of experimental biology*, 182(1):173–189, 1993.
- [44] SA Combes and TL Daniel. Flexural stiffness in insect wings i. scaling and the influence of wing venation. *Journal of experimental biology*, 206(17):2979–2987, 2003.
- [45] Pooya Ghaderi, Andrew J Dick, Jason R Foley, and Gregory Falbo. Spectral domain force identification of impulsive loading in beam structures. In *Topics in Nonlinear Dynamics, Volume 3*, pages 157–165. Springer, 2012.
- [46] James F Doyle. Force identification from dynamic responses of a bimaterial beam. *Experimental Mechanics*, 33(1):64–69, 1993.
- [47] Peter F Lester. *Turbulence: A new perspective for pilots*. Jeppesen Sanderson, 1994.
- [48] Francois Vandenberghe Robert Sherman. Turbulence forecast for manned and unmanned aerial vehicle, 2010.
- [49] Aviation Explorer Magazine. Atmospheric turbulence. <http://www.aviationexplorer.com/>. Last accessed: June 22 2015.
- [50] Michael V Cook. *Flight dynamics principles: a linear systems approach to aircraft stability and control*. Butterworth-Heinemann, 2012.
- [51] Stacey Gage. Creating a unified graphical wind turbulence model from multiple specifications. In *AIAA Modeling and simulation technologies conference and exhibit*, page 5529, 2003.
- [52] Frederic M Hoblit. *Gust loads on aircraft: concepts and applications*. Aiaa, 1988.
- [53] JT Vance, I Faruque, and JS Humbert. Kinematic strategies for mitigating gust perturbations in insects. *Bioinspiration & biomimetics*, 8(1):016004, 2013.

- [54] Hugh J Schmittle. Ultra-light aircraft with freely rotating rigid wing, February 4 1986. US Patent 4,568,043.
- [55] Vikramjit Singh, Logan Warren, Nathan Putnam, B Walther, P Becker, A Danielson, Babar Koraisy, W Wood, Dan Jensen, and Andy Szmerekovsky. A novel exploration into gust resistant operation of mavs/uavs through transformation. In *Second US-Euro MAV Conference, Destin, FL*, 2006.
- [56] Adetunji Oduyela and Nathan Slegers. Gust mitigation of micro air vehicles using passive articulated wings. *The Scientific World Journal*, 2014, 2014.
- [57] Matt Shields and Kamran Mohseni. Passive mitigation of roll stall for low aspect ratio wings. *Advanced Robotics*, 27(9):667–681, 2013.
- [58] Ted L. Lomax. *Structural loads analysis for commercial transport aircraft: theory and practice*. Aiaa, 1996.
- [59] WF Grosser, WW Hollenbeck, and DC Eckholdt. The c-5 a active lift distribution control system. *AGARD Impact of Active Control Technol. on Airplane Design 18 p(SEE N 75-30027 21-01)*, 1971.
- [60] Mordechai Karpel. Design for active flutter suppression and gust alleviation using state-space aeroelastic modeling. *Journal of Aircraft*, 19(3):221–227, 1982.
- [61] Richard W Wlezien, Garnett C Horner, Anna-Maria R McGowan, Sharon L Padula, Michael A Scott, Richard J Silcox, and Joycelyn S Harrison. Aircraft morphing program. In *5th Annual International Symposium on Smart Structures and Materials*, pages 176–187. International Society for Optics and Photonics, 1998.
- [62] Jie Zeng, Boris Moulin, Raymond De Callafon, and Martin Brenner. Adaptive feedforward control for gust load alleviation. *Journal of Guidance, control, and dynamics*, 33(3):862–872, 2010.
- [63] Santiago Basualdo. Load alleviation on wind turbine blades using variable airfoil geometry. *Wind Engineering*, 29(2):169–182, 2005.
- [64] D McLean. Gust-alleviation control systems for aircraft. In *Proceedings of the Institution of Electrical Engineers*, volume 125, pages 675–685. IET, 1978.
- [65] Volk J. A. Dreim D. R. & Applewhite K. A. Britt, R. T. aeroservoelastic characteristics of the b-2 bomber and implications for future large aircraft, structural aspects of flexible aircraft. 1999.
- [66] H Böhret, B Krag, and J Skudridakis. Olga: An open loop gust alleviation system. *AGARD Active Control Systems: Rev, Evaluation and Projections 16 p(SEE N 85-27883 17-08)*, 1985.

- [67] RM Rennie and EJ Jumper. Gust alleviation using trailing-edge flaps. In *37th AIAA Aerospace Sciences Meeting and Exhibit, Reno, NV*, 1999.
- [68] David C Soreide, Rodney K Bogue, LJ Ehernberger, and Harold R Bagley. Coherent lidar turbulence measurement for gust load alleviation. In *SPIE's 1996 International Symposium on Optical Science, Engineering, and Instrumentation*, pages 61–75. International Society for Optics and Photonics, 1996.
- [69] Raymond L Bisplinghoff and Holt Ashley. Half man, robert l.: Aeroelasticity, 1955.
- [70] Raymond L Bisplinghoff, Holt Ashley, and Robert L Halfman. *Aeroelasticity*. Courier Corporation, 2013.
- [71] Donald McLean. Automatic flight control systems(book). *Englewood Cliffs, NJ, Prentice Hall, 1990, 606*, 1990.
- [72] Mark Drela. Aswing 5.81 technical description, steady formulation. Technical report, Technical report, MIT, 2008.
- [73] TH Skopinski, William S Aiken, and Wilber B Huston. *Calibration of strain-gage installations in aircraft structures for the measurement of flight loads*. US Government Printing Office, 1954.
- [74] Boyd Perry III. Qualitative comparison of calculated turbulence responses with with an active control system. 1981.
- [75] M Frederick, EC Kerrigan, and JMR Graham. Gust alleviation using rapidly deployed trailing-edge flaps. *Journal of Wind Engineering and Industrial Aerodynamics*, 98(12):712–723, 2010.
- [76] Peter Bjoern Andersen, Lars Henriksen, Mac Gaunaa, Christian Bak, and Thomas Buhl. Deformable trailing edge flaps for modern megawatt wind turbine controllers using strain gauge sensors. *Wind Energy*, 13(2-3):193–206, 2010.
- [77] Eric Lee Brown. *Integrated strain actuation in aircraft with highly flexible composite wings*. PhD thesis, Massachusetts Institute of Technology, 2003.
- [78] Kenneth B Lazarus, Edward F Crawley, and Charrissa Y Lin. Multivariable active lifting surface control using strain actuation: analytical and experimental results. *Journal of Aircraft*, 34(3):313–321, 1997.
- [79] Charrissa Y Lin, Edward F Crawley, and Jennifer Heeg. Open-and closed-loop results of a strain-actuated active aeroelastic wing. *Journal of Aircraft*, 33(5):987–994, 1996.
- [80] Nhan Nguyen and Ilhan Tuzcu. Flight dynamics of flexible aircraft with aeroelastic and inertial force interactions. In *AIAA Atmospheric Flight Mechanics Conference, AIAA Paper*, volume 6045, 2009.

- [81] A De Gaspari, Sergio Ricci, Luca Riccobene, and Alessandro Scotti. Active aeroelastic control over a multisurface wing: Modeling and wind-tunnel testing. *AIAA journal*, 47(9):1995–2010, 2009.
- [82] Bing Feng Ng, Rafael Palacios, J Michael R Graham, and Eric C Kerrigan. Robust control synthesis for gust load alleviation from large aeroelastic models with relaxation of spatial discretisation. *Proceedings of the EWEA*, 2012.
- [83] Peter M Suh, Alexander W Chin, and Dimitri N Mavris. Virtual deformation control of the x-56a model with simulated fiber optic sensors. In *Proceedings AIAA Atmospheric, Flight Mechanics Conference*, 2014.
- [84] Animesh Chakravarthy, Katie A Evans, and Johnny Evers. Sensitivities & functional gains for a flexible aircraft-inspired model. In *American Control Conference (ACC), 2010*, pages 4893–4898. IEEE, 2010.
- [85] Stephen Chiu, Sujeet Chand, Doug Moore, and Ashwani Chaudhary. Fuzzy logic for control of roll and moment for a flexible wing aircraft. *Control Systems, IEEE*, 11(4):42–48, 1991.
- [86] M Cicala, VR Baraniello, and A Sollazzo. A load alleviation application of an elastic motion estimator for a flexible uav. In *Control & Automation (MED), 2011 19th Mediterranean Conference on*, pages 1229–1234. IEEE, 2011.
- [87] Y Matsuzaki, T Ueda, Y Miyazawa, and H Matsushita. Gust load alleviation of a transport-type wing-test and analysis. *Journal of aircraft*, 26(4):322–327, 1989.
- [88] Mayuresh J Patil and Dewey H Hodges. Flight dynamics of highly flexible flying wings. *Journal of Aircraft*, 43(6):1790–1799, 2006.
- [89] Gregory Gremillion. Bio-inspired disturbance rejection with ocellar and distributed acceleration sensing for small unmanned aircraft systems. 2015.
- [90] Rizwan Butt. *Introduction to Numerical Analysis Using MATLAB®*. Jones & Bartlett Learning, 2009.
- [91] Padula Sharon L and Kincaid Rex K. Optimization strategies for sensor and actuator placement. Technical report, NASA Langley Technical Report Server, 1999.
- [92] Firdaus E Udwardia. Methodology for optimum sensor locations for parameter identification in dynamic systems. *Journal of Engineering Mechanics*, 120(2):368–390, 1994.
- [93] Giuseppe Quaranta, Giuseppe Carlo Marano, Francesco Trentadue, and Giorgio Monti. Numerical study on the optimal sensor placement for historic swing bridge dynamic monitoring. *Structure and Infrastructure Engineering*, 10(1):57–68, 2014.

- [94] Giuseppe C Marano, Giuseppe Quaranta, Rita Greco, and Giorgio Monti. Sensor network design for monitoring a historic swing bridge. In *Proceedings of the International Symposium on Engineering under Uncertainty: Safety Assessment and Management (ISEUSAM-2012)*, pages 493–502. Springer, 2013.
- [95] Daniel C Kammer. Sensor placement for on-orbit modal identification and correlation of large space structures. *Journal of Guidance, Control, and Dynamics*, 14(2):251–259, 1991.
- [96] Masoud Sanayei and Chitra N Javdekar. Sensor placement for parameter estimation of structures using fisher information matrix. *Proc., Application of Advanced Technology in Transportation*, pages 386–393, 2002.
- [97] Wodek K Gawronski. Actuator and sensor placement. In *Dynamics and Control of Structures*, pages 100–128. Springer, 1998.
- [98] Daniel C Kammer. Optimal sensor placement for modal identification using system-realization methods. *Journal of Guidance, Control, and Dynamics*, 19(3):729–731, 1996.
- [99] COMSOL Multiphysics. Structural mechanics module–users guide, 2013.
- [100] William L Oberkampf, MM Sindir, and AT Conlisk. Guide for the verification and validation of computational fluid dynamics simulations. *Am. Institute of Aeronautics and Astronautics*, 1998.
- [101] NASA NPARC. Computational fluid dynamics (cfd) verification and validation. <http://www.grc.nasa.gov/WWW/wind/valid/>. Last accessed: June 22 2015.
- [102] Max Chtangeev. Borealis composites. max.chtangeev@borealiscomposites.com. Last accessed: June 22 2015.
- [103] Patrick R Amestoy, Ian S Duff, and J-Y L'Excellent. Mumps multifrontal massively parallel solver version 2.0. 1998.
- [104] Mark F Costello. Theory for the analysis of rotorcraft operating in atmospheric turbulence. In *Annual Forum Proceedings- American Helicopter Society*, volume 2, pages 1003–1015, 1990.
- [105] Professor Inderjit Chopra. Alfred gessow rotorcraft center, university of maryland, college park. <http://www.agrc.umd.edu/>. Last accessed: June 22 2015.
- [106] Professor Allen Winkelmann. Aerospace engineering laboratories -aerolab, university of maryland, college park. <http://www.aero.umd.edu/research-labs>. Last accessed: June 22 2015.

- [107] University of Florida. Reef aerodynamic characterization facility wind tunnel. www.reef.ufl.edu. Last accessed: June 22 2015.
- [108] Michael Sytsma and Lawrence Ukeiley. Wind tunnel generated turbulence. *AIAA Paper*, 1159, 2011.
- [109] GA Williamson, BD McGranahan, BA Broughton, RW Deters, JB Brandt, and MS Selig. Summary of low-speed airfoil data. *University of Illinois Low Speed Airfoil Tests*, 2012.